

On the effect of laser altimeter crossover observables on orbit determination with the JUICE mission as case study

Master Thesis

Sebastian Villamil

On the effect of laser altimeter crossover observables on orbit determination with the JUICE mission as case study

Master Thesis

by

Sebastian Villamil

To obtain the degree of Master of Science
at the Delft University of Technology,
to be defended publicly on Wednesday August 28, 2019 at 02:00 PM.

Student number: 4748417
Project duration: January 28, 2019 – August 28, 2019
Thesis committee: Dr. ir. D. Dirkx, TU Delft, supervisor
Prof. Dr. L.L.A. Vermeersen, TU Delft
Angelo Cervone, TU Delft
Dr. H. Hußmann, German Aerospace Center (DLR)

An electronic version of this thesis is available at <http://repository.tudelft.nl/>.
Cover image courtesy of the European Space Agency.

Abstract

This thesis' work aims to evaluate the potential added benefit to spacecraft orbit determination procedures upon using non-conventional measurements for orbit reconstruction. As a spacecraft orbits a celestial body, its ground tracks will naturally cross previous ground tracks at many points. These locations, known as crossover points, yield valuable information about the orbited body and the spacecraft trajectory using the spacecraft altitude measured during both passages at each crossover location.

To evaluate the impact of altimetry crossover measurements on orbit determination, the mission scenario of the planetary mission Jupiter Icy moons Explorer (JUICE) by the European Space Agency (ESA) is used as case study. As the mission's measurements will only be available several years from now, the resulting analysis is done with synthetic measurements obtained through numerical simulations. Herein, the necessary mathematical expressions for the inclusion of crossover measurements into orbit determination algorithms are presented, verified and evaluated. In doing so, it is shown that a first-order approximation of these expressions, as used in previous efforts, is insufficient and a more detailed expression is developed. Furthermore, the used crossover determination algorithm is presented in detail as well as the crossover selection filters in accordance to mission requirements. Finally, the sensitivities and intricacies of crossover measurements are discussed and their added value to orbit determination schemes is shown.

Contents

| | |
|--|-------------|
| Abstract | iii |
| Contents | v |
| List of Figures | vii |
| List of Tables | xi |
| Nomenclature | xiii |
| 1 Introduction | 1 |
| 1.1 Research Question, Aims and Objectives | 2 |
| 1.2 Thesis Outline | 2 |
| 2 The JUICE Mission | 3 |
| 2.1 JUICE Instruments | 4 |
| 2.2 Measurement Campaign | 5 |
| 2.3 Mission Science Objectives | 6 |
| 2.4 Ganymede | 8 |
| 3 Laser Altimetry | 11 |
| 3.1 The Ganymede Laser Altimeter (GALA) | 11 |
| 3.2 Altimetry Measurements | 12 |
| 3.3 Altimetry Crossovers | 13 |
| 4 Orbital Dynamics | 15 |
| 4.1 Central Body Geopotential | 16 |
| 4.2 Tidal Potential | 18 |
| 4.3 Third Bodies Effects | 20 |
| 4.4 Radiation Pressure | 20 |
| 4.5 Atmospheric Drag | 22 |
| 5 Precise Orbit Determination | 25 |
| 5.1 Definition of the Loss Function | 25 |
| 5.2 Application of the Loss Function | 27 |
| 5.3 Covariance Analysis | 30 |
| 5.4 Tracking Observables | 31 |
| 5.4.1 Range-Rate Data | 32 |
| 5.4.2 Viability Conditions | 32 |
| 5.5 Crossovers. | 33 |
| 5.5.1 Crossover Determination | 33 |
| 5.5.2 Crossover Selection | 35 |
| 5.5.3 Inclusion Into POD | 37 |
| 5.6 Measurement Errors | 41 |
| 5.6.1 Doppler Error Budget | 42 |
| 5.6.2 GALA Error Budget. | 43 |
| 5.6.3 Conclusion | 46 |

| | | |
|----------|--|------------|
| 5.7 | Definition of Tidal Partial | 46 |
| 6 | Numerical Simulation | 49 |
| 6.1 | SPICE | 49 |
| 6.2 | Mission Environment | 50 |
| 6.3 | Integrator and Propagator Settings | 50 |
| 6.4 | Trajectory Validation | 53 |
| 7 | Estimation Setup, Verification & Validation | 57 |
| 7.1 | Evaluation Scheme | 57 |
| 7.2 | Estimated Parameters | 58 |
| 7.3 | Numerical Partial Verification | 59 |
| 7.4 | Crossover Partial Verification | 62 |
| 7.5 | POD Verification | 67 |
| 7.6 | POD Validation | 69 |
| 7.7 | Verification of Tidal Partial | 70 |
| 8 | Results | 71 |
| 8.1 | Nominal Estimation Cases | 71 |
| 8.2 | Influence of Arc Length | 79 |
| 8.3 | Influence of Measurement Errors | 85 |
| 8.4 | Influence of Estimated Parameters | 87 |
| 8.5 | Crossover-Only Case | 91 |
| 8.6 | Estimation of Tidal Amplitude | 95 |
| 9 | Conclusion and Recommendations | 97 |
| 9.1 | Conclusion | 97 |
| 9.2 | Recommendations | 98 |
| A | Appendix | 101 |
| A.1 | Ganymede Gravity Field | 102 |
| A.2 | Jupiter Gravity Field | 103 |
| A.3 | JUICE Instruments | 103 |
| A.4 | Downlink Times | 104 |
| A.5 | Numerical Partial Derivatives | 105 |
| A.6 | Single Arc Verification | 106 |
| A.7 | Multi Arc Verification | 108 |
| A.8 | Effect of Arc Length | 112 |
| A.9 | Effect of Measurement Errors | 119 |
| A.10 | Effect of Estimated Parameters | 123 |
| A.11 | Crossover Only | 125 |
| | Bibliography | 127 |

List of Figures

| | | |
|-----|--|----|
| 2.1 | JUICE trajectory to the Jovian system using Earth and Venus for flybys to reach Jupiter [ESA, 2018a]. | 4 |
| 2.2 | JUICE mission logo [ESA, 2018a]. | 4 |
| 2.3 | Strategy to characterise Ganymede’s icy crust and liquid layer using combined techniques [ESA, 2014] | 7 |
| 2.4 | Deformation pattern on Ganymede in the presence of a global ocean [Steinbruegge et al., 2015] | 8 |
| 2.5 | Ganymede as seen by Galileo [Lissauer and de Pater, 2013] | 9 |
| 3.1 | Principle of two-way altimetry [van der Wal, 2017]. | 12 |
| 3.2 | Direct altimetry POD [Mazarico et al., 2018]. | 13 |
| 3.3 | Schematic of altimeter crossover geometry [Neumann et al., 2001]. | 13 |
| 4.1 | Accelerations acting on JUICE during GCO500. t_0 as defined in section 6.3. | 16 |
| 4.2 | Radial density of elements at equatorial (l.) and polar (r.) latitude for Ganymede [Marconi, 2007]. | 23 |
| 5.1 | Available communication windows for JUICE during GCO500 mission phase, with t_0 as defined in section 6.3. | 33 |
| 5.2 | All possible crossover locations during JUICE’s GCO500 mission phase. No crossover selection filters have been applied, see subsection 5.5.2. | 35 |
| 5.3 | Remaining crossovers between two downlink periods. t_0 as defined in section 6.3. | 36 |
| 5.4 | Crossover filter due to interpolation errors. t_0 as defined in section 6.3. | 36 |
| 5.5 | Filtered crossover locations during JUICE’s GCO500 mission phase using an arc length of 1 day. | 37 |
| 5.6 | Overview of some error sources: Alignment and point errors (A), spacecraft position errors (B), ranging/measurement errors (C) [Steinke, 2015]. | 41 |
| 5.7 | “Schematic representation of difference between accuracy and precision. The four plots show two-dimensional measurements (blue) on the same, arbitrary scale. Truth value indicated in red.” [Dirkx, 2015] | 42 |
| 5.8 | Geometry for pointing errors [Thomas et al., 2007] | 44 |
| 6.1 | Interpolation error for t_1 during crossover (xover) determination using a stepsize of 1 second as baseline. | 52 |
| 6.2 | Definition of initial ephemeris time t_0 onto JUICE’s trajectory, as within CReMA 3.0. | 53 |
| 6.3 | MultiArc trajectory validation, arc length: 10 days. Difference in radial distance to Ganymede’s centre of mass. | 53 |
| 6.4 | Difference in radial distance to Ganymede’s centre of mass between ESA CReMA 3.0 and MultiArc trajectories. | 54 |
| 6.5 | Evolution of JUICE’s Semi-major axis during GCO500 mission phase. | 54 |
| 6.6 | Evolution of JUICE’s eccentricity during GCO500 mission phase. | 54 |
| 6.7 | Evolution of JUICE’s inclination during GCO500 mission phase. | 55 |

| | | |
|------|---|----|
| 6.8 | Evolution of JUICE's Right Ascension of the Ascending Node (RAAN) during GCO500 mission phase. | 55 |
| 6.9 | Evolution of JUICE's Argument of Periapsis during GCO500 mission phase. | 55 |
| 7.1 | Numerically obtained partial derivatives for $\delta h_{\infty}/\delta x_0$ | 60 |
| 7.2 | Numerically obtained partial derivatives for $\partial h_{\infty}/\partial v_{x0}$ | 61 |
| 7.3 | Relative errors of analytical crossover partials w.r.t. numerical crossover partials for $\delta\Delta h/\delta z_0$. Two cases are shown for analytical crossovers: A basic one, based on Equation 5.55, and a more detailed one, based on Equation 5.75 and Equation 5.78. | 64 |
| 7.4 | Comparison of analytical and numerical crossover partials for $\delta\Delta h/\delta v_{x0}$. Two cases are shown for analytical crossovers: A basic one, based on Equation 5.55, and a more detailed one, based on Equation 5.75 and Equation 5.78. | 65 |
| 7.5 | "Spacecraft position error in the orbital frame (radial, across-track and along-track.)" [Parisi and Iess, 2012]. | 69 |
| 7.6 | Position uncertainty using Doppler data only, arc length: 1 day. Nominal parameter estimation. | 69 |
| 7.7 | Absolute difference between numerical and analytical tidal partial derivatives. | 70 |
| 8.1 | Position uncertainty using Doppler data only, arc length: 1 day. Nominal parameter estimation. | 72 |
| 8.2 | Position uncertainty using Doppler and crossover data, arc length: 1 day. | 72 |
| 8.3 | Comparison of position uncertainty between nominal Dopp and DoXo cases, arc length: 1 day. | 73 |
| 8.4 | Velocity uncertainty using Doppler and crossover data, arc length: 1 day. | 74 |
| 8.5 | Spherical Harmonics (SH) uncertainty using Doppler data only, arc length: 1 day. | 75 |
| 8.6 | Comparison of spherical harmonics (SH) uncertainty between nominal Dopp and DoXo cases, arc length: 1 day. | 75 |
| 8.7 | Correlation between estimated parameters using Doppler data only, arc length: 1 day. | 76 |
| 8.8 | Correlation between estimated parameters using Doppler and crossover data, arc length: 1 day. | 77 |
| 8.9 | Average, absolute off-diagonal correlation between state elements for each individual arc using Doppler data only (Dopp) and both Doppler and crossover data (DoXo). Arc length: 1 day. | 77 |
| 8.10 | Dopp design matrix H weighted by measurement uncertainty, arc length: 1 day. | 78 |
| 8.11 | DoXo design matrix H weighted by the respective measurement uncertainties, arc length: 1 day. | 79 |
| 8.12 | Position uncertainty using Doppler data only, arc length: custom, 1 day baseline. | 81 |
| 8.13 | Average, absolute off-diagonal correlation between state elements for each individual arc using Doppler data only (Dopp) and both Doppler and crossover data (DoXo). Arc length: 10 days. | 83 |
| 8.14 | Comparison of correlation between state elements. Arc length 1 day, state estimation only. | 88 |
| 8.15 | Empirical accelerations uncertainty for the Doxo case using an arc length of 1 day. Extended parameter estimation. | 89 |
| 8.16 | Empirical accelerations uncertainty for the Doxo case using an arc length of 1 day. Extended parameter estimation. | 90 |
| 8.17 | Comparison of empirical accelerations uncertainty between nominal Dopp and DoXo cases, arc length: 1 day. | 90 |

| | |
|--|-----|
| 8.18 Comparison of correlation between state elements. Arc length 1 day, extended parameter estimation. | 91 |
| 8.19 Position uncertainty using crossover data only. | 92 |
| 8.20 Position uncertainty using crossover data only. | 92 |
| 8.21 Spherical Harmonics (SH) uncertainty using crossover data only, arc length: 1 day. | 93 |
| 8.22 Parameter correlation using crossover data only. | 93 |
| 8.23 Parameter correlation using crossover data only. | 94 |
| 8.24 Comparison of correlation between state elements using crossover data only. Arc length 1 day. | 94 |
| | |
| A.1 Normalized Ganymede gravity field coefficients. n stands for degree, m for order, C for cosine coefficients and S for sine coefficients. Reference radius: 2634.0 km; gm : $9887.83445333 \text{ km}^3\text{s}^{-2}$ | 102 |
| A.2 JUICE Instruments [ESA, 2014]. | 103 |
| A.3 Numerically obtained partial derivatives for $\partial h_{\otimes}/\partial y_0$ | 105 |
| A.4 Numerically obtained partial derivatives for $\partial h_{\otimes}/\partial z_0$ | 105 |
| A.5 Numerically obtained partial derivatives for $\partial h_{\otimes}/\partial v_{y0}$ | 105 |
| A.6 Numerically obtained partial derivatives for $\partial h_{\otimes}/\partial v_{z0}$ | 106 |
| A.7 Comparison of analytical and numerical crossover partials for $\partial h_{\otimes}/\partial x_0$ | 106 |
| A.8 Comparison of analytical and numerical crossover partials for $\partial h_{\otimes}/\partial y_0$ | 106 |
| A.9 Comparison of analytical and numerical crossover partials for $\partial h_{\otimes}/\partial v_{y0}$ | 107 |
| A.10 Comparison of analytical and numerical crossover partials for $\partial h_{\otimes}/\partial v_{z0}$ | 107 |
| A.11 Comparison of analytical and numerical crossover partials for $\partial h_{\otimes}/\partial x_0$ in arc 1 | 108 |
| A.12 Comparison of analytical and numerical crossover partials for $\partial h_{\otimes}/\partial y_0$ in arc 1 | 108 |
| A.13 Comparison of analytical and numerical crossover partials for $\partial h_{\otimes}/\partial z_0$ in arc 1 | 108 |
| A.14 Comparison of analytical and numerical crossover partials for $\partial h_{\otimes}/\partial v_{x0}$ in arc 1 | 109 |
| A.15 Comparison of analytical and numerical crossover partials for $\partial h_{\otimes}/\partial v_{y0}$ in arc 1 | 109 |
| A.16 Comparison of analytical and numerical crossover partials for $\partial h_{\otimes}/\partial v_{z0}$ in arc 1 | 109 |
| A.17 Comparison of analytical and numerical crossover partials for $\partial h_{\otimes}/\partial x_0$ in arc 2 | 110 |
| A.18 Comparison of analytical and numerical crossover partials for $\partial h_{\otimes}/\partial y_0$ in arc 2 | 110 |
| A.19 Comparison of analytical and numerical crossover partials for $\partial h_{\otimes}/\partial z_0$ in arc 2 | 110 |
| A.20 Comparison of analytical and numerical crossover partials for $\partial h_{\otimes}/\partial v_{x0}$ in arc 2 | 111 |
| A.21 Comparison of analytical and numerical crossover partials for $\partial h_{\otimes}/\partial v_{y0}$ in arc 2 | 111 |
| A.22 Comparison of analytical and numerical crossover partials for $\partial h_{\otimes}/\partial v_{z0}$ in arc 2 | 111 |
| A.23 Relative error for multi arc verification. Within the first arc $z_{1,0}$ is perturbed by +0.1 m. Within the second arc $v_{x2,0}$ is perturbed by +0.0001 m/s. | 112 |
| A.24 Position uncertainty using Doppler data only, arc length: 2 days. | 112 |
| A.25 Position uncertainty using Doppler measurements only, arc length: 2 days. | 113 |
| A.26 Position uncertainty using Doppler data only, arc length: 3 days. | 113 |
| A.27 Position uncertainty using Doppler measurements only, arc length: 3 days. | 113 |
| A.28 Position uncertainty using Doppler data only, arc length: 4 days. | 114 |
| A.29 Position uncertainty using Doppler measurements only, arc length: 4 days. | 114 |
| A.30 Position uncertainty using Doppler data only, arc length: 5 days. | 114 |
| A.31 Position uncertainty using Doppler measurements only, arc length: 5 days. | 115 |
| A.32 Position uncertainty using Doppler data only, arc length: 6 days. | 115 |
| A.33 Position uncertainty using Doppler measurements only, arc length: 6 days. | 115 |
| A.34 Position uncertainty using Doppler data only, arc length: 7 days. | 116 |
| A.35 Position uncertainty using Doppler measurements only, arc length: 7 days. | 116 |
| A.36 Position uncertainty using Doppler data only, arc length: 8 days. | 116 |

| | |
|--|-----|
| A.37 Position uncertainty using Doppler measurements only, arc length: 8 days. . . . | 117 |
| A.38 Position uncertainty using Doppler data only, arc length: 9 days. | 117 |
| A.39 Position uncertainty using Doppler measurements only, arc length: 9 days. . . . | 117 |
| A.40 Position uncertainty using Doppler data only, arc length: 10 days. | 118 |
| A.41 Position uncertainty using Doppler measurements only, arc length: 10 days. . . | 118 |
| A.42 Position uncertainty degradation, Dopp error case 2. | 119 |
| A.43 Position uncertainty improvement using both Doppler and crossover measure- ments, DoXo error case 1. | 119 |
| A.44 Position uncertainty improvement using both Doppler and crossover measure- ments, DoXo error case 2. | 120 |
| A.45 Position uncertainty improvement using both Doppler and crossover measure- ments, DoXo error case 3. | 120 |
| A.46 Position uncertainty improvement using both Doppler and crossover measure- ments, DoXo error case 4. | 121 |
| A.47 SH uncertainty degradation, Dopp error case 2. | 121 |
| A.48 SH uncertainty improvement using both Doppler and crossover measurements, DoXo error case 1. | 121 |
| A.49 SH uncertainty improvement using both Doppler and crossover measurements, DoXo error case 2. | 122 |
| A.50 SH uncertainty improvement using both Doppler and crossover measurements, DoXo error case 3. | 122 |
| A.51 SH uncertainty improvement using both Doppler and crossover measurements, DoXo error case 4. | 122 |
| A.52 Dopp position uncertainty improvement w.r.t. nominal case when estimating fewer parameters. | 123 |
| A.53 DoXo position uncertainty improvement when estimating fewer parameters. . . | 123 |
| A.54 Dopp position uncertainty degradation w.r.t. nominal case when estimating additional parameters. | 124 |
| A.55 Dopp SH uncertainty degradation w.r.t. nominal case when estimating addi- tional parameters. | 124 |
| A.56 DoXo position uncertainty improvement when estimating additional parameters. | 124 |
| A.57 Velocity uncertainty using crossover measurements only, arc length: 1 day. State estimation only. | 125 |
| A.58 Velocity uncertainty using crossover measurements only, arc length: 1 day. Nominal parameter estimation. | 125 |

List of Tables

| | | |
|-----|--|----|
| 4.1 | Simplified parameters for Ganymede’s atmosphere [Lissauer and de Pater, 2013]. | 23 |
| 5.1 | Best and worst Doppler precision using an integration time of 60s. | 43 |
| 5.2 | Best and worst GALA instrument errors, 1σ values as defined by GALA’s Instrument Requirements Document [Lingenauber, 2019]. | 43 |
| 5.3 | Best and worst GALA pointing errors, 1σ values. | 45 |
| 5.4 | Best and worst GALA interpolation errors, 1σ values. | 45 |
| 5.5 | Best and worst error budgets for GALA measurements, 1σ values. | 45 |
| 5.6 | Best and worst crossover measurement error budgets, 1σ values. | 46 |
| 5.7 | Error cases based on Table 5.1 and Table 5.6. | 46 |
| 6.1 | Largest relative difference in orbital elements between this thesis’ and ESA’s trajectory. | 55 |
| 7.1 | Average relative error [%] for partial of position elements x_0 , y_0 and z_0 . | 60 |
| 7.2 | Average relative error [%] for partial of velocity elements v_{x0} , v_{y0} and v_{z0} . | 61 |
| 7.3 | Average relative error for analytical partial derivatives after 10 days using various stepsizes. | 63 |
| 7.4 | Average relative error [%] for basic and detailed analytical partial derivatives. Position elements only. | 63 |
| 7.5 | Average relative error [%] for basic and detailed analytical partial derivatives. Velocity elements only. | 65 |
| 7.6 | Average relative error [%] for analytical partial derivatives. Position elements only. | 66 |
| 7.7 | Average relative error [%] for analytical partial derivatives. Position elements only. | 66 |
| 7.8 | Average relative error for analytical and numerical partial derivatives after 1 and 10 days. | 67 |
| 7.9 | Average relative error [%] for analytical partial derivatives. Position elements only. | 68 |
| 8.1 | DoXo improvement for position uncertainty. Nominal case. | 73 |
| 8.2 | DoXo improvement for position uncertainty. Nominal case. | 74 |
| 8.3 | Average position uncertainty using Doppler measurements only. Arc with no Doppler data are not considered. | 80 |
| 8.4 | Average position uncertainty improvement by using Doppler and crossover measurements. Arc with no Doppler data are not considered. | 80 |
| 8.5 | Average SH uncertainty using Doppler measurements only. | 82 |
| 8.6 | Average improvement in SH uncertainty using crossover and Doppler measurements. | 82 |
| 8.7 | Number of crossovers depending on arc length. | 83 |
| 8.8 | Design matrix H file size depending on arc length. | 84 |
| 8.9 | Design matrix H condition number depending on arc length. | 85 |

| | |
|--|-----|
| 8.10 Error cases based on Table 5.1 and Table 5.6. | 85 |
| 8.11 Degradation of position uncertainty resulting from worse Doppler measurement uncertainty. | 86 |
| 8.12 Improvement in position uncertainty using both crossover and Doppler measurement for the 4 error cases shown in Table 8.10. | 86 |
| 8.13 Degradation of position uncertainty resulting from worse Doppler measurement uncertainty. | 86 |
| 8.14 Improvement in position uncertainty using both crossover and Doppler measurement for the 4 error cases shown in Table 8.10. | 87 |
| 8.15 Position uncertainty improvement resulting from fewer estimation parameter. | 87 |
| 8.16 Degradation of position uncertainty resulting from worse Doppler measurement uncertainty. | 88 |
| 8.17 Dopp degradation in estimation uncertainty for an extended parameter estimation. | 89 |
| 8.18 Improvement in position uncertainty from using both Doppler and crossover measurements. Extended parameters estimation. | 89 |
| 8.19 DoXo improvement in emp. acc. uncertainty. | 91 |
| A.1 Normalized Jupiter gravity field coefficients. n stands for degree, m for order, C for cosine coefficients and S for sine coefficients. Reference radius: 71398 km; gm: $126712767.85779597 \text{ km}^3\text{s}^{-2}$ | 103 |
| A.2 List of JUICE's DownLink times. Downlink times around an occultation window are marked bold | 104 |

Nomenclature

Acronyms

| | | | |
|---------|--|-------|---|
| 3GM | Gravity & Geophysics of Jupiter and Galilean Moons | IK | Instrument Kernel |
| ABM | Adam-Bashforth-Moulton integration method | ISRP | Indirect Solar Radiation Pressure |
| BELA | BepiColombo Laser Altimeter | J-MAG | JUICE MAGnetometer |
| CK | Camera matrix (orientation) Kernel | JANUS | Jovis, Amorum ac Natorum Undique Scrutator |
| COE | Classical Orbital Elements | JOI | Jupiter Orbit Insertion |
| CP | Contractivity-Preserving | LRO | Lunar Reconnaissance Orbiter |
| CR3BP | Circular Restricted 3 Body Problem | LSK | LeapSeconds Kernel |
| Cyl | Cylindrical coordinates | MAJIS | Moons and Jupiter Imaging Spectrometer |
| CylHz | Cylindrical with H_z coordinates | MCPI | Modified Chebyshev-Picard Iteration |
| DLR | German Aerospace Center | MGS | Mars Global Surveyor |
| DOP | Dormand & Prince integration method | MK | Meta-Kernel |
| DSK | Digital Shape Kernel | MOLA | Mars Observer Laser Altimeter |
| DST | Digital Shape Model | NAIF | Navigation and Ancillary Information Facility |
| e.g. | (latin, <i>exempli gratia</i>) for example | NASA | National Aeronautics and Space Administration |
| EccHill | Eccentric Hill variables | PCK | Planetary constants Kernel |
| EK | Events Kernel | PEP | Particle Environment Package |
| ESA | European Space Agency | POD | Precise Orbit Determination |
| ET | Ephemeris Time | PRIDE | Planetary Radio Interferometer & Doppler Experiment |
| FE | Finite Elements | RAAN | Right Ascension of the Ascending Node |
| FK | reference Frame Kernel | RIME | Radar for Icy Moons Exploration |
| GALA | GANymede Laser Altimeter | RK4 | Runge-Kutta 4 |
| GL-IRK | Gauss-Legendre implicit Runge-Kutta | RKFB | Runge-Kutta-Fehlberg |
| GLAS | Geoscience Laser Altimeter | RPWI | Radio & Plasma Wave Investigation |
| GOI | Ganymede Orbit Insertion | SCLK | Spacecraft CLock Kernel |
| GRAIL | Gravity Recovery and Interior Laboratory | SNR | Signal-to-Noise Ratio |
| HO | Hermite-Obrechhoff | SPK | SPacecraft and planet ephemeris Kernel |
| HOTM | High-Order Transfer Map | SRP | Solar Radiation Pressure |
| HST | Hubble Space Telescope | SSB | Solar System Barycenter |
| i.e. | (latin, <i>id est</i>) In other words | SVD | Singular Value Decomposition |
| IERS | International Earth Rotation Service | SWI | Sub-millimeter Wave Instrument |
| | | TRP | Thermal radiation pressure |
| | | USM | Unified State Model |
| | | USMEM | USM Exponential Method |
| | | UTC | Universal Time Coordinated |

| | | | | | |
|----------------------|-----------------------------------|--|---------------------|----------------------------------|--|
| UVS | UV imaging Spectrograph | | d | Distance | [d] |
| VLBI | Very-Long-Baseline Interferometry | | e | Eccentricity | [-] |
| w.r.t. | with respect to | | f | Frequency | [s ⁻¹] |
| WOL | Wheel-off-loading | | f | Function | [-] |
| Greek Symbols | | | | | |
| ρ | Distance (vector) | [km] | G | Gaussian distribution | |
| ρ | Range measurement (vector) | [km] | G | Universal gravitational constant | [m ³ kg ⁻¹ s ⁻²] |
| Δ | Difference | | g | Gravitational acceleration | [km s ⁻²] |
| $\dot{\rho}$ | Range-rate measurement | [km/s] | i | Inclination | [degrees] |
| η | Quaternion | [-] | M | Mass | [kg] |
| μ | Gravitational constant | [m ³ kg ⁻¹ s ⁻²] | m | Mass | [kg] |
| μ | Mean error | | m | Order | [-] |
| ν | Quaternion | | n | Degree | [-] |
| Ω | RAAN | [rad] | n | Number of elements | [-] |
| ω | Argument of perigee | [rad] | P | SRP at d from the Sun | [N m ⁻²] |
| Φ | State transition matrix | | r | Radial distance (scalar) | [km] |
| ϕ | Latitude | [rad] | T | Time | [s] |
| ϕ | Pointing | [rad] | t | Time | [s] |
| ρ | Density (scalar) | [kg m ⁻³] | v | Velocity (scalar) | [km s ⁻¹] |
| ρ | Distance (scalar) | [km] | AU | Astronomical Unit | [km] |
| τ | Time | [s] | C | Coefficient | [-] |
| ε | Error | | c | Speed of light | [km s ⁻¹] |
| ζ | Eccentricity component | | H | Angular momentum | [kg m ² s ⁻¹] |
| Roman Symbols | | | | | |
| F | Force (vector) | [N] | h | Altitude | [km] |
| p | Parameter vector | | h | Time step | [s] |
| q | Force model parameter vector | | S | Sensitivity matrix | |
| r | Radial distance (vector) | | s | Shrinking factor | |
| s | State vector | | Superscripts | | |
| v | Velocity vector | | – | Normalised | |
| x | x-axis | | · | First derivative | |
| y | Measurements vector | | ^ | POD solution term | |
| y | y-axis | | T | Transpose | |
| z | z-axis | | Subscripts | | |
| H | Design matrix | [-] | ⊗ | Crossover | |
| A | Area | [m ²] | 0 | Linearisation point | |
| a | Acceleration | [km s ⁻²] | 0 | Zero | |
| a | Semi-major axis | [km] | a | Absolute | |
| | | | a | Alignment | |
| | | | a | Ascending track | |

| | | | |
|----------|---------------------------------------|-----------|--|
| Basic | Basic crossover partial derivative | n | Element of series |
| D | Drag | Numerical | Numerical crossover partial derivative |
| d | Descending track | | |
| Detailed | Detailed crossover partial derivative | R | Radiation |
| F | First | R | Receiver |
| g | geodetic | r | Relative |
| i | Element of series | req | Required |
| j | Element of series | s | Geocentric |
| k | Element of series | Sph | Sphere |
| L | Last | SRP | Solar Radiation Pressure |
| l | Element of series | SSB | Solar System Barycentre |
| m | Element of series | T | Transmitter |

1

Introduction

The Jupiter ICy moons Explorer (JUICE) mission has been selected by the European Space Agency (ESA) as the first large mission within its Cosmic Vision Program 2015-2025, see [chapter 2](#). The mission's goal is to study and further characterise the Jovian system, with its main focus being the further characterisation of the Jovian moon Ganymede [[Grasset et al., 2013](#)]. The strong evidence for subsurface oceans within Jupiter's icy moons is particularly revolutionary as the occurrence of liquid water drastically increases the number of potential habitats for life in the universe, whereas previously only Earth-like environments were considered. Thus, a deeper understanding of the Jovian system would not only provide insights into the formation of gas giants and their satellites, but also into the conditions for habitability within icy moons. One major challenge JUICE faces are the strong constraints regarding its measurement periods leading to an alternation between measurement intervals and downlink periods. Within this alternation, tracking is only available during its downlink periods leading to large intervals of time for which JUICE's trajectory suffers from large uncertainties [[Grasset et al., 2013](#); [Vallat, 2019](#); [ESOC, 2015](#)].

This thesis uses the JUICE mission as a case study to analyse the effect of the inclusion of altitude differences at crossover points has on orbit determination procedures. A crossover point, refers to the points where a satellite's ground tracks and/or measurements cross one another in the body-fixed frame of the orbited body. For further details on crossovers see [section 3.3](#). Previous studies on satellites orbiting Earth, Earth's moon and Mars have shown that the use of altimetry crossover measurements can lead to an improvement in orbit determination [[Rowlands et al., 1999](#); [Neumann et al., 2001](#); [Rowlands et al., 2008](#); [Mazarico et al., 2010, 2011, 2018](#)]. Here, the effect of crossovers shall be quantified and its potential benefit to future missions shall be established. The altimetry measurements whose effect on orbit determination this thesis studies, are obtained by JUICE's instrument GALA (GANymede Laser Altimeter). GALA's primary task is to determine the Jovian moons' topography while also aiding in constraining Ganymede's tidal deformation to infer knowledge about its internal structure and rheology, see [section 2.3](#).

Since the mission's scientific data will only be after the year 2033, their analysis must be done with synthetic measurements obtained through numerical simulations. Therein, only the final mission phase shall be studied during which JUICE is in a stable orbit around Ganymede.

1.1. Research Question, Aims and Objectives

To evaluate the potential benefits of including altimetry crossover observables for the orbit determination of planetary missions, this thesis' **research question** is:

- To what extent do laser altimetry crossover observables improve orbit determination errors for the JUICE spacecraft?

To answer the overarching research question above, the following **primary subquestions** must be answered:

- What is the mathematical formulation that includes all required dependencies to implement laser altimetry crossovers into an orbit determination procedure?
 - Which parameter correlations are relevant to the inclusion of laser altimeter crossovers observables into a precise orbit determination (POD) scheme?
- To obtain representative estimation uncertainties, what are the budgets which must be considered for:
 - laser altimetry measurement errors?
 - pointing and attitude errors?
 - tracking measurement errors?
 - POD estimation errors?
- What are relevant force model elements to include in the simulation?
- Which numerical propagation and integration schemes yield an adequate trade-off between numerical accuracy and computational times for JUICE's orbit and its orbit perturbations?

The analysis' results shall be used to make recommendations whether to apply crossover observables onto JUICE's orbit determination procedures once data is acquired. Additionally, the thesis shall help define potential added value to altimeters for planetary missions.

1.2. Thesis Outline

Within [chapter 2](#), the motivation and design of the JUICE mission are presented as well as its scientific targets and the current knowledge on the scientific objectives. In the following [chapter 3](#), the instrument which enables the collection of crossover measurements is presented and the concept of laser altimetry crossover observables is detailed. In [chapter 4](#), the driving effects for JUICE's motion during the treated mission phase are presented and the main influencing factors are determined for inclusion in the numerical simulation. Within [chapter 5](#), the mathematical foundation for orbit determination algorithms is elaborated upon, as are the necessary expressions for the inclusion of crossover measurements therein. Additionally, relevant error sources and budgets for the relevant measurements are established. [Chapter 6](#) covers the settings of the numerical simulation, while [chapter 7](#) describes the used evaluation scheme in detail. Finally, [chapter 8](#) presents and evaluates the results of orbit determination efforts with and without crossover measurements allowing [chapter 9](#) to reach a conclusion on the added effect of crossover measurements to orbit determination schemes.

2

The JUICE Mission

The results of the previous mission to the Jovian system, obtained by the Galileo spacecraft which was launched by the National Aeronautics and Space Administration (NASA), have fuelled a spike in interest towards the further characterisation of the Jovian system [Niemann et al., 1998; Fanale et al., 1999; Zimmer et al., 2000; Plainaki et al., 2015]. In particular, the strong evidence for subsurface oceans within Jupiter's icy moons is particularly revolutionary as the existence of liquid water drastically increases their potential habitability, whereas only Earth-like environments with surface oceans were considered previously. Further remarkable results include insights into the Jovian's atmosphere and magnetosphere and Ganymede's internal magnetic field [Kivelson et al., 1996, 2002; Niemann et al., 1998; Ragent et al., 1998; Zimmer et al., 2000; Spohn and Schubert, 2003]. Thus, a deeper understanding of the Jovian system would not only provide insights into the formation of gas giants and their satellites, but also into the conditions for habitability within icy moons.

To advance our understanding in these areas the European Space Agency (ESA) has selected the JUpiter ICy moons Explorer (JUICE) mission as the first large mission (L-mission) for its Cosmic Vision Program 2015-2025. This choice covers two of the key science themes of the Cosmic Vision Program [ESA, 2011, 2014; Grasset et al., 2013]:

- What are the conditions for planet formation and the emergence of life?
- How does the Solar System work?

In order to find answers to these questions JUICE will study the Jovian system as a miniature solar system. Therein, Jupiter and its plethora of interactions with its satellites will be further characterised as well as the interactions between the Galilean moons Io, Europa and Ganymede in particular. Overall, the mission's main focus is on Ganymede as an archetype satellite around a gas giant and its unique characteristics such as its intrinsic magnetic field [Kivelson et al., 1996]. These goals are encompassed into the mission's design by multiple flybys around the Galilean moons with the mission's final phase consisting of a stable orbit around Ganymede. Incidentally, the mission will conclude with JUICE being plunged onto Ganymede's surface [ESA, 2014; Grasset et al., 2013].

Any potential findings are not confined to the Jovian system however. It is expected that many are transferable to exoplanetary systems, as the Jovian system is regarded as an archetype for exoplanets. As such, the overarching theme for the JUICE mission is the emergence of habitable worlds around gas giants with its key science goals being [ESA, 2014; Grasset et al., 2013]:

- Explore the habitable zone: Ganymede, Europa, and Callisto,
- Explore the Jupiter system as an archetype for gas giants.

JUICE's launch is scheduled for June 2022 on an Ariane 5 launcher to initiate its 7.5-year long journey to the Jovian system. To achieve this interplanetary transfer, using less propellant than otherwise necessary, JUICE will have several flybys around Earth and Venus, with a Venus flyby leading the spacecraft as close as 0.64 Astronomical Units (AU) to the Sun.

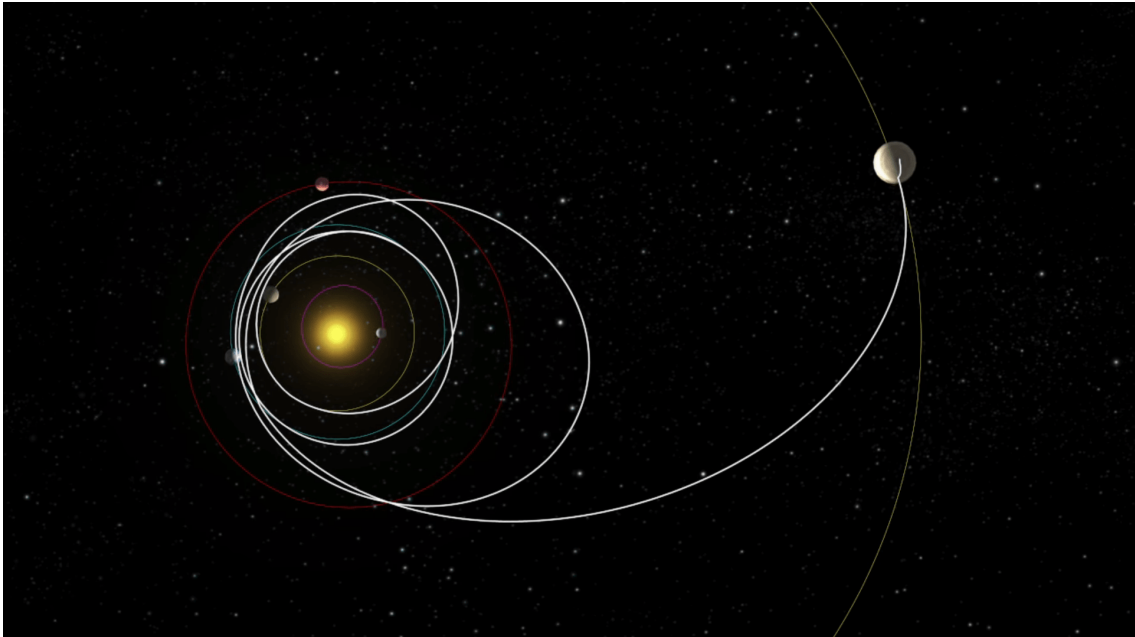


Figure 2.1: JUICE trajectory to the Jovian system using Earth and Venus for flybys to reach Jupiter [ESA, 2018a].

After successful Jupiter Orbit Insertion (JOI), JUICE will start its 3.5-year tour in the Jovian system, with its nominal science phase being described in [section 2.2](#). The chosen prime contractor for the JUICE spacecraft is Airbus Defence and Space [ESA, 2014; Grasset et al., 2013].

2.1. JUICE Instruments

To further characterise the Jupiter system the JUICE spacecraft carries ten scientific instruments presented in [Appendix A.3](#) which are grouped in three packages due to their respective tasks and goals. The *remote sensing package* consists of the instruments JANUS, MAJIS, UVS and SWI with their main tasks being imaging and spectral-imaging. The *geophysical package* is made up of the laser altimeter GALA and the radar sounder RIME to analyse surfaces and subsurfaces. Due to its importance to this thesis, the instrument GALA is presented individually further in [section 3.1](#).

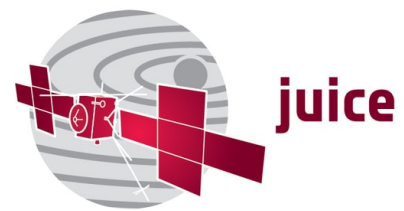


Figure 2.2: JUICE mission logo [ESA, 2018a].

Another member of the geophysical package is the radio science package 3GM, whose main scientific goal is to characterise the Jovian gravity fields. Within its orbit determination additional parameters such as accelerometer biases shall also be estimated. The algorithm to achieve such an estimation is discussed further in [chapter 5](#). The final package is the *in situ package* which includes the instruments PEP, J-MAG and RPWI whose goal is to study the particle and plasma environments as well as the magnetic fields of the Jovian system. While

not an on-board instrument the PRIDE experiment will determine JUICE's transverse celestial position to improve its POD and determine the ephemeris of the Jovian bodies via Earth-based Very-Long-Baseline Interferometry (VLBI) [Dirkx et al., 2017].

Due to Jupiter's particularly strong magnetic field and the resulting high energy particles, shielding plays a major role in instrument design often making up a large part of the instruments' mass and volume. For GALA, shielding makes up $\sim 20\%$ of the total mass budget [Rech, 2019] - a substantial amount, especially regarding the highly limited mass budget satellites have due to immense costs associated with their launch [Wakker, 2015].

2.2. Measurement Campaign

Once within Jupiter's sphere of influence JUICE will begin its scientific phase, which is divided into several sub-phases: *Jupiter Equatorial Phase*, *Europa Phase*, *Inclined Orbit Phase* and the *Ganymede Orbit Phases*. For the definition of *sphere of influence* see [section 4.1](#).

Within the *Jupiter Equatorial Phase*, several flybys are performed around Jupiter and its Galilean moons Ganymede, Callisto and Europa to perform both orbit adjustments and initial scientific measurements. The follow-up *Europa Phase* is dedicated to study Europa via two flybys over identified regions of interest. Therein, adequate illumination conditions must met to fulfil requirements by imaging systems and spectrometers. During the *Inclined Orbit Phase* JUICE will investigate Jupiter's poles in the ultra-violet spectrum while reaching a maximum inclination of 22° with the help of several Callisto-flybys. Thereafter, JUICE will enter its primary and final mission phase: the *Ganymede Orbit Phases*. The Ganymede Orbit Insertion (GOI) into these phases is achieved via several Ganymede and Callisto flybys leading up to polar bound orbits around Ganymede. The first Ganymede orbit phase is the Ganymede Circular Orbit phase at an altitude of 5000 km (GCO5000) which is highly eccentric and has an orbital period of ~ 12 hours. The GCO5000 phase is followed by the circular orbit phase at an altitude of 500 km (GCO500) which has an orbital period of 3 hours and a nominal duration of 133 days. The GCO500 mission phase is the main focus of this thesis' orbit determination studies, which are detailed in [chapter 7](#).

Since JUICE does not have a steerable high-gain antenna for communication and data downlink, the entire spacecraft must be rotated to establish communication with the Malargüe ground station. Therefore, JUICE will have a nominal, daily 8 hour period for data downlink and tracking leading to uncertainties regarding JUICE's state until the next tracking period commences. This is a particularly critical factor regarding the orbit reconstruction of JUICE as it operates in a perturbed environment which has yet to be tightly constrained, with JUICE having an orbital period of merely 3 hours. These factors are principal drivers for the orbit estimation process as described further in [chapter 5](#). Equally, instruments which require nadir pointing can only collect new scientific measurements during the time between tracking windows [ESA, 2014, p.103]. The implications of these alternating windows is discussed further in [subsection 5.4.2](#). The Malargüe ground station, which has been assigned as single communication point for JUICE, is ESA's newest tracking station and is located in Argentina. The coordinates of the antenna are $35^\circ 46' 33.63''$ S (35.776° S), $69^\circ 23' 53.51''$ W (69.398° W), and the station is located 1550 m above sea level [Estrack, 2019].

Nominally, GCO-500 is JUICE's final mission phase before being impacted on Ganymede at mission's end. However, there is the possibility for a mission extension of up to an additional year made up of a GCO-200 phase which would greatly improve the characterisation of Ganymede.

2.3. Mission Science Objectives

While the key science objective of JUICE's mission is understanding ***the emergence of habitable worlds around gas giants***, this document will merely deal with the objective of characterising ***Ganymede as planetary object and potential habitat*** as this thesis only deals with GCO500 as described in [section 2.2](#). The science objectives for Ganymede are [ESA, 2011, 2014; Grasset et al., 2013]:

- Characterise the extent of the **ocean** and its relation to the **deeper interior**
- Characterise the **ice shell**
- Determine global composition, distribution and evolution of **surface materials**
- Understand the formation of **surface features** and search for past and present activity
- Characterise the local environment and its interaction with the Jovian **magnetosphere**

Naturally, achieving these objectives requires close collaboration using the instruments' scientific results as shown in [Figure 2.3](#) and discussed further below. Another example is how GALA measurements help constraining surface characteristics together with the data obtained through sounding by the RIME instrument. While RIME's main focus is the structure within the ice, it will also offer insights on Ganymede's surface structure. In particular, surface characteristics such as ridges, elevations or cracks can be validated with the digital shape model created with GALA's measurements. It should be noted that the precise orbit determination (POD) of JUICE is of utmost importance as any uncertainty in JUICE's state inevitably not only leads to additional uncertainties in the estimated parameters, such as spherical harmonic coefficients, it also leads to larger uncertainties in the measurements of all instruments.

JUICE's POD is achieved mainly via spacecraft tracking through 3GM making use of radial range-rate information on JUICE's state. For details on the mathematical background see [section 5.1](#) and [section 5.2](#), with range-rate measurements being detailed in [subsection 5.4.1](#). While the PRIDE experiment aids in JUICE's POD by providing radial range-rate data as well as JUICE's transverse celestial position, it is primarily concerned with the ephemeris of Jupiter and the Galilean satellites [Dirkx et al., 2017]. For 3GM, one of its main goals regarding Ganymede is the estimation of its gravity field up to a degree and order of 12. For more details on gravity fields see [section 4.1](#). Besides the generation of a global topography model for Ganymede, one of GALA's major goals is to estimate Ganymede's love number h_2 which is a measure for the radial tidal deformation of the body, see [section 4.2](#) for further details.

For several moons in the Jovian system previous studies have shown that under the solid ice mantle of these moons, either global or partially global subsurface oceans can be expected [Steinbruegge, 2018; Hussmann et al., 2016; Jia et al., 2018; Moore and Schubert, 2000]. Due to the topic of this document: The potential improvement of POD algorithms with crossover altimetry data using JUICE as case study, the characterisation of the ice shell and the subsurface ocean will be elaborated upon as the behaviour of the ice shell directly affects crossover measurements. In addition to their effect on altimetry crossover measurements through surface deformation, these planetary features also affect Ganymede's gravity field and in turn JUICE's trajectory. The characterisation of Ganymede's ice shell and subsurface ocean goes hand in hand, aptly demonstrated by the following figure: JUICE aims to further constrain Ganymede's ice-shell and ocean thickness by diminishing all four uncertainty areas shown in [Figure 2.3](#). Therein, the melting curve correlates to the stability of ice, which is dependent on Ganymede's temperature profile and its volatiles. Besides Ganymede's intrinsic magnetic field, there is also a measurable induced one due to the electrical conductivity of the subsurface ocean which JMAG will measure precisely. While challenging to measure, the amplitude of variations in Ganymede's rotational rate, depend largely on the density contrast between the surface ice and the ocean [Moore and Schubert, 2003; Steinbruegge et al., 2015]. Here, GALA's, 3GM's and JANUS' temporal coverage will provide insights regarding the rotation rate

and the orientation of the spin pole. Last but not least, the Love numbers k_2 and h_2 describe the satellite's material response to tidal forcing due to its rigidity, viscosity and the tidal frequency [Hussmann et al., 2016; Jara-Oru  and Vermeersen, 2016; Kamata et al., 2016].

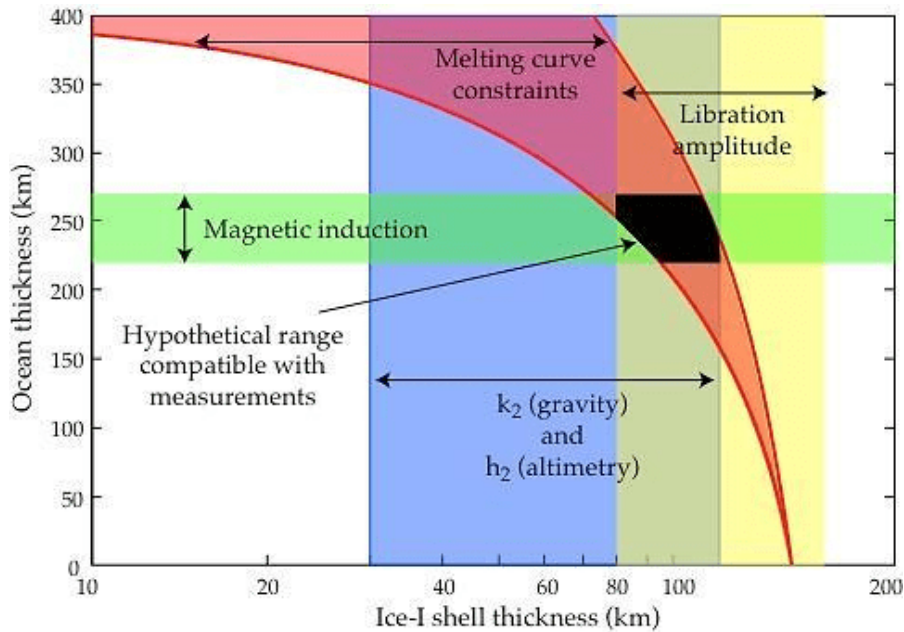


Figure 2.3: Strategy to characterise Ganymede's icy crust and liquid layer using combined techniques [ESA, 2014]

Not shown in Figure 2.3 is the Love number l_2 as it is not measured by any of JUICE's instruments. l_2 describes the surface's lateral/tangential displacement due to tidal forcing. The love number k_2 describes the change in gravity potential caused by the redistribution of mass due to the deforming potential, therefore most aptly measured by 3GM through temporal changes in the gravitation field. Conversely, the Love number h_2 describes the radial deformation amplitude resulting from the tidal forcing. One possible method to determine h_2 is by comparing GALA range measurements of the same locations at different tidal phases, discussed further in section 5.7. These points, where subsequent ground tracks intersect are known as ground tracks crossovers, see section 5.5 for more details. In the presence of a subsurface ocean, the deformation amplitude is consequently much larger than without a subsurface ocean due to the decoupling of core and surface material. The deeper the ocean, the larger the deformation and the Love number h_2 [Moore and Schubert, 2003]. The resulting deformation from tidal forcing over one orbital period of Ganymede around Jupiter can be seen on the left half of Figure 2.4. The pattern therein results from the maximum deformation experienced by different areas on Ganymede due to Jupiter's tidal forcing. It clearly shows that while some equatorial areas experience a maximum deformation of 7 meters not all equatorial areas do so and there are even some areas on Ganymede that are not deformed at all. Since the planetary deformation has its highest amplitude at the equator, the occurrence of a large number of crossovers at this latitude at different tidal phases is an important mission requirement of GALA. Within Figure 2.4 both plots display Ganymede's tidal signal during one orbital revolution around Jupiter, with the right plot being the tidal signal as measured by GALA. Therein, white areas display locations where no crossover was obtained and no difference in ground height could be established. For more information on crossovers see section 5.5. The several black areas within GALA's measurements, which denote a deformation of zero meters, arise from the GALA measurements in those areas being repeatedly during the same orbital phase.

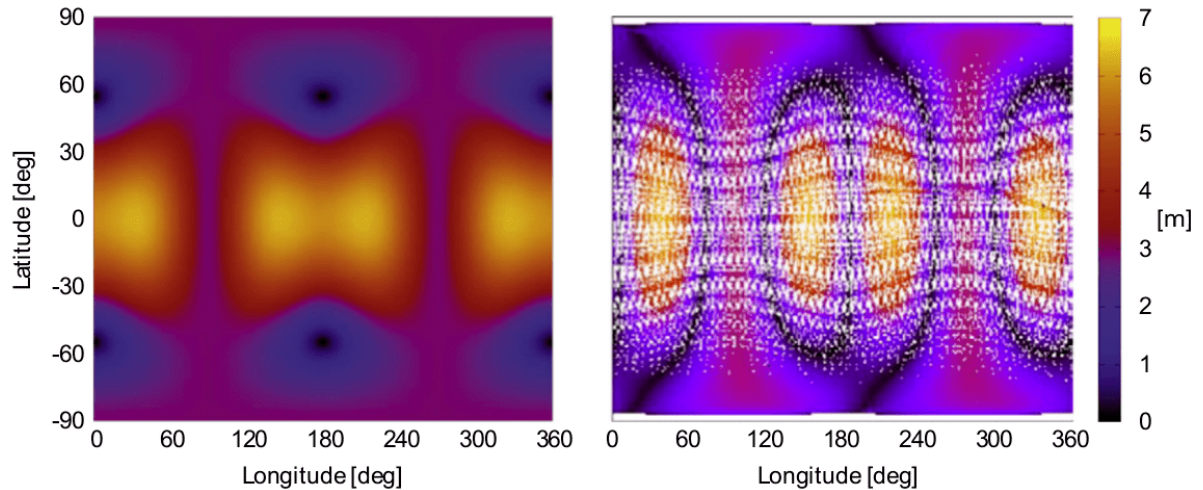


Figure 2.4: Deformation pattern on Ganymede in the presence of a global ocean [Steinbruegge et al., 2015]

As Ganymede's deformation is the same during its orbital phases GALA no differences in topography are measured, resulting in the pattern shown. Naturally, this pattern is highly orbit dependent.

2.4. Ganymede

As mentioned in section 2.2, JUICE's goal is to further characterise all Jovian moons. As altimetry crossover measurements as discussed in section 3.3 are collected continuously during the GCO500 mission phase, only Ganymede is presented here in detail. Ganymede is the third and largest Galilean moon around Jupiter. Its density measurements suggest a composition of 60% rock and 40% ice with its moment of inertia suggesting that its mass is heavily concentrated at its centre [Anderson et al., 2004]. The potentially most stunning feature of Ganymede, is the existence of an intrinsic magnetic field as measured by Galileo which is indicative of a liquid metallic core, with current estimates expecting it to have a radius of 400-1300 km [Rückriemen et al., 2015, 2018; Anderson et al., 1996; Showman et al., 1999].

The tidal forcing on Ganymede due to Jupiter, dictates many of the geological features found on its surface. One such feature is that Ganymede's impact craters are flattened with time [Nimmo, 2004; Thomas and Schubert, 1986]. This flattening is attributed to the relaxation and movement of the surface ice which originates directly and indirectly from Jupiter's tidal forcing [Strom et al., 1981; Pappalardo and Collins, 2005]. Directly due to the surface deformation and indirectly due to the tidal forces leading to internal heating. However, it is expected that radiogenic heating is mostly responsible for Ganymede's subsurface ocean and its expected surface deformations as discussed in section 2.2.

Nevertheless, in spite of Ganymede's internal heating there is not much evidence for active surface rejuvenation. While there are areas which are distinctively younger, it is assumed that they originate in cryovolcanism that is no longer active. The argument for an old planetary surface is strengthened by the large number of visible impact craters which suggest that many of its surface areas have remained mostly the same since Ganymede's period of heavy meteor bombardment [Strom et al., 1981]. Another argument for Ganymede's old surface is its low albedo which is indicative of its surfaces being exposed to sputtering and sublimation over long periods of time [McCord et al., 2001].

Sublimation of surface particles occurs due to the large pressure difference between Ganymede's surface and its tenuous atmosphere with most sublimation occurring on the side facing the Sun. For more details on Ganymede's atmosphere see [section 4.5](#). Sputtering describes the impact of high energy particles which leads to particles being ejected from the ice. Sputtering leads to lighter particles, such as hydrogen or oxygen, being ejected from the moon's surface while heavier particles remain on the upper most surface layer [[McCord et al., 1998](#); [Ip et al., 1998](#)]. The highly energetic particles that cause sputtering rotate due and with Jupiter's strong, rapidly rotating magnetic field. Since Jupiter rotates much faster than Ganymede's orbital period it is mainly Ganymede's trailing side that is affected by particle bombardment.



Figure 2.5: Ganymede as seen by Galileo [[Lissauer and de Pater, 2013](#)]

Jupiter has a rotation period of 10 hours, while Ganymede's orbital period is approximately 7 days. This effect is further exacerbated by Ganymede's tidal lock with Jupiter, leading to the same side continuously facing Jupiter and to the Ganymede's trailing side continuously being sputtered. Both sublimation and sputtering ultimately lead to water particles being freed from Ganymede's surface while the heavier contaminants in the ice remain on the surface. It should be noted however, that mass spectroscopy analyses of Ganymede still show the surface consisting mainly of ice. These processes lead to the older surfaces on Ganymede having a lower albedo with bright, younger regions making up to ~65% of the surface. Ganymede's ancient, dark terrain is mostly visible on the trailing side and covers the rest of the moon's surface [[Alday et al., 2017](#)]. The resulting global albedo average has a strong impact on GALA's error budget, as explained further in [subsection 5.6.2](#).

Overall, processes due to tidal forcing on Ganymede occur at a lower pace than on the two inner Jovian moons Io and Europa due to the weaker tidal forces Ganymede experiences. These lesser forces are attributed to a handful of reasons: For one, Ganymede's orbit has a larger semi-major axis which weakens Jupiter's pull on it. In turn, a larger semi-major axis is naturally accompanied by a longer orbital period which leads to spikes in tidal forcing occurring less often. Last but not least, Ganymede's orbit is less eccentric with eccentricity being the most dominant factor regarding the effect of tidal forcing [[Greenberg, 1989](#); [Ferraz-Mello, 2003](#)]. Ganymede is attributed an eccentricity of 0.001 while Io's and Europa's is 0.004 and 0.009 respectively [[NASA, 2018](#)]. Eccentricity as a dominant factor can be explained by a satellite with rapid mean orbital motion and low eccentricity experiencing frequent but ultimately small deformations. Naturally, a satellite with large eccentricity will experience dramatically larger deformations and the accompanying friction induced heating even if the frequency of the tidal excitation is much lower. The forced eccentricity on Ganymede due to the Laplace resonance between the Galilean satellite originates mainly from Europa's pull on Ganymede [[Yoder, 1979](#); [Peale et al., 1979](#); [Yoder and Peale, 1981](#); [Husmann and Spohn, 2004](#); [Tobie et al., 2005](#); [Lainey et al., 2009](#)]. Comparatively, it does not have a too large impact however, due to Europa's lower mass. It should be mentioned however, that Ganymede's free eccentricity is larger than its forced eccentricity [[Morrison and Matthews, 1982](#); [Greenberg, 1989](#); [Peale, 2003](#); [Ferraz-Mello, 2003](#)].

3

Laser Altimetry

3.1. The Ganymede Laser Altimeter (GALA)

The GALA instrument builds up on the heritage of the BepiColombo Laser Altimeter (BELA) [Gunderson et al., 2006; Thomas et al., 2007], with the German Aerospace Center (DLR) being responsible for the development of GALA. GALA's main components are its transmitter and receiver. The transmitter emits laser pulses at a wavelength of 1064 nm (i.e. in the infrared spectrum) with an adjustable pulse rate of 10 up to 50 Hz. The nominal pulse rate for the GCO500 phase, as described in [section 2.2](#), is 30 Hz with the maximum pulse rate of 50 Hz being reserved for flybys or specific areas. Before leaving the transmitter, the laser pulse is expanded leading to a surface spot diameter of ~ 50 m at the nominal altitude of 500 km. A surface spot is defined as laser signal reflection surface as shown in [Figure 3.1](#). At the altitude of 500 km, the nominal pulse rate of 30 Hz leads to a distance of ~ 50 m between laser-spot centres and an spot-edge distance of ~ 0 m, resulting in an improvement in GALA's interpolation errors compared to BELA [Thomas et al., 2007; Gunderson et al., 2006]. For further details on how interpolation errors see [subsection 5.6.2](#). GALA's required Signal-to-Noise Ratio (SNR) allows for reliable measurement at altitudes up to 1600 km, such as those encountered during Europa flybys. The SNR depends strongly on the surface albedo, resulting in a strong impact on instrument intrinsic errors as discussed in [subsection 5.6.2](#). This results in the maximum altitude for measurements being albedo dependent and reducing down to 1400 km for Ganymede and 1100 km for Callisto due to unfavourable, low surface albedos [Steinbruegge et al., 2015]. For details on Ganymede's albedo see [section 2.4](#). Further factors that negatively impact maximum measurement altitudes are surface slopes and roughness. These surface characteristics both lead to a broadening of the laser pulse, resulting in a decrease in signal amplitude at the receiver. More details on these effects can be found in [subsection 5.6.2](#).

GALA's receiver is expected to attain a ranging precision of ~ 0.1 meters, due to intrinsic errors and a ranging accuracy of ~ 1 meter, due to pointing errors. For details regarding the distinction of precision and accuracy see [section 5.6](#). Naturally, the final attainable range precision also depends on the attainable precision of the orbit determination scheme as discussed in [section 2.2](#). GALA's range measurements are used to create height and topography profiles as well as digital terrain models of the Jovian moons. In addition to the range measurements, GALA is capable to infer additional data from the backscattered laser pulses such as surface roughness, slope and albedo at the wavelength of 1064 nm.

3.2. Altimetry Measurements

Laser altimeters, such as GALA, function based on the principle of two-way laser ranging. Their measurement principle relies on the precise time-of-flight measurement of a transmitted laser pulse which is backscattered at the satellite's surface and subsequently detected, as shown in [Figure 3.1](#). Assuming that the signal is scattered diffusely at the reflector, the recorded pulse can yield many insights into the reflector characteristics such as its roughness, albedo and slope since the wavelength and intensity of the sent pulse is known precisely [[Steinbruegge et al., 2015](#)].

Altimetry data can also be processed into Digital Shape Models (DST) which provide precise insights onto the body's shape and surface characteristics. In doing so, the tide response mentioned in [section 2.4](#) must be considered. This is more so the case, if topographical changes are above the range noise level to properly distinguish between the body's static topography and any changes upon it.

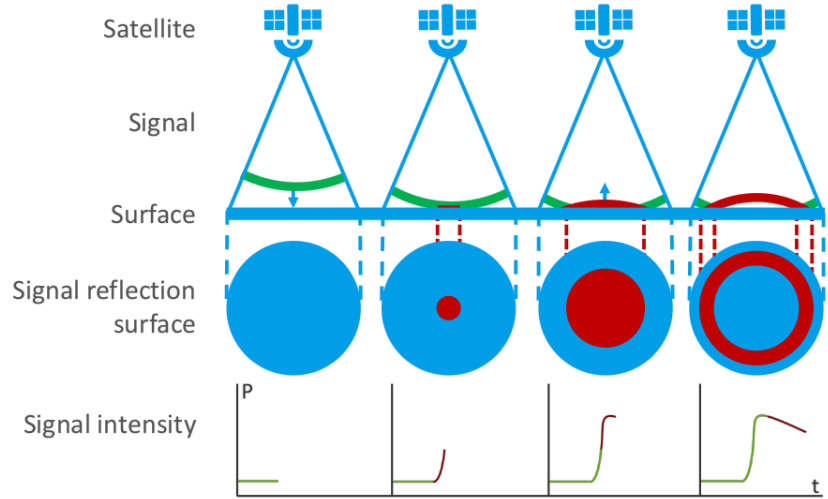


Figure 3.1: Principle of two-way altimetry [[van der Wal, 2017](#)].

This is a widely used measurement technique applied to many fields such as the monitoring of Earth's oceans as done by the SEAsat or Sentinel satellites [[ESA, 2018b](#)]. Previous works have shown that it is possible to determine the topographical deformation amplitude in bodies which experience large deformation bulges such as Earth, as well as in bodies with small deformation bulges such as the Moon [[Mazarico et al., 2011](#)]. A future mission where measurable deformation bulges are expected is the BepiColombo mission as Mercury undergoes strong tidal forces due to the Sun [[Gunderson et al., 2006](#)]. As mentioned in [section 2.2](#), JUICE is expected to witness up to 7 meters due to Jupiter's tidal forcing upon Ganymede, assuming an h_2 value of 1.3.

The topography deformation ΔT due to Ganymede's tidal response can be described using the time varying tidal potential Φ_{Tidal} with g being the gravitational acceleration at the reference geoid's surface [[Steinbruegge et al., 2015](#)]:

$$\Delta T = \frac{h_2 \Phi_{Tidal}}{g}. \quad (3.1)$$

This time varying tidal potential is discussed further in [section 4.2](#). Provided high quality topographic datasets of the orbited body are available it is possible to use individual altimetry measurements for orbit determination. However, for altimetry-only POD strong requirements must be fulfilled such as a highly detailed knowledge of the topographic field for measurement fitting as well as the body's gravitational field to predict the satellite's motion [[Mazarico et al., 2018](#)].

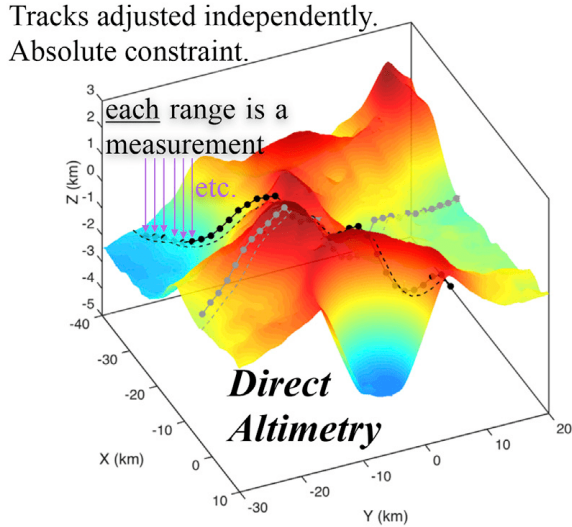


Figure 3.2: Direct altimetry POD [Mazarico et al., 2018].

Within this *direct altimetry* method, the state of the spacecraft is adjusted directly using the topography model and altimetric ranges resulting in accurate position and pointing solutions independent from tracking data. For the Moon, an exhaustively studied body, this method was used to establish the LRO's state with an ambiguity of $\sim 10 \pm 8$ m along-track, $\sim 13 \pm 9$ m cross-track and $\sim 2 \pm 2$ m radially, resulting in a total position ambiguity of $\sim 18 \pm 12$ m [Mazarico et al., 2018]. Naturally, this method is only applicable to extensively mapped bodies making it unsuitable for the JUICE mission. Overall, previous findings show that altimetry data can support and improve orbit determination by using altimetry crossovers as presented in section 3.3 below.

3.3. Altimetry Crossovers

A crossover location is a point where spacecraft measurements intersect, as shown in Figure 3.3. If these measurements are done with nadir pointing, they coincide with the spacecraft ground tracks. Ground tracks herein refer to the trajectory of a spacecraft in the body-fixed frame of the orbited body. Since the crossover point thus occurs over the same latitude and longitude, see following condition holds for each crossover point:

$$\hat{r}_1 = \hat{r}_2, \quad (3.2)$$

with \hat{r}_i being the body-fixed unit vector of the crossover position vector on the respective pass as shown in Figure 3.3. In the following, the passes shown in Figure 3.3 are referred to as ground track arcs.

These common locations are particularly useful as their difference in altitude h_{\otimes} yields information about the dynamical behaviour of the orbited body, such as the Love number h_2 as discussed in section 2.3 [Mazarico et al., 2014; Steinbruegge et al., 2015; Steinbrügge et al., 2018]. The crossover altitude difference h_{\otimes} is defined as shown below, with t_2 and t_1 being the crossover times on the respective arcs as shown in Figure 3.3

$$h_{\otimes}(t_2, t_1) = h(t_2) - h(t_1). \quad (3.3)$$

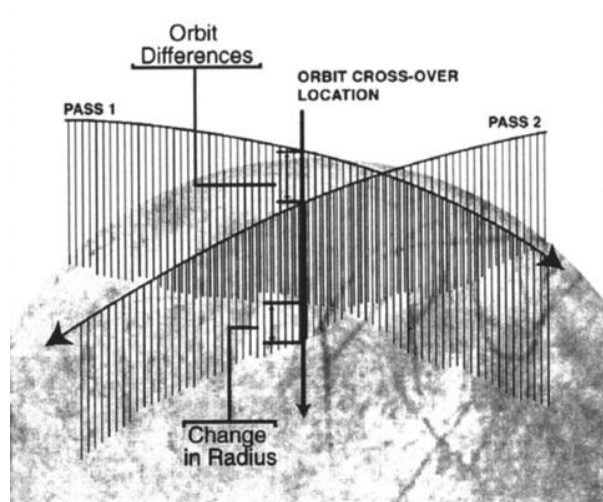


Figure 3.3: Schematic of altimeter crossover geometry [Neumann et al., 2001].

Furthermore, the use of crossovers has been shown useful in improving estimates for spacecraft orbits and their attitude as well as the estimation of the rotational state of celestial bodies. Within POD schemes, previous studies have successfully used crossover altitude differences as additional observables for missions such as the Mars Global Surveyor (MGS) [Rowlands et al., 1999; Neumann et al., 2001] and the Lunar Reconnaissance Orbiter (LRO) [Rowlands et al., 2008; Mazarico et al., 2010, 2011, 2018]. The results of applying crossover measurements for JUICE's orbit determination are discussed in [chapter 8](#). Unfortunately, the use of crossovers is computationally intensive and yields diminishing returns for POD with increasingly precise tracking data. While previous missions were limited by the tracking uncertainties of X-band links, the drastic increase in tracking uncertainties results from using both X- and Ka-band links, as presented further in [subsection 5.4.1](#).

Although the JUICE mission makes use of state-of-the-art tracking methods, the use of crossover observables might still be warranted due to the discontinuous tracking of the spacecraft. As described in [section 2.2](#), JUICE's nominal tracking periods consist of merely a daily eight-hour period during which it also sends its accumulated scientific data to Earth. Furthermore, this 8-hour daily period cannot be attained fully due to occultations and unfavourable angles towards the Sun. JUICE's tracking periods are discussed further in [subsection 5.4.2](#). Conversely, the accumulation of crossover points during its daily 16-hour measuring period as well as during occultations is continuous and might be used to improve the spacecraft trajectory during its untracked periods.

The potential added benefit of altimeter crossover observables depends largely on the data coverage and quality. If the altimetric footprints are not exactly at the crossover location, the respective altitudes must be obtained by interpolation, as described further in [subsection 5.5.1](#). Due to GALA's high pulse rate, the nominal footprint spot-edge distance is about zero meters which leads to relatively small interpolation errors as discussed in [subsection 5.6.2](#). As shown in [Figure 5.8](#) however, unfavourable surface slopes might lead to unaccounted, rapid changes in topography that result in crossover discrepancies. Therefore, unfavourable crossover points with too large off-nadir pointing or with footprints which are too spaced over sloped terrain must be discarded as confirmed by previous studies [Neumann et al., 2001; Rowlands et al., 2008].

For crossovers to improve orbit reconstruction significantly a large number of crossover locations is required. Assuming that each orbit track intersects every other track approximately twice, the number of crossovers n_{\otimes} grows quadratically with time as described by:

$$n_{\otimes} = n_r(n_r - 1), \quad (3.4)$$

with n being the number of orbit revolutions [Neumann et al., 2001]. Additionally, previous studies with Earth-orbiting spacecraft over the oceans have shown that altimetry crossover measurements are insensitive to horizontal orbit errors if they are done over relatively flat surfaces [Rowlands et al., 1999]. This leads to crossover observables being unaffected if there are horizontal errors in the a priori orbits. Unfortunately, this characteristic leads to the expectation that crossovers cannot be used to improve a satellite's horizontal position precisely, as discussed further in [section 8.1](#). As described in [chapter 1](#), the addition of crossover measurements for orbit determination schemes will be assessed for the JUICE GCO500 mission phase.

4

Orbital Dynamics

This chapter discusses the orbital dynamics and perturbing forces relevant for the simulation of JUICE's trajectory during the mission phase GCO500. During this phase JUICE's motion can be described as a perturbed, low eccentricity orbit, as discussed in [section 2.2](#). The treatment of JUICE's motion during its interplanetary transfer, flybys or orbit insertions are outside this document's scope. This trajectory simulation is necessary to create synthetic tracking and crossover measurements for JUICE's POD as treated further in [chapter 5](#). While a rudimentary, simple orbit propagation would suffice for an initial POD analysis an increase in orbit fidelity makes measurements more representative as well.

Within its orbit propagation, the JUICE spacecraft will be treated as a rigid, massless point particle due to its negligible size and mass in comparison to the bodies influencing its motion. The spacecraft attitude is also discarded and the motion regarded is that of its centre of mass. The only exception to this rule is made for the analysis of solar radiation pressure and atmospheric drag for which the spacecraft mass, area and attitude are not negligible, as explained further in [section 4.4](#) and [section 4.5](#). Satellite inherent dynamical issues, such as propellant sloshing and the motion of JUICE's centre of mass due to propellant consumption are assumed to be accounted for sufficiently by the satellite's attitude control system and accelerometers [[Lee and Stupik, 2015](#); [Enright and Wong, 1994](#)].

As mentioned in [section 2.2](#), this document deals exclusively with the GCO-500 mission phase. To successfully simulate JUICE's motion in time its mission environment must be properly understood and defined to account for factors that may significantly influence spacecraft motion. Due to the limitation of computational resources well founded simplifications must be made to ensure the manageability of the simulation and its analysis, leading to a trade-off in orbit accuracy. Additionally, it must be kept in mind that the simulated trajectory can only be an approximation due to the large environment uncertainties, such as the lack of knowledge of Ganymede's gravity field. During the simulation setup, a useful indicator for the inclusion or exclusion of perturbing forces is the magnitude of their effect on the spacecraft's motion over time. Consistent with ESA's propagation of JUICE's nominal trajectory during the GCO500 mission phase, a perturbing acceleration is only included if its magnitude is equal or larger than that of the Galilean moons as shown in [Figure 4.1](#). The smallest Galilean moon perturbation is due to Callisto and has a minimum magnitude of 8.578×10^{-10} . Thus, any effects whose accelerations have a lower magnitude than 10^{-10} m/s are assumed not to have a significant effect on JUICE's orbit within this thesis' propagation periods of up to 10 days as discussed in [section 6.4](#). [Figure 4.1](#) shows the accelerations acting on JUICE during the GCO500 mission phase. Therein, t_0 refers to the initial epoch of the simulation. Except for Ganymede and Jupiter, the accelerations due to celestial bodies are calculated treating these bodies as point

masses as discussed in [section 4.3](#). For Ganymede, its gravity field up to degree and order 12 is considered while for Jupiter only its J_2 term was taken into account. For further details on the respective gravity fields see [section 6.2](#).

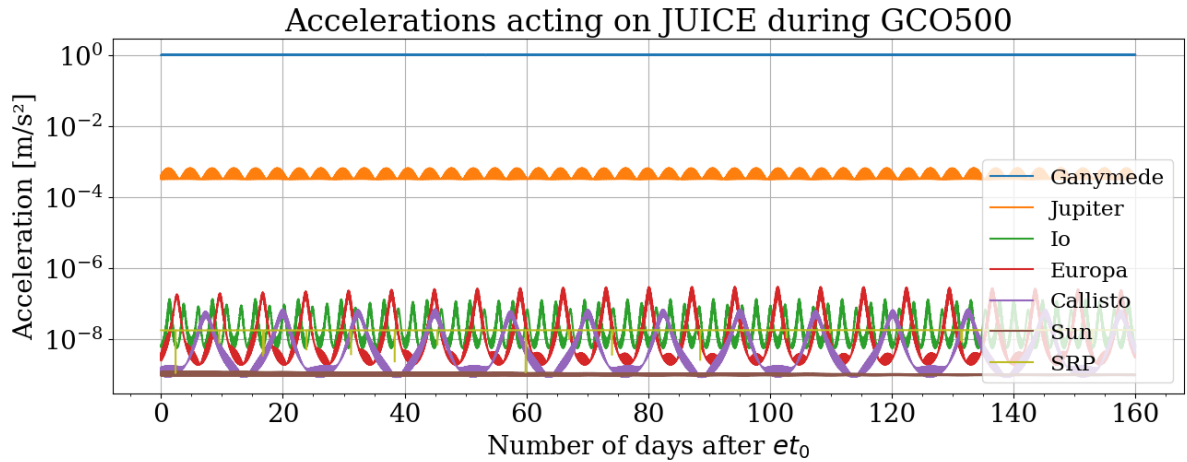


Figure 4.1: Accelerations acting on JUICE during GCO500. et_0 as defined in [section 6.3](#).

These accelerations were obtained using the trajectory validation settings discussed in [section 6.4](#). From it, it can be seen how JUICE is within Ganymede's sphere of influence as discussed in [section 4.1](#). Furthermore, it can be inferred that JUICE's trajectory is largely circular due to consistency in acceleration magnitudes and the periodic behaviour of the perturbing accelerations, as alluded to in [section 2.2](#). This periodicity demonstrates the Laplace resonance between the Jovian moons as mentioned in [section 2.4](#). Additionally, the periodicity of Jupiter's acceleration coincides with Ganymede's orbital period of 7.1 days. The two acceleration peaks within these 7.1 days are due to JUICE's inertial orientation, with the highest Jupiter accelerations occurring when JUICE's orbital plane coincides with the Ganymede-Jupiter position vector. While Jupiter's perturbation has a strong effect on JUICE's orbit, it is kept circular by orbit maintenance manoeuvres. Since other accelerations are several magnitudes smaller than Ganymede's acceleration, they can be treated as perturbing accelerations in JUICE's orbit [[Grasset et al., 2013](#); [Wakker, 2015](#); [Montenbruck and Gill, 2000](#)]. In the following, the perturbing forces acting on JUICE are presented and discussed.

4.1. Central Body Geopotential

Although both Jupiter and the Sun have substantially more mass than Ganymede, JUICE's orbit in GCO500 is mainly dictated by Ganymede's gravitational pull, while Jupiter, the Galilean moons, the Sun and all the other planets merely act as perturber. [[Villamil, 2019](#)]. Therefore, we can approximate JUICE's motion to first-order by only regarding Ganymede's effect on it. Furthermore, we conclude that the effect of any other celestial body can also be regarded as a perturbation since both the Sun and Jupiter are the most massive celestial bodies in our solar system.

Although of limited interest to this document, the condition when a body's motion is no longer primarily governed by one single body shall also be presented. The concept of *sphere of influence*, describes the sphere around a celestial body within which the motion of a particle is dictated mainly by that celestial body while other bodies can be treated as perturbers. The

sphere of influence R_{Sph} of a body is calculated as [Wakker, 2015, Eq.4.26]:

$$R_{\text{Sph}} = \rho \left(\frac{m_1}{m_3} \right)^{2/5}, \quad (4.1)$$

with ρ being the distance between the celestial bodies in question and m_i describing their respective masses. For the case treated here, ρ refers to Ganymede's semi-major axis, i.e. its distance to Jupiter $\rho = r_{\text{Gan}}$. Regarding Ganymede as the centre of motion with $m_1 = m_{\text{Gan}}$ and $m_3 = m_{\text{Jup}}$ we obtain that Ganymede's sphere of influence extends to $R_{\text{Sph}} = 24.3528 \times 10^3$ km around it. As JUICE's orbit during its GCO500 mission phase is well within R_{Sph} we can indeed approximate JUICE's motion to first-order by only regarding Ganymede's effect on it.

The gravitational field of a spherical body with radially symmetric mass distribution can be simplified to a point mass located at the body's centre [Wakker, 2015]. For the precise description of a spacecraft's motion however, the body's irregular gravitational field must be considered. Mathematically, the body's gravity potential U can be expressed with the unnormalised *spherical harmonics* series expansion [Montenbruck and Gill, 2000]:

$$U(r, \varphi, \lambda) = \frac{GM}{r} \sum_{n=0}^{n_{\text{max}}} \sum_{m=0}^n \frac{R^n}{r^n} P_{nm}(\sin \varphi) [C_{nm} \cos(n\lambda) + S_{nm} \sin(m\lambda)], \quad (4.2)$$

Therein, P_{nm} is the associated Legendre function of degree n and order m and the spherical harmonic coefficients C_{nm} and S_{nm} describe the potential's deviation from an ideal sphere due to the body's internal mass distribution. The spherical harmonics series can be divided into zonal ($m = 0$), sectoral ($n = m$) and tesseral ($n \neq m$) harmonics. Zonal coefficients describe the longitude independent part of the potential, with the notation $J_n = -C_{n0}$ being commonly used. All terms S_{n0} are zero by definition.

Due to the wide range of orders of magnitude covered by the geopotential coefficients C_{nm} and S_{nm} , oftentimes the *normalised* coefficients \bar{C}_{nm} and \bar{S}_{nm} are used:

$$\begin{Bmatrix} \bar{C}_{nm} \\ \bar{S}_{nm} \end{Bmatrix} = \sqrt{\frac{(n+m)!}{(2-\delta_{0m})(2n+1)(n-m)!}} \begin{Bmatrix} C_{nm} \\ S_{nm} \end{Bmatrix}. \quad (4.3)$$

The normalised associated Legendre function \bar{P}_{nm} is defined as:

$$\bar{P}_{nm} = \sqrt{\frac{(2-\delta_{0m})(2n+1)(n-m)!}{(n+m)!}} P_{nm}. \quad (4.4)$$

A reason for using the normalised coefficients \bar{C}_{nm} and \bar{S}_{nm} is that they behave more uniformly, with their order of magnitude described approximately by Kaula's rule [Kaula, 1966]:

$$\bar{C}_{nm}, \bar{S}_{nm} \approx \frac{10^{-i}}{n^2}, \quad (4.5)$$

with the Kaula factor i determining how rapidly the order of magnitude of the coefficients decreases with an increase in the field's degree n . In this thesis the simplification is made that i is a constant value for all degrees n . As shown in Equation 4.2 the magnitude of the body's gravitational potential decreases rapidly with increasing degree due to the term $(R/r)^n$. Additionally, as shown in Equation 4.5, the coefficients' magnitudes also decline with increasing degree due to the term $1/n^2$ further leading to a decrease in the potential U . Most commonly, the second zonal element J_2 is the strongest series element. It describes the body's polar flattening due to its rotation.

Unfortunately, for Ganymede's gravitational field only the coefficients J_2 and C_{22} have been determined [Campbell and Synnott, 1985; Anderson et al., 1996; Jacobson et al., 1999]. Furthermore, the encounters used for the determination of these coefficients were highly correlated and an a priori hydrostatic constraint $J_2 = C_{22}(10/3)$ was used for their determination. The validity of this hydrostatic constraint for Ganymede has not been established beyond doubt [Anderson et al., 1996]. The current knowledge about the gravity fields in the Jovian system was obtained from Pioneer, Voyager, Galileo and most recently Juno tracking data. Naturally, JUICE's mission builds upon that knowledge and aims to deepen it to degree and order 12 or higher for Ganymede, as 3GM's scientific goal as described in section 2.3 [ESA, 2014]. For comparison, Earth's gravity field has been established on a global scale with degree 280 and up to degree 2190 locally [Mazarico et al., 2011; Bauer et al., 2016; for Global Earth Models (ICGEM), 2018].

While the mission's nominal orbits give us a good estimate of the spacecraft's motion, the actual spacecraft motion will deviate however. During the orbit determination, the individual origins of the deviations can be estimated as force model parameters, as presented further in section 5.1. Should the spacecraft be equipped with accelerometers, as JUICE is, the effects of non-conservative forces are recorded and do not need to be estimated. Unfortunately, accelerometers suffer from measurement errors such as bias, bias rate and scale factor which need to be estimated regularly. Once these perturbations have been established, the residual effects can be assigned to gravitational fields to obtain the respective spherical coefficients. Since a body's gravitational field can be more aptly described by a point mass with increasing distance to it, the lower a spacecraft's altitude is the more precise the gravity field that can be established. This is also the main reason why the Moon's gravity field can be determined more easily than Earth's to a higher resolution, as its lack of atmosphere allows for lower, stable orbits around it for Global Earth Models (ICGEM) [2018].

Since Ganymede's gravity field is so poorly constrained, previous scientific studies have used the gravitational fields of other bodies instead, such as Earth's moon, for their analyses [Marabucci, 2012; Steinke, 2015]. A similar approach is used here by using the gravity field ESA employed for the propagation of JUICE's nominal trajectory. To increase the fidelity of JUICE's perturbation environment Ganymede's gravity field up to degree and order 12 is implemented, as detailed further in section 6.2.

4.2. Tidal Potential

The spherical harmonics coefficients presented in Equation 4.2 describe a body's *static* gravitational field. In the following, the effect and description of gravitational field *variations* is presented. Such variations can arise from internal processes (plate tectonics, volcanism, etc.) and external forces. For Ganymede, the largest gravity variation arises from tidal forces due to Jupiter as mentioned in section 2.4.

If a body within a gravity potential is not a point mass, the unequal distances of its different areas to the centre of the potential lead to unequal gravitational forces acting on these different areas. Within a *tidal response* the body undergoes a gravitational *tidal potential* and is elongated, noticeable by *tidal bulges* as mentioned in section 2.3. The tidal response is characterised by the Love numbers h_i , k_i and l_i which depend on the rigidity and viscosity of the body's interior as well as the frequency of the tidal forcing, see section 2.3 [Moore and Schubert, 2003]. The love number h_2 influences altimetry measurements directly as it affects Ganymede's radial deformation, while k_2 influences GALA indirectly, as it affects JUICE's orbit. Conversely, l_2 affects the surface's lateral/tangential displacement which effect is assumed not to affect GALA's measurements. Here, only the second order Love numbers h_2 and k_2 are considered as these are the only terms which affect JUICE's POD. The potential that results

from the deformation of the body Φ_{Tidal} is described as [Moore and Schubert, 2000]:

$$\Phi_{\text{Tidal}}(r, \theta, \lambda, t) = k_2 \Phi(r, \theta, \lambda, t), \quad (4.6)$$

with r , θ , λ and t being the radius, co-latitude, longitude and time, respectively, in the body-fixed frame of the body undergoing tidal deformation. In Equation 4.6 Φ describes the time-dependent tidal potential which is described, up to second degree for a satellite in synchronous rotation, by [Steinbrügge et al., 2018]:

$$\Phi(r, \theta, \lambda, t) = \frac{GM r^2}{8a^3} [12e \cos(M) P_2^0(\sin(\theta)) + (e \cos(2M + 2\lambda) - 2 \cos(M + 2\lambda)) P_2^2(\sin(\theta))]. \quad (4.7)$$

Therein e , ω and M are the eccentricity, main tidal frequency and mean anomaly in the body-fixed frame of the body undergoing tidal deformation. Due to the evolution of Ganymede's orbit as described in section 2.4, and as shown in previous works, Ganymede's eccentricity is not constant [Steinbruegge, 2018]. Therefore, it is more advantageous to use the following formula for Φ instead [Steinbrügge et al., 2018]:

$$\Phi(r, \theta, \lambda, t) = \frac{GM^2 r^2}{d^3} P_2^0(\cos \phi), \quad (4.8)$$

with r being the distance to Ganymede's centre of mass, GM describing Jupiter's gravitational parameter and d being the distance of the evaluated point on Ganymede to Jupiter's center of mass. Lastly, P_2^0 is the associated Legendre polynomial and ϕ is the angle to the sub-Jupiter point.

Depending on the body's viscosity the tidal potential can also have a phase lag, known as *tidal lag* [Steinbruegge et al., 2015]. Such a phase lag is described using imaginary numbers and leads to a larger moment acting on the deformed body leading up to larger energy dissipation. While this would normally lead to a decrease of orbital eccentricity for the deformed body, the forced eccentricity of the Galilean moons maintains the moons' eccentricity and their energy dissipation, as described in section 2.4. The effect of the tidal potential described in Equation 4.6 onto Ganymede's static gravity field is most conveniently included in the form of variations in Ganymede's spherical harmonics coefficients as [Petit and (eds.), 2010]:

$$\Delta \bar{C}_{nm} - i \Delta \bar{S}_{nm} = \frac{k_{nm}}{2n + 1} \sum_{j=2}^3 \frac{GM_{Jup}}{GM_{Gan}} \left(\frac{R_{Gan}}{r_{Jup}} \right)^{n+1} \bar{P}_{nm}(\sin \Phi_{Jup}) e^{-im\lambda_{Jup}}, \quad (4.9)$$

with k_{nm} being the Love number of degree and order n and m , R_{Gan} being Ganymede's equatorial radius, GM_{Jup} and GM_{Gan} being Jupiter's and Ganymede's gravitational parameters, r_{Jup} being the distance between Jupiter's and Ganymede's geocenters, Φ_{Jup} being the geocentric latitude of Jupiter in Ganymede's body-fixed frame and λ_{Jup} being the longitude of Jupiter in Ganymede's body-fixed frame. It has been shown that the inclusion of the degree 2 Love number k_2 has a noticeable effect on the gravity coefficients \bar{C}_{2m} and \bar{S}_{2m} with additional minor effects on the coefficients \bar{C}_{4m} and \bar{C}_{4m} [Petit and (eds.), 2010].

If the tidally forced body's rotation is faster than its orbital period the tidal lag causes a *tidal torque* which slows down the body's rotation until it is *tidally locked*. This tidal lock leads to a synchronous rotation wherein the body's same side faces its central body, as is the case for Ganymede and Earth's moon among others [Lissauer and de Pater, 2013]. Jupiter also experiences tidal forcing due to the Galilean moons leading to a decrease in its rotational speed. However, the effect of tidal forcing on Jupiter have a much lower magnitude due to the difference in mass between Jupiter and the Galilean moons.

Unfortunately, Ganymede's tidal amplitude and tidal potential are not well constrained and it is one of JUICE's goals to measure Ganymede's tidal response to infer the existence of a sub-surface ocean, see [section 2.3](#). Current estimates for Ganymede yield typical values of $h_2 = 1.1 - 1.7$ and $k_2 = 0.36 - 0.57$ [[Steinbruegge et al., 2015](#); [Kamata et al., 2016](#)]. These values are based on terrestrial observations in addition to those made by the Pioneer, Voyager and Galileo missions and they make a strong argument for the existence of a subsurface ocean within Ganymede. As the varying tidal potential is measurable beyond doubt it cannot be neglected and shall be included in the study of JUICE's POD.

4.3. Third Bodies Effects

As discussed in [section 4.1](#), the perturbations caused by the gravity of a celestial body depend strongly on its distance to the perturbed body. Naturally, the same effect holds true for extended-body effects of perturbing bodies since the effect of the coefficients at degree and order $n = m = 0$ corresponds to the effect of a point mass gravity. This leads to the conclusion that if a body's gravitational field is far enough, their effect can be described by that of a point mass without compromising on accuracy. [Figure 4.1](#) shows that the perturbation due to the Sun is not negligible. However, due to the small magnitude of its perturbation and its large distance to Jupiter its extended body effects are neglected and it is treated as a point mass. The next largest celestial body is Saturn. Its perturbation as point mass on JUICE was evaluated and since its largest perturbation was shown to have a magnitude of 2.485×10^{-14} , its effect on JUICE is neglected as it is well below the discussed threshold of 10^{-10} . While for JUICE the extended-body effects of most celestial bodies can be safely neglected, it is expected that those of Jupiter are not negligible, in particular since it is the most massive planet in our solar system [[Grasset et al., 2013](#); [Boutonet, 2019](#); [Lissauer and de Pater, 2013](#)].

Of Jupiter's gravitational coefficients, it is expected that its J_2 term has the largest impart on JUICE's orbit due to the decrease of the gravitational coefficients' magnitude with degree n as discussed in [section 4.1](#). In addition to its large mass, Jupiter's J_2 coefficient, defined in [Appendix A.2](#), is expected to be particularly noticeable due to Jupiter's exceptionally rapid rotational rate: it completes a full turn once every 10 hours [[Lissauer and de Pater, 2013](#)]. Additionally, since Jupiter is a gas planet this effects are more pronounced than on rigid bodies with higher resistance to deformations. As for the central propagated body, the extended-body effects for a perturbing body can be included into the simulation by describing its gravity potential U with [Equation 4.2](#). Formerly, Jupiter's gravity field was known up to a degree $n = 6$ and order $m = 2$ [[Campbell and Synnott, 1985](#)]. NASA's ongoing Juno mission to the Jovian system however, has already managed to improve Jupiter's zonal harmonics up to J_{12} [[Folkner et al., 2017](#); [Iess et al., 2018](#)]. Due to the reasons provided, Jupiter's extended-body effects during the analysis of JUICE's POD are included. Unfortunately, the inclusion of these effects has a large effect computational loads and only the J_2 term is included, consistent with ESA's propagation of JUICE's nominal trajectory during its GCO500 mission phase [[Grasset et al., 2013](#); [ESA, 2014](#); [Boutonet, 2019](#)].

4.4. Radiation Pressure

For the computation of gravitational accelerations, spacecraft are often simplified to massless particles due to their comparatively negligible mass in comparison to the bodies determining the spacecraft motion. However, for the calculation of the Solar Radiation Pressure (SRP), where the momentum of solar photons acts on the spacecraft, the spacecraft's mass contribution is not negligible. Therein, the spacecraft mass variation due to propellant consumption is neglected due to the low requirements for orbit maintenance in stable orbits, such as during GCO500, and the large increase of computational time otherwise required. For further details

on the evolution of JUICE's orbit during the GCO500 mission phase see [section 6.4](#). Assuming the spacecraft's solar panels always point towards the Sun to continuously supply the spacecraft with electric power, a commonly used model for the calculation of the SRP is the so called *cannonball* model. As its name suggests, it describes the spacecraft shape as a sphere with an equivalent surface area A which facilitates calculations by not requiring to consider spacecraft attitude or solar panels orientation. Naturally, this results in an overestimation of the effect of SRP as the solar panels do not always point towards to the sun and self-occultations are neglected. Of those effects, self-occultations is noticeably the lesser one as the decrease of radiated surfaces due to shadows is much smaller than the decrease of radiated surfaces due to misalignment of the solar panels. Therein, any additional accelerations due to the simplified shape are in balance due to the sphere's symmetry and do not negatively affect their representation of the solar panels. The acceleration force a_{SRP} due to SRP can be described as [[Wakker, 2015](#)]:

$$a_{\text{SRP}} = -C_R \frac{WA}{Mc}, \quad (4.10)$$

with C_R being the satellite's reflectivity coefficient, W being the power density of the solar radiation in W/m^2 , A being the effective cross-sectional area of the satellite, M being the satellite's mass and c being the speed of light in vacuum. The coefficient C_R is determined by the radiation reflected and absorbed by the spacecraft, with typically used values being $C_R = 1.2 - 1.4$. Possible values for C_R range from 0 to 2, with 0 representing a transparent object, 1 being an object that absorbs all radiation and 2 an object that reflects all radiation. The actual value of C_R must be estimated as additional model parameter during orbit determination, as detailed further in [section 5.1](#).

Assuming the heat flux to be uniformly distributed around the Sun, its solar radiation power density at Jupiter's radial distance to the Sun ($r_{\text{Jup}} = 778.57 \times 10^9 \text{ m}$) can be calculated using the luminosity of the Sun L as [[Lissauer and de Pater, 2013](#)]:

$$W = \frac{L}{4\pi r_{\text{Jup}}^2} = \frac{3.827 \times 10^{26} \text{ W}}{4\pi r_{\text{Jup}}^2} = 50.24 \text{ W}/\text{m}^2, \quad (4.11)$$

using a reflectivity coefficient of $C_R = 1.3$, an effective area of $A = 97 \text{ m}^2$, a satellite mass of $M = 2000 \text{ kg}$ [[ESA, 2014](#)] and a speed of light of $c = 299792458 \text{ m/s}$ [[Wakker, 2015](#)], a SRP-acceleration of $a_{\text{SRP}} = 1.0567 \times 10^{-8} \text{ m/s}^2$ is obtained. In comparison to the perturbing accelerations shown in [Figure 4.1](#), the magnitude of a_{SRP} shows that while SRP has a small impact on JUICE's motion its effect is not negligible.

Besides solar radiation, other radiations include the Indirect Solar Radiation Pressure (ISRP) and the Thermal Radiation Pressure (TRP). As the name suggests, the ISRP occurs only above the day side of the orbited body and it originates from backscattered solar radiation. The magnitude of the ISRP depends strongly on the albedo of the backscattering body and its distance to the Sun. Previous studies have shown that the perturbation effect of the ISRP, even as close to the Sun as Mercury, is several magnitudes below the effect of SRP due to its reflective nature [[McCarthy and T., 1977](#); [Knocke et al., 1988](#); [Bahloul, 2013](#)]. Thus making ISRP negligibly small for this thesis.

Conversely, thermal radiation pressure (TRP) originates from a celestial body's infrared radiation due to its heat loss constantly affecting orbiting bodies depending on their distance and the celestial body's local temperature. Previous studies for interplanetary mission have shown that the detailed calculation of radiation pressure can potentially be necessary for high precision orbit determination, in particular if the spacecraft has a Radioisotope Thermoelectric Generator (RTG) for power generation. Therein, the precise shape and orientation of the spacecraft must be known to include effects such as self-shadowing and thermal radiation

originating from within the spacecraft. The modelling of radiation forces is particularly important for the analysis of long-period motions as for the Pioneer mission, whose anomaly could only be explained after studies on its anisotropic heat radiation [Rievers et al., 2010; Rievers and Lämmerzahl, 2011]. However, within this thesis the effect of TRP can be neglected due to the comparatively short length of the GCO500 mission phase as noted in section 2.2. Furthermore, unlike the Pioneer spacecraft, JUICE does not have radioisotope thermoelectric generators which radiate strongly enough to affect its orbit.

Regarding the scientific question treated in this document, the effects of SRP shall be included while those of ISRP and TRP on JUICE can be neglected as discussed above. The ISRP can be safely neglected due to its low magnitude in comparison to other perturbing forces while the TRP can be neglected due to the low equilibrium temperatures at Ganymede's surface of 126 K [Moore and Schubert, 2003] and JUICE's lack of RTG, unlike Voyager, Pioneer and Galileo. Furthermore, the simulation periods treated are comparatively short and it can be assumed that the accumulative effect of ISRP and TRP within a propagation length of up to 10 days, as discussed in section 6.4, is negligible.

4.5. Atmospheric Drag

As with the calculation of the SRP, the calculation of the atmospheric drag requires knowledge on the spacecraft mass, surface area and attitude. As in section 4.4, for the calculation of the drag accelerate the spacecraft's shape can be simplified to an ideal sphere with a representative area A and drag coefficient C_D . Usual values for Earth satellites' drag coefficient are $C_D = 2 - 3$ with satellites at higher altitudes having a C_D closer to 3 [Wakker, 2015; Lissauer and de Pater, 2013]. While a satellite's interactions with the atmosphere can also induce lift and side forces in addition to drag, their effect is several magnitudes lower than that of drag and they can therefore be neglected safely [Wakker, 2015; Cook, 1964]. Therefore, the drag's acceleration vector can be assumed to be always opposite the velocity vector. The magnitude of the drag acceleration vector a_{drag} depends on the atmospheric density ρ at the orbital height via:

$$a_{drag} = \frac{F_{drag}}{M} = \frac{AC_D\rho}{2M}\mathbf{v} \cdot \mathbf{v}. \quad (4.12)$$

As observed via Galileo's UV spectrometer and the Hubble Space Telescope (HST), Ganymede's atmosphere can be described as highly tenuous since it is only collisional around the subsolar region and collisionless elsewhere. Its main components are H_2 , O_2 and H_2O , as shown in 4.2. These constituents originate from sublimation at the subsolar point and sputtering at the polar regions, as described in section 2.4 [Marconi, 2007]. Although several works have demonstrated locally distinct atmospheric models [Marconi, 2007; Plainaki et al., 2015], herein a simplified model is assumed due to the atmosphere's tenuous perturbation effect on JUICE as shown by previous studies [Villamil, 2019].

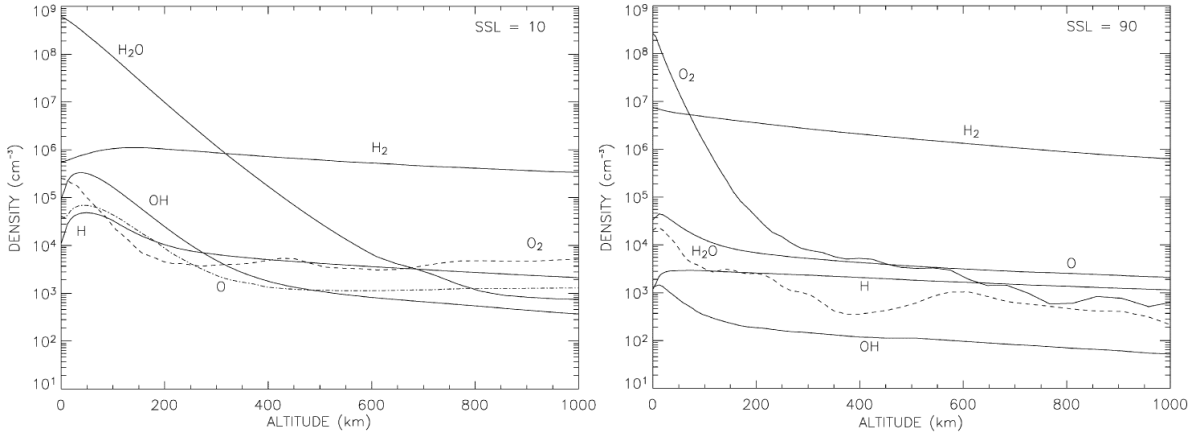


Figure 4.2: Radial density of elements at equatorial (l.) and polar (r.) latitude for Ganymede [Marconi, 2007].

Assuming that Ganymede's atmosphere is isothermic and that its density w.r.t. altitude can be described by [Lissauer and de Pater, 2013]

$$\rho = \rho_0 \exp\left(-\frac{\Delta h_{atm}}{H_s}\right), \quad (4.13)$$

with ρ being the atmospheric density at a given height, ρ_0 being the atmospheric density at the surface, Δh_{atm} being the height from the surface and H_s being the atmospheric scale height. Under these assumptions, Ganymede's atmosphere can be described by the following parameters to a first approximation [Villamil, 2019]:

| Scale height [m] | Ground temp. [K] | Ground density [kg/m ³] | Gas const. [J/(kg K)] |
|------------------|------------------|-------------------------------------|-----------------------|
| 65204.71 | 120.0 | 1.6965×10^{-11} | 163.24 |

Table 4.1: Simplified parameters for Ganymede's atmosphere [Lissauer and de Pater, 2013].

Resulting in an atmospheric density of $7.884 \times 10^{-5} \text{ kg km}^{-3}$ at JUICE's altitude of 500 km during the GCO500 phase.

As for the calculation of the SRP, the simplified shape of the spacecraft implies a continuous worst-case scenario. Herein, the assumption is made that the solar panels are perpendicular to the flight direction, yielding a maximum effective area. This conservative approach is acceptable due to the large uncertainties regarding the atmospheric composition.

To evaluate the drag's acceleration on JUICE a drag coefficient of $C_D = 2.8$, an effective area of $A = 97 \text{ m}^2$ and a satellite mass of $M = 2000 \text{ kg}$ is assumed [ESA, 2014]. For JUICE's orbital velocity, it can be safely assumed that its orbit in its GCO500 phase is circular. Making use of a gravitational constant of $GM_{Gan} = 9887.83 \text{ km}^3 \text{ s}^{-2}$ and a planetary radius of $r_{Gan} = 2634.0 \text{ km}$ for Ganymede, we obtain:

$$v = \sqrt{GM_{Gan}/(r_{Gan} + 500 \text{ km})} = 1.777 \text{ km/s} \quad (4.14)$$

Inserting these values into Equation 4.12 yields an atmospheric drag acceleration for JUICE of $a_{drag} = 1.689 \times 10^{-11} \text{ km/s}$. This particularly low value, especially in comparison with the SRP discussed in section 4.4 and the perturbing accelerations shown in Figure 4.1, makes the acceleration due to drag safely negligible for the study of JUICE's POD.

5

Precise Orbit Determination

Within this chapter the mathematical foundation of orbit determination procedures is presented, including a discussion of the conventionally used measurements therein. Additionally, the definition of crossovers is elaborated upon further as is their mathematical inclusion into an orbit determination algorithm. In doing so, the crossover determination and selection is discussed for JUICE's POD. Lastly, potential error sources for all used measurements are discussed and the respective error budgets are established.

5.1. Definition of the Loss Function

To determine the state of a body at an epoch j we require tracking measurements of the body's motion. Using measurements for multiple epochs, together with prediction models for the body's motion, we can estimate the body's orbit in time. Since the prediction models for motion and environment are incomplete, there are estimation errors in the form of residuals which can be used to improve these models by residual minimisation, i.e. by attributing unassigned effects to their respective origin. Unfortunately, residuals also arise from measurement errors that are random and/or biased in nature. With \mathbf{y} being the measurements, \mathbf{p} being parameters of interest and $\boldsymbol{\varepsilon}$ being residuals due to measurement and model errors, the measurements at a given epoch j can be described by:

$$\mathbf{y}(t_j) = A(\mathbf{p}(t_j)) + \boldsymbol{\varepsilon}(t_j). \quad (5.1)$$

Therein, the function $A(\mathbf{p}(t_j))$ links the non-linear relationships between the parameters \mathbf{p} and the measurements. The parameter vector $\mathbf{p}(t_j)$ is made up of the body's state vector $\mathbf{s}(t_j)$ and force and observation (e.g. biases) parameter vector \mathbf{q} . The body's state vector consist of the body's position and velocity vector, $\mathbf{r}(t_j)$ and $\mathbf{v}(t_j)$ respectively and is therefore of dimension six:

$$\mathbf{p}(t_j) = \begin{pmatrix} \mathbf{s}(t_j) \\ \mathbf{q} \end{pmatrix} \quad \text{with} \quad \mathbf{s}(t_j) = \begin{pmatrix} \mathbf{r}(t_j) \\ \mathbf{v}(t_j) \end{pmatrix}. \quad (5.2)$$

The purpose of an orbit determination procedure, is to estimate a set of parameters $\mathbf{p}(t_j)$ with which the obtained measurements $\mathbf{y}(t_j)$ can be approximated most closely using the environment and body model as described by the function $A(\mathbf{p}(t_j))$. Thus, it is of utmost importance that the environment force model represents the spacecraft's actual environment as adequately as possible as its accuracy and completeness directly impacts the quality of the POD. While the initial environment model within $A(\mathbf{p}(t_j))$ is bound to be error afflicted, it can be iteratively improved with progressively better estimates of \mathbf{q} . To solve this non-linear problem, it is necessary to first *linearise* the observation equations, effectively turning [Equation 5.1](#) into

an initial value problem. This is done by linearising all non-linear relationships within $A(\mathbf{p}(t_j))$ around a reference state \mathbf{x}_0^{ref} at the linearization epoch t_0 resulting in [Montenbruck and Gill, 2000, p.260]:

$$\mathbf{y} \approx A(\mathbf{p}_0^{ref}) + H\Delta\mathbf{p} + \varepsilon, \quad (5.3)$$

$$\text{with } \Delta\mathbf{p} = \mathbf{p}_0 - \mathbf{p}_0^{ref}, \quad (5.4)$$

$$\text{and } H = \left. \frac{\partial A}{\partial \mathbf{p}_0} \right|_{\mathbf{p}_0 = \mathbf{p}_0^{ref}}. \quad (5.5)$$

$$\mathbf{y} - A(\mathbf{p}_0^{ref}) = H\Delta\mathbf{p} + \varepsilon, \quad (5.6)$$

$$\Rightarrow \Delta\mathbf{y} = H\Delta\mathbf{p} + \varepsilon. \quad (5.7)$$

Within Equation 5.6 the function $A(\mathbf{p}_0^{ref})$ yields modelled measurements using the parameter vector \mathbf{p}_0 . The Jacobian matrix H is central to any POD scheme and is called the *design matrix*. It describes changes in the modelled observations $A(\mathbf{p}_0^{ref})$ due to changes in the vector \mathbf{p}_0^{ref} .

To approximate the tracking measurements \mathbf{y} as closely as possible with the modelled measurements obtained with $A(\mathbf{p}_0^{ref})$, it is necessary to minimise the errors ε which arise from a wrong estimate of \mathbf{p}_0^{ref} as well as measurement and model errors. Ideally, the tracking measurements \mathbf{y} have *no* errors and the environment model within $A(\mathbf{p}_0^{ref})$ perfectly represents reality, in which case a perfect estimate of \mathbf{p}_0^{ref} would lead to $\varepsilon = 0$. To solve Equation 5.7, the square sum of ε must be minimized, leading to the loss function:

$$\varepsilon = \Delta\mathbf{y} - H\Delta\mathbf{p}, \quad (5.8)$$

$$\min \varepsilon^T \varepsilon = \min (\Delta\mathbf{y} - H\Delta\mathbf{p})^T (\Delta\mathbf{y} - H\Delta\mathbf{p}). \quad (5.9)$$

$$\Rightarrow \min \Delta\mathbf{y}^T (\Delta\mathbf{y} - H\Delta\mathbf{p})^T - \Delta\mathbf{p}^T H^T (\Delta\mathbf{y} - H\Delta\mathbf{p}). \quad (5.10)$$

As the left term of Equation 5.10 cannot be further minimized once $H\Delta\mathbf{p}$ approaches $\Delta\mathbf{y}$, the least-squares problem (lsq) reduces to finding a vector $\Delta\mathbf{p}_0^{lsq}$ which minimises the right term. Excluding the solution $\Delta\mathbf{p}_0^{lsq} = 0$ we obtain:

$$\Delta\mathbf{p}_0^{lsq,T} H^T \Delta\mathbf{y} - \Delta\mathbf{p}_0^{lsq,T} H^T H \Delta\mathbf{p}_0^{lsq} \stackrel{!}{=} 0, \quad (5.11)$$

$$H^T (\Delta\mathbf{y} - H\Delta\mathbf{p}_0^{lsq}) \stackrel{!}{=} 0, \quad (5.12)$$

$$\Rightarrow H^T H \Delta\mathbf{p}_0^{lsq} = H^T \Delta\mathbf{y}, \quad (5.13)$$

$$\Rightarrow \Delta\mathbf{p}_0^{lsq} = (H^T H)^{-1} H^T \Delta\mathbf{y}, \quad (5.14)$$

with $\Delta\mathbf{p}_0^{lsq}$ being the correction vector with which the loss function attains a minimum. Unfortunately, this approach treats the influence of all measurements equally, though their uncertainties might vary strongly. A solution to handle the influence of observations is weighting the measurements according to their accuracies, resulting in a *weighted* solution of the least-squares problem. Assuming all measurement errors have a Gaussian distribution with zero mean and are uncorrelated, the measurement uncertainties can be implemented via the measurement covariance matrix P_y as:

$$P_y = \text{diag}(\sigma_1^{-2}, \dots, \sigma_n^{-2}) = \begin{pmatrix} \sigma_1^{-2} & \dots & 0 \\ \vdots & \ddots & \vdots \\ 0 & \dots & \sigma_n^{-2} \end{pmatrix}. \quad (5.15)$$

$$(5.16)$$

Therein, σ represents the standard deviations of the total *measurement errors*, i.e. due to both random and systematic errors which are assumed to have a zero mean value. However, these simplifications make the resulting formal errors too optimistic as error correlations are neglected, as are biases which lead to a non-zero mean value. P_y can be implemented into [Equation 5.9](#) as:

$$\min \varepsilon^T P_y^{-1} \varepsilon = \min (\Delta \mathbf{y} - H \Delta \mathbf{p})^T P_y^{-1} (\Delta \mathbf{y} - H \Delta \mathbf{p}), \quad (5.17)$$

$$\Rightarrow \min \Delta \mathbf{y}^T P_y^{-1} (\Delta \mathbf{y} - H \Delta \mathbf{p})^T - \Delta \mathbf{p}^T H^T P_y^{-1} (\Delta \mathbf{y} - H \Delta \mathbf{p}). \quad (5.18)$$

$$(\Delta \mathbf{p}_0^{lsq})^T H^T P_y^{-1} (\Delta \mathbf{y} - H \Delta \mathbf{p}_0^{lsq}) \stackrel{!}{=} 0, \quad (5.19)$$

$$\Rightarrow H^T P_y^{-1} H \Delta \mathbf{p}_0^{lsq} = H^T P_y^{-1} \Delta \mathbf{y}, \quad (5.20)$$

$$\Rightarrow \underline{\Delta \mathbf{p}_0^{lsq}} = (H^T P_y^{-1} H)^{-1} H^T P_y^{-1} \Delta \mathbf{y}, \quad (5.21)$$

which provides the *weighted* solution $\Delta \mathbf{p}_0^{lsq}$. If the measurement errors are correlated P_y is a non-diagonal matrix instead. The covariance matrix P_x of the *estimated parameters* is defined as:

$$P_x = (H^T P_y^{-1} H)^{-1}. \quad (5.22)$$

The matrix $(H^T P_y^{-1} H)$ is known as the *normal matrix* and its diagonal elements yield the standard deviation of the estimated elements within $\Delta \mathbf{p}_0^{lsq}$ while its off-diagonal elements describe the error correlation between these elements. Importantly, the diagonal elements merely yield the *formal uncertainties* of the estimated parameters. It must be expected that these uncertainties are overly optimistic as they do not consider model and environment errors. The effect of these errors on the estimation uncertainties can be described by so called *consider parameter* whose inclusion yields a more representative attainable POD accuracy. Unfortunately, Tudat does not yet have the necessary functions and their inclusion is outside of the scope of this thesis leading to too optimistic estimation uncertainties.

When solving for $\Delta \mathbf{p}_0^{lsq}$ use can be made of information on the accuracy of the estimated parameters expressed by the a priori covariance matrix Λ . This a priori information is imperative should the normal matrix suffer from rank deficiency, e.g. if the number of estimated parameters in \mathbf{p} is larger than the number of available measurements in \mathbf{y} , as the normal matrix would otherwise not be invertible. Additionally, the use of a priori information helps to prevent the degradation of the orbit determination around another celestial body due to poor geometrical constrains, as discussed further in [section 8.1](#) [[Montenbruck and Gill, 2000](#); [Bonanno and Milani, 2002](#); [Folkner et al., 2017](#)]. Including the a priori information Λ into the least-squares problem leads to [Equation 5.21](#) and [Equation 5.22](#) becoming [[Montenbruck and Gill, 2000](#)]:

$$\Delta \mathbf{p}_0^{lsq} = (\Lambda + H^T P_y^{-1} H)^{-1} (\Lambda \Delta \mathbf{p}_0 H^T P_y^{-1} \Delta \mathbf{y}), \quad (5.23)$$

$$P_x = (H^T P_y^{-1} H + \Lambda)^{-1}. \quad (5.24)$$

The study of the potential added benefit of including crossover measurements treated here relies heavily on [Equation 5.24](#) with the resulting covariance analysis being discussed further in [section 5.3](#).

5.2. Application of the Loss Function

To estimate a body's trajectory in time the tracking measurements can be processed in sequence or in batches. Of those, sequential approaches are most useful for real-time applications where on-board predictions are evaluated with real-time measurements. Within a *batch*

approach, the measurements \mathbf{y} of all epochs are evaluated simultaneously. Using \mathbf{p}_0^{ref} as defined in section 5.1, a first-estimate orbit is calculated to obtain $\Delta\mathbf{y}$, as defined in Equation 5.5, by propagating the initial state, i.e. the linearization point, using an environment force model which predicts the body's motion in time. With this initial estimate for the spacecraft state, known as a *a priori state*, the iterative calculation of the initial spacecraft state \mathbf{s}_0 and the environment model parameters \mathbf{q} is initiated. As mentioned in section 5.1, it is of utmost importance that the environment force model represents the spacecraft environment as adequately as possible as its accuracy and exhaustiveness directly impacts the quality of the POD. Having established a prediction for the spacecraft's state in time, it now remains to correlate the measurements at later epochs to the linearization point $\mathbf{p}_0 = \mathbf{p}(t_0)$. To this purpose the first order differential function $F(t, \mathbf{s}(t), \mathbf{q})$ is defined:

$$\frac{d}{dt}\mathbf{p}(t) = \dot{\mathbf{p}}(t) = \mathbf{F}(t, \mathbf{s}(t), \mathbf{q}). \quad (5.25)$$

Solely regarding the dependency of the tracking measurements of the spacecraft state $\mathbf{s}(t)$, the measurements at later epochs are related to the linearization point \mathbf{p}_0 via the so called *State Transition Matrix* Φ :

$$\Phi(t, t_0) = \frac{\partial \mathbf{s}(t)}{\partial \mathbf{s}_0} \quad ; \quad \mathbf{s}(t) = \Phi(t, t_0)\mathbf{s}_0. \quad (5.26)$$

For the first epoch, i.e. the linearization point \mathbf{p}_0 , Φ is an identity matrix as there have not yet been any changes in state. To obtain Φ at later epochs an expression for the change of the state transition matrix with time is also required [Montenbruck and Gill, 2000, Eq.7.41]:

$$\dot{\Phi}(t, t_0) = \frac{\partial \mathbf{F}(t, \mathbf{s}(t), \mathbf{q})}{\partial \mathbf{s}(t)} \cdot \Phi(t, t_0) \quad ; \quad \dot{\mathbf{s}}(t) = \dot{\Phi}(t, t_0)\mathbf{s}_0, \quad (5.27)$$

With $\dot{\Phi}(t_0, t_0)$ being defined as an identity matrix. In many cases however, we want to correlate measurements not only to the spacecraft state at the linearization point but to force model and/or observation parameters \mathbf{q} as well to also estimate these parameters when solving Equation 5.23. As shown in Equation 5.2, these parameters can be included in the parameter vector as $\mathbf{p}(t) = (\mathbf{s}(t), \mathbf{q})^T$ for the POD process. Their effect on the spacecraft's state $\mathbf{s}(t)$ at a later epoch is described by the *Sensitivity Matrix* \mathbf{S} , defined as:

$$\mathbf{S}(t) = \frac{\partial \mathbf{s}(t)}{\partial \mathbf{q}} \quad \text{resulting in} \quad \mathbf{p}(t) = (\Phi(t, t_0), \mathbf{S}(t)) \cdot \mathbf{p}_0. \quad (5.28)$$

Equally, the change of the sensitivity matrix with time is described by:

$$\dot{\mathbf{S}}(t) = \frac{d}{dt}\mathbf{S}(t) = \frac{\partial \mathbf{F}(t)}{\partial \mathbf{s}(t)} \cdot \frac{\partial \mathbf{s}(t)}{\partial \mathbf{q}} + \frac{\partial \mathbf{F}(t)}{\partial \mathbf{q}} = \frac{\partial \mathbf{F}(t)}{\partial \mathbf{s}(t)} \cdot \mathbf{S}(t) + \frac{\partial \mathbf{F}(t)}{\partial \mathbf{q}}. \quad (5.29)$$

Combining the derivatives of the state transition and sensitivity matrix yields:

$$\frac{d}{dt}(\Phi(t, t_0), \mathbf{S}(t)) = \frac{\partial \mathbf{F}(t)}{\partial \mathbf{s}(t)} \cdot (\Phi(t, t_0), \mathbf{S}(t)) + \left(0_{[6 \times 6]}, \frac{\partial \mathbf{F}(t)}{\partial \mathbf{q}} \right). \quad (5.30)$$

The sensitivity matrix at the linearization point is zero ($\mathbf{S}(t_0) = 0$) since the state at t_0 does not depend on the force model parameters \mathbf{q} .

Having obtained $\dot{\Phi}$ and $\dot{\mathbf{S}}$, we can obtain the respective state transition and sensitivity matrices at later epochs to relate all measurements to the linearization point. Together with the measurements $\mathbf{y}(t)$, the propagated states $\mathbf{s}(t)$ from the linearization point \mathbf{p}_0 , the design

matrices H_j and the state transition matrices Φ_j the linearised problem described in Equation 5.7 becomes:

$$\begin{pmatrix} \Delta \mathbf{y}_j \\ \Delta \mathbf{y}_{j+1} \\ \vdots \\ \Delta \mathbf{y}_n \end{pmatrix} = \begin{pmatrix} H_j \cdot (\Phi_j, S_j) \\ H_{j+1} \cdot (\Phi_{j+1}, S_{j+1}) \\ \vdots \\ H_n \cdot (\Phi_n, S_n) \end{pmatrix} \Delta \mathbf{p} + \varepsilon. \quad (5.31)$$

Therein, the design matrices H_j are the partial derivatives of the measurements with respect to their *current epoch*. As shown in Equation 5.31, the change of measurements at later epochs is linked to the linearisation point with the matrices Φ_j and S_j . As shown in equations 5.26 and 5.28, Φ and S describe changes in the spacecraft's state at an epoch t due to changes in $s(t_0)$ and \mathbf{q} , respectively. As discussed in section 5.1, the Jacobian matrix H first presented in Equation 5.5 describes changes in the modelled observations due to changes in the spacecraft's state $s(t)$. Together, these partial derivatives make up the *mapping matrix* M which connects the estimated measurement equations to the linearization point p_0 . Making use of Equation 5.21, we can now solve for \hat{p} to obtain a more accurate linearization point. Doing so iteratively until the values of Δp_0^{lsq} are lower than a pre-defined tolerance, i.e. convergence is reached, yields the best attainable estimate for spacecraft state and environment force/observation model parameters at t_0 .

If the used environment force/observation models do not perfectly match the actual measurement environment and the free parameters are not constrained well enough, measurement fitting degrades with increasing distance to the linearisation point due to errors in the propagated states. In practice, this degradation is dealt with by solving for several linearisation points, with the distance between these points based on propagation intervals for which propagation predictions are reliable. The use of several linearisation points leads to the spacecraft orbits being subdivided into multiple *arcs* whose length inevitably is a trade-off decision. While longer arcs provide more measurements to fit a propagated solution onto, errors such as those in the environment force model accumulate with time. The shorter the arcs, the more precise measurement fitting becomes at the cost of higher computational loads. Overall, shorter arcs are preferred since they ensure that the propagated states are reliable and they allow to estimate highly periodic effects within shorter time intervals. Therefore, when choosing an arc lengths effects such as planetary rotation and orbital periods should be considered also. If the arcs become too short however, there might not be enough measurements to adequately estimate all parameters within p , leading to potentially unstable solutions. Such unstable solutions often arise from rank deficiency problems, which arise if the number of available measurements is lower than the number of estimated parameters or if the measurement geometry is insufficiently diverse, as further discussed in chapter 8. For previous studies, typical arc lengths are between two and seven days, with their individual length being impacted by data coverage and manoeuvres for orbit adjustment or keeping [Neumann et al., 2001; Baù et al., 2015]. Of those effects, orbit manoeuvres are particularly impactful since they introduce large uncertainties in the spacecraft state and attitude. For the Lunar Reconnaissance Orbiter (LRO) the used arc lengths were between two and seven days with individual arcs of up to two-week length, depending on data coverage [Baù et al., 2015]. For the Mars Global Surveyor (MGS) arcs lengths extended usually over seven days, offset by five days to obtain overlapping epochs which can be used to evaluate estimation accuracy.

Within such a *multiarc* approach, there are usually some global force model parameters g which are time invariant, such as the gravitational parameter μ of the orbited body, which affect all arcs equally. Conversely, time variant parameters l such as the spacecraft state $s(t)$ or the drag coefficient C_D must be solved within each arc individually. By subdividing the parameter vector $p(t)$ into local and global components, l and g respectively, we obtain in

the case of three arcs, the linearised equation shown in Equation 5.32 [Marabucci, 2012]. Therein, the design matrix H is not evaluated with respect to all parameters of p , as defined in Equation 5.5, but separately for the local and global parameters l and g .

$$\begin{pmatrix} \Delta y_1 \\ \Delta y_2 \\ \Delta y_3 \end{pmatrix} = \begin{pmatrix} \left. \frac{\partial A}{\partial l} \right|_{t_1} & 0 & 0 & \frac{\partial A}{\partial g} \\ 0 & \left. \frac{\partial A}{\partial l} \right|_{t_2} & 0 & \frac{\partial A}{\partial g} \\ 0 & 0 & \left. \frac{\partial A}{\partial l} \right|_{t_3} & \frac{\partial A}{\partial g} \end{pmatrix} \begin{pmatrix} \Delta l_1 \\ \Delta l_2 \\ \Delta l_3 \\ g \end{pmatrix} + \varepsilon. \quad (5.32)$$

In Equation 5.32 the subscripts 1, 2 and 3 refer to the evaluated initial epochs t_1 , t_2 and t_3 of the estimation arcs. While each arc can be regarded as an independent, linearised problem, global force model parameters connect all arcs with l_i describing the linearization point of each individual arc.

As described further in subsection 5.5.3, the use of crossovers for JUICE's POD leads to the necessity of evaluating the spacecraft's state with respect to two different arcs if the crossover times t_1 and t_2 do not occur during the same arc. With $h_{\otimes,1}$ being a crossover in the arcs 1 and 3 and $h_{\otimes,2}$ being a crossover in the arcs 2 and 3 Equation 5.32 expands to:

$$\begin{pmatrix} \Delta y_1 \\ \Delta y_2 \\ \Delta y_3 \\ \Delta h_{\otimes,1} \\ \Delta h_{\otimes,2} \end{pmatrix} = \begin{pmatrix} \left. \frac{\partial A}{\partial l} \right|_{t_1} & 0 & 0 & \frac{\partial A}{\partial g} \\ 0 & \left. \frac{\partial A}{\partial l} \right|_{t_2} & 0 & \frac{\partial A}{\partial g} \\ 0 & 0 & \left. \frac{\partial A}{\partial l} \right|_{t_3} & \frac{\partial A}{\partial g} \\ \left. \frac{\partial h_{\otimes,1}}{\partial l} \right|_{t_1} & 0 & \left. \frac{\partial h_{\otimes,1}}{\partial l} \right|_{t_3} & \frac{\partial h_{\otimes,1}}{\partial g} \\ 0 & \left. \frac{\partial h_{\otimes,2}}{\partial l} \right|_{t_2} & \left. \frac{\partial h_{\otimes,2}}{\partial l} \right|_{t_3} & \frac{\partial h_{\otimes,2}}{\partial g} \end{pmatrix} \begin{pmatrix} \Delta l_1 \\ \Delta l_2 \\ \Delta l_3 \\ g \end{pmatrix} + \varepsilon. \quad (5.33)$$

The inclusion of these crossovers into the POD scheme is detailed further in subsection 5.5.3.

5.3. Covariance Analysis

Within the covariance matrix of the estimated parameters P_x , the diagonal elements play a major role as they yield the attainable *formal errors* of the POD scheme. These errors are denoted formal, since they represent the attainable errors within a highly simplified setup which neglects many systematic force and measurement model errors. With the estimated parameter being the mean value, the formal estimation errors herein describe the $1\sigma_x$ range where the true value is estimated to lie. The magnitude of these errors is obtained as:

$$\sigma_x = \sqrt{\text{diag}(P_x)}. \quad (5.34)$$

Conversely, the off-diagonal elements of P_x indicate the correlation between the formal errors of the estimated parameters. While certain estimated parameters might actually be correlated to one another, correlations can also result from insufficient geometrical constraints which are particularly prominent in the orbit determination around another celestial body than Earth [Bonanno and Milani, 2002]. As Doppler measurements only give insight into the change of radial distance between spacecraft and ground station, no immediate information can be

gained regarding the orientation of the spacecraft orbit in space. This effect is summarised by the following, simplified example: If both the ground station and the spacecraft are at the equator of their respective central bodies, with the equator of both bodies lying in the same plane and spacecraft and ground station being at their closest point to one another, the resulting Doppler measurements will indicate that the spacecraft is moving away from the ground station. However, these measurements are unable to tell in which direction the spacecraft is moving. Whether the spacecraft is moving North, South or any other direction is indiscernible from Doppler measurements alone. To aid in determination of the orbit's orientation in space range and VLBI measurements are used.

When analysing the 3×3 position sub-matrix $P_{x,s}$ of an estimated state, its diagonal elements define the size of an ellipsoidal region which represents the 1σ confidence region of the estimate. As the analysis of the estimated x , y and z components does not yield direct insights into the nature of the formal errors, these results are rotated into the more insightful spacecraft-fixed reference frame. For this rotation, the off-diagonal elements within $P_{x,s}$ are required as they describe the orientation of the estimation ellipsoid in space. The axes of the spacecraft reference frame, denoted RSW -frame, point towards the spacecraft radial (R), along-track (S) and cross-track (W) direction. The covariance matrix $P_{x,RSW}$ of the estimate state in the RSW -frame is obtained by:

$$P_{x,RSW} = R^{RSW/I} \cdot P_{x,s} \cdot R^{I/RSW}, \quad (5.35)$$

with $R^{RSW/I}$ being the rotation matrix from the inertial (xyz) to the spacecraft-fixed (RSW) reference frame. The rows of $R^{RSW/I}$ are the **unit vectors** in the radial \hat{R} , along-track \hat{S} and cross-track \hat{W} direction of the estimated state. While \hat{R} is obtained directly from the estimated state, \hat{S} and \hat{W} are obtained as:

$$\hat{W} = \hat{R} \times \hat{V} \quad \text{and} \quad \hat{S} = \hat{W} \times \hat{R}, \quad (5.36)$$

with \hat{V} being the unit vector of the estimated velocity vector.

5.4. Tracking Observables

At present, orbit determination for planetary missions is achieved mainly by using range-rate (Doppler) data, together with range and angular position data [Dirkx et al., 2018]. However, previous studies have shown that altimetry data can be used as observable for POD, see section 3.3 [Tai, 1989; Neumann et al., 2001; Mazarico et al., 2010, 2018]. As mentioned in section 2.3, the instrument 3GM provides the mission's scientific range-rate and range data for JUICE. The VLBI experiment PRIDE also provides range-rate data and JUICE's transversal position on the celestial sphere as by-product while mainly providing the ephemerides of the Jovian bodies [ESA, 2014].

Herein, only the methods and accuracies applicable to the JUICE mission will be treated. Previous works have shown that within POD procedures the spacecraft state vector is almost exclusively computed through Doppler data. For spacecraft POD range data only is used to obtain initial information on the spacecraft position since Doppler data is a relative measurement as discussed further in subsection 5.4.1. Conversely, signals of much longer periods than the spacecraft's orbit, such as the ephemerides of celestial bodies, are retrieved more reliably with range and angular position data [Dirkx et al., 2018]. Other methods, such as Laser Ranging and Interplanetary Laser Ranging, are also not applicable to JUICE's POD and shall not be considered either.

In the following, the principle of range-rate and altimetry measurements is presented with the degree of their attainable precision and accuracy being presented in subsection 5.6.1 and subsection 5.6.2.

5.4.1. Range-Rate Data

Range-rate observables are obtained from the observed shift Δf on the communication carrier wave due to the relative, radial velocity v_d between the transmitter and the receiver. This shift can be obtained via one-way or two-way measurements, with one-way measurements requiring precise oscillator frequency standards as frequencies at transmitter and receiver might differ due factors such as general relativity or clock errors, among others. Therein, errors in frequency keeping can lead to large measurement errors due to the measured signal travelling at the speed of light. Even while using precise frequency standards substantial noise is introduced and the actual frequency difference must be estimated during POD. For two-way measurements, as is the case for JUICE, a signal is sent by the transmitter on ground, which is retransmitted at the receiver on JUICE and recorded and evaluated at the initial transmitter. This setup has the advantage that no separate time keeping is necessary for both transmitter and receiver as it is the same instrument in both cases. For two-way range-rate measurements $\dot{\rho}$ can be modeled as the difference of the two-way range over the count of time as [Montenbruck and Gill, 2000]:

$$\dot{\rho} = \frac{1}{2} \frac{c(\tau_2 - \tau_1)}{t_2 - t_1} = \frac{\rho_2 - \rho_1}{t_2 - t_1}, \quad (5.37)$$

with c being the speed of light, ρ_2 being the reflection range, ρ_1 being the transmission range and τ_1 and τ_2 being the signal travel times at t_1 and t_2 respectively. Naturally, Equation 5.37 is a simplification, as the proper calculation of the Doppler shift is affected by various effects such as the different gravity potentials at the transmitter and the receiver, the general and special theory of relativity, aberration, transponder delay and light-time must be considered [Montenbruck and Gill, 2000]. The consideration of these effects is outside the scope of this document however. Naturally, relative changes in frequencies can be detected more precisely using higher frequencies, provided the wave oscillator is stable enough. Additionally, using several frequencies at the same time has allowed to improve the attainable precision for Doppler data substantially as detailed further in subsection 5.6.1. This is a property which has been implemented in current missions such as Juno and is implemented for the BepiColombo mission [Marabucci, 2012; Iess et al., 2018].

5.4.2. Viability Conditions

As mentioned in section 2.2, JUICE's nominal downlink period consists of a daily 8 hour period during which communication is established to the Malargue ground station. This communication window is used both to transfer any obtained scientific data to Earth and to track JUICE's motion. Naturally, there are viability conditions that must be satisfied to establish communication. Unsurprisingly, one such condition is that there are no bodies occulting the line of sight between JUICE and the Malargue station. For JUICE, the major occulting bodies to consider are Jupiter and the Sun. Furthermore, 3GM has the requirement that Malargue's minimum viewing angle of JUICE above the horizon must be 15 degrees [Iess, 2019]. This requirement ensures that neither errors due to reflections along the line of sight nor atmospheric effects afflict measurements in an impactful manner. Lastly, all communication windows must be larger than 3.5 hours [Vallat, 2019].

Applying these conditions to JUICE's nominal trajectory as in CReMA 3.0 yields the downlink windows shown in Figure 5.1 with the complete list of the downlink times listed in Appendix A.4. As shown in Figure 5.1, there is a large communication gap from day 32 until day 46 due to an occultation by the Sun. The resulting loss of tracking periods during CReMA 3.0 is the main reason why the nominal duration of the GCO500 phase was raised from 130 days up to 160 days. In previous nominal trajectories, this superior conjunction occurred during

the previous mission phase, GCO5000. Other minor occultations occur at days 0-2, 9, 81 and 117.

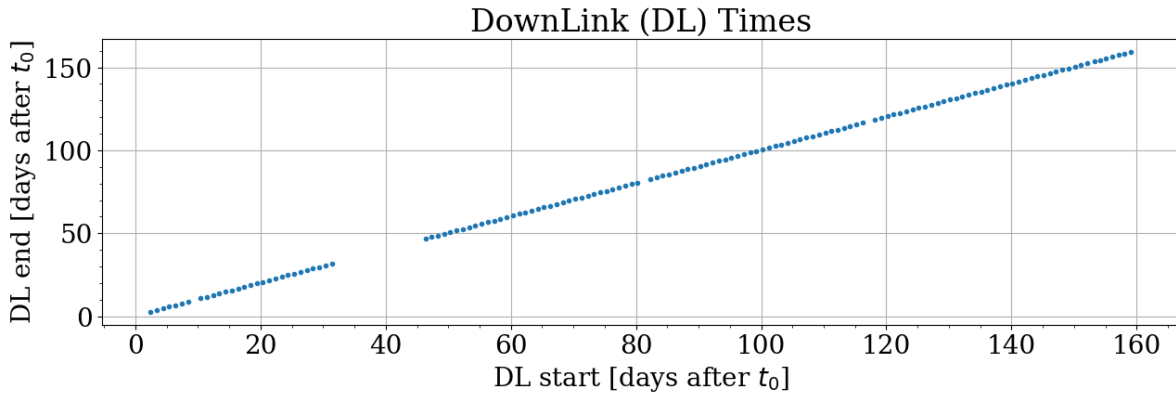


Figure 5.1: Available communication windows for JUICE during GCO500 mission phase, with t_0 as defined in section 6.3.

These occultations result from Jupiter blocking the communication line of sight and they have an average duration of two days. Naturally, communication gaps have a strong impact on JUICE's POD with the occultation due to the Sun being particularly impactful, as discussed further in section 8.2.

5.5. Crossovers

With the definition of altimetry crossovers being covered in section 3.3, this section presents the particular methods used for their determination, selection and inclusion into this thesis' orbit determination scheme, detailed further in section 7.1. Therein, the assumption is made that all measurements are nadir pointing leading them to coincide with the spacecraft ground tracks. It is expected that this assumption results in the formal estimation errors being too optimistic. This influence is mitigated by including pointing errors as discussed in section 5.6.

5.5.1. Crossover Determination

Of the different possible crossover determination schemes that have been used in previous studies [Tai, 1989; Kim, 1997; Wang and Luo, 2017], this thesis employs a method where crossover candidates are tested against analytical conditions. The method's initial coarse search finds potential crossover locations by locating the footprints with the smallest spherical distances to one another. The respective measurement satellite tracks at these potential crossover locations are then evaluated by a search routine, which tests whether they cross by testing the conditions described below. If these conditions are met, the crossover times t_1 and t_2 are used to obtain the respective spacecraft states and altitude. Since we are dealing with specific, individual, discrete measurements the consideration must be made that crossovers do not occur at the given measurement epochs. This in turn leads to the crossover times t_1 and t_2 being obtained by interpolation. Herein a linear interpolation is used, which is reasonable as it is assumed that the footprint distances are negligible in comparison to the curvature of the reference sphere representing the orbited body. For the definition of the fine search routine, Equation 3.3 is rewritten as [Stark, 2019]:

$$h_{\otimes}(\mathbf{r}(t_1), \mathbf{r}(t_2)) = |\mathbf{r}(t_2)| - |\mathbf{r}(t_1)| = |\mathbf{r}_2| - |\mathbf{r}_1|. \quad (5.38)$$

To calculate the crossover location for a given arc i , the respective spacecraft state as projected onto the planetary surface in a body-fixed frame is required. Therefore, within the following

discussion regarding crossover determination all the presented vectors are in the *body-fixed frame* of the orbited body, unless stated otherwise.

If there is a crossover between two ground track arcs as identified by the coarse search, in the following denoted as arc 1 and arc 2, there is a crossover location \mathbf{r}_i^x on each track. The location of \mathbf{r}_i^x is defined as the distance from a given measurement/spacecraft epoch $\mathbf{r}(t_i)$ on track i while travelling at the spacecraft velocity $\mathbf{v}(t_i)$ as defined in Equation 5.39. The factor s_i defined in Equation 5.40 represents the required time to reach the crossover location while travelling at the speed $\mathbf{v}(t_i)$, starting from the location $\mathbf{r}(t_i)$. Therein, t_i^x is the crossover time on the respective arc.

$$\mathbf{r}_i^x = \mathbf{r}(t_i) + (t_i^x - t_i)\mathbf{v}(t_i) = \mathbf{r}(t_i) + s_i\mathbf{v}(t_i). \quad (5.39)$$

$$s_i = t_i^x - t_i. \quad (5.40)$$

Here, a linear approximation is sufficient since the specific measurements that yield the starting vectors \mathbf{r}_1 for arc 1 and \mathbf{r}_2 for arc 2 as projected onto the planetary surface must be so close to one another that the planetary curvature can be neglected. To confirm that we can neglect the planetary curvature the unit vector \mathbf{e} of a given body-fixed measurement is defined as:

$$\mathbf{e}_i = \frac{\mathbf{r}_i}{|\mathbf{r}_i|}. \quad (5.41)$$

The unit vector defined in Equation 5.41 is used to obtain the vector connecting the two measurement states \mathbf{r}_1 and \mathbf{r}_2 as $\mathbf{e}_{21} = \mathbf{e}_2 - \mathbf{e}_1$. Furthermore, to obtain the second vector which defines the plane tangential to the planetary surface upon which GALA's laser beam is reflected we define:

$$\mathbf{e}_i^* = \frac{\mathbf{e}_i \times \mathbf{e}_{21}}{|\mathbf{e}_i \times \mathbf{e}_{21}|}. \quad (5.42)$$

Therein, the condition must be met that \mathbf{r}_1 and \mathbf{r}_2 are located closely enough to one another that the planetary curvature of the sphere can be safely neglected. Thus, leading to the planes defined by $(\mathbf{e}_{21}, \mathbf{e}_1^*)$ and $(\mathbf{e}_{21}, \mathbf{e}_2^*)$ being the same.

To evaluate Equation 5.39 merely the velocity vector \mathbf{v}_i^* along the above defined plane is required, with:

$$\mathbf{v}_i^* = \mathbf{v}_i - (\mathbf{v}_i \cdot \mathbf{e}_i)\mathbf{e}_i. \quad (5.43)$$

If there is a crossover point, there is a solution to the following set of equations [Stark, 2019]:

$$\mathbf{e}_1 + s_1\mathbf{v}_1^* = \mathbf{e}_2 + s_2\mathbf{v}_2^* \quad (5.44)$$

$$\mathbf{e}_{21} = \mathbf{e}_2 - \mathbf{e}_1 = s_1\mathbf{v}_1^* - s_2\mathbf{v}_2^* = \mathbf{V}^* \cdot \mathbf{s} \quad (5.45)$$

$$\mathbf{e}_{21} = (\mathbf{V} - \mathbf{E}) \cdot \mathbf{s}. \quad (5.46)$$

With the factor of interest \mathbf{s} obtained as:

$$\mathbf{s} = (\mathbf{V}^*)^{-1}\mathbf{e}_{21}. \quad (5.47)$$

Therein, $(\mathbf{V}^*)^{-1}$ is the pseudo inverse of \mathbf{V}^* obtained as $(\mathbf{V}^*)^{-1} = (\mathbf{V}^{*,T} \cdot \mathbf{V}^*)^{-1} \cdot \mathbf{V}^{*,T}$ since \mathbf{V}^* is not a square matrix. Having obtained \mathbf{s} , the crossover times t_1 and t_2 result from the times at the evaluated measurements with Equation 5.40. Making use of Equation 5.38 and Equation 5.39, the crossover measurement can be rewritten as:

$$h_{\otimes} = |\mathbf{r}(t_2) + ((\mathbf{V}^*)^{-1}\mathbf{e}_{21})_2\mathbf{v}(t_2)| - |\mathbf{r}(t_1) + ((\mathbf{V}^*)^{-1}\mathbf{e}_{21})_1\mathbf{v}(t_1)|, \quad (5.48)$$

with the subscripts 1 and 2 referring to the respective element of \mathbf{s} in Equation 5.47. Applying this crossover search routine onto JUICE's projected trajectory onto Ganymede during its GCO500 mission phase results in the following crossover locations.

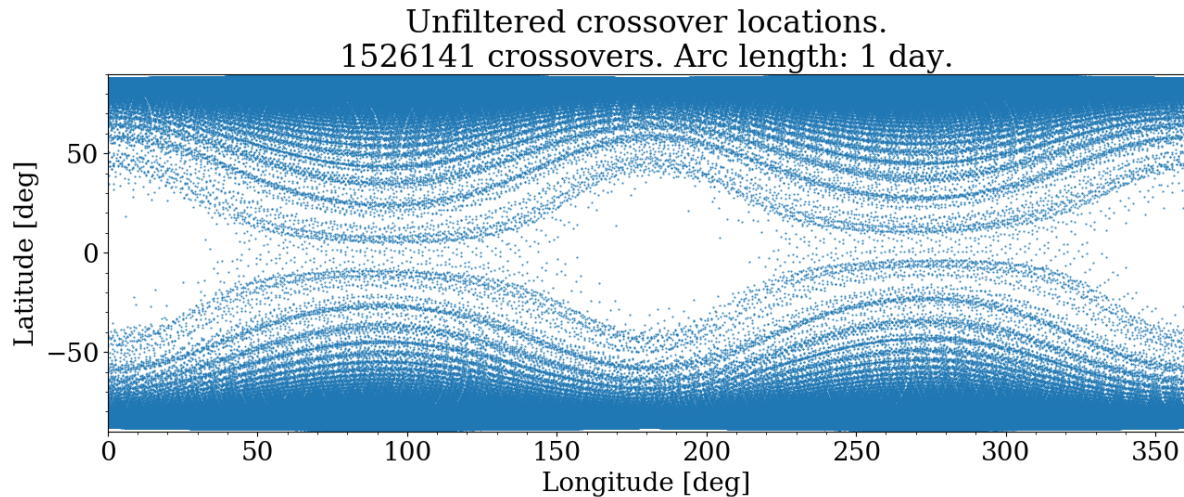


Figure 5.2: All possible crossover locations during JUICE’s GCO500 mission phase. No crossover selection filters have been applied, see [subsection 5.5.2](#).

Naturally, the choice of propagation arc length leads to different numbers of possible crossovers since the longer the arc, the larger the deviation to JUICE’s nominal trajectory becomes. For additional information regarding the trajectory propagation settings see [section 6.3](#).

5.5.2. Crossover Selection

As initially presented in [section 2.2](#) and further elaborated upon in [subsection 5.4.2](#), depending on the fulfilment of the viewing viability conditions, JUICE will have a daily 8 hour period dedicated to data downlink as well as tracking. Unfortunately, these downlink windows severely hinder the accumulation of scientific measurements as the entire spacecraft must be rotated in order for JUICE’s high gain antenna to point towards the Malargüe ground station.

To filter and use only the crossovers that are realistically obtained during the mission, any crossovers that occur during downlink windows as shown in [Figure 5.1](#) must be neglected. For the crossover selection, initially all crossover points are determined irrespective of the downlink periods, as shown in [Figure 5.2](#). Then, a filter routine is applied that only returns the crossovers which are within GALA’s measurement periods.

In addition to the downlink periods, the time required for the slew of the spacecraft must also be considered. Naturally, the slew time is variable as it highly depends on the spacecraft’s position and orientation at slew start. While slew manoeuvres are expected to require an average of 20 minutes, additional 10 minutes must also be included for settling-in effects to subside allowing for pointing requirements to be fulfilled [[Erd, 2019](#)].

Furthermore, Wheel-Off-Loading (WOL) manoeuvres must also be considered. These manoeuvres are necessary to prevent the spacecraft’s reaction wheels from saturating, ensuring that they can adjust the spacecraft’s attitude adequately. The final, nominal trajectory for JUICE remains yet to be determined. While the final JUICE WOL requirements have not been established, current planning assumes one WOL manoeuvre before each tracking period [[Val-lat, 2019](#)]. This choice in design aims at lowering spacecraft state and pointing uncertainties, as the results of the WOL on the spacecraft orbit are measured immediately after they occur. Thus, enabling a more stable estimate of the spacecraft trajectory until the next measurement window. Taking a conservative approach, such a WOL manoeuvre is also estimated to take up to 30 minutes [[Erd, 2019](#)]. Unfortunately, these manoeuvres effectively reduce the average, daily available time for GALA measurements from 16 to 14.5 hours as shown in [Figure 5.3](#).

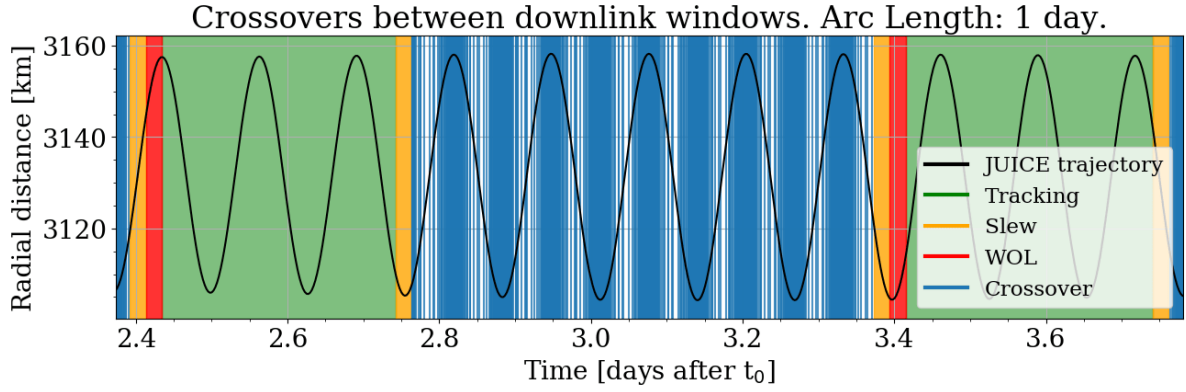


Figure 5.3: Remaining crossovers between two downlink periods. t_0 as defined in [section 6.3](#).

In addition to the exclusion of crossovers that occur during downlink windows, crossovers that occur close to the beginning or ending of a propagation arc must also be excluded:

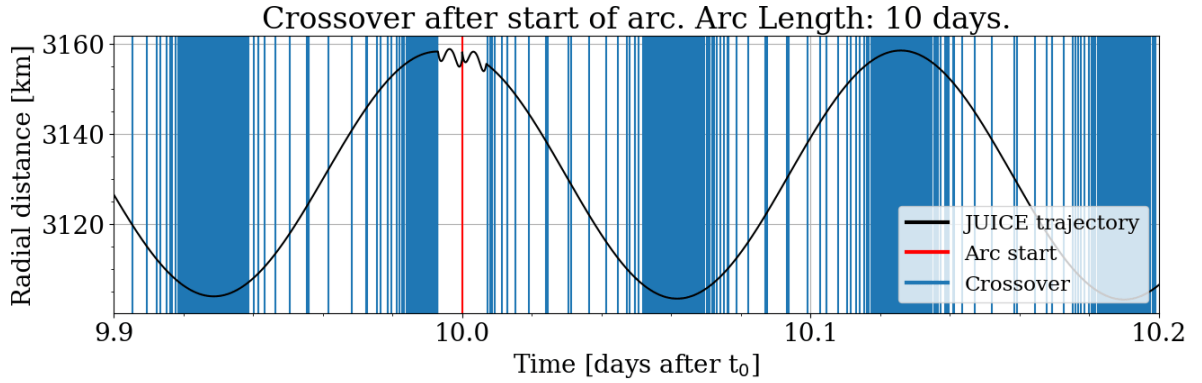


Figure 5.4: Crossover filter due to interpolation errors. t_0 as defined in [section 6.3](#).

The reason for this exclusion lies in the trajectory analysed for crossover determination being obtained through interpolation as explained further in [section 6.3](#). The used interpolator is a Lagrange interpolator of order 8, meaning that it fits the discrete trajectory states using a polynomial of degree 8. At both the beginning and end of each arc, the used interpolator does not have enough state epochs to draw an accurate orbit state estimation from, leading to an unstable trajectory behaviour as shown in [Figure 5.4](#). These interpolation errors are more prominent for propagations with longer arc lengths. This originates in the respectively larger discrete changes in position introduced at the beginning of each arc as discussed further in [section 6.4](#). As discussed in [section 6.3](#), the used integrator stepsize is 200 seconds. Since the period of interpolation errors is uniformly 600 seconds before/after each arc end/beginning, as seen in [Figure 5.4](#), it can be surmised that the used interpolator only yields reliable results once it has at least four state epochs available. Therefore an additional crossover filter is applied to neglect crossovers close to arc start/end epochs. To prevent numerical errors, a buffer of additional 10 seconds is chosen resulting in a exclusion time of ± 610 seconds around each arc start/end time which corresponds to a duration of about 20.3 minutes. While this filter does noticeably affect the total number of available crossovers it does not affect results in a noticeable manner. Additionally, the loss of crossovers due to this filter can be seen as an approximation to previous studies where crossover measurements were discarded due to unfavourable surface or pointing conditions.

Applying these filters shown in [Figure 5.3](#) and [Figure 5.4](#) onto the determined trajectory

crossovers results in the following, global crossover distribution:

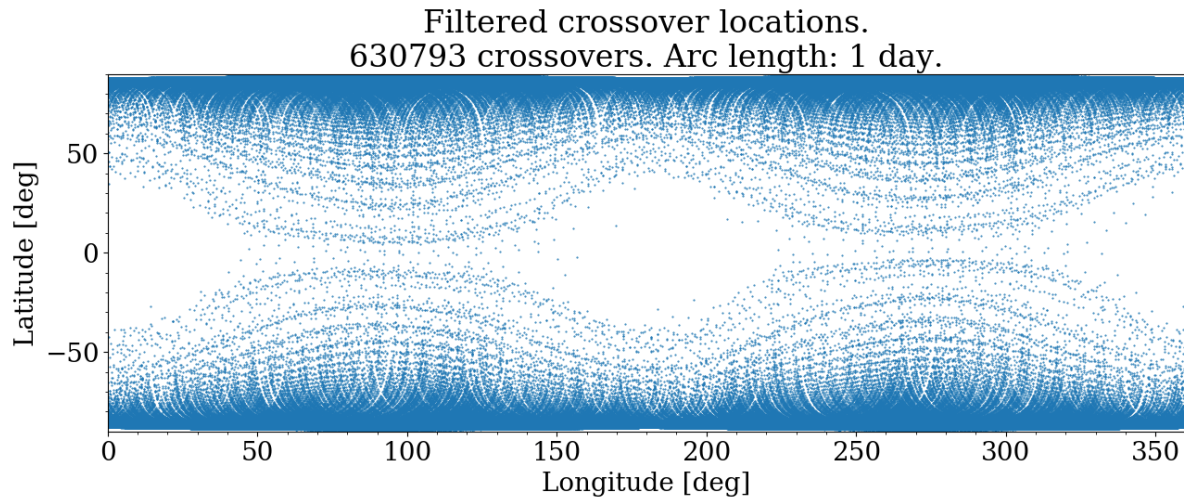


Figure 5.5: Filtered crossover locations during JUICE’s GCO500 mission phase using an arc length of 1 day.

It should be noted that the crossover distribution shown both in [Figure 5.3](#) and [Figure 5.4](#) is consistent with the one shown in [Figure 5.2](#) and the orbit discussion within [section 6.4](#). Therein, it was shown that JUICE has a polar orbit which results in ground tracks having the largest average distance to one another at the equator and having the highest likelihood for crossing one another at the poles. During the long communication gap due to a Sun occultation, there is no expected scientific data loss due to JUICE’s internal storage being large enough to accumulate data until the next communication period. This leads to a particularly long, uninterrupted period of crossover collection whose effect is discussed further in [section 8.1](#).

5.5.3. Inclusion Into POD

In the following, the mathematical framework for the inclusion altimetry crossover measurements into an orbit determination scheme is presented.

As described by [Equation 3.3](#), a crossover observable describes the measured altitude difference between two passes over the same topography. For a first approximation, changes in topography due to effects such as tidal forcing, or variations in Ganymede’s rotation are neglected. This approximation is possible since it can be assumed that the partial derivatives of crossover measurements due to Ganymede’s deformation are negligibly small. The origin of this assumption is that even if the location of a crossover changes strongly, it will not change in a range that makes the deformation of Ganymede noticeable on measurements. While Ganymede experiences a radial deformation of up to 7 meters, it does so with respect to a planetary radius of 2634 km. Taking the planetary deformation into account results in the modified crossover measurement equation discussed in [section 5.7](#). However, within the approximation treated here only Ganymede’s *static* topography remains to be considered. As shown in [Equation 5.49](#), Ganymede’s static topography T can also be discarded as it is the same during both passes:

$$h_{\otimes} = h_2 - h_1 = [r_2 - T] - [r_1 - T] = r_2 - r_1. \quad (5.49)$$

As discussed in [section 5.1](#), in order to estimate the spacecraft state the partial derivatives of the respective measurements with respect to the spacecraft state $s(t)$ are required to obtain

the design matrix H . To calculate the required partial derivatives, Equation 3.3 is rewritten as before with:

$$h_{\otimes}(\mathbf{r}(t_1), \mathbf{r}(t_2)) = |\mathbf{r}(t_2)| - |\mathbf{r}(t_1)| = |\mathbf{r}_2| - |\mathbf{r}_1|. \quad (5.50)$$

Furthermore, at the crossover point the following condition must be satisfied:

$$\hat{\mathbf{r}}^B(t_1) = \hat{\mathbf{r}}^B(t_2), \quad (5.51)$$

with $\hat{\mathbf{r}}$ being the unit vector of \mathbf{r} and B referring to the body-fixed orientation frame. The condition described in Equation 5.51 ensures that both crossovers arc-components occur over the same longitude and latitude in frame B . To a first approximation, the partial derivative of a crossover observable w.r.t. a change in the initial state $\mathbf{s}(t_0)$ can be described as:

$$\frac{\partial h_{\otimes}(t)}{\partial \mathbf{s}(t_0)} = \frac{\partial h_{\otimes}}{\partial \mathbf{s}(t_1)} \frac{\partial \mathbf{s}(t_1)}{\partial \mathbf{s}(t_0)} + \frac{\partial h_{\otimes}}{\partial \mathbf{s}(t_2)} \frac{\partial \mathbf{s}(t_2)}{\partial \mathbf{s}(t_0)}, \quad (5.52)$$

In Equation 5.52 the assumption is made that both crossover times t_1 and t_2 occur in the same arc. Should they occur at different arcs with these arcs starting at $t_{1,0}$ and $t_{2,0}$, Equation 5.52 becomes:

$$\frac{\partial h_{\otimes}(t)}{\partial \mathbf{s}(t_{1,0}, t_{2,0})} = \frac{\partial h_{\otimes}}{\partial \mathbf{s}(t_1)} \frac{\partial \mathbf{s}(t_1)}{\partial \mathbf{s}(t_{1,0})} + \frac{\partial h_{\otimes}}{\partial \mathbf{s}(t_2)} \frac{\partial \mathbf{s}(t_2)}{\partial \mathbf{s}(t_{2,0})}, \quad (5.53)$$

As shown in Equation 5.50, a crossover measurement is merely dependent on the spacecraft position, not on the spacecraft velocity, making it possible to reduce Equation 5.52 to:

$$\frac{\partial h_{\otimes}}{\partial \mathbf{s}(t_0)} = \frac{\partial h_{\otimes}}{\partial \mathbf{r}(t_1)} \frac{\partial \mathbf{r}(t_1)}{\partial \mathbf{s}(t_0)} + \frac{\partial h_{\otimes}}{\partial \mathbf{r}(t_2)} \frac{\partial \mathbf{r}(t_2)}{\partial \mathbf{s}(t_0)}. \quad (5.54)$$

Evaluating Equation 5.54 using Equation 5.50 for Δh yields:

$$\frac{\partial h_{\otimes}}{\partial \mathbf{s}(t_0)} = - \frac{\partial |\mathbf{r}(t_1)|}{\partial \mathbf{r}(t_1)} \frac{\partial \mathbf{r}(t_1)}{\partial \mathbf{s}(t_0)} + \frac{\partial |\mathbf{r}(t_2)|}{\partial \mathbf{r}(t_2)} \frac{\partial \mathbf{r}(t_2)}{\partial \mathbf{s}(t_0)}. \quad (5.55)$$

Equally, should the crossover times t_1 and t_2 occur in different arcs Equation 5.55 becomes:

$$\frac{\partial h_{\otimes}}{\partial \mathbf{s}(t_{1,0}, t_{2,0})} = - \frac{\partial |\mathbf{r}(t_1)|}{\partial \mathbf{r}(t_1)} \frac{\partial \mathbf{r}(t_1)}{\partial \mathbf{s}(t_{1,0})} + \frac{\partial |\mathbf{r}(t_2)|}{\partial \mathbf{r}(t_2)} \frac{\partial \mathbf{r}(t_2)}{\partial \mathbf{s}(t_{2,0})}. \quad (5.56)$$

To evaluate the validity of Equation 5.55, it is possible to compare its results to numerically obtained partial derivatives which are fully representative of all crossover partials effects. As discussed further in section 7.4, the results obtained by this first approximation in the form of Equation 5.55 is insufficiently reliable to be used for orbit determination purposes. Thus, due to the large discrepancy between the results of numerically obtained partial derivatives and those obtained with Equation 5.52, any analysis which relies merely on this first approximation should be regarded critically.

A more elaborate expression which also takes into account the change in the crossover times t_1 and t_2 is obtained by rewriting Equation 3.3 as:

$$h_{\otimes}(\mathbf{r}_1, \mathbf{r}_2, t_1, t_2) = |\mathbf{r}_2(\mathbf{r}_2, t_2(\mathbf{r}_1, \mathbf{r}_2))| - |\mathbf{r}_1(\mathbf{r}_1, t_1(\mathbf{r}_1, \mathbf{r}_2))|. \quad (5.57)$$

As before, an expression for Equation 5.54 must be found. Using Equation 5.57 for Δh , the crossover partial derivative w.r.t. its current position vector \mathbf{r}_1 is [Dirkx, 2019]:

$$\frac{\partial h_{\otimes}}{\partial \mathbf{r}_1} = \frac{\partial |\mathbf{r}_2|}{\partial t_2} \frac{\partial t_2}{\partial \mathbf{r}_1} - \frac{\partial |\mathbf{r}_1|}{\partial \mathbf{r}_1} - \frac{\partial |\mathbf{r}_1|}{\partial t_1} \frac{\partial t_1}{\partial \mathbf{r}_1}. \quad (5.58)$$

The derivatives for the times t_1 and t_2 w.r.t. r_1 are:

$$\frac{\partial t_2}{\partial r_1} = \frac{\partial t_2}{\partial r_1^B} \frac{\partial r_1^B}{\partial r_1}, \quad (5.59)$$

$$\frac{\partial t_1}{\partial r_1} = \frac{\partial t_1}{\partial r_1^B} \frac{\partial r_1^B}{\partial r_1}. \quad (5.60)$$

Of the terms above, the following can be obtained directly:

$$\frac{\partial |r_2|}{\partial t_2} = v_2 \cdot \hat{r}_2 \quad ; \quad \frac{\partial |r_1|}{\partial t_1} = v_1 \cdot \hat{r}_1, \quad (5.61)$$

$$\frac{\partial |r_2|}{\partial r_2} = (\hat{r}_2)^T, \quad (5.62)$$

$$\frac{\partial r_1^B}{\partial r_1} = R^{B/I}(t_1) \quad ; \quad \frac{\partial r_2^B}{\partial r_2} = R^{B/I}(t_2), \quad (5.63)$$

with $R^{B/I}(t)$ being the rotation matrix from the inertial frame to the body-fixed frame at time t . Thus, only an expression of the terms $\partial t_2 / \partial r_1^B$ and $\partial t_1 / \partial r_1^B$ remains to be defined. In order to constrain the three independent elements of $r_1^B = (x_1^B, y_1^B, z_1^B)$ the following three conditions for $\partial t_2 / \partial r_1^B$ are defined. Therein, the discussed changes are infinitesimally small which allows any change to be regarded as linear, vastly simplifying the conditions.

- Any change in radial direction $\hat{r}_1^B = \hat{r}_2^B$ has no effect on either t_1 or t_2 , as the condition presented in [Equation 5.51](#) remains unaffected. Therein, only the crossover measurement is affected, while the crossover location remains the same.

$$\frac{\partial t_2}{\partial r_1^B} \cdot \hat{r}_2^B = 0. \quad (5.64)$$

- Any change of r_1^B in the direction of \hat{v}_1^B has no effect on the crossover time t_2 , as the crossover point on the arc of t_2 remains the same, while only inducing a change in t_1 :

$$\frac{\partial t_2}{\partial r_1^B} \cdot \hat{v}_1^B = 0. \quad (5.65)$$

- Lastly, a change of r_1^B in the direction of \hat{v}_2^B induces a change in t_2 . This change in t_2 is directly proportional to the magnitude of the horizontal component of $\hat{v}_2^B = |\hat{v}_{2,H}^B|$ which, as discussed in [subsection 5.5.1](#), gives the time/distance from a given measurement to the crossover itself. Hereby no changes are introduced to t_1 :

$$\frac{\partial t_2}{\partial r_1^B} \cdot \hat{v}_2^B = \frac{1}{|\hat{v}_{2,H}^B|}. \quad (5.66)$$

As for [Equation 5.43](#), the horizontal component of \hat{v}_2^B is obtained via subtracting its radial velocity component:

$$\hat{v}_{2,H}^B = \hat{v}_2^B - \hat{v}_2^B \cdot \hat{r}_2^B. \quad (5.67)$$

These conditions can be summarised as:

$$\begin{pmatrix} \hat{\mathbf{r}}_{2,x}^B & \hat{\mathbf{r}}_{2,y}^B & \hat{\mathbf{r}}_{2,z}^B \\ \hat{\mathbf{v}}_{1,x}^B & \hat{\mathbf{v}}_{1,y}^B & \hat{\mathbf{v}}_{1,z}^B \\ \hat{\mathbf{v}}_{2,x}^B & \hat{\mathbf{v}}_{2,y}^B & \hat{\mathbf{v}}_{2,z}^B \end{pmatrix} \cdot \begin{pmatrix} \frac{\partial t_2}{\partial x_1^B} \\ \frac{\partial t_2}{\partial y_1^B} \\ \frac{\partial t_2}{\partial z_1^B} \end{pmatrix} = \begin{pmatrix} 0 \\ 0 \\ \frac{1}{|\hat{\mathbf{v}}_{2,H}^B|} \end{pmatrix} \quad (5.68)$$

$$\text{with } \mathbf{A}_{t_2 r_1} = \begin{pmatrix} (\hat{\mathbf{r}}_2^B)^T \\ (\hat{\mathbf{v}}_1^B)^T \\ (\hat{\mathbf{v}}_2^B)^T \end{pmatrix}, \quad \mathbf{b}_{t_2 r_1} = \begin{pmatrix} 0 \\ 0 \\ \frac{1}{|\hat{\mathbf{v}}_{2,H}^B|} \end{pmatrix}, \quad (5.69)$$

$$\Rightarrow \frac{\partial t_2}{\partial \mathbf{r}_1^B} = \mathbf{A}_{t_2 r_1}^{-1} \mathbf{b}_{t_2 r_1}. \quad (5.70)$$

Equally, the three independent elements of \mathbf{r}_1^B for $\partial t_1 / \partial \mathbf{r}_1^B$ can be constrained with the following conditions [Dirkx, 2019]:

$$\frac{\partial t_1}{\partial \mathbf{r}_1^B} \cdot \hat{\mathbf{r}}_1^B = 0. \quad (5.71)$$

$$\frac{\partial t_1}{\partial \mathbf{r}_1^B} \cdot \hat{\mathbf{v}}_2^B = 0. \quad (5.72)$$

Contrary to Equation 5.66, if \mathbf{r}_1^B experiences a change in the direction in the in-plane direction of \mathbf{v}_1^B , i.e. along its own arc, the new crossover location will occur earlier in time. As t_1 becomes smaller, this results in a negative derivative :

$$\frac{\partial t_1}{\partial \mathbf{r}_1^B} \cdot \hat{\mathbf{v}}_1^B = \frac{1}{|\hat{\mathbf{v}}_{1,H}^B|}. \quad (5.73)$$

Within the scenario of Equation 5.73, t_2 experiences no changes. These conditions lead to:

$$\frac{\partial t_2}{\partial \mathbf{r}_1^B} = \mathbf{A}_{t_1 r_1}^{-1} \mathbf{b}_{t_1 r_1} \quad \text{with} \quad \mathbf{A}_{t_1 r_1} = \begin{pmatrix} (\hat{\mathbf{r}}_1^B)^T \\ (\hat{\mathbf{v}}_2^B)^T \\ (\hat{\mathbf{v}}_1^B)^T \end{pmatrix} \quad \text{and} \quad \mathbf{b}_{t_1 r_1} = \begin{pmatrix} 0 \\ 0 \\ \frac{-1}{|\hat{\mathbf{v}}_{1,H}^B|} \end{pmatrix}. \quad (5.74)$$

Making use of the equations above, Equation 5.58 can be rewritten as:

$$\frac{\partial h_{\otimes}}{\partial \mathbf{r}_1} = \frac{\partial |\mathbf{r}_2|}{\partial t_2} \left(\frac{\partial t_2}{\partial \mathbf{r}_1^B} \frac{\partial \mathbf{r}_1^B}{\partial \mathbf{r}_1} \right) - \frac{\partial |\mathbf{r}_1|}{\partial \mathbf{r}_1} - \frac{\partial |\mathbf{r}_1|}{\partial t_1} \left(\frac{\partial t_1}{\partial \mathbf{r}_1^B} \frac{\partial \mathbf{r}_1^B}{\partial \mathbf{r}_1} \right), \quad (5.75)$$

$$= (\mathbf{v}_2 \cdot \hat{\mathbf{r}}_2) \cdot ((\mathbf{A}_{t_2 r_1}^{-1} \cdot \mathbf{b}_{t_2 r_1}) \cdot \mathbf{R}^{B/I}(t_2)) \hat{\mathbf{r}}_1^T - \hat{\mathbf{r}}_1^T \quad (5.76)$$

$$- (\mathbf{v}_1 \cdot \hat{\mathbf{r}}_1) \cdot ((\mathbf{A}_{t_1 r_1}^{-1} \cdot \mathbf{b}_{t_1 r_1}) \cdot \mathbf{R}^{B/I}(t_1)). \quad (5.77)$$

Equally, the partial derivative of the crossover observable w.r.t. a change in \mathbf{r}_2 is obtained symmetrically yielding:

$$\frac{\partial h_{\otimes}}{\partial \mathbf{r}_2} = \frac{\partial |\mathbf{r}_2|}{\partial \mathbf{r}_2} + \frac{\partial |\mathbf{r}_2|}{\partial t_2} \left(\frac{\partial t_2}{\partial \mathbf{r}_2^B} \frac{\partial \mathbf{r}_2^B}{\partial \mathbf{r}_2} \right) - \frac{\partial |\mathbf{r}_1|}{\partial t_1} \left(\frac{\partial t_1}{\partial \mathbf{r}_2^B} \frac{\partial \mathbf{r}_2^B}{\partial \mathbf{r}_2} \right), \quad (5.78)$$

$$= \hat{\mathbf{r}}_2^T + (\mathbf{v}_2 \cdot \hat{\mathbf{r}}_2) \cdot ((\mathbf{A}_{t_2 r_2}^{-1} \cdot \mathbf{b}_{t_2 r_2}) \cdot \mathbf{R}^{B/I}(t_2)) \quad (5.79)$$

$$- (\mathbf{v}_1 \cdot \hat{\mathbf{r}}_1) \cdot ((\mathbf{A}_{t_1 r_2}^{-1} \cdot \mathbf{b}_{t_1 r_2}) \cdot \mathbf{R}^{B/I}(t_1)), \quad (5.80)$$

$$\text{with } A_{t_2 r_2} = \begin{pmatrix} (\hat{r}_2^B)^T \\ (\hat{v}_1^B)^T \\ (\hat{v}_2^B)^T \end{pmatrix}, \quad b_{t_2 r_2} = \begin{pmatrix} 0 \\ 0 \\ \frac{-1}{|\hat{v}_{2,H}^B|} \end{pmatrix}, \quad (5.81)$$

$$A_{t_1 r_2} = \begin{pmatrix} (\hat{r}_1^B)^T \\ (\hat{v}_2^B)^T \\ (\hat{v}_1^B)^T \end{pmatrix} \quad \text{and} \quad b_{t_1 r_2} = \begin{pmatrix} 0 \\ 0 \\ \frac{1}{|\hat{v}_{1,H}^B|} \end{pmatrix}. \quad (5.82)$$

These expressions describe the change of a crossover measurement due to a change in either r_1 or r_2 . Inserting these more detailed crossover partial derivatives into the design matrix H as defined in Equation 5.5 for the respective crossover measurements makes it possible to use crossovers for orbit determination. As for Equation 5.55, the accuracy of the more elaborate crossover partials above is evaluated in section 7.4.

5.6. Measurement Errors

So far, measurement errors have been included indiscriminately into the term ε as discussed in Equation 5.1. To properly include these errors into simulation and analysis, their nature must be understood to correctly implement their impact on measurements, as shown in Figure 5.6.

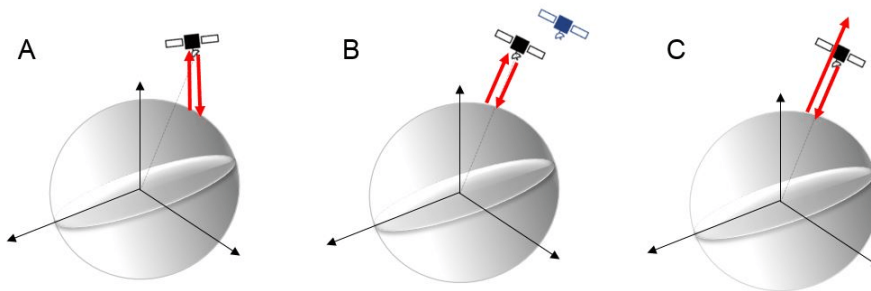


Figure 5.6: Overview of some error sources: Alignment and point errors (A), spacecraft position errors (B), ranging/measurement errors (C) [Steinke, 2015].

Herein, merely those errors shall be considered which are potentially critical for the topic of this document: The potential improvement of POD schemes with crossover-altimeter data using the JUICE mission as case study. Regarding error characterisation, it is important to make a distinction between random errors (precision) and systematic errors (accuracy), fittingly depicted by Figure 5.7 below:

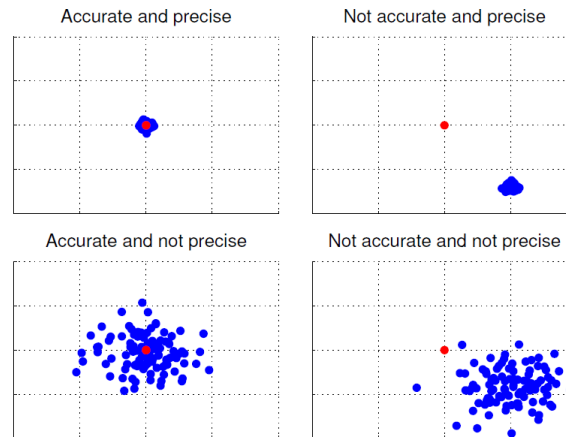


Figure 5.7: “Schematic representation of difference between accuracy and precision. The four plots show two-dimensional measurements (blue) on the same, arbitrary scale. Truth value indicated in red.” [Dirkx, 2015]

Of these two error types, random errors can successfully be averaged out by using a sufficient number of measurements. Conditionally, the same holds true for systematic errors if their spread is uniform around the true value over a number of measurements.

Below, the contributing error budgets for JUICE’s Doppler tracking data and GALA’s altimetry crossover measurements are established. As discussed in [section 5.4](#), neither VLBI nor radio-range measurements are included for JUICE’s POD treated here.

5.6.1. Doppler Error Budget

As mentioned in [subsection 5.4.1](#), errors in frequency keeping can have a large impact on measurements especially since the link end speed is exceptionally high. Conversely, Earth-bound range and range-rate measurements suffer noticeably more under relativistic effects, due to the large distance between Earth and JUICE, the different gravity potentials and their relative motion. Nevertheless, relativity effects are not treated here further due to their complex nature and small contribution to the scientific question of this document.

For Doppler measurements, previous efforts indicate that systematic errors are negligible [Iess et al., 2014, 2018]. While non-negligible, the magnitude of random errors for JUICE’s Doppler data is expected to be exceptionally low as their error sources, such as interplanetary plasma noise, are cancelled out in large part. This is done by using multi-frequency radio bands (X- and Ka-band links) to exploit carrier waves of different frequency being afflicted differently. Furthermore, the noise from tropospheric effects on Earth is reduced by continuously monitoring the path delay along the line of sight to the spacecraft with radiometers placed near the ground antenna [Iess et al., 2018]. Using these methods, JUICE’s expected range-rate precision is 1×10^{-5} m/s for an integration time of 60 seconds, with a precision as high as 1×10^{-6} m/s being possible using an integration time of 1000s. However, typical integration times for Doppler data are 60s or shorter, to obtain less sparse tracking data. Denser measurements are highly preferable, as they allows for high-periodic effects such as spherical harmonics or empirical accelerations, to be updated more regularly. This high Doppler precision represents state-of-the-art advancements for tracking measurements. While these high precisions might appear optimistic, they have been proven possible by NASA’s Juno mission to Jupiter which has already demonstrated an attainable precision of 1.5×10^{-5} m/s for an integration time of 60s [Folkner et al., 2017]. Conversely, the previously attainable precision values using X-band links was in the best case only 0.02 m/s at an integration time of 60 s [Dirkx et al., 2018]. Unfortunately, there is no further publicly available information regard-

ing the precision conditions for JUICE’s Doppler data and the assumption is made that the measurement noise is Gaussian. To gain insights into the effect of Doppler uncertainty onto the POD, a second case shall also be analysed. This shall be a worst case scenario wherein multi-link differencing failed. As shown by the Galileo mission to the Jovian system, the attainable Doppler precision during flybys around Ganymede was merely 5×10^{-4} mm/s [Jacobson, 2013].

In summary, the two precision cases that shall be analysed regarding the use of Doppler data for the POD of JUICE are:

| Doppler uncertainty cases | |
|---------------------------|------------------------|
| Best case | Worst case |
| 1×10^{-5} m/s | 5×10^{-4} m/s |

Table 5.1: Best and worst Doppler precision using an integration time of 60s.

5.6.2. GALA Error Budget

For the calculation of the error budget for laser altimetry measurements three significant error contributors were established: Instrument intrinsic errors, pointing and alignment errors and interpolation errors [Villamil, 2019]. During the determination of the magnitudes of these errors, two cases shall be considered as defined by GALA’s Instrument Requirements Document [Lingenauber, 2019]:

- Nominal Measurement Conditions: Surface slope < 8 degrees, albedo > 44% and a pointing error of < 10 arcsec
- Limited Measurement Conditions: Surface slope < 20 degrees, an albedo > 22% and a pointing error of < 10 arcsec

For the definition of the instrument intrinsic errors, GALA’s Instrument Requirements Documents yields a 2σ uncertainty of 1m for the Nominal Measurement Conditions. Conversely, in the case of Limited Measurement Conditions, a measurement uncertainty of 5m at a confidence level of 80% is defined, which equals to 1.5468σ . Thus, GALA’s instrument intrinsic errors δz_{GALA} the following 1σ uncertainties can be established:

| GALA instrument uncertainty | |
|-----------------------------|------------|
| Best case | Worst case |
| 0.5 m | 3.48 m |

Table 5.2: Best and worst GALA instrument errors, 1σ values as defined by GALA’s Instrument Requirements Document [Lingenauber, 2019].

Contrary to JUICE’s Doppler measurements, GALA’s laser measurements are highly susceptible to systematic errors resulting in a loss of accuracy as defined in Figure 5.7. For GALA, it is expected that these systematic errors arise from misalignment or calibration errors both instrument intrinsically and due to spacecraft attitude.

Therein, the largest systematic error source are pointing errors, even after in-cruise calibration [Steinbruegge et al., 2015]. Errors in pointing knowledge are assumed to originate from GALA's thermo-elastic distortion, the accuracy of the star trackers. Additional error inducing factors are spacecraft manoeuvres together with oscillations on the spacecraft, particularly on its solar panels. In Figure 5.8, the effect of pointing errors is shown. Therein, $\Delta\phi$ describes the error in the pointing angle while θ_T describes the laser pulse divergence as described in section 3.1. While the expected range is the black dashed line, unaccounted errors lead to an off-nadir pointing angle ϕ and the range z being measured instead.

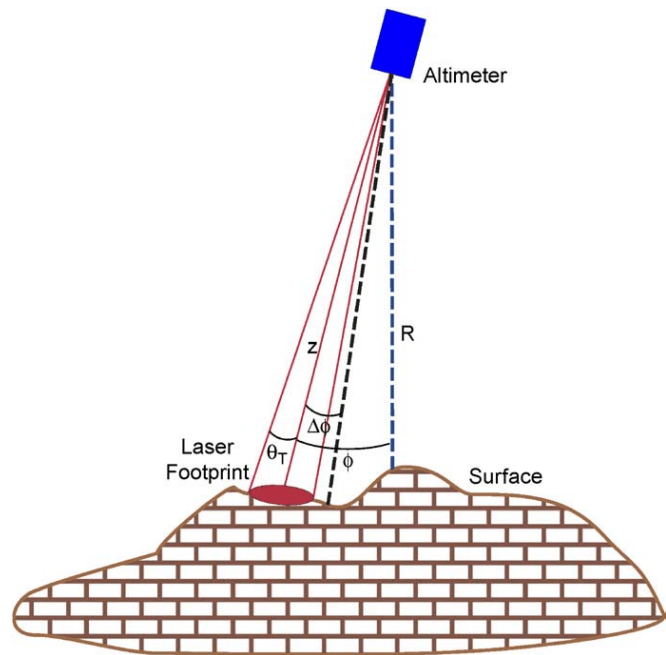


Figure 5.8: Geometry for pointing errors [Thomas et al., 2007]

If satellite pointing is not accounted for during the POD procedure, such erroneous measurements can lead to higher altitude estimates. Therein, the assumption is made that the pointing error jitters around nadir pointing as pointing errors due to the frequently occurring slew manoeuvres are random in nature. Thus, errors due to pointing shall also be treated as having a Gaussian distribution to a first approximation.

As alluded to in Figure 5.8, errors in altimetry measurements due to pointing errors are further exacerbated by the surface's slope. While a nominal altimetry measurement of 500 km is expected during JUICE's GCO500 mission phase, rapid changes in slope due to surface features such as rims, ridges or cracks among others can strongly affect measurements. Making use of global slope distributions derived from Voyager and Galileo data, Ganymede's slope can be assigned statistically. These previous missions found that roughly 90% of slopes on Ganymede are between 3.5° to 8° [Berquin et al., 2013]. The Limited Measurement Conditions mention a slope of 20° , as that is the slope that is expected at crater walls. Using the slope estimate from Voyager and Galileo, Ganymede's average global slope shall be approximated by $(3.5^\circ \times 90\% + 20^\circ \times 10\%) = 5.15^\circ$ for the Nominal Measurement Conditions. Equally, the average global slope for the Limited Measurement Conditions shall be approximated by $(8^\circ \times 90\% + 20^\circ \times 10\%) = 9^\circ$. These are merely rough estimates, as the slopes on the scale of GALA's footprint size are still unknown. Although Ganymede's surface is expected to be comparatively smooth due to the ice relaxation as discussed in section 2.4, it can be expected that these global slopes lead to too optimistic formal errors due to surface characteristics on GALA's footprint size such as boulders or rifts.

For altimetry measurements, the pointing error δz_p can be described as a function of pointing angle error $\Delta\phi$, altitude H and slope α as:

$$\Delta\phi_p = H \tan(\Delta\phi) \tan(\alpha). \quad (5.83)$$

Making use of Equation 5.83 and the Nominal and Limited Measurement Conditions defined above, the following pointing and alignment errors can be established for GALA's laser altimetry measurements:

| GALA pointing uncertainty | |
|----------------------------------|------------|
| Best case | Worst case |
| 2.18 m | 3.92 m |

Table 5.3: Best and worst GALA pointing errors, 1σ values.

Finally, the error contribution due to interpolation errors must also be considered for the calculation of the surface's height profile. Interpolation is necessary when describing the planetary surface continuously since altimeter measurements are only given at discrete epochs. Taking into account GALA's measurement frequency f_q of 30Hz as described in [section 3.1](#), interpolation errors δz_i can be calculated via [[Steinbruegge et al., 2015](#)]:

$$\delta z_i = \frac{v_{surf}}{2f_q} \tan \alpha, \quad (5.84)$$

with v_{surf} being velocity at which the planetary surface is measured. As discussed in [chapter 4](#), JUICE's trajectory during its GCO500 mission phase can be described as a circular orbit to a first approximation leading to a circular velocity around Ganymede of $v_{circ} = 1777$ m/s as previously calculated in [Equation 4.14](#). The velocity at which Ganymede's surface is scanned is equal to JUICE's circular velocity scaled to Ganymede's radius r_{Gan} as shown in [Equation 5.85](#). Therein, ω_{circ} is JUICE's angular velocity around Ganymede, r_{JUICE} is JUICE's radial distance to Ganymede's geopotential centre and v_{circ} is JUICE's velocity as projected on Ganymede's surface.

$$\omega_{circ} = v_{circ}/r_{JUICE} \Rightarrow v_{surf} = \omega_{circ} \times r_{Gan} = 1492.86\text{m/s}. \quad (5.85)$$

As before, using the Nominal and Limited Measurement Conditions defined for [Equation 5.84](#), the following interpolation errors δz_i can be established:

| GALA interpolation uncertainty | |
|---------------------------------------|------------|
| Best case | Worst case |
| 2.24 m | 4.02 m |

Table 5.4: Best and worst GALA interpolation errors, 1σ values.

Due to the assumption that GALA's instrument, pointing and interpolation errors are independent from one another their total contribution to GALA's error budget can be calculated as:

$$\Delta z = \sqrt{\Delta z_{GALA}^2 + \Delta z_p^2 + \Delta z_i^2}. \quad (5.86)$$

Using [Equation 5.86](#) and the error magnitudes defined above, the following total error budgets can be established:

| GALA total uncertainty | |
|-------------------------------|------------|
| Best case | Worst case |
| 3.17 m | 6.84 m |

Table 5.5: Best and worst error budgets for GALA measurements, 1σ values.

Since a crossover measurement consists of two individual, uncorrelated altimetry measurements the error contribution of these measurements is obtained as:

$$\Delta z_{xover} = \sqrt{\Delta z_1^2 + \Delta z_2^2}. \quad (5.87)$$

| Crossover measurement uncertainty | |
|--|------------|
| Best case | Worst case |
| 4.48 m | 9.68 m |

Table 5.6: Best and worst crossover measurement error budgets, 1σ values.

For the calculation of these crossover measurement error budgets a conservative approach was chosen. For the actual measurements spacecraft pointing might be better than required and it is expected that algorithm improvements mitigate interpolation errors.

5.6.3. Conclusion

The random errors ϵ discussed above can be described by the *central limit theorem* and they follow a Gaussian distribution G , which is dependent on the mean error μ and their Gaussian distribution σ as [ESA, 2014]:

$$G(\mu, \sigma) = \frac{1}{\sigma\sqrt{2\pi}} \exp\left(-\frac{(\epsilon - \mu)^2}{2\sigma^2}\right). \quad (5.88)$$

It is assumed that the mean value of the random errors treated in this document equal to zero. Error magnitudes represent a 1σ value, which equals a 67% confidence level, i.e. a 67% probability that any given error lies within the mentioned magnitude. Equally, a 2σ value represents a 95% confidence level and a 3σ value represents a 99% confidence. Considering the presented error budgets for Doppler and altimetry data, the four following cases shall be analysed for JUICE's POD using both Doppler and crossover data:

| POD uncertainties | |
|---|--|
| Case 1 | Case 2 |
| Best Doppler: 1.5×10^{-5} m/s | Worst Doppler: 5×10^{-4} m/s |
| Best GALA: 4.48 m | Best GALA: .4.48 m |
| Case 3 | Case 4 |
| Best Doppler: 1.5×10^{-5} m/s | Worst Doppler: 5×10^{-4} m/s |
| Worst GALA: 9.68 m | Worst GALA: 9.68 m |

Table 5.7: Error cases based on Table 5.1 and Table 5.6.

5.7. Definition of Tidal Partial

As discussed in section 2.3, it is expected that Ganymede's surface experiences a deformation of up to 7 meters due to Jupiter's tidal forcing. The parameter that relates radial surface deformation to its internal structure is the Love number h_2 which can so be used to constrain the existence of an internal ocean within Ganymede, see Figure 2.3. Since GALA measures Ganymede's topography, comparing measurements at different epochs over the same location enable the estimation of h_2 [Steinbruegge, 2018; Steinbruegge et al., 2015]. In the following, the necessary partial derivatives shall be presented to enable the estimation of h_2 using crossover measurements.

Similarly to Equation 4.6, where the connection of the love number to the tidal potential was described, the radial displacement $u_r(t)$ at a certain location on Ganymede is described

by:

$$u_r(t) = h_2 \frac{\Phi(r, \theta, \lambda, t)}{g(r)}, \quad (5.89)$$

with $\Phi(r, \theta, \lambda, t)$ being defined in [Equation 4.7](#) and $g(r)$ being the gravity on Ganymede's surface as $g = GM_{Gan}/r_{Gan}^2$.

While the effect of Ganymede's deformation was discarded within definition of the crossover partial derivatives discussed in [subsection 5.5.3](#), it is compulsory to include it to estimate h_2 . To do so, [Equation 5.49](#) is rewritten to include Ganymede's radial displacement at the crossover times t_1 and t_2 :

$$h_{\otimes} = \left(|\mathbf{r}_2| - T - \frac{h_2}{g} \Phi_2 \right) - \left(|\mathbf{r}_1| - T - \frac{h_2}{g} \Phi_1 \right), \quad (5.90)$$

$$= |\mathbf{r}_2| - \frac{h_2}{g} \Phi_2 - |\mathbf{r}_1| + \frac{h_2}{g} \Phi_1, \quad (5.91)$$

$$= |\mathbf{r}_2| - |\mathbf{r}_1| - \frac{h_2}{g} (\Phi_2 - \Phi_1). \quad (5.92)$$

Now all that remains is to establish the dependency of a crossover measurement $\delta\Delta h$ on the Love number h_2 :

$$\frac{\partial h_{\otimes}}{\partial h_2} = -\frac{1}{g} (\Phi_2 - \Phi_1). \quad (5.93)$$

The inclusion of such partial derivatives $\delta\mathbf{y}/\delta\mathbf{k}$ which affect the measurement model, instead of the spacecraft motion, are included into the POD algorithm by expanding the definition of the design matrix presented in [Equation 5.31](#) to [[Montenbruck and Gill, 2000](#)]:

$$\Delta\mathbf{y}(t) = \left(\mathbf{H}(t) \cdot (\Phi(t, t_0)\mathbf{S}(t)) \quad \frac{\partial\mathbf{y}}{\partial\mathbf{k}} \right) \Delta\mathbf{p} + \varepsilon. \quad (5.94)$$

With this inclusion of the tidal partials into the design matrix \mathbf{H} , it is possible to estimate the Love number h_2 by including in in the parameter vector \mathbf{p} .

6

Numerical Simulation

Since JUICE's scientific Doppler and GALA laser data will only be available several years from now, it is necessary to use synthetic data to study JUICE's POD. To this purpose, this thesis makes use of the TU Delft Astrodynamics Toolbox (Tudat) for trajectory propagation and measurement simulation [TUDelft, 2019]. To attain the largest possible authenticity therein, a trajectory is propagated that resembles the currently planned trajectory for JUICE, as described in [section 2.2](#). In the following, the chosen simulation settings are presented.

6.1. SPICE

While the calculation of the perturbing forces presented in [chapter 4](#) appears straightforward, the calculation of their interactions can be rather complex, which is particularly true for the motion of perturbing celestial bodies. To this purpose, a tool which simplifies simulations of orbital dynamics is the SPICE Toolkit developed by NASA's Navigation and Ancillary Information Facility (NAIF) [Acton, 1996]. Its data sets, the SPICE kernels, include the ephemeris of many celestial bodies, consisting of past observations and predictions for future epochs. Additionally, it provides celestial body information such as radii, gravitational constant, rotational speed and direction among others as well as information on leap-seconds introduced with time. Knowledge on leap-seconds is necessary to calculate between the non-continuous Universal Time Coordinated (UTC) and the continuous Ephemeris Time (ET). For the Ephemeris Time the Barycentric Dynamical Time (TDB) is used, which represents the passing of time experienced by a clock at rest at the barycenter of the Solar system. As a reminder, UTC is the time format we use on Earth which is subject to changes due to variations in Earth's rotation, while TDB describes the continuous passing of time.

For the simulation treated here, JUICE's nominal state in time and the relevant data on the perturbing celestial bodies is obtained from ESA's publicly available Consolidated Report on Mission Analysis (CReMA) 3.0 for the JUICE mission [ESOC, 2015]. Using the planetary ephemerides provided in these kernels ensures that JUICE's nominal trajectory can be reproduced as closely as possible, while also leading to significantly lower computational loads, as only JUICE's motion in time must be simulated [NAIF, 2018]. While there are later CReMA versions available, version 3.0 was chosen as baseline due to its high Ganymede coverage. A high coverage was chosen as key parameter, as it is of major importance for GALA's scientific goals. It is expected that JUICE's final, nominal mission trajectory incorporates a high coverage due to instrument requirements. To diminish the impact of numerical errors and to include spacecraft manoeuvres such as orbit corrections, attitude changes or wheel-off-loading events, JUICE's state is retrieved at regular intervals resulting in a Multi-Arc propagation.

6.2. Mission Environment

The perturbations used to calculate JUICE's trajectory as in CReMA 3.0 are [ESOC, 2015, p.88]:

- Sun point mass
- Ganymede point mass
- Ganymede 10x10 gravity model
- Jupiter point mass
- Jupiter zonal coefficient J_2
- Other Galilean moons as point masses

The position of all these celestial bodies in time is obtained via the respective ephemeris kernels used within CReMA 3.0, making use of SPICE as discussed in [section 6.1](#).

As mentioned in [section 4.1](#) for Ganymede's gravitational field only the coefficients J_2 and C_{22} have been determined. It was therefore necessary to use a synthetically generated gravity field to generate an orbit prediction affected by a central geopotential. The synthetic gravity field for Ganymede ESA's used was created based on observations for Titan. In doing so, three gravity models were created: a weak field, a strong field and a very strong field. Of these, JUICE's trajectory within CReMA 3.0 was simulated using the very strong field to obtain a conservative estimate for the stability of JUICE's orbit and the required manoeuvres during the GCO500 mission phase. Contrary to the settings of CReMA 3.0, this thesis makes use of a Ganymede gravity model up to degree and order 12 to study JUICE's POD as representative as possible. The degree and order of 12 were chosen as upper limits as their estimation is one of the major scientific goals of the 3GM instrument, as discussed in [section 2.3](#) [ESA, 2014]. The additional coefficients were obtained by calculating the Kaula coefficient of the very strong gravity field using [Equation 4.5](#). Establishing a Kaula value of $i=4.16$ as a mean value for all the coefficients of the very strong gravity field, the additional coefficients were obtained using Python's random number generator from -1 to 1 with seed number 0. The resulting Ganymede 12x12 gravity model can be found in [Appendix A.1](#).

As discussed in [section 4.4](#), the effect of solar radiation pressure (SRP) on JUICE is not negligible as its magnitude is comparable to that of the perturbing Jovian moons. For its inclusion, the spacecraft parameters presented in [section 4.4](#) are used. Currently, Tudat supports the calculation of Sun occultations by one body only. Therein, the choice was made to consider the occultations due to Jupiter. This choice results in longer continuous Sun occultations, resulting in more prominent secular orbit changes due to SRP. If occultations by Ganymede were considered instead, occultations would occur more often but for noticeably shorter periods.

In summary, the perturbations used in this thesis are:

- Sun point mass
- Ganymede point mass
- Ganymede 12x12 gravity model
- Jupiter point mass
- Jupiter zonal coefficient J_2
- Other Galilean moons as point masses
- Solar radiation pressure

In [section 6.4](#) it is shown how well these settings approximate the ESA nominal trajectory as published in CReMA 3.0.

6.3. Integrator and Propagator Settings

As was the case for [section 6.2](#), this thesis' integrator and propagator settings are chosen in accordance with JUICE's nominal trajectory as published in CReMA 3.0. Therein a Lagrange integrator of degree 8 was used with a fixed step size of 16 degrees in the true anomaly

[Boutonet, 2019]. This normalised step size results in an average step size of 348 s, with a minimum step size of 343 s and a maximum step size of 352.5 s. It is possible to use such a large step size for the simulation of JUICE's trajectory due to its nearly circular orbit and its weakly perturbed environment as previously shown in Figure 4.1. Indeed, Ganymede's attraction is the main driver for JUICE's orbit evolution during its GCO500 phase which is as expected, as JUICE is well within of Ganymede's sphere of influence as discussed in section 4.1.

To approximate JUICE's trajectory as published in CReMA 3.0 as closely as possible it is necessary to use the same settings to ensure that the trajectory simulation is affected by the same numerical error. Unfortunately, Tudat does not have the necessary functions to variate a simulation's stepsize based on the orbit's true anomaly and the implementation of such a stepsize control is outside the scope of this thesis. Initially it was planned to approximate ESA's stepsize by using a constant stepsize of 343 seconds. However, as shown in section 7.4 a stepsize of maximum 200 seconds is necessary to ensure a reliable calculation of the crossover partial derivatives necessary for JUICE's POD treated here. This approximation is justifiable due to JUICE's near circular orbit as discussed above, which is further emphasised in the small stepsize variations of the nominal trajectory. The use of relative and absolute errors cannot be successfully used to control the stepsize since the differences in state between evaluations are too small due to JUICE's circular orbit. Conversely, such a stepsize control is much more viable for eccentric orbits where the rapid state changes at the orbit's periapsis can be used to shorten the dynamical stepsize according to pre-set integration tolerances. Equally, at the orbit's apoapsis the slow state changes in the spacecraft orbit allow for longer stepsizes between integration steps, noticeably reducing overall computation times [Villamil, 2019].

As discussed in subsection 5.5.2, interpolation errors have a negative impact on the determination of crossovers and should thus be kept to a minimum. While a large stepsize is advantageous regarding computational loads, it is utterly detrimental for the determination of crossovers. As mentioned in subsection 5.5.1, the precise crossover times and location are obtained through linear interpolation between discrete GALA measurements, which as shown in Equation 5.54 can be substituted by JUICE's state vectors. Therein, the assumption is made that all measurements have nadir-pointing. To obtain highly dense data, while maintaining low computational loads, the reference trajectory of 200 s is interpolated using a Lagrange interpolator of order 8. To evaluate the effects of different interpolation stepsizes, a reference trajectory is propagated using a propagation length of 10 days and the environment model discussed in section 6.2. Using an Lagrange interpolator of degree 8, the reference trajectory was used to obtain trajectories with more dense output. Therein, the evaluated stepsizes between evaluated state output epochs range between 1s and 100s as shown in Figure 6.1. Using these trajectories, which have different spacecraft epoch density, the trajectories' crossovers were determined as discussed in subsection 5.5.1. To evaluate the crossover determination results of each trajectory, all trajectories are compared to the trajectory with the most dense results, the one with a stepsize of 1s, under the assumption that the trajectory with the most dense results has the most accurate crossover determination. Figure 6.1 shows the difference of the calculated crossover time t_1 obtained with each of the interpolated trajectories, as compared to the crossovers of the interpolated trajectory with a stepsize of 1s. Additionally, the total number of determined crossovers for each trajectory is shown with the 1s trajectory having determined 5913 crossovers.

The results shown in Figure 6.1 demonstrate the degradation in crossover determination due to increasingly large stepsizes. For small stepsizes the crossover determination error for t_1 increases linearly. However, if the stepsize becomes too large not only does the error in t_1 increase rapidly but the total number of determined crossovers decreases. It can be assumed, that this decrease in number of crossovers originates in individual crossovers becoming con-

glomerated during the crossover determination scheme presented in subsection 5.5.1. Thus, Figure 6.1 shows that in order to obtain a reliable crossover determination dense GALA measurements/JUICE state vectors are required.

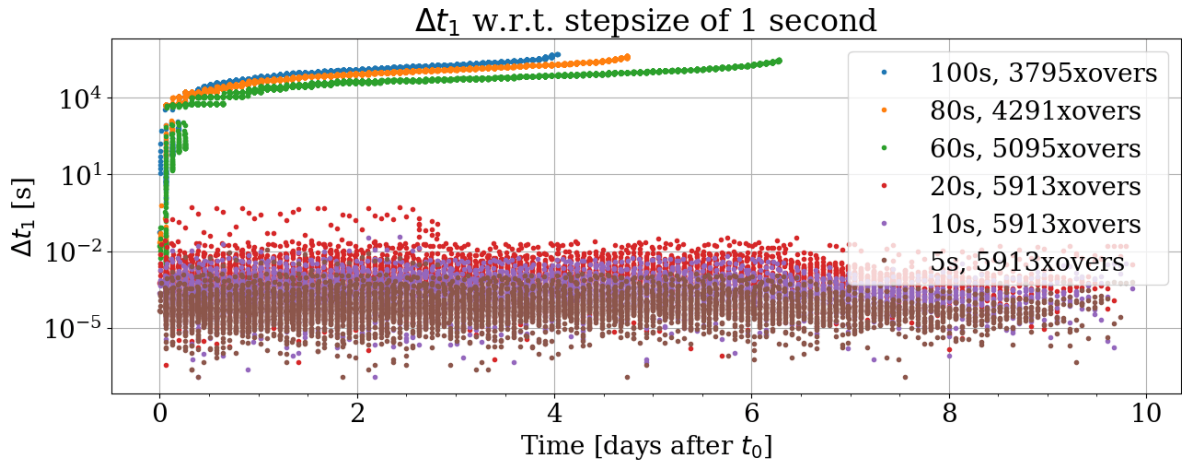


Figure 6.1: Interpolation error for t_1 during crossover (xover) determination using a stepsize of 1 second as baseline.

While representative of the actual mission scenario, GALA's nominal laser shot frequency of 30Hz shall **not** be used as guideline for the interpolator stepsize selection as it would lead to unjustifiably high computational loads for crossover determination. For the choice of interpolation stepsize, the effect the chosen stepsize has on the crossover determination must be defined first. On average, an interpolation stepsize of 5 seconds has a t_1 error of 0.097 seconds in comparison to a stepsize of 1 second. With a ground velocity of 1492.86 m/s, as calculated in Equation 4.14, an error of 0.097 s results in a crossover position error of 144.8 m. This is a non-negligible error, which also affects the crossover time t_2 . Additionally, an interpolation stepsize of 5 seconds has a maximum error of up to 20.36 s leading to a crossover position error of 30.39 km. For these reasons, a stepsize of 1 second is chosen as baseline for trajectory interpolation. Due to JUICE's orbital velocity an even shorter interpolation stepsize could be considered. Such a short stepsize is discarded however due to its high computational loads during crossover determination.

For the choice of the reference frame orientation, it is advantageous to choose an inertial reference frame as it allows to neglect the effect of fictitious forces [Wakker, 2015]. Commonly used ones are the J2000 and ECLIPJ2000 reference frames. Their orientation in space is based upon Earth's mean orbital plane and the Sun's mean Equator at the epoch J2000.0, respectively. For consistency reasons, the reference frame J2000 is used as consistent with CReMA 3.0. Furthermore, the chosen reference frame origin is Ganymede, consistent with the CReMA frame origin during JUICE's GCO500 mission phase [Boutonet, 2019]. This choice is advantageous for JUICE's simulation as it increases the numerical accuracy of Ganymede's gravitational attraction on JUICE while leading to a loss of accuracy for JUICE's perturbing bodies. This effect originates in computational limitations in the storage of large numbers, such as the distance between celestial bodies, resulting in a loss of accuracy when calculating the influence of bodies at large distances [Villamil, 2019].

Regarding the simulation's starting epoch, the second apoapsis after orbit insertion into the GCO500 phase was chosen resulting in $t_0=1,040,913,652.087404$ TDB s. At this epoch JUICE has already settled into a steady state as shown in Figure 6.2: An epoch at JUICE's apoapsis was chosen since at this point JUICE's motion is slowest, allowing for the trajectory

interpolator to settle in better into JUICE’s motion.

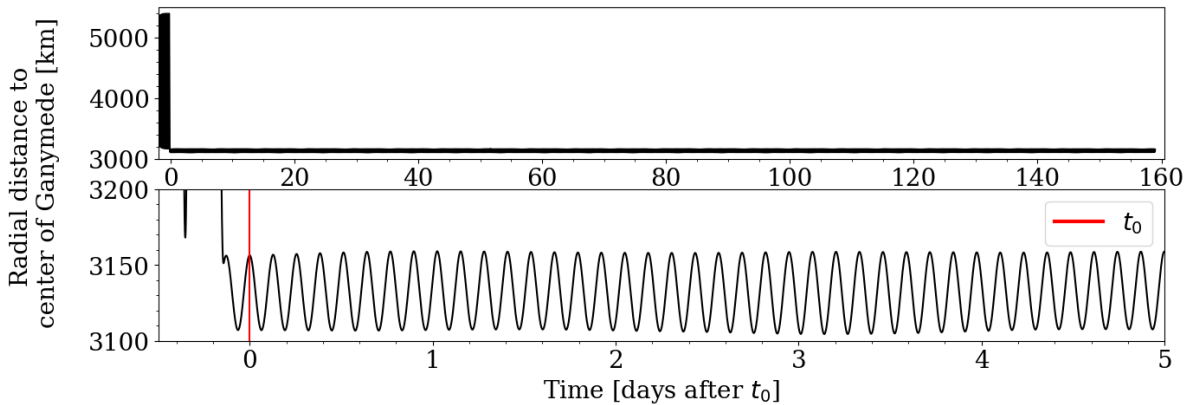


Figure 6.2: Definition of initial ephemeris time t_0 onto JUICE’s trajectory, as within CReMA 3.0.

It should be noted however, that this choice is of little importance due to JUICE’s orbit being almost circular and thus not being prone to large changes in speed and acceleration.

6.4. Trajectory Validation

In the following, this thesis’ propagation of JUICE’s motion during the GCO500 mission phase shall be validated by comparison to ESA’s nominal mission trajectory as published in CReMA 3.0 [Boutonet, 2019]. A description of the used numerical simulation settings can be found in section 6.3 and section 6.2, which approximate ESA’s simulation settings to a high degree. The requirements for a correct trajectory validation are not strict as it is expected that this thesis’ trajectory behaves differently due to the different environment model used, as discussed in section 6.2. Thus, already a trajectory propagation which loosely approximates ESA’s trajectory is regarded as sufficiently.

As mentioned in section 6.1, JUICE’s trajectory propagation is split into several arcs to enable a multi-arc orbit estimation as discussed in section 5.2. JUICE’s state at the beginning of each arc is obtained from JUICE’s CReMa 3.0 kernel at the respective epoch using SPICE. Since any discrepancies in propagation with respect to JUICE’s nominal trajectory accumulate in time, the longest arc length is used for validation. The longest evaluated arc length, as discussed further in section 8.2, equals 10 days. Figure 6.3 shows the difference in JUICE’s radial distance to Ganymede’s centre of mass between this thesis’ and ESA’s nominal trajectory:

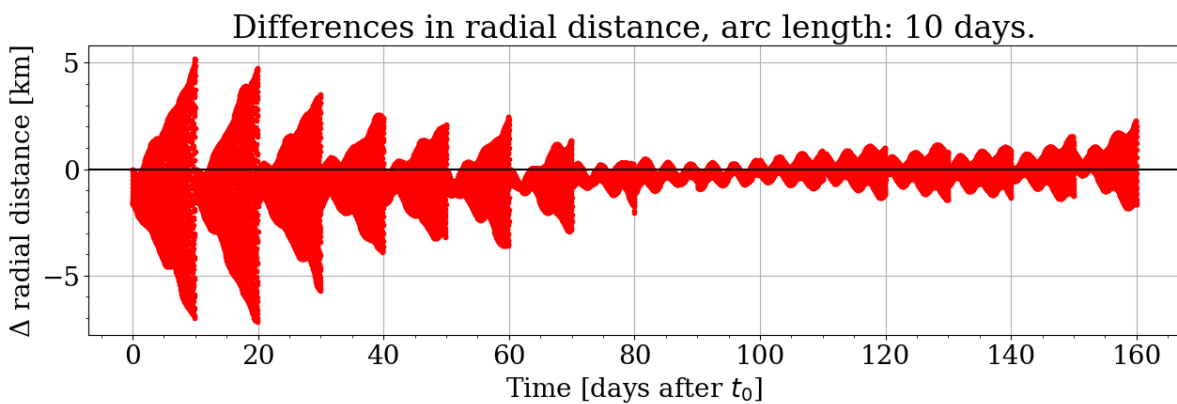


Figure 6.3: MultiArc trajectory validation, arc length: 10 days. Difference in radial distance to Ganymede’s centre of mass.

Naturally, a propagation with a shorter arc length is closer to ESA's nominal trajectory since JUICE state is obtained from it more often. For comparison, the difference in radial distance to the nominal trajectory while using an arc length of 1 day is shown in Figure 6.4:

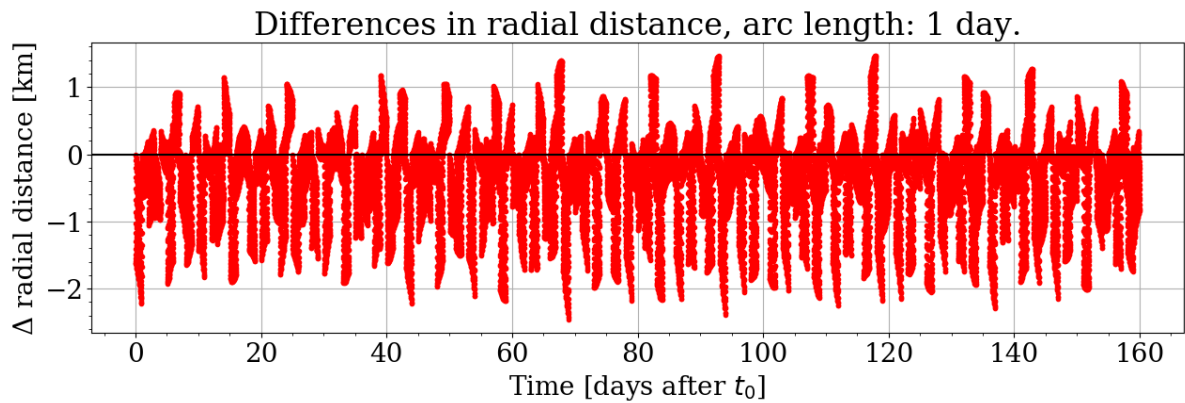


Figure 6.4: Difference in radial distance to Ganymede's centre of mass between ESA CReMA 3.0 and MultiArc trajectories.

Additionally, the simulated orbit evolution of JUICE as calculated in this thesis' with an arc length of 10 days and published in CReMA 3.0 is shown below:

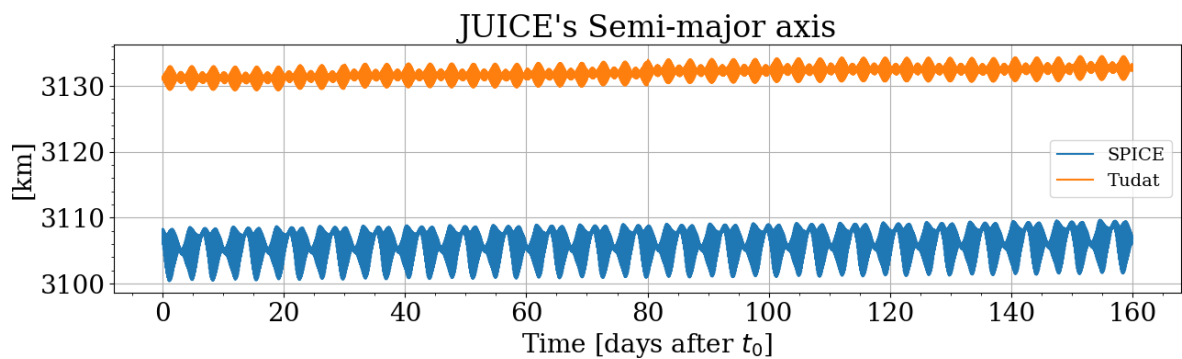


Figure 6.5: Evolution of JUICE's Semi-major axis during GCO500 mission phase.

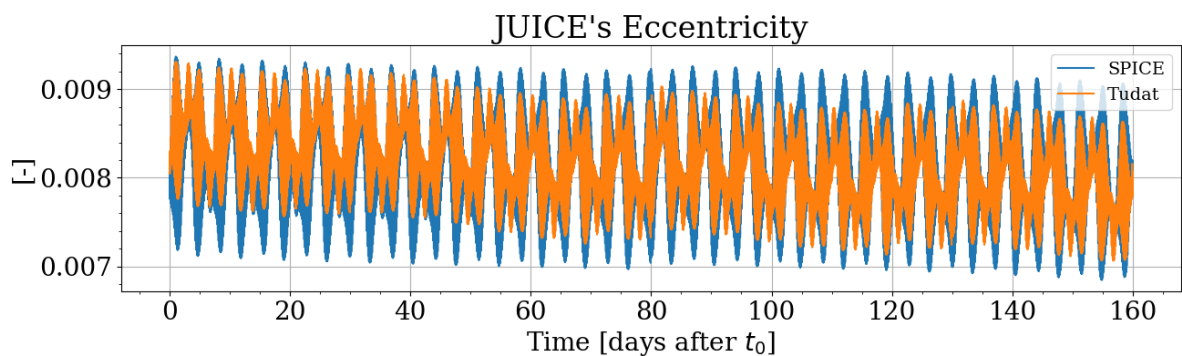


Figure 6.6: Evolution of JUICE's eccentricity during GCO500 mission phase.

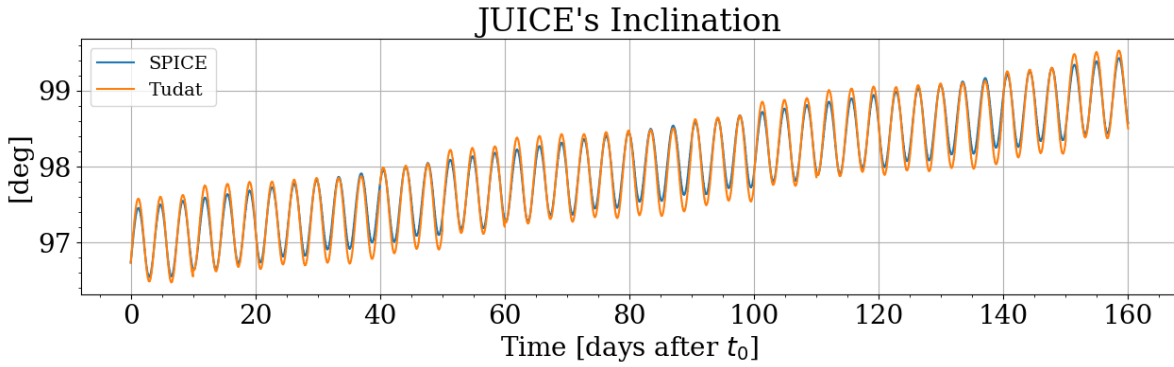


Figure 6.7: Evolution of JUICE's inclination during GCO500 mission phase.

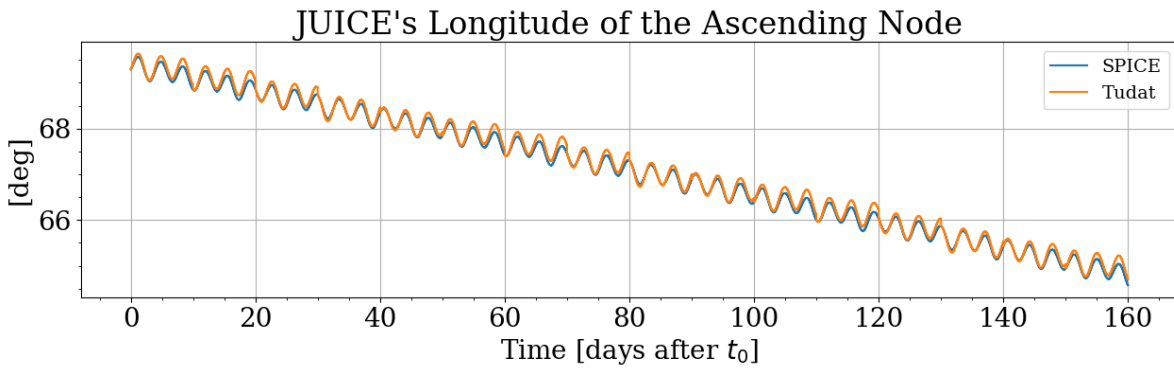


Figure 6.8: Evolution of JUICE's Right Ascension of the Ascending Node (RAAN) during GCO500 mission phase.

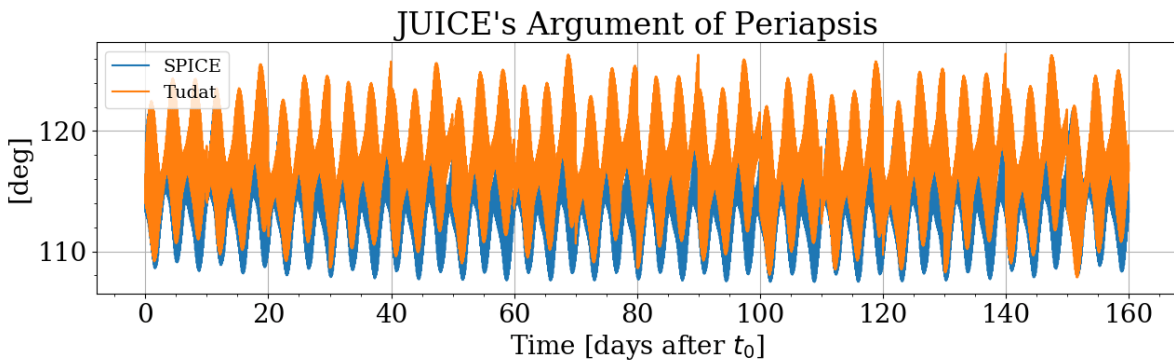


Figure 6.9: Evolution of JUICE's Argument of Periapsis during GCO500 mission phase.

The largest relative error for the orbital elements shown in the figures above is:

| Largest relative difference [%] | | | | |
|---------------------------------|--------------|-------------|-------|-----------------|
| Semi-major axis | Eccentricity | Inclination | RAAN | A. of Periapsis |
| 0.955 | 8.722 | 0.161 | 0.304 | 5.637 |

Table 6.1: Largest relative difference in orbital elements between this thesis' and ESA's trajectory.

While the evaluated orbital parameters are not reproduced exactly, the orbital elements of the trajectory of this thesis' approximate those of ESA's trajectory closely as quantified in [Table 6.1](#). While only a loose approximation of ESA's trajectory is required, the low relative differences between the evaluated trajectories as shown in [Table 6.1](#) fulfil the requirements for trajectory validation. It is expected that the difference in orbital elements arise from

differences in the environment model, as well as due to numerical errors. While the difference in stepsize is bound to introduce differences within the trajectories, the additional spherical coefficients this thesis makes use of are expected to be the largest driver for the differences above. Due to these differences in trajectory propagation, there is a discontinuity in spacecraft state, most easily noticed in [Figure 6.3](#) and [Figure 6.8](#). Naturally, these differences equal zero every 10 days as at the beginning of each arc JUICE's initial state is set equal to CReMA's at that epoch. Overall, these differences in orbit propagation are not only expected but desired for the study of JUICE's POD as they introduce discrete changes in JUICE's state which are used to approximate spacecraft manoeuvres.

Regarding the plots above, the difference in semi-major axis suggest a fundamental difference in the gravitational parameter used for the calculation of the trajectories. Due to the largest relative difference in semi-major axis as shown in [Table 6.1](#), this error is neglected as it does not affect the results of JUICE's POD discussed in [chapter 8](#). Additionally, the statement made in [chapter 4](#) regarding the circularity of JUICE's orbit is confirmed as its eccentricity is very low as shown in [Figure 6.6](#). Furthermore, [Figure 6.9](#) shows that JUICE's pericenter is slightly past Ganymede's north pole, thus confirming JUICE's orbit being polar and the resulting crossover location as discussed in [subsection 5.5.2](#). Lastly, while JUICE's inclination and Right Ascension of the Ascending Node (RAAN) do experience a secular evolution trend their variation is not strong over the 160 days of the GCO500 mission phase further emphasising the stability of JUICE's orbit.

7

Estimation Setup, Verification & Validation

For the analysis of JUICE's POD two distinctive scenarios shall be compared to one another:

- JUICE's POD using only Doppler measurements (Dopp).
- JUICE's POD using both Doppler and crossover measurements (DoXo).

Within both scenarios the exact same environment model and integrator/propagator settings are used, as presented in [section 6.3](#) and [section 6.2](#), with both scenarios estimating the same parameters at the same epochs. The only exception to this rule is made for the estimation of the Love number h_2 , which cannot be estimated using Doppler measurements only. This particular setup has the advantage that it demonstrates the *relative* effect of crossover measurements, allowing to make statements about their impact on orbit estimation uncertainties in comparison to conventional POD measurements. Therefore, this analysis' main focus will not lie on the ultimately attainable estimate precision using crossover measurements. Instead, it will lie on the potential added value the inclusion of crossover observables brings to POD routines. In [section 7.1](#), the used evaluation setup is discussed with the estimated parameters for JUICE's POD being presented in [section 7.2](#). A numerical benchmark to verify the crossover partial derivatives is established in [section 7.3](#), followed up by the verification of the crossover partials in [section 7.4](#). The POD itself is verified and validated in [section 7.5](#) and [section 7.6](#), respectively. Lastly, the partial derivatives for the estimation of h_2 are verified in [section 7.7](#).

7.1. Evaluation Scheme

In the following, the overarching POD scheme is presented which is based on a multi-arc approach as discussed in [section 5.2](#). For the trajectory propagation, JUICE state vectors at the beginning of each arc are obtained from JUICE's CReMA 3.0 mission trajectory, as discussed in [section 6.1](#). While it is possible to obtain JUICE's state from the reference trajectory used for crossover determination, this approach is not chosen as it yields additional interpolation errors resulting in slightly different initial states than for the reference trajectory itself.

The used environment model is presented in [section 6.2](#), which is more elaborate than ESA's nominal mission trajectory to make the JUICE's POD more representative. All simulations use a stepsize of 200 seconds, as mentioned in [section 6.3](#) with the underlying reasons for the chosen stepsize being elaborated upon in [section 7.4](#). As discussed in [section 6.3](#), large stepsizes are detrimental for crossover determination. To achieve an accurate crossover determination, the nominal trajectory is interpolated using a Lagrange interpolator of order 8 to obtain a trajectory output with a stepsize of one second, as discussed in [section 6.3](#). The

main reason why the trajectory is interpolated and not propagated to obtain such a dense output, is the decrease in computational loads with increasing stepsize. Low computational loads are particularly critical for this thesis' analysis, as a dense orbit output is only required for crossover determination. Neither the generation of the synthetic measurements, nor the parameter estimation require a dense output. Furthermore, it is necessary that trajectory propagation in all estimation cases is done with the exact same simulation settings as for the reference trajectory used for crossover determination to ensure that all the simulated trajectories are the same. This can only be ensured if all numerical simulations are affected by the same numerical and truncation errors. This is more so the case, since crossovers are highly sensitive to changes in initial state, as shown in [section 7.4](#). As discussed in [subsection 5.4.1](#), a Doppler integration time of 60 seconds is used with Doppler measurements being accumulated only during the respective downlink windows as described in [subsection 5.4.2](#). Conversely, crossover measurements are accumulated outside of the downlink, slew and WOL windows as discussed in [subsection 5.5.2](#). With these considerations in mind, the overarching evaluation scheme is the following:

1. As a first step, a reference mission trajectory is propagated using the simulation settings discussed in [section 6.2](#) and [section 6.3](#).
2. Using the aforementioned reference trajectory with an interpolated output of high density, the nominal crossover times and locations are determined, as presented in [subsection 5.5.1](#) and subsequently filtered as discussed in [subsection 5.5.2](#).
3. Using the exact same settings as for the reference trajectory, simulations are started wherein JUICE's POD is calculated using Doppler measurements only. As declared in [subsection 5.6.1](#), JUICE's POD is analysed using two distinctive Doppler error budgets. These two distinctive cases are simulated at this point, one after the other. Since the case with the higher precision is representative for the mission scenario, its results are used for POD validation in [section 7.6](#).
4. Using the exact same settings as for the reference trajectory, simulations are started wherein JUICE's POD is calculated using both Doppler and crossover measurements. As declared in [subsection 5.6.3](#), JUICE's POD is analysed using four distinctive measurement error budgets. These four distinctive cases shall be simulated at this point, one after the other.

Once the data of the respective POD algorithms is obtained, their results are evaluated, interpreted and compared as elaborated upon further in [chapter 8](#).

7.2. Estimated Parameters

In order to make JUICE's POD scheme and its resulting formal errors as representative as possible, several parameters shall be estimated besides JUICE's state vector within the parameter vector p , see [section 5.1](#). The choice in parameters is mainly driven by the requirements and scientific goals of the 3GM instrument, as it is JUICE's instrument responsible for its POD.

For the estimation of *local* parameters a priori covariances are used as defined in [Equation 5.23](#) and [Equation 5.24](#). The use of this a priori information is imperative to evaluate [Equation 5.24](#) since the normal matrix $H^T P_y^{-1} H$ is otherwise not invertible, as discussed further in [section 8.1](#). The magnitude of the a priori covariances for the estimated parameters are particularly conservative to ensure that they are at least two orders of magnitude higher than their attainable estimation uncertainties, in accordance with previous studies [[Montenbruck and Gill, 2000](#); [Bonanno and Milani, 2002](#); [Folkner et al., 2017](#)]. For the estimation of JUICE's position parameters a priori uncertainty of 1 km is used, with the an a priori uncertainty for its velocity parameters being 1 m/s .

As discussed in [section 2.3](#), one of 3GM's mission goals is to estimate Ganymede's gravity

field up to degree and order 12. However, the nominal CReMA 3.0 mission trajectory only makes use of a 10x10 gravity field for Ganymede. To make the estimation more representative, Ganymede's gravity field was extended to degree and order 12 making use of Kaula's rule as defined in Equation 4.5. For further details on the generation of the additional gravity field coefficients see section 6.2.

Additionally, empirical accelerations are also estimated with their directions being in radial, cross-track and along-track direction. These accelerations are usually estimated to compensate the effect of small unmodeled forces in precise orbit reconstruction procedures [Montenbruck and Gill, 2000; van der Wal, 2017]. It has been shown, that 3GM's mission goals can only be met by using an on-board accelerometer to account for non-conservative accelerations such as the included SRP defined in section 4.4 and in particular propellant sloshing [Cappuccio and Cascioli, 2018]. While the accelerometer's readings solve the sloshing problems, the accelerometer itself suffers under measurement errors such as bias, bias rate and scale factor. Unfortunately, these errors change whenever the accelerometer is turned on making it necessary to estimate them accordingly. Herein, only the accelerometer bias is estimated as an empirical acceleration under the simplification that its value stays constant until the next estimation epoch. For the estimation of the accelerometer bias error a conservative a priori covariance of $1 \times 10^{-5} \text{ m/s}^2$ is used [Cappuccio and Cascioli, 2018].

Lastly, Ganymede's Love number h_2 is also estimated as it is one of GALA's mission goals. The measurement and subsequent estimation of h_2 is done based on Equation 3.1, with the respective partial derivatives being detailed further and verified in section 7.7.

7.3. Numerical Partial Verification

Within this section a numerical benchmark for the calculation of numerical crossover partial derivatives is developed and verified. In section 7.4 this benchmark is used to evaluate and verify the *analytical* crossover partial derivatives developed in subsection 5.5.3. The calculation of the numerical partials relies on the Central Difference Theorem whose application onto crossover measurements results in [Urkullu et al., 2019]:

$$\frac{\partial h_{\otimes}}{\partial \mathbf{s}_0} = \left(h_{\otimes}(\mathbf{s}_0) \Big|_{\mathbf{s}_0 = \mathbf{s}_0 + \Delta \mathbf{s}_0} - h_{\otimes}(\mathbf{s}_0) \Big|_{\mathbf{s}_0 = \mathbf{s}_0 - \Delta \mathbf{s}_0} \right) / (2 \cdot \Delta \mathbf{s}_0). \quad (7.1)$$

The estimated parameter vector \mathbf{p}_0 at the linearisation point of the orbit estimation consists of both the body's state vector \mathbf{s}_0 and the parameter vector \mathbf{q} as defined in Equation 5.2. Here, only perturbations in \mathbf{s}_0 are considered. For each perturbation case, the crossover times t_1, t_2 and the crossover measurements h_{\otimes} are calculated anew to include all changes in crossover measurements. Naturally, only one element of \mathbf{s}_0 is perturbed at a time to distinguish the perturbation's effect clearly. To gain a better understanding of the effect orbital perturbations have on crossover measurements, it would be more insightful to describe and perturb the state vector at the linearisation point \mathbf{s}_0 in terms of its Kepler elements. Nevertheless, the Cartesian state vector $\mathbf{s}_0 = [x_0, y_0, z_0, v_{x0}, v_{y0}, v_{z0}]^T$ is regarded instead, as those are the vector elements the analytical partial derivatives are calculated in, as presented in subsection 5.5.3. Since the numerical partial derivatives calculated using Equation 7.1 make use of the resulting measurements after a perturbation $\pm \Delta \mathbf{s}_0$ at \mathbf{s}_0 has been applied, they can be seen as fully representative of all effects governing these derivatives.

In the following, these numerical partial derivatives are verified and the sensitivity of crossover measurements to perturbations at the linearisation point \mathbf{s}_0 is discussed. Furthermore, a baseline benchmark case is established to be used in section 7.4. For the calculation of the numerical partial derivatives the environment model and integrator/propagator settings as presented in section 6.3 and section 6.2 are used. Only the propagation length differs with

the analysed simulations having a length of 10 days. As discussed in [section 5.1](#), measurement partial derivatives aim to adequately predict the change in measurements Δh_{\otimes} due to a perturbation Δs_0 at the linearisation state s_0 . To evaluate the accuracy of numerical partials calculated with [Equation 7.1](#) the relative error ε_{rel} of their prediction is calculated as:

$$\varepsilon_{rel} = \left| \left(\frac{\partial h_{\otimes}}{\partial s_0} \cdot \Delta s_0 - \Delta h_{\otimes} \right) / \Delta h_{\otimes} \right| \cdot 100, \quad (7.2)$$

$$\text{with } \Delta h_{\otimes} = h_{\otimes}(s_0 + \Delta s_0) - h_{\otimes}(s_0). \quad (7.3)$$

[Table 7.1](#) shows the average relative error ε_{rel} of the numerical partials for JUICE's position elements calculated with [Equation 7.1](#) using a wide range of perturbations Δs_0 . Therein, Δn_{\otimes} denotes the change in the total number of crossovers n_{\otimes} due to a positive/negative perturbation as defined in [Equation 7.1](#).

| Perturbation [m] | Average relative error for partials [%]: | | | | | |
|---------------------|--|----------------------|---------------------------------------|----------------------|---------------------------------------|----------------------|
| | $\partial h_{\otimes} / \partial x_0$ | Δn_{\otimes} | $\partial h_{\otimes} / \partial y_0$ | Δn_{\otimes} | $\partial h_{\otimes} / \partial z_0$ | Δn_{\otimes} |
| 0.01 | 0.166 | 0/0 | 0.057 | 0/0 | 0.178 | 0/0 |
| 0.1 | 0.01 | 0/0 | 0.007 | 0/0 | 0.022 | 0/0 |
| 1.0 | 0.003 | 0/0 | 0.01 | 0/0 | 0.049 | 0/0 |
| 10.0 | 228.06 | 0/0 | 0.152 | 0/0 | 0.206 | 0/0 |
| 100.0 | 114.726 | 0/0 | 12.122 | 0/0 | 35.511 | 0/0 |
| 1000.0 | 120.29 | +1/0 | 439.155 | -2/+1 | 6383.426 | +1/-27 |

Table 7.1: Average relative error [%] for partial of position elements x_0 , y_0 and z_0 .

Surprisingly, the smallest perturbation Δs_0 does not directly lead to the lowest error for the prediction of Δh_{\otimes} . Instead, a perturbation of 0.1 m leads to the lowest average relative error for all position elements x_0 , y_0 and z_0 making it the best benchmark candidate of the tested position perturbations. Using a perturbation of 0.1 m, [Figure 7.1](#) shows the relative errors ε_{rel} of all crossover measurements for $\partial h_{\otimes} / \partial x_0$. The plots showing the relative errors for the numerical partial derivatives $\partial h_{\otimes} / \partial y_0$ and $\partial h_{\otimes} / \partial z_0$ for a perturbation of 0.1 m can be found in [Appendix A.5](#).

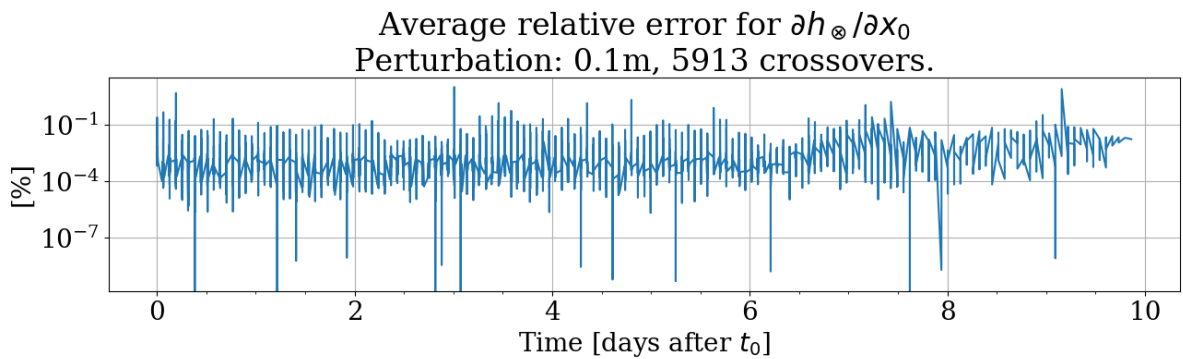


Figure 7.1: Numerically obtained partial derivatives for $\delta h_{\otimes} / \delta x_0$.

As shown in [Figure 7.1](#) the errors for $\partial h_{\otimes} / \partial x_0$ are for most cases well under 1% with only 8 out of 5913 crossover measurements having an error larger than 1%. Due to the magnitude of the errors shown in [Table 7.1](#) and [Figure 7.1](#) the numerical position partial derivatives can be regarded as reliable.

For a perturbation of 10 m the average relative error for the partials in x_0 and z_0 increase strongly due to individual, large outliers. A potential reason for these outliers is the used crossover storage and sorting system which cannot rule out that the exact same crossovers are compared to one another after a perturbation in the initial state s_0 . The used crossover sorting system works based on using t_1 as sorting parameter and is thus vulnerable to changes in t_1 leading to a different sorting of the crossover measurements. By using another sorting index, e.g. a tagging system, or using the orbit numbers of crossing tracks, a reliable comparison could be maintained resulting in a comparable error as for small perturbations. However, the implementation of such a system is outside of the scope of this thesis.

The number of outliers increases for a perturbation of 100 m, further leading to a degradation of the relative errors. For a perturbation of 1000.0 m the particularly large average error for $\partial h_{\otimes}/\partial z_0$ originates in the trajectory becoming so different that the number of crossover measurements is no longer the same. While for smaller perturbations the total number of 5913 crossovers remains the same, a perturbation of +1000 m in z_0 leads to the addition of a crossover ($\Delta n_{\otimes} = +1$) as shown in Table 7.1. Conversely, using a perturbation of -1000 m in z_0 leads to the loss of 27 crossovers ($\Delta n_{\otimes} = -27$), resulting in unreliable partial derivatives using Equation 7.1. The change in the number of crossover measurements also is prominent for $\partial h_{\otimes}/\partial x_0$ and $\partial h_{\otimes}/\partial y_0$, although not to such a large extent. This change in number of measurements is an effect not encountered in other tracking measurements such as range, range-rate or VLBI data and unique to crossover measurements.

A similar observation is made when evaluating the average relative errors of the velocity partial derivatives shown in Table 7.2.

| Perturbation [m/s] | Average relative error [%] for partial | | | | | |
|--------------------|--|----------------------|--|----------------------|--|----------------------|
| | $\partial h_{\otimes}/\partial v_{x0}$ | Δn_{\otimes} | $\partial h_{\otimes}/\partial v_{y0}$ | Δn_{\otimes} | $\partial h_{\otimes}/\partial v_{z0}$ | Δn_{\otimes} |
| 0.0001 | 0.019 | 0/0 | 0.007 | 0/0 | 0.003 | 0/0 |
| 0.001 | 0.029 | 0/0 | 0.022 | 0/0 | 0.009 | 0/0 |
| 0.01 | 0.148 | 0/0 | 0.177 | 0/0 | 0.108 | 0/0 |
| 0.1 | 52.414 | 0/0 | 20.867 | -1/0 | 4.424 | 0/0 |
| 1.0 | 163.881 | -4/0 | 87.977 | -73/+1 | 211.366 | -10/0 |
| 10.0 | 808.514 | -76/+77 | 374.109 | -251/+156 | 333.508 | -145/+79 |

Table 7.2: Average relative error [%] for partial of velocity elements v_{x0} , v_{y0} and v_{z0} .

Contrary to Table 7.1, in Table 7.2 the smallest perturbation leads to the smallest average relative errors for all velocity partial derivatives making it the best benchmark candidate of the tested velocity perturbations. Figure 7.2 shows the relative errors ε_{rel} of all crossover measurements for $\partial h_{\otimes}/\partial v_{x0}$ using a perturbation of 0.0001 m/s. The plots showing the relative errors for the numerical partial derivatives $\delta\Delta h_{\otimes}/\delta v_{y0}$ and $\partial\Delta h_{\otimes}/\partial v_{z0}$ for a perturbation of 0.0001 m/s can be found in Appendix A.5.

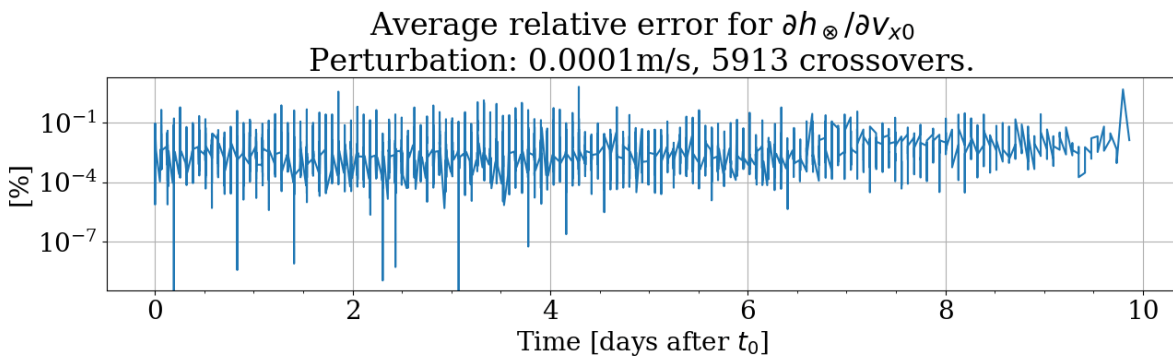


Figure 7.2: Numerically obtained partial derivatives for $\partial h_{\otimes}/\partial v_{x0}$.

As with the position partials, due to the magnitude of the errors shown in [Table 7.2](#) and [Figure 7.2](#) the numerical velocity partial derivatives can be regarded as reliable.

As for the position partial derivatives, an increase in perturbation leads to a degradation in the relative errors. Furthermore, if the perturbations become too large the orbit changes lead to the number of the crossovers measurements being affected. For the velocity partials, the change in number of crossovers occurs for perturbations of 0.1 m/s already making the resulting partials unreliable. This effect, together with the higher average errors in [Table 7.2](#) and the larger changes in n_{\otimes} show that crossovers and the spacecraft trajectory itself are particularly sensitive to velocity perturbations within s_0 . As mentioned for the position partials, a change in the number of crossovers leads to changes in crossover sorting due to the introduction/removal of crossovers leading to unreliable partials using [Equation 7.1](#).

From the analysis above, it can be surmised that the numerically calculated partial derivatives are reliable, as long as the perturbation used does not introduce changes in the spacecraft trajectory which affect the total number of crossover measurements n_{\otimes} . It was also found that within the treated perturbations those of 0.1 m in position and 0.0001 m/s in velocity yield the most reliable results. Therefore, for the evaluation of the analytically obtained partial derivatives in [section 7.4](#) the partial derivatives obtained with these perturbations are used as benchmark. While these perturbations might lead to changes in the number of crossovers for longer propagation arcs, the results above demonstrate that they do not affect the number of crossovers for arc lengths of 10 days.

7.4. Crossover Partial Verification

As discussed in [section 5.1](#), the estimation of parameters during orbit determination heavily depends on the ability to predict how measurements change due to a change in parameters at the linearisation point p_0 . This change in measurements is predicted using the *design matrix* H , as defined in [Equation 5.5](#). The importance of the design matrix H to any orbit determination scheme, is further emphasised by the two functions central to orbit determination algorithms, [Equation 5.23](#) and [Equation 5.24](#). It is therefore of major importance to verify the correct calculation of H . As already alluded to within [subsection 5.5.3](#) and further elaborated upon in [section 7.3](#), a robust method to evaluate the accuracy of the partial derivatives within H is to compare them to partial derivatives which were obtained *numerically* while relying on the central difference theorem as defined in [Equation 7.1](#). These numerical partials can be seen as highly reliable since they are obtained from the resulting measurements after a perturbation at the linearisation point.

In the following, the basic derivation of the analytical partial derivatives defined in [Equation 5.55](#) is evaluated, as well as the more detailed expression defined in [Equation 5.75](#) and [Equation 5.78](#). Therein, two different cases are analysed:

- Within the *single-arc* case, both crossover times t_1 and t_2 as defined in [Equation 3.3](#) occur within the same arc. This setup allows to rapidly evaluate the calculation of crossover partial derivatives as defined in [Equation 5.54](#).
- Within the *multi-arc* case, the crossover times t_1 and t_2 occur at different arcs. Via introducing perturbations at the linearisation point of one arc at a time, this case is particularly useful to separately analyse and verify the partial derivatives $\frac{\partial |r(t_1)|}{\partial r(t_1)}$ $\frac{\partial r(t_1)}{\partial s(t_{1,0})}$ and $\frac{\partial |r(t_2)|}{\partial r(t_2)}$ $\frac{\partial r(t_2)}{\partial s(t_{2,0})}$ as defined in [Equation 5.56](#).

Consistent with [section 7.3](#), the same environment model and integrator/propagator settings as presented in [section 6.2](#) and [section 6.3](#) are used, with the same simulation length of 10 days.

Single-Arc Verification

As in [section 7.3](#), the calculation of the analytically obtained partial derivatives is verified through an analysis of their relative error ε_{rel} to a defined benchmark. This benchmark is the one defined in [section 7.3](#), i.e. the analytical partials are evaluated w.r.t. the numerical partials. The relative error of the analytical partial derivatives is calculated as:

$$\varepsilon_{rel} = \left| \left(\frac{\partial h_{\otimes}}{\partial \mathbf{s}_0} \text{ (analytical)} - \frac{\partial h_{\otimes}}{\partial \mathbf{s}_0} \text{ (numerical)} \right) / \frac{\partial h_{\otimes}}{\partial \mathbf{s}_0} \text{ (numerical)} \right| \cdot 100. \quad (7.4)$$

Naturally, the attainable relative error ε_{rel} has a strong dependency on the chosen stepsize due to errors in the propagation of the state transition matrix Φ_j at an epoch j . A reliable propagation of Φ_j is imperative as it links all measurements to the linearisation point as shown in [Equation 5.31](#). [Table 7.3](#) shows the average relative error of the detailed analytical partials w.r.t. the numerical partials, calculated with [Equation 7.4](#), after 10 days using various stepsizes. Therein, *detailed* refers to the partials based on [Equation 5.75](#) and [Equation 5.78](#). Conversely, in the following *basic* refers to the analytical partials based on [Equation 5.55](#).

| Stepsize | Average relative error after 10 days for detailed partials [%]: | | | | | |
|----------|---|-------------------------------------|-------------------------------------|--|--|--|
| | $\partial h_{\otimes}/\partial x_0$ | $\partial h_{\otimes}/\partial y_0$ | $\partial h_{\otimes}/\partial z_0$ | $\partial h_{\otimes}/\partial v_{x0}$ | $\partial h_{\otimes}/\partial v_{y0}$ | $\partial h_{\otimes}/\partial v_{z0}$ |
| 10 s | 0.014 | 0.013 | 0.049 | 0.056 | 0.034 | 0.018 |
| 100 s | 0.058 | 0.273 | 0.131 | 0.194 | 0.128 | 0.057 |
| 200 s | 0.334 | 0.766 | 3.349 | 3.763 | 1.382 | 0.826 |
| 250 s | 0.875 | 2.101 | 8.647 | 34.386 | 8.508 | 2.054 |
| 300 s | 1.758 | 4.362 | 40.47 | 22.357 | 11.562 | 5.471 |
| 343 s | 4.889 | 8.656 | 34.897 | 43.285 | 58.892 | 20.222 |

Table 7.3: Average relative error for analytical partial derivatives after 10 days using various stepsizes.

Initially, a stepsize of 343s was chosen to approximate ESA's propagation of JUICE's motion during the GCO500 mission phase as discussed in [section 6.3](#). However, the results in [Table 7.3](#) demonstrate that the largest viable stepsize to obtain consistently reliable partial derivatives is 200 s. While shorter stepsizes lead to better results, they are discarded due to their increase in computational loads resulting in the choice of a stepsize of 200 s for the simulations of this thesis.

Having established a stepsize that leads to a consistently reliable crossover partial derivatives, the *basic* and *detailed* analytical expressions for these partial derivatives are analysed further below. [Table 7.4](#) shows the average relative error for the partial derivatives due to positional elements using these analytical partial derivatives. The average relative error of the partials was calculated for crossovers which occur during the first day of the simulation as well as after 10 days of the simulation. The degradation of the error average from 1 to 10 days is expected and is attributed to the accumulation of numerical errors.

| | Average relative error for analytical partials [%]: | | | |
|-------------------------------------|---|------------------|-----------------|--------------------|
| | Basic (1 day) | Detailed (1 day) | Basic (10 days) | Detailed (10 days) |
| $\partial h_{\otimes}/\partial x_0$ | 47.593 | 0.265 | 313.59 | 0.334 |
| $\partial h_{\otimes}/\partial y_0$ | 283.902 | 0.229 | 886.306 | 0.766 |
| $\partial h_{\otimes}/\partial z_0$ | 556.824 | 0.419 | 6769.526 | 3.349 |

Table 7.4: Average relative error [%] for basic and detailed analytical partial derivatives. Position elements only.

In addition to the degradation of the partials with time, [Table 7.4](#) also shows that the

partial derivatives are more sensitive to errors in certain directions. As mentioned in [section 7.3](#), it would be insightful to study the effect of orbital changes on crossover measurements. However, that analysis is outside the scope of this thesis. From [Table 7.4](#) it becomes immediately clear, that the basic analytical expression for crossover partial derivatives as a first-approximation is insufficient in describing crossover partials and leads to unreliable results. Conversely, the detailed expression can be seen as highly reliable.

In [Figure 7.3](#) the relative errors ε_{rel} of both analytical expressions for $\partial h_{\otimes}/\partial z_0$ are shown for the evaluated 10 simulation. Here, only the position partial derivatives due to z_0 are shown as that element is the most critical case in [Table 7.4](#). The relative errors ε_{rel} of the partial derivatives due to x_0 and y_0 can be found in [Appendix A.6](#).

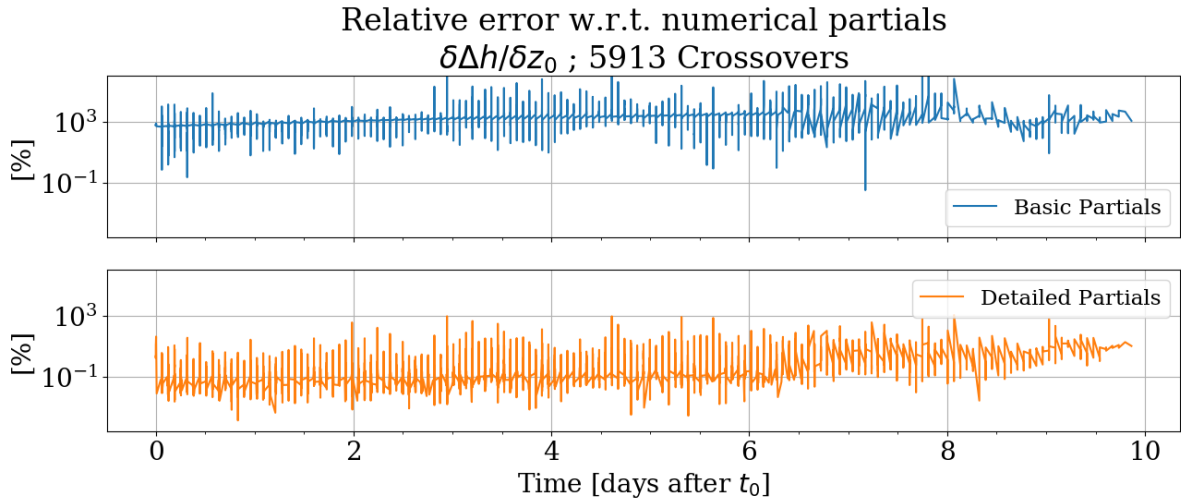


Figure 7.3: Relative errors of analytical crossover partials w.r.t. numerical crossover partials for $\delta\Delta h/\delta z_0$. Two cases are shown for analytical crossovers: A basic one, based on [Equation 5.55](#), and a more detailed one, based on [Equation 5.75](#) and [Equation 5.78](#).

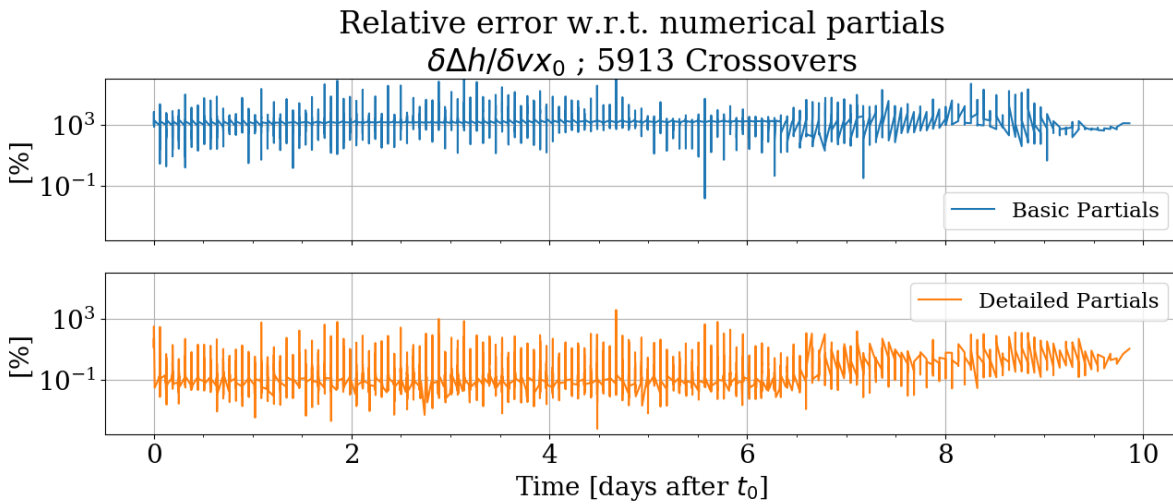
[Figure 7.3](#) shows the degradation of the position partials with time in detail. While the error of the detailed partials remains low for several days, there is a large error increase after day 6. This leads to the conclusion that shorter estimation arcs are preferable when using crossover measurements for orbit estimation for the simulation settings used here. However, as the average error of the last 3 days for the detailed analytical partials remains under 1% for $\partial h_{\otimes}/\partial x_0$ and $\partial h_{\otimes}/\partial y_0$ and under 4% for $\partial h_{\otimes}/\partial z_0$ arc lengths of 10 days are also viable. A potential error source for the error increase at later epochs is the clumping of crossovers at the polar regions. Unfortunately, with the used crossover storage and sorting system it cannot be ruled out that changes in crossovers leads to different crossovers being compared to one another. The crossover sorting system used here works based on using t_1 as organisational parameter, thus being vulnerable to changes in t_1 leading to a different sorting of the crossover measurements. Additionally, it is expected that the accumulation of numerical errors leads to the degradation of the partial derivatives.

[Table 7.4](#) shows the average relative error for the partial derivatives of velocity elements for both analytical expressions. As for [Table 7.4](#), the average relative errors after 1 day and after 10 days are shown. As for the partial derivatives due to position elements, the partial derivatives due to velocity elements show a degradation in time. For the velocity elements errors after 1 day are on average worse than for the position elements also resulting in larger average errors after 10 days. This further confirms that with the simulation settings used here, short arc lengths are preferred for orbit estimation.

| | Average relative error for analytical partials [%]: | | | |
|--|---|------------------|-----------------|--------------------|
| | Basic (1 day) | Detailed (1 day) | Basic (10 days) | Detailed (10 days) |
| $\partial h_{\otimes} / \partial v_{x0}$ | 1357.759 | 1.608 | 3862.462 | 3.763 |
| $\partial h_{\otimes} / \partial v_{y0}$ | 443.71 | 0.378 | 1327.543 | 1.382 |
| $\partial h_{\otimes} / \partial v_{z0}$ | 152.499 | 0.139 | 925.642 | 0.826 |

Table 7.5: Average relative error [%] for basic and detailed analytical partial derivatives. Velocity elements only.

Figure 7.4 shows the degradation of the position partials with time in detail. Here, only the velocity partial derivatives due to v_{x0} are shown as that element is the most critical case in Table 7.5. The relative errors ε_{rel} of the partial derivatives due to v_{y0} and v_{z0} can be found in Appendix A.6. As before, the error of the detailed partials remains low for the initial days with a large error increase after day 6. However, as the average error of the last 3 days for the detailed analytical partials remains under 4% for $\partial h_{\otimes} / \partial v_{x0}$, under 2% for $\partial h_{\otimes} / \partial v_{y0}$ and under 1% for $\partial h_{\otimes} / \partial v_{z0}$ arc lengths of 10 days are also viable. Here also, changes in t_1 and numerical errors are attributed for the increase in error magnitude with time.

Figure 7.4: Comparison of analytical and numerical crossover partials for $\delta\Delta h / \delta v_{x0}$. Two cases are shown for analytical crossovers: A basic one, based on Equation 5.55, and a more detailed one, based on Equation 5.75 and Equation 5.78.

Above, the errors of both basic and detailed analytical partial derivatives are quantified using numerical partials as benchmark whose calculation was defined and verified in section 7.3. It was found that the partial derivatives as calculated with the detailed analytical expression based on Equation 5.75 and Equation 5.78 can be regarded as highly reliable due to their excellent results. Conversely, it was shown that the basic analytical partial derivatives are insufficient in their description of crossover partials. Therefore, any studies that make use of such a simple crossover partials approximation should be regarded critically [Marabucci, 2012]. Due to the difference in the mathematical expressions of the basic and detailed analytical partial derivatives it is clear that the higher precision of the detailed partials originates in the inclusion of changes in the crossover location. In the detailed analytical expression the change in crossover location is defined via the changes in the crossover times t_1 and t_2 .

Multi-Arc Verification

For the multi-arc verification of the analytical partial derivatives the same simulation settings as for the single-arc case are used, with the difference that the total simulation length of 10 days

is split into two arcs of 5 days length each. To evaluate the the partial derivatives with respect to $s(t_{1,0})$ and $s(t_{2,0})$ as defined in Equation 5.56 separately, any crossover measurements whose t_1 occurs during the second arc are discarded, as are any crossover measurements whose t_2 occurs during the first arc. In the evaluations shown below, only the state vector elements of one arc are perturbed with the other arc remaining constant.

When perturbing an state vector element in $s(t_{1,0})$ only the partial derivatives $\frac{\partial |r(t_1)|}{\partial r(t_1)} \frac{\partial r(t_1)}{\partial s(t_{1,0})}$ are compared to the numerical partial derivatives, as the partials $\frac{\partial |r(t_2)|}{\partial r(t_2)} \frac{\partial r(t_2)}{\partial s(t_{2,0})}$ have no impact on the crossover measurement h_{\otimes} since $\Delta s(t_2) = 0$:

$$\Delta h_{\otimes}(s_{1,0} + \Delta s_{1,0}, s_{2,0} + 0) = \frac{\partial |r(t_1)|}{\partial r(t_1)} \frac{\partial r(t_1)}{\partial s(t_{1,0})} \cdot \Delta s_{1,0} + \frac{\partial |r(t_2)|}{\partial r(t_2)} \frac{\partial r(t_2)}{\partial s(t_{2,0})} \cdot 0 \quad (7.5)$$

For the results shown in Table 7.6, only the state vector elements of the first arc are perturbed with the second arc remaining constant. The respective plots showing the relative error of all partial derivatives can be found in Appendix A.7. As for the single arc verification, the numerical partial derivatives are calculated using Equation 7.1.

| | Average relative error [%] for analytical partial: | | | |
|--|--|------------------|-----------------|--------------------|
| | Basic (1 day) | Detailed (1 day) | Basic (10 days) | Detailed (10 days) |
| $\partial h_{\otimes} / \partial x_0$ | 4.877 | 0.007 | 88.724 | 0.024 |
| $\partial h_{\otimes} / \partial y_0$ | 1.662 | 0.001 | 76.023 | 0.006 |
| $\partial h_{\otimes} / \partial z_0$ | 1.476 | 0.001 | 19.052 | 0.004 |
| $\partial h_{\otimes} / \partial v_{x0}$ | 883.652 | 1.032 | 1426.078 | 0.603 |
| $\partial h_{\otimes} / \partial v_{y0}$ | 84.15 | 0.149 | 275.381 | 0.087 |
| $\partial h_{\otimes} / \partial v_{z0}$ | 9.817 | 0.014 | 90.61 | 0.016 |

Table 7.6: Average relative error [%] for analytical partial derivatives. Position elements only.

As for the single arc case, the detailed partials approximate the numerical partials much closer than the basic ones. The basic partials show low average errors within the first day, but only in the position elements. Conversely, the average errors for the velocity elements are too large to be considered reliable.

For the results shown in Table 7.7, only the state vector elements of the second arc are perturbed with the first arc remaining constant. The respective plots showing the relative error of all partial derivatives can be found in Appendix A.7. Equal to the results shown in Table 7.6, perturbations in the second arc only lead to reliable results for the detail partial derivatives. Conversely, the partial derivatives obtained with the basic analytical expression have error magnitudes that are too large to be used for orbit estimation.

| | Average relative error [%] for analytical partial: | | | |
|--|--|------------------|-----------------|--------------------|
| | Basic (1 day) | Detailed (1 day) | Basic (10 days) | Detailed (10 days) |
| $\partial h_{\otimes} / \partial x_0$ | 44.146 | 0.04 | 100.051 | 0.03 |
| $\partial h_{\otimes} / \partial y_0$ | 5.317 | 0.004 | 21.591 | 0.013 |
| $\partial h_{\otimes} / \partial z_0$ | 4.265 | 0.004 | 12.768 | 0.004 |
| $\partial h_{\otimes} / \partial v_{x0}$ | 909.597 | 0.361 | 1288.572 | 0.289 |
| $\partial h_{\otimes} / \partial v_{y0}$ | 43.434 | 0.03 | 251.524 | 0.066 |
| $\partial h_{\otimes} / \partial v_{z0}$ | 13.25 | 0.009 | 73.761 | 0.013 |

Table 7.7: Average relative error [%] for analytical partial derivatives. Position elements only.

Above, the errors of both, basic and detailed, analytical expressions are quantified using numerical partials as benchmark whose calculation was defined and verified in [section 7.3](#). In confirmation with the analysis for the single arc case, it was found that the partial derivatives as calculated with the detailed analytical expression based on [Equation 5.75](#) and [Equation 5.78](#) can be regarded as highly reliable due to their excellent results. Conversely, it was shown that the basic analytical partial derivatives are insufficient in their description of crossover partials.

7.5. POD Verification

In [section 7.4](#) the analytical partial derivatives are verified using the numerical partial derivatives which are discussed and verified in [section 7.3](#). Therein it is shown that the detailed analytical partials based on [Equation 5.75](#) and [Equation 5.78](#) yield highly reliable results, while the basic analytical partials based on [Equation 5.55](#) can be discarded due to their erroneous results. For this reason, only the detailed partials are regarded here as the basic partials are not used for JUICE's POD. In this section the focus lies on the verification of the POD algorithm using crossover measurements with previous studies having sufficiently verified and validated the other functions of Tudat required for orbit estimation [[TUDelft, 2019](#)]. As an initial verification step, JUICE's state was estimated using a multi-arc approach with the initial guess for p_0 being the true value of p_0 itself. Using only Doppler as well as Doppler and crossover measurements, the code recognised a perfect fitting between the synthetic and the predicted measurements and no p_0 adjustment was made.

As an additional verification test, the design matrix H is tested once more using a single arc setup as in [section 7.4](#). In such a setup both crossover times t_1 and t_2 are affected by a perturbation at the linearisation point. As for the verification of the numerical crossover partials in [section 7.3](#), a small perturbation is introduced into s_0 and the predicted change in measurements is evaluated against the actual measurement change. As defined in [section 7.3](#) and consistent with [section 7.4](#), the perturbation for position elements is 0.1 m with the perturbation for velocity elements being 0.0001 m/s. The relative error of the prediction of changes in measurements is calculated as:

$$\varepsilon_{rel} = \left| \left(\frac{\partial h_{\otimes}}{\partial \mathbf{s}_0}_{Detailed} \cdot \Delta \mathbf{s}_0 - \Delta h_{\otimes} \right) / \Delta h_{\otimes} \right| \cdot 100, \quad (7.6)$$

$$\text{with } \Delta h_{\otimes} = h_{\otimes}(\mathbf{s}_0 + \Delta \mathbf{s}_0) - h_{\otimes}(\mathbf{s}_0). \quad (7.7)$$

[Table 7.8](#) shows the average error for all partial derivatives after 1 day and after 10 days. For convenience the average errors of the numerical partial derivatives already presented in [section 7.3](#) are shown here once more.

| Average relative error after 10 days for <i>analytical</i> partials [%]: | | | | | | |
|--|---------------------------------------|---------------------------------------|---------------------------------------|--|--|--|
| | $\partial h_{\otimes} / \partial x_0$ | $\partial h_{\otimes} / \partial y_0$ | $\partial h_{\otimes} / \partial z_0$ | $\partial h_{\otimes} / \partial v_{x0}$ | $\partial h_{\otimes} / \partial v_{y0}$ | $\partial h_{\otimes} / \partial v_{z0}$ |
| 1 day | 0.263 | 0.233 | 0.419 | 1.609 | 0.378 | 0.139 |
| 10 days | 0.344 | 0.743 | 3.394 | 3.711 | 1.386 | 0.824 |
| Average relative error after 10 days for <i>numerical</i> partials [%]: | | | | | | |
| | $\partial h_{\otimes} / \partial x_0$ | $\partial h_{\otimes} / \partial y_0$ | $\partial h_{\otimes} / \partial z_0$ | $\partial h_{\otimes} / \partial v_{x0}$ | $\partial h_{\otimes} / \partial v_{y0}$ | $\partial h_{\otimes} / \partial v_{z0}$ |
| 1 day | 0.007 | 0.005 | 0.004 | 0.012 | 0.002 | 0.001 |
| 10 days | 0.01 | 0.007 | 0.022 | 0.019 | 0.007 | 0.003 |

Table 7.8: Average relative error for analytical and numerical partial derivatives after 1 and 10 days.

Due to the low average errors the analytical partial derivatives attain for the prediction of changes in crossover measurements with the used settings, the POD scheme whose results

are discussed in [chapter 8](#) can be regarded as verified. Furthermore, since the average errors obtained with the numerical partial derivatives are consistently several magnitudes lower than those of the analytical partial derivatives, [Table 7.8](#) reinforces the ability of the numerical partials to verify the analytical partials.

As an additional and last verification test, the design matrix H is tested using a multi arc setup as in [section 7.4](#) with the difference that a perturbation is introduced for both arcs. In the first arc, a perturbation is introduced into one of its initial position elements. In the second arc, a perturbation is introduced into one of its initial velocity elements. In accordance with [Table 7.8](#), the elements which are perturbed are z and v_x since these are the elements which yield the worst results. As in [section 7.4](#), the perturbation in position equals 0.1 m while the perturbation in velocity equals 0.0001 m/s. Thus, the perturbations are:

$$\Delta \mathbf{s}_{1,0} = z_{1,0} + 0.1m \quad ; \quad \Delta \mathbf{s}_{2,0} = v_{x2,0} + 0.0001m/s \quad (7.8)$$

The assumption is made that the results obtained by perturbing any other combination of two elements are more accurate since the relative error for all the other elements are lower, see [Table 7.8](#). The average relative error after 1 day and 10 days of the prediction of changes in crossover measurements due to these perturbations is calculated as:

$$\varepsilon_{rel} = \left| \left(\left[\frac{\partial |\mathbf{r}(t_1)|}{\partial \mathbf{r}(t_1)} \frac{\partial \mathbf{r}(t_1)}{\partial \mathbf{s}(t_{1,0})} \cdot \Delta \mathbf{s}_{1,0} + \frac{\partial |\mathbf{r}(t_2)|}{\partial \mathbf{r}(t_2)} \frac{\partial \mathbf{r}(t_2)}{\partial \mathbf{s}(t_{2,0})} \cdot \Delta \mathbf{s}_{2,0} \right] - \Delta h_{\otimes} \right) / \Delta h_{\otimes} \right| \cdot 100, \quad (7.9)$$

$$\text{with } \Delta h_{\otimes} = h_{\otimes}(\mathbf{s}(t_{1,0}) + \Delta \mathbf{s}_{1,0}, \mathbf{s}(t_{2,0}) + \Delta \mathbf{s}_{2,0}) - h_{\otimes}(\mathbf{s}(t_{1,0}), \mathbf{s}(t_{2,0})). \quad (7.10)$$

[Table 7.9](#) shows the relative average error of the predicted changes in crossover measurements as calculated with [Equation 7.10](#) after 1 day and after 10 days. The respective plot which shows the relative error for all crossover measurements can be found in [Appendix A.7](#).

| Average relative error [%] Multi-arc perturbation | |
|--|---------|
| 1 day | 10 days |
| 0.003 | 0.004 |

Table 7.9: Average relative error [%] for analytical partial derivatives. Position elements only.

The low relative errors shown in [Table 7.9](#) further cement the correct calculation and high accuracy of the crossover partial derivatives which make up the design matrix H. The design matrix can therefore be safely regarded as verified for the analysis of JUICE's POD discussed in [chapter 8](#).

7.6. POD Validation

To validate the POD scheme used for this thesis' analyses, its formal uncertainties are compared to those of previous 3GM studies for the JUICE mission. In one such study JUICE's state vector was estimated on a daily basis for the total duration of 130 days during the GCO500 mission phase. Additionally, 118 global parameters were estimated: Ganymede's gravity coefficients up to degree and order 10 ($\sum 2l + 1 = 117$ for $l=1,\dots,10$) and its Love number k_2 . In doing so, they obtained the formal uncertainties for JUICE's position shown in Figure 7.5 [Parisi and Iess, 2012]. Using the same arc length, and estimating the parameters discussed in section 7.2 for a period of 160 days this thesis' formal errors as shown in Figure 7.6.

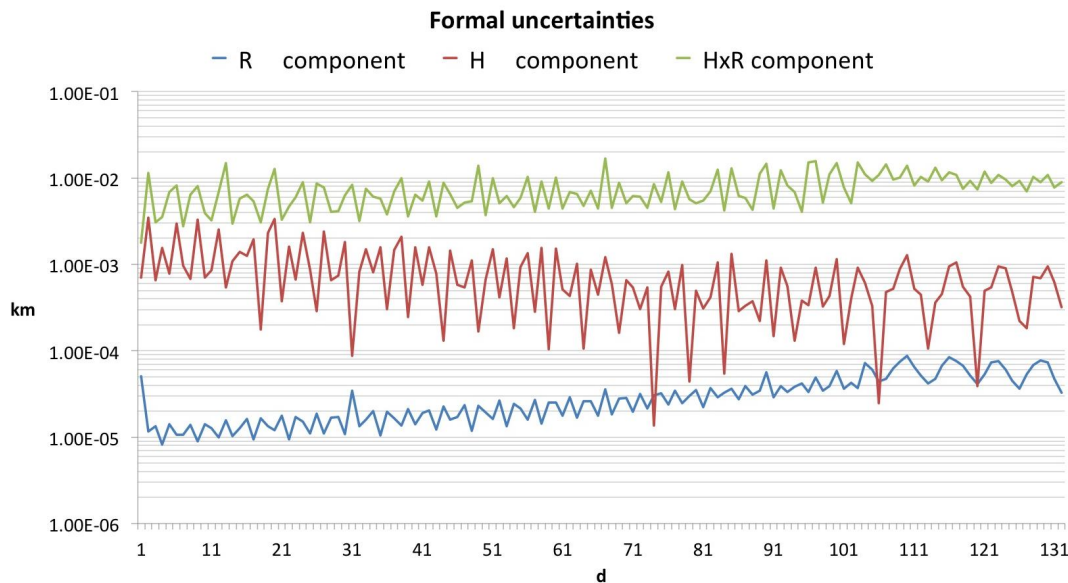


Figure 7.5: "Spacecraft position error in the orbital frame (radial, across-track and along-track.)" [Parisi and Iess, 2012].

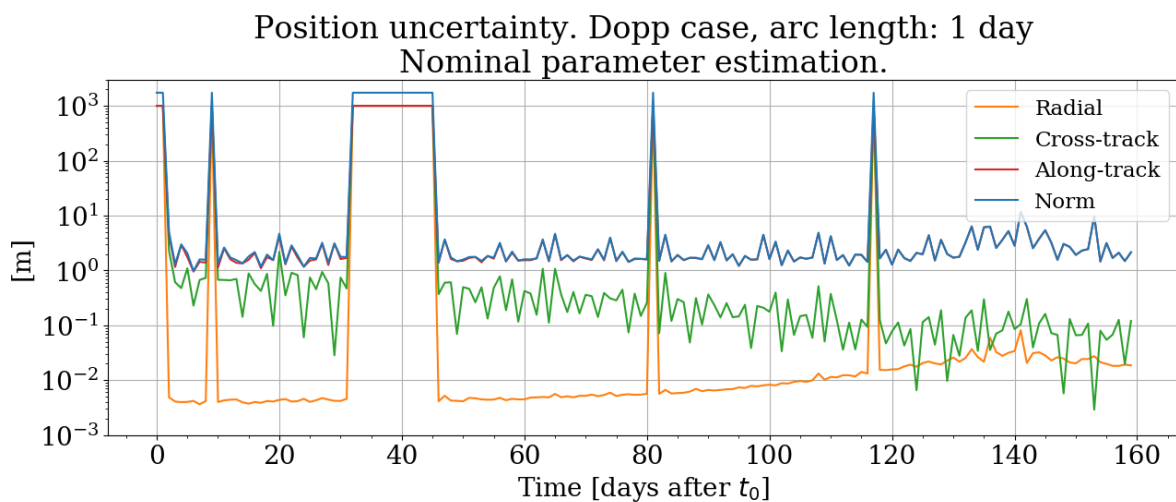


Figure 7.6: Position uncertainty using Doppler data only, arc length: 1 day. Nominal parameter estimation.

As the magnitude of both formal estimation uncertainties are in the same range, the POD scheme within this thesis can be seen as reliable.

7.7. Verification of Tidal Partial Derivatives

In the following, the calculation of the tidal partial derivatives defined in Equation 5.93 is verified. As was the case for the verification of the crossover partial derivatives, the Central Difference Theorem discussed in section 7.3 is used for verification. The respective numerical partial derivatives are calculated as:

$$\frac{\partial h_{\otimes}}{\partial h_2} = \left(h_{\otimes}(\mathbf{p}_0) \Big|_{\mathbf{p}_0=\mathbf{p}_0+\Delta h_2} - h_{\otimes}(\mathbf{p}_0) \Big|_{\mathbf{p}_0=\mathbf{p}_0-\Delta h_2} \right) / (2 \cdot \Delta h_2), \quad (7.11)$$

$$\text{with } h_{\otimes} = |\mathbf{r}_2| - |\mathbf{r}_1| - \frac{h_2}{g} (\Phi_2 - \Phi_1). \quad (7.12)$$

For the calculation of the numerical partial derivatives a value of 0.001 was chosen, with typical estimates for Ganymede's h_2 being between 1.1-1.7 [Grasset et al., 2013; Steinbruegge et al., 2015]. Figure 7.7 shows the relative errors of the analytical tidal partials with respect to the numerical partials, calculated as:

$$\varepsilon_{rel} = \left| \left(\frac{\partial h_{\otimes}}{\partial h_2} (analytical) - \frac{\partial h_{\otimes}}{\partial h_2} (numerical) \right) / \frac{\partial h_{\otimes}}{\partial h_2} (numerical) \right| \cdot 100. \quad (7.13)$$

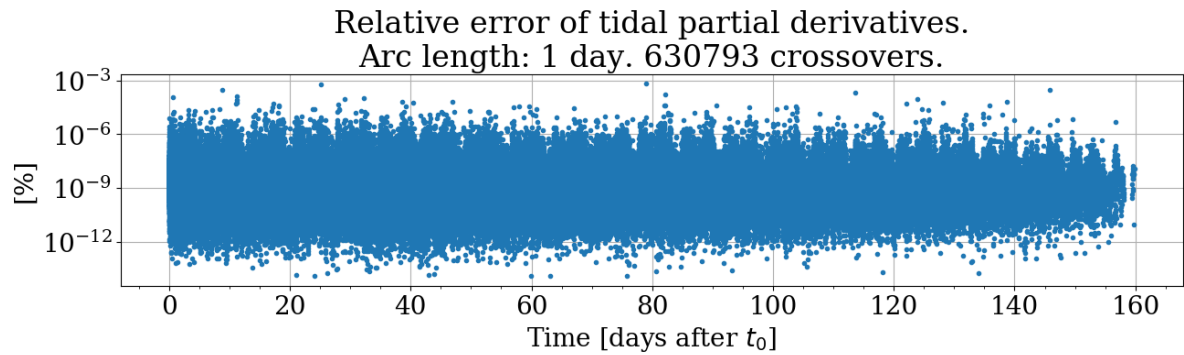
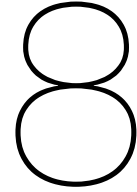


Figure 7.7: Absolute difference between numerical and analytical tidal partial derivatives.

Due to the simple nature of Equation 5.93 it is unsurprising that the values of the analytical partials are so close to the numerical ones resulting in an average relative error of 2.08×10^{-8} %. Due to the low error magnitudes shown in Figure 7.7 the calculation of the tidal partial derivatives can be regarded as verified.



Results

In the following, the *formal estimation errors* of the two POD schemes defined in [section 7.1](#) are analysed and compared. The most prominent difference between these two schemes is that in one only Doppler measurements are used for orbit estimation (Dopp), while in the other one both Doppler and crossover measurements are employed (DoXo). The evaluated formal errors are obtained from the covariance matrix of the estimated parameters $P_{x,t}$ as defined in [Equation 5.24](#).

For POD schemes the iterative application of [Equation 5.23](#) allows to calculate continuously better estimates for \hat{p} until convergence is reached. However, this thesis' goal is not to evaluate the ultimately attainable estimate precision for orbit determination procedures. Instead, its focus lies on the effect altimetry crossovers have on POD schemes relative to using conventional tracking measurements only.

In the following, the nominal case for JUICE's POD is analysed in [section 8.1](#), followed up by the analysis of POD-influencing factors such as the estimation's arc length in [section 8.2](#), the effect of different measurement error budgets in [section 8.3](#) and the number of estimated parameters in [section 8.4](#). Lastly, in [section 8.5](#) an additional POD case is analysed wherein only crossover measurements are used for orbit estimation.

8.1. Nominal Estimation Cases

The nominal estimation cases elaborated upon here use the environment model discussed in [section 6.2](#) together with the simulation settings presented in [section 6.3](#). The nominal error budgets for Doppler and crossover measurements correspond to the error case 1, as defined in [subsection 5.6.3](#). In the nominal case, the parameters which are estimated are JUICE's state, Ganymede's gravity field up to degree and order 12 as well as Ganymede's Love number k_2 . This leads to a total of 1126 estimated parameters: $6 \times 160 = 960$ JUICE state parameters, $\sum 2l + 1 = 165$ ($l=2, \dots, 12$) gravity coefficients and one k_2 parameter. Of the 165 gravity coefficients, 88 are cosine coefficients C_{nm} and 77 are sine coefficients S_{nm} . The respective a priori uncertainties for parameter estimation are presented within [section 7.2](#). The arc length for JUICE's POD trajectory propagation and estimation is 1 day, see [section 7.1](#) for further details. This choice in arc length coincides with previous JUICE POD studies, as conducted by the 3GM-Team and presented in [section 7.6](#), as well as the nominal arc length once JUICE's scientific data has been obtained [[Iess, 2019](#)].

Using these settings and Doppler data only, results in the formal position uncertainties shown in [Figure 8.1](#). The most prominent features in [Figure 8.1](#) are the five peaks in estimation uncertainty. These peaks coincide with the occultation periods mentioned in [subsec-](#)

tion 5.4.2 at the days 0-2, 9, 32-46, 81 and 117. Due to these occultations, there are no Doppler measurements for parameter estimation in the respective arcs. In fact, if no a priori information were used, the resulting rank deficiency would lead to a non-invertible normal matrix ($H^T P_y^{-1} H$) making it impossible to calculate the covariance matrix as defined in Equation 5.22. At these peaks the uncertainty values for the radial, cross-track and along-track component are 1 km, which equals the a priori uncertainties used for all position elements of JUICE. Thus, the five estimation uncertainty peaks within Figure 8.1 represent arcs for which no reliable orbit estimation can be made using Doppler data only. Of the estimated directions, the along-track uncertainty consistently has the largest uncertainty. As its name suggest, and shown in Equation 5.36, this uncertainty coincides with the direction of JUICE's velocity vector. Additionally, it is noticeable that JUICE's radial position estimate degenerates with time, while the cross-track estimation improves. The degradation of radial uncertainty with time can be assigned to the insufficient geometrical constraints yielded by Doppler measurements for the orbit determination around another celestial body as discussed in section 5.3.

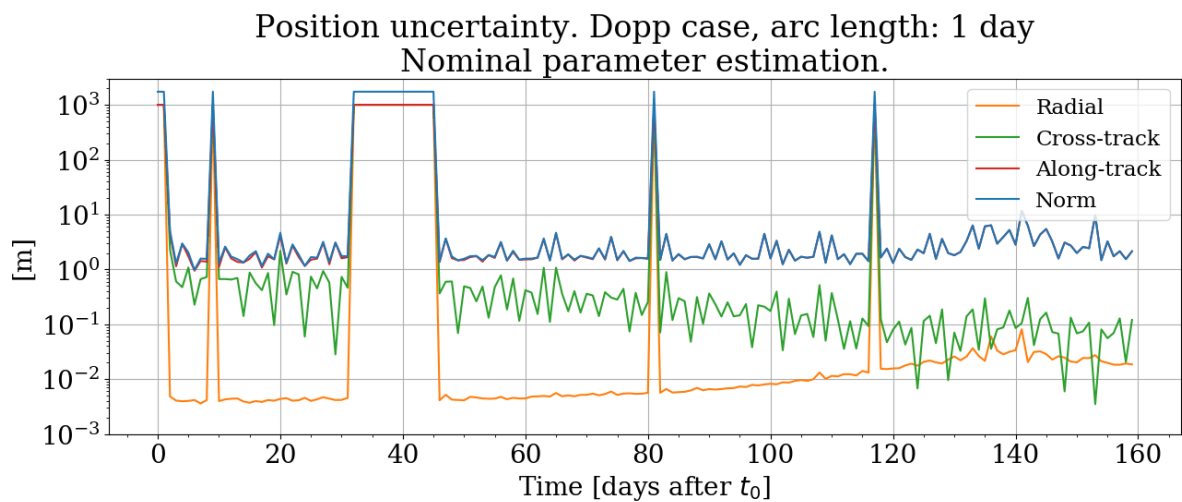


Figure 8.1: Position uncertainty using Doppler data only, arc length: 1 day. Nominal parameter estimation.

Conversely, the obtained position estimate uncertainties using both Doppler and crossover measurements are shown in Figure 8.2.

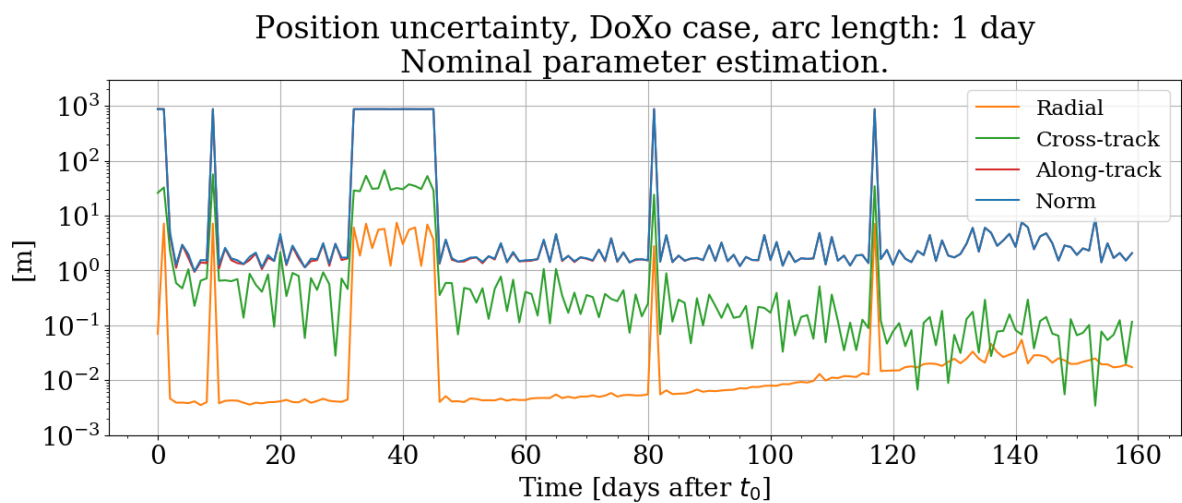


Figure 8.2: Position uncertainty using Doppler and crossover data, arc length: 1 day.

The most noticeable difference between Figure 8.2 and Figure 8.1 are the uncertainty peaks during occultation periods which originates in the availability of enough crossover measurements within every arc for orbit estimation. This coincides with the finding that the use of an a priori covariance is not compulsory when using crossover measurements, leading to the normal matrix ($H^T P_y^{-1} H$) being always invertible. However, while the crossover measurements do improve upon the a priori uncertainty the attained uncertainties during occultations are several magnitudes worse than those when Doppler data is available. Additionally, during occultation periods the DoXo position along-track uncertainty has an average of 869.8 m which is only a slight improvement upon the a priori uncertainty.

Disregarding the differences due to occultations, Figure 8.3 below shows the improvement in position uncertainty when crossover measurements are included:

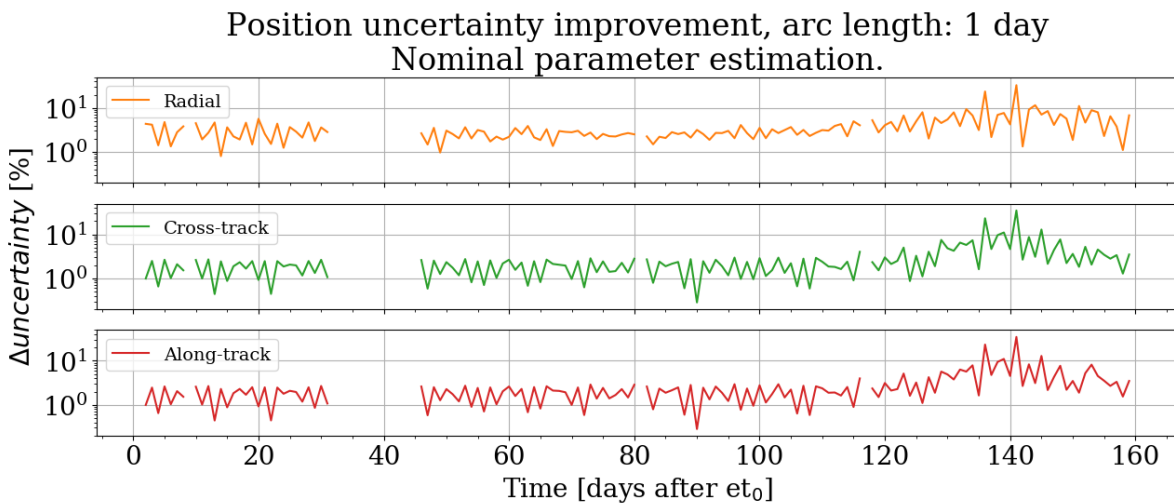


Figure 8.3: Comparison of position uncertainty between nominal Dopp and DoXo cases, arc length: 1 day.

As Figure 8.3 shows, the improvement in uncertainty noticeably increases towards the last estimation days. It is surmised that this improvement originates in the additional geometrical orbit constraints offered by crossover measurements which alleviate the orbit estimation degradation when only Doppler measurements are used. Table 8.1 details the estimation improvement of the DoXo case in comparison to the Dopp case. Therein the larger relative improvement after day 100 is quantified, and the magnitudes of the largest improvements are shown.

| | DoXo average improvement in position uncertainty [%] | | | | | |
|--------------|--|--------|-------------|--------|-------------|--------|
| | Radial | | Cross-track | | Along-track | |
| | Avg. | max. | Avg. | max. | Avg. | max. |
| pre day 100 | 2.692 | 5.649 | 1.794 | 2.963 | 1.785 | 2.94 |
| post day 100 | 5.639 | 32.892 | 4.455 | 34.961 | 4.542 | 34.957 |
| total | 3.925 | 32.892 | 2.907 | 34.961 | 2.939 | 34.957 |

Table 8.1: DoXo improvement for position uncertainty. Nominal case.

While the addition of crossover measurements consistently improves the estimation uncertainties obtained with Doppler data only, the magnitude of this improvement can be regarded as marginal. A potential approach to deal with the orbit estimation degradation inherent to the insufficient geometrical constraints of Doppler measurements is to subdivide the total estimation into several sub-problems. However, it can be expected that such a division of the

estimation problem is detrimental to the estimation uncertainty of global parameters and thus also to the estimation uncertainty of all local parameter therefore presenting an argument to include measurements which aid in constrain the orbit's geometry in space.

The estimation uncertainties of JUICE's velocity show a similar behaviour, with the major difference between Dopp and DoXo being the uncertainty peaks during occultation windows. As was the case for [Figure 8.1](#), in the Dopp case the estimation uncertainties during occultations equal the used a priori information, being 1 m/s for JUICE's velocity components. Similarly, during periods where Doppler tracking is available the estimation uncertainties are slightly better in the DoXo case. Due to these similarities to the estimation of JUICE's position, only the velocity uncertainty for the DoXo case is shown in [Figure 8.4](#).

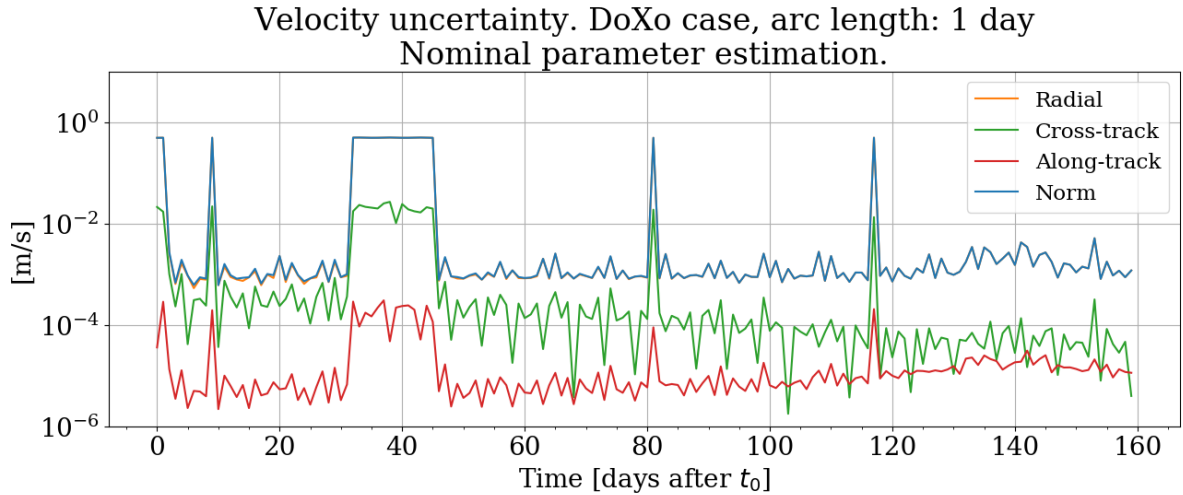


Figure 8.4: Velocity uncertainty using Doppler and crossover data, arc length: 1 day.

As for the uncertainty improvement in position elements shown in [Table 8.1](#), [Table 8.2](#) shows the DoXo average velocity uncertainty improvement in comparison to the Dopp case. Therein, the same distinction is made between the uncertainty improvement before day 100 and after day 100 further emphasising the DoXo uncertainty improvement for later estimation periods.

| DoXo average improvement in velocity uncertainty [%] | | | | | | |
|--|--------|--------|-------------|--------|-------------|--------|
| | Radial | | Cross-track | | Along-track | |
| | Avg. | max. | Avg. | max. | Avg. | max. |
| pre day 100 | 1.834 | 3.011 | 1.816 | 3.211 | 2.142 | 5.364 |
| post day 100 | 4.62 | 35.313 | 4.534 | 35.282 | 5.302 | 26.591 |
| total | 3.0 | 35.313 | 2.953 | 35.282 | 3.464 | 26.591 |

Table 8.2: DoXo improvement for position uncertainty. Nominal case.

For the rotation of the velocity uncertainties from the xyz frame to the RSW the same procedure was applied as for the position elements, as defined in [Equation 5.36](#). Noticeably, for the velocity estimation the along-track component has the lowest uncertainty while for the position estimation it was the radial component. This results from these being the components which directly impact orbital energy via the kinetic and potential energy, respectively. Since changes in these two components result in changes in the orbit, they can be constrained more tightly. Conversely, infinitesimal changes in cross-track or along-track *position*, do not change the orbit's shape as strongly. Instead, they introduce bounded periodical variations in

their respective plane. Equally, infinitesimal changes in radial or cross-track *velocity* merely induce bounded variations instead of introducing secular changes to the orbit. Due to the stark similarities between the estimation and DoXo uncertainty improvement of JUICE's position and velocity parameter only the position estimation and uncertainty improvements are discussed in detail in the following results discussion.

Regarding the estimation of global parameters, [Figure 8.5](#) shows the estimation uncertainties of spherical harmonic coefficients for the Dopp case with [Figure 8.6](#) showing the uncertainty improvement when crossover measurements are used in addition to Doppler measurements.

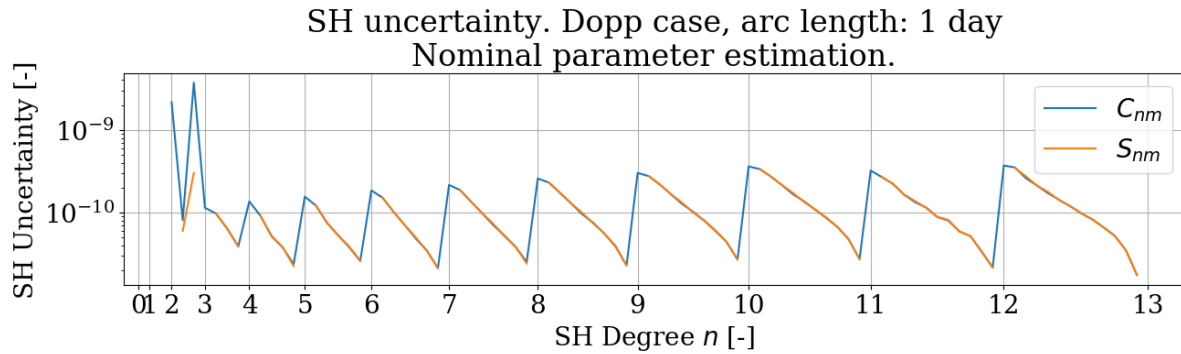


Figure 8.5: Spherical Harmonics (SH) uncertainty using Doppler data only, arc length: 1 day.

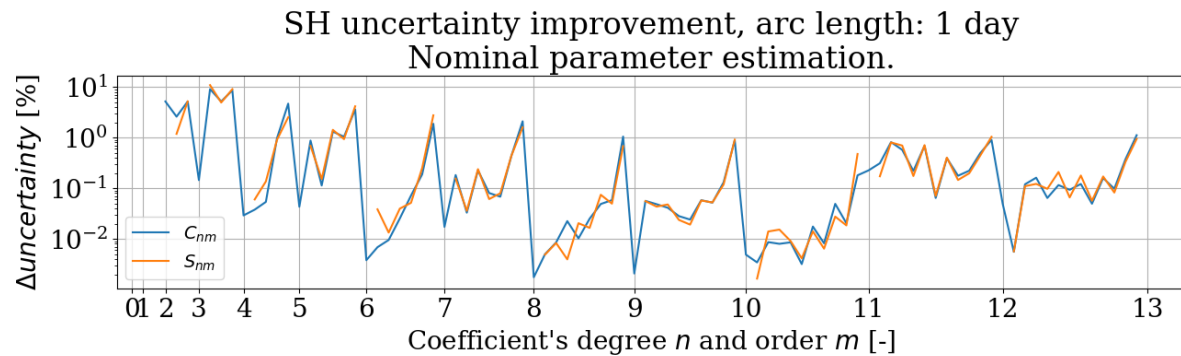


Figure 8.6: Comparison of spherical harmonics (SH) uncertainty between nominal Dopp and DoXo cases, arc length: 1 day.

As [Figure 8.5](#) shows, sudden changes in uncertainty coincide with an increase in the estimated coefficient's degree n with the estimation uncertainty decreasing with an increase in the coefficient's order m . The discontinuous plots for the estimation of the sine coefficients S_{nm} is expected as no S_{n0} coefficients exist per definition. The average improvement in estimation uncertainty using crossover measurements is 0.75% for C_{nm} and 0.769% for S_{nm} . As the Dopp SH estimation does not show signs of being affected strongly by communication gaps, it can be surmised that the estimation of global parameters only suffers marginally from unfavourable individual arcs. For the last estimated parameter, Ganymede's Love number k_2 , the attained uncertainty is 5.061×10^{-5} with the addition of crossovers leading to an improvement in uncertainty of 5.307%. The k_2 estimation uncertainty is noticeably lower than in previous studies where the attained uncertainty had magnitudes between 10^{-2} to 10^{-3} [[Konopliv and Yoder, 1996](#); [Genova et al., 2016](#); [Konopliv et al., 2020](#)]. The difference in uncertainty is attributed to those studies using actual mission data, whereas for the estimation

treated here the environment model perfectly matches the environment model in which the tracking measurements were obtained while also using highly reliable measurements. Additionally, it is expected that the high correlation between k_2 and the gravity coefficients C_{2m} and S_{2m} discussed in [section 4.1](#) is responsible for the noticeably larger uncertainty for those SH coefficients shown in [Figure 8.5](#) and the optimistically low uncertainty of k_2 .

Regarding the estimated parameter correlation shown in [Figure 8.7](#) and [Figure 8.8](#), in the nominal Dopp and DoXo cases the first $160 \times 6 = 960$ estimated parameters are estimates for JUICE state at the respective arcs/days. The following 165 parameters are gravitational coefficients and the last parameter is the k_2 estimate. In [Figure 8.7](#) and [Figure 8.8](#) a value of 1 corresponds to a value correlation of 100%, while -1 corresponds to an anti-correlation of 100% and value of 0 denotes that the respective values are uncorrelated.

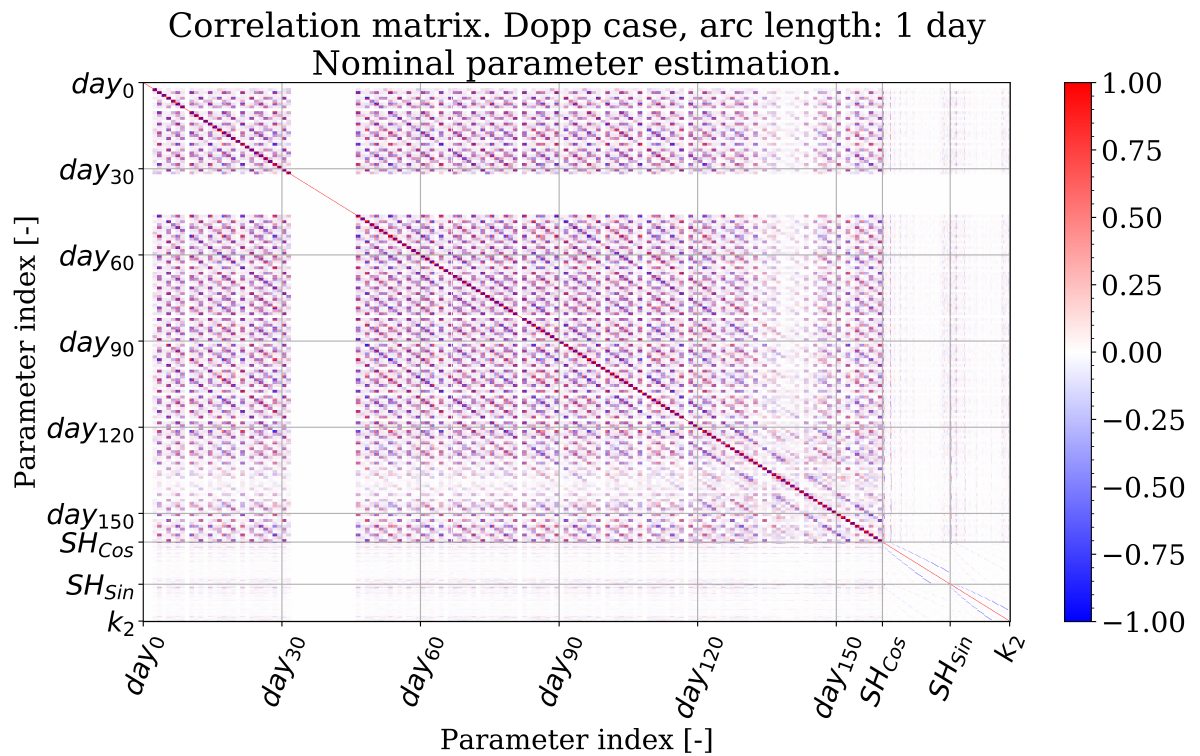


Figure 8.7: Correlation between estimated parameters using Doppler data only, arc length: 1 day.

As for the estimation of local parameters, tracking occultations yield the most prominent features in [Figure 8.7](#) and [Figure 8.8](#). For the Dopp case, there are no correlations during occultation periods, which occur during the days 0-2, 9, 32-46, 81 and 117 as discussed in [subsection 5.4.2](#). During these periods there are no correlations between the elements of each arc, nor between the elements of different arcs. Consistent with the results shown in [Figure 8.1](#), these results show that for the Dopp case no state estimation is possible during occultation periods. Since there are discrete orbit changes at the beginning of each arc, every arc could be regarded as an independent one when using Doppler data only. However, due to the estimation of global parameters correlations between the individual states are introduced, as discussed further in [section 8.4](#). Within the DoXo correlation case shown in [Figure 8.8](#), contrary to the Dopp case, there are correlations during occultation periods. While these correlations are particularly weak between different arcs, there are quite noticeable within the elements of each arc.

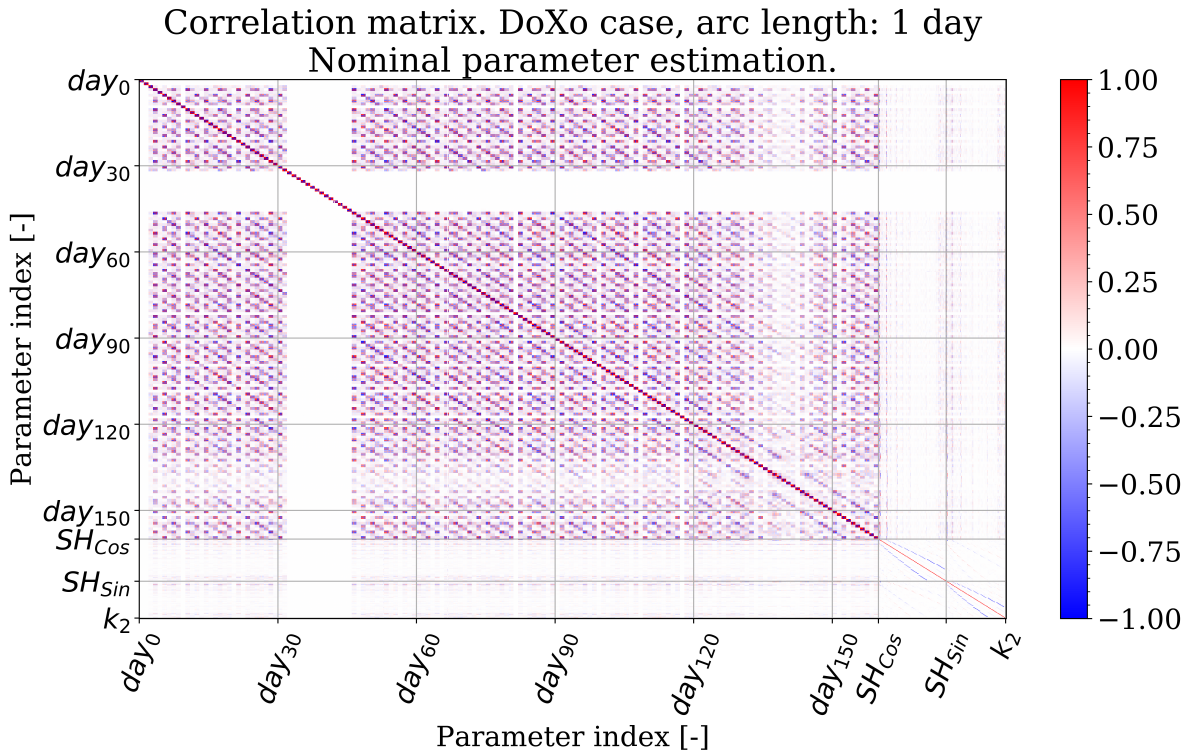


Figure 8.8: Correlation between estimated parameters using Doppler and crossover data, arc length: 1 day.

This notion is further deepened by analysing the average, absolute correlation values between the off-diagonal elements within each 6x6 arc estimate as shown in Figure 8.9. Therein, the upper plot shows the average off-diagonal correlations for the Dopp and DoXo case, while the lower plot shows the numerical difference between the two cases. The cases where the addition of crossover leads to an improvement in correlation are denoted as Dopp > DoXo. For the DoXo case, the average correlation not only remains high but becomes larger in many cases. Outside of occultation periods there are 86 arcs for which Dopp < DoXo, while there are only 55 Dopp > DoXo arcs, demonstrating that crossovers do not consistently improve intra-arc correlation.

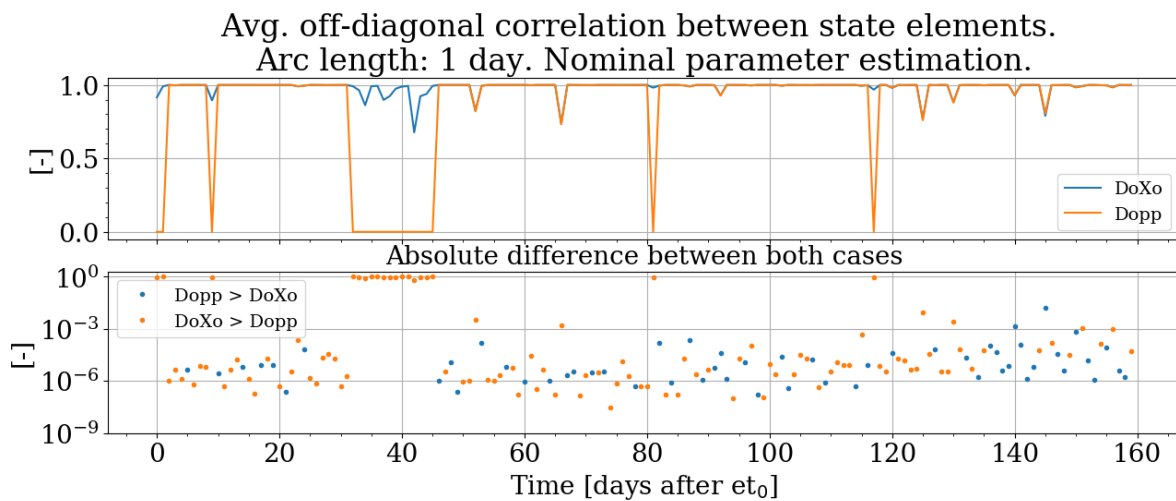


Figure 8.9: Average, absolute off-diagonal correlation between state elements for each individual arc using Doppler data only (Dopp) and both Doppler and crossover data (DoXo). Arc length: 1 day.

As discussed for the estimation of local parameters, DoXo correlation improvements are more noticeable for estimation arcs past day 100 leading to decreases in correlation up to 2.33×10^{-4} . However, even the best correlation improvement is low and foremost these improvements are not consistent as shown in the lower plot of [Figure 8.9](#). For the correlation of the state elements low correlation values are advantageous, since they indicate that all state elements can be solved for independently. However, the correlation values of zero for the Dopp case do not originate from particularly good estimates. Instead, they originate from there being no Doppler state estimates for those arcs, consistent with the results shown in [Figure 8.7](#). These occultation windows give initial insights into the attainable correlation when only crossover measurements are used for orbit estimation, resulting in noticeably lower average off-diagonal correlations. As discussed in [section 5.3](#), Doppler measurements do not sufficiently constrain the orientation of the orbit in space. This in turn leads to a high dependency of the estimation of all elements between one another as clearly visible in [Figure 8.9](#).

The results of the nominal case so far suggest that Doppler measurements have a much higher impact on the orbit estimation than the crossover measurements do. This notion is further enhanced by evaluating the respective Dopp and Doxo design matrices as weighted by the square root of their respective measurement uncertainties shown in [Figure 8.10](#) and [Figure 8.11](#). Consistent with previous results, the communication gaps are well visible within [Figure 8.10](#) as jumps within the otherwise diagonal line of partial derivatives for JUICE's state. As shown in [Equation 5.16](#) the least squares orbit determination algorithm used here is a *weighted* one. Thus, the high precision of Doppler measurements results in these measurements having a larger impact in the orbit estimation algorithm. For JUICE's position elements the weighted magnitude of Doppler measurements is in the order of 10^3 to 10^4 , while for crossover measurements it is in the order of 10^{-2} to 10^{-1} . For JUICE's velocity elements the weighting magnitude of Doppler measurements is in the order of 10^5 to 10^6 , while for crossover measurements it is in the order of 10^1 to 10^3 , resulting in a difference of up to 5 orders of magnitude for both position and velocity elements.

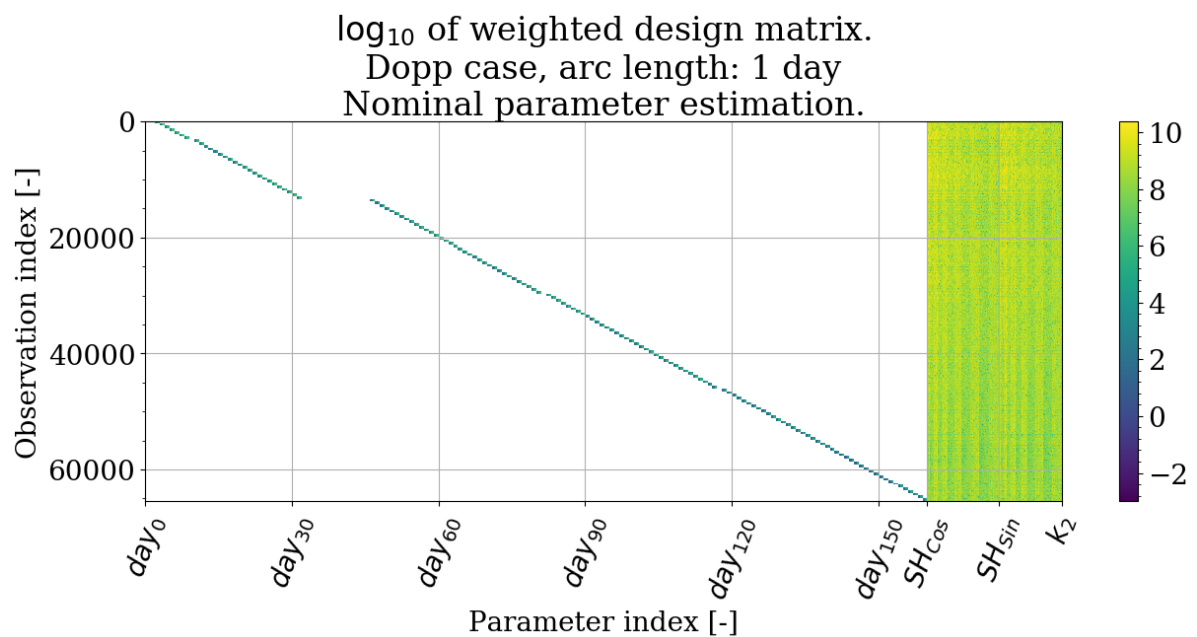


Figure 8.10: Dopp design matrix H weighted by measurement uncertainty, arc length: 1 day.

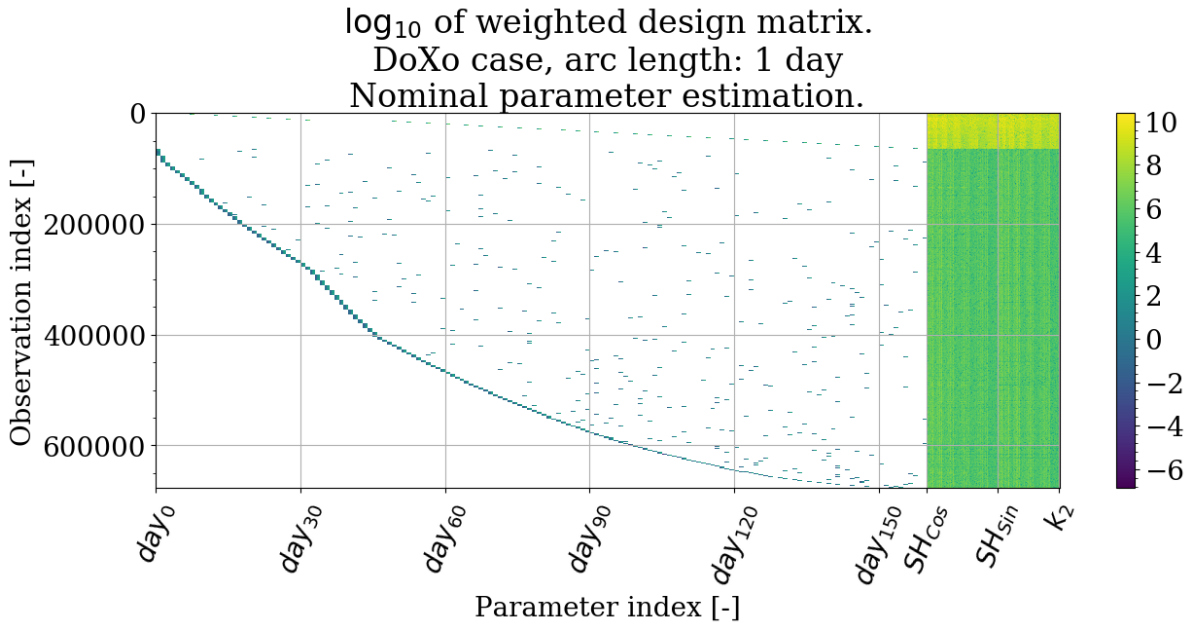


Figure 8.11: DoXo design matrix H weighted by the respective measurement uncertainties, arc length: 1 day.

Although Doppler measurements have a much higher weight, it is noteworthy that they impact the POD scheme so heavily since this analysis uses 65,485 Doppler measurements and while using 630,793 crossover measurements - an entire order of magnitude more crossover measurements. However, as discussed in [section 5.6](#) random errors can successfully be averaged out by using a sufficient number of measurements. This improvement presents a reason to include crossover measurements into POD schemes as the results shown in [Table 8.1](#) and [Table 8.2](#) show that they consistently improve estimation uncertainties for local parameters, as well as for global parameters.

8.2. Influence of Arc Length

To analyse the influence different arc lengths have on JUICE's Dopp and DoXo POD schemes, the same settings are used as for the nominal case discussed in [section 8.1](#), with the only difference being the number of days within each estimation arc. Starting from t_0 each arc is propagated with the reference arc length, with the last arc being merged with the previous one if its length is less than half the reference arc length.

[Table 8.3](#) clearly shows the linear decrease in estimation uncertainty for the Dopp case with increasing arc length for the estimation of JUICE's position parameter at each arc. For the calculation of the uncertainty average arcs which have no Doppler measurements have been filtered out from the total number of estimation arcs n_{arcs} . The number of arcs which has been filtered out due to occultations is denoted by n_{occ} . The plots showing the position uncertainties in detail for arc lengths between 2 and 10 days can be found in [Appendix A.8](#). Using an arc length longer than the duration of the occultations leads to an availability of enough measurements to estimate parameters at the beginning of the given arc, even when using Doppler data only. This effect is already visible for an arc length of 2 days resulting in position estimates for the occultations during the days 9, 81 and 117. The occultation during the days 0-2 is only affected for arc lengths longer than 2 days since the first communication window starts well into day 2, see [Appendix A.4](#). Additionally, the occultation between the days 32-46 is only properly resolved with an arc length of 10 days as shown in

| Arc length [days] | n_{arcs} | n_{occ} | Average position uncertainty [m] | | |
|----------------------|------------|-----------|----------------------------------|-------------|-------------|
| | | | Radial | Cross-track | Along-track |
| 1 | 160 | 19 | 0.0118 | 0.3117 | 2.3747 |
| 2 | 80 | 8 | 0.0064 | 0.0475 | 0.3178 |
| 3 | 54 | 4 | 0.0053 | 0.0685 | 0.2013 |
| 4 | 40 | 3 | 0.0045 | 0.0121 | 0.0776 |
| 5 | 32 | 2 | 0.0042 | 0.016 | 0.0676 |
| 6 | 27 | 1 | 0.0038 | 0.0122 | 0.0629 |
| 7 | 23 | 1 | 0.0035 | 0.0093 | 0.0532 |
| 8 | 20 | 1 | 0.0032 | 0.0081 | 0.0455 |
| 9 | 18 | 1 | 0.0032 | 0.0069 | 0.0415 |
| 10 | 16 | 0 | 0.0031 | 0.0139 | 0.0485 |

Table 8.3: Average position uncertainty using Doppler measurements only. Arc with no Doppler data are not considered.

Table 8.3, as for shorter arc lengths there is always at least 1 arc with begins and starts during this large occultation due to the Sun as discussed in subsection 5.4.2. Furthermore, uncertainty peaks due to the Sun occultation become noticeably narrower with increasing arc length since the arcs at the beginning and end of the occultation contain measurements. While a large peak is still visible when using an arc length of 9 days, see Appendix A.8, this peak mostly diminishes upon using an arc length of 10 days. With an arc length of 10 days, the occultation due to the Sun between days 32-46 is now divided up in two arcs starting on day 30 and 40 leading to an availability of measurements for both cases.

As for the nominal DoXo case, the additional use of crossover measurements consistently leads to uncertainty improvements. However, increases in arc length result in lower average uncertainty improvements as shown in Table 8.4. For the calculation for the results shown in Table 8.4 the same arcs were filtered out as in Table 8.3. The increase in average improvement for arc lengths longer than 7 days is attributed to the estimation degradation discussed in section 8.1 which becomes more noticeable for longer arcs as shown in Appendix A.8. This degradation, visible in worse position uncertainties in radial direction while those in cross-track direction become better, leads to noticeably larger improvements. With an increase in arc length the total number of arcs decreases, leading to the later arcs with higher improvements affecting the average more, resulting in higher average uncertainty improvements.

| Arc length [days] | Improvement in position uncertainty [%] | | |
|----------------------|---|-------------|-------------|
| | Radial | Cross-track | Along-track |
| 1 | 3.9249 | 2.9071 | 2.9389 |
| 2 | 1.2351 | 0.0669 | 0.0705 |
| 3 | 1.202 | 0.0971 | 0.124 |
| 4 | 1.1953 | 0.0133 | 0.0524 |
| 5 | 0.845 | 0.0091 | 0.1041 |
| 6 | 1.1663 | 0.0101 | 0.0811 |
| 7 | 1.0966 | 0.0087 | 0.0733 |
| 8 | 1.2986 | 0.01 | 0.0441 |
| 9 | 1.2204 | 0.01 | 0.0925 |
| 10 | 0.8505 | 0.0113 | 0.1228 |

Table 8.4: Average position uncertainty improvement by using Doppler and crossover measurements. Arc with no Doppler data are not considered.

While the lower position estimation uncertainties for longer arcs suggest that a choice of longer arcs is always more beneficial, they only do so since the environment that affected measurement generation is *exactly* the same as the one used for the orbit estimation. As already mentioned within [section 5.2](#), once JUICE's measurements are available the environment model used for initial orbit estimation schemes will inevitably have strong deviations from reality. It is possible to improve the environment model used for orbit estimation by estimating the model parameters during orbit determination. Unfortunately, even best attainable model estimates will result in overly optimistic formal errors. The differences between the estimation's true and formal errors result from effects which are *not* considered in the estimation's model such as measurements biases or perturbing forces. An example of such forces is given by the estimation of gravity coefficients: While we might obtain highly accurate estimates for Ganymede's spherical harmonic coefficients up to degree and order 12, we completely disregard any higher coefficients whose effect inevitably influences the uncertainty of the estimated gravity coefficients. This negligence on model parameters can potentially lead to entirely wrong parameter estimates, as the formal errors do not give any insight into the quality of the used model even if their uncertainty is extremely low. Thus, formal estimation errors only yield a best case estimation uncertainty.

Prior to the orbit estimation with JUICE's measurements, the current Juno mission will yield deeper insights into Jupiter in particular. However, the main driver for JUICE's motion is Ganymede as discussed in [chapter 4](#). For Ganymede there are only estimates for its J_2 and C_{22} coefficients, which still require further validation as they were estimated using an a priori hydrostatic constraint, as discussed in [section 4.1](#). Thus, for JUICE's POD with real measurements, the prediction of JUICE's motion will degenerate rapidly in time making it necessary to use short estimation arcs until Ganymede's gravity field has been further constrained, in addition to the location of the Jovian moons and Jupiter itself. Therein, the estimation of empirical accelerations will be of particular use to estimate the magnitude of unmodeled forces as discussed further in [section 8.4](#).

A possible solution to deal with the lack of Doppler measurements due to communication gaps is to use custom arc lengths. In [Figure 8.12](#) such a case is shown which uses the nominal arc length of 1 day and custom arc lengths for each occultation period. Therein, the custom arc lengths were determined such that during occultations, the respective arcs start at the beginning of the occultation and end so that they include the first measurement window after the occultation.

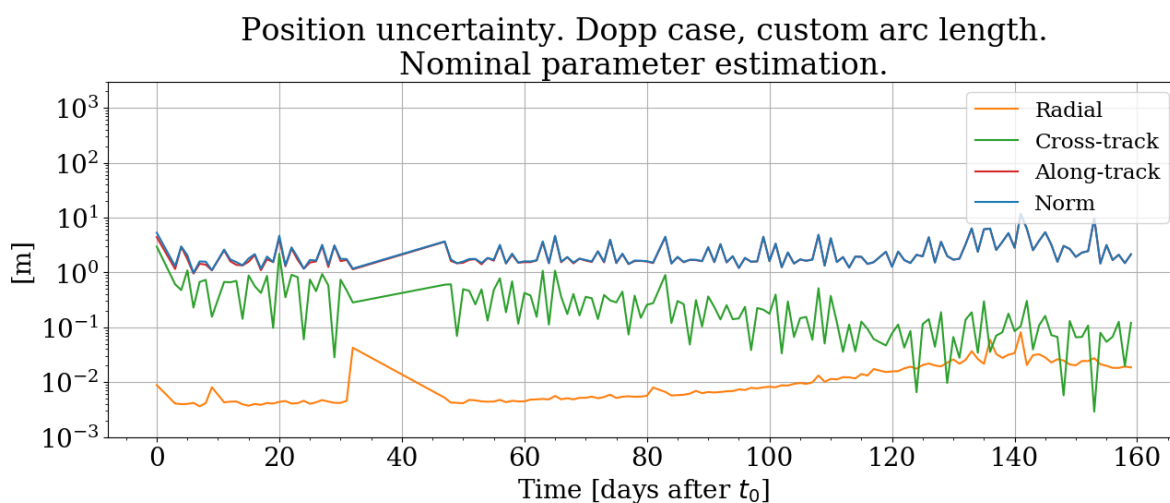


Figure 8.12: Position uncertainty using Doppler data only, arc length: custom, 1 day baseline.

This choice of arc results in the uncertainty peaks in the cross and along-track directions not having noticeably higher uncertainties than for regular arcs. Merely the uncertainties in the radial direction for the first 3 occultations at days 0, 9 and 32 are noticeably higher. As before, a favourable measurement fitting for the occultation periods could only be achieved since the prediction environment model is exactly the same as for the measurement creation. Similarly to the nominal case with an arc length of 1 day, the uncertainty improvement of using both crossover and Doppler measurements is 4.601% in radial, 3.847% in cross-track and 3.845% in along-track direction.

As with the estimation of JUICE's position, the Dopp estimation uncertainty of global parameters is improved with increasing arc length. Table 8.5 shows the average Dopp uncertainties for the estimation of Ganymede's spherical harmonics up to degree and order 12 and Ganymede's Love number k_2 using different arc lengths. Additionally, Table 8.6 shows the uncertainty improvement when using crossover measurements in addition to Doppler data. As Table 8.6 shows, the improvement in estimation uncertainty when using crossover measurements in addition to Doppler measurements becomes rapidly smaller with increasing arc length.

| Average Dopp SH uncertainty [-] | | | | | |
|---------------------------------|------------------------|------------------------|------------------------|------------------------|------------------------|
| Arc length [days] | 1 | 2 | 3 | 4 | 5 |
| C_{nm} | 1.86×10^{-10} | 1.2×10^{-10} | 1.15×10^{-10} | 1.14×10^{-10} | 1.13×10^{-10} |
| S_{nm} | 1.09×10^{-10} | 9.89×10^{-11} | 9.63×10^{-11} | 9.5×10^{-11} | 9.49×10^{-11} |
| k_2 | 5.06×10^{-5} | 5.68×10^{-6} | 2.91×10^{-6} | 2.73×10^{-6} | 2.56×10^{-6} |
| Arc length [days] | 6 | 7 | 8 | 9 | 10 |
| C_{nm} | 1.13×10^{-10} |
| S_{nm} | 9.47×10^{-11} | 9.47×10^{-11} | 9.45×10^{-11} | 9.44×10^{-11} | 9.44×10^{-11} |
| k_2 | 2.53×10^{-6} | 2.55×10^{-6} | 2.44×10^{-6} | 2.4×10^{-6} | 2.41×10^{-6} |

Table 8.5: Average SH uncertainty using Doppler measurements only.

The decrease in uncertainty with increasing arc length further emphasises the point already made in section 5.6: random errors can successfully be averaged out by using a sufficient number of measurements. Thus, it can be expected that once JUICE's measurements are available initially only short arc lengths will be viable for POD purposes due to model errors. However, the better constrained the models become, the longer the estimation arc lengths can be resulting in lower uncertainties as more measurements can be used for the estimation of each arc.

| Average DoXo improvement in position uncertainty [%] | | | | | | | | | | |
|--|-------|-------|-------|-------|-------|-------|-------|-------|-------|-------|
| Arc l. [days] | 1 | 2 | 3 | 4 | 5 | 6 | 7 | 8 | 9 | 10 |
| C_{nm} | 0.732 | 0.056 | 0.04 | 0.035 | 0.032 | 0.029 | 0.027 | 0.025 | 0.024 | 0.023 |
| S_{nm} | 0.752 | 0.048 | 0.035 | 0.028 | 0.026 | 0.024 | 0.022 | 0.019 | 0.019 | 0.017 |
| k_2 | 5.194 | 0.056 | 0.008 | 0.007 | 0.004 | 0.002 | 0.003 | 0.001 | 0.001 | 0.001 |

Table 8.6: Average improvement in SH uncertainty using crossover and Doppler measurements.

Naturally, the correlations between the state elements are also affected by the arc length

as shown in Figure 8.13 for an arc length of 10 days. While Figure 8.13 might suggest that the state elements at later arcs are estimated more independently of one another using larger arc length, the actual reason for the decline in correlation is the estimation degradation noticeable in the increase in radial uncertainty while the cross-track uncertainty decreases. As discussed in section 5.3, this degradation originates in the insufficient geometrical orbit constrains obtained with Doppler measurements. Contrary to an arc length of 1 day, the radial uncertainty does eventually become worse than that of the cross-track direction. This occurs even for an arc length of 2 days already, as shown within Appendix A.8. As already shown for the nominal case in Figure 8.24, the additional use of crossover measurements does not consistently improve the correlation between state elements with only 2 out of 16 arcs having lower correlations.

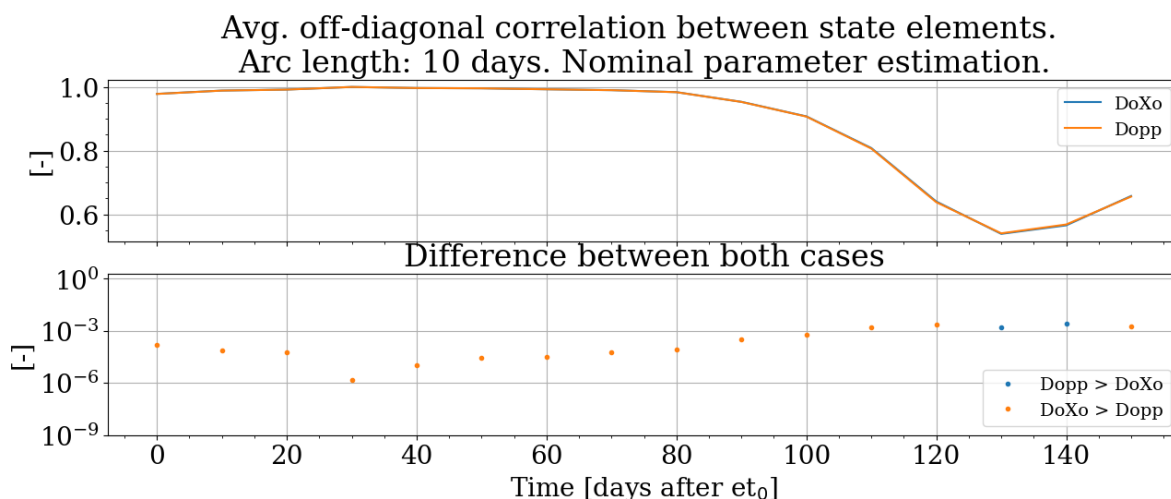


Figure 8.13: Average, absolute off-diagonal correlation between state elements for each individual arc using Doppler data only (Dopp) and both Doppler and crossover data (DoXo). Arc length: 10 days.

Another effect the choice of arc length has, is the number of available, selected and actually used crossover measurements, referred to as covers, is shown in Table 8.7.

| | | | | | |
|-------------------|-----------|-----------|-----------|-----------|-----------|
| Arc length: | 1 day | 2 days | 3 days | 4 days | 5 days |
| Number of arcs: | 160 | 80 | 54 | 40 | 32 |
| Available covers: | 1,526,142 | 1,526,946 | 1,526,858 | 1,526,044 | 1,525,858 |
| Selected covers: | 659,149 | 659,861 | 660,225 | 659,672 | 658,837 |
| Used covers: | 630,793 | 646,352 | 650,522 | 652,652 | 656,141 |
| Arc length: | 6 days | 7 days | 8 days | 9 days | 10 days |
| Number of arcs: | 27 | 23 | 20 | 18 | 16 |
| Available covers: | 1,526,079 | 1,526,016 | 1,527,722 | 1,525,525 | 1,525,753 |
| Selected covers: | 659,127 | 659,317 | 659,936 | 658,674 | 659,064 |
| Used covers: | 653,885 | 656,419 | 655,969 | 656,664 | 658,706 |

Table 8.7: Number of crossovers depending on arc length.

Within Table 8.7, available crossovers refer to all existing ground track crossovers during JUICE’s simulated trajectory, independent of their occurrence in time. Conversely, the number of selected crossovers refers to the number of remaining crossover measurements after those which occurred during communication, slew or wheel-off-loading (WOL) periods were filtered

out, as presented in [subsection 5.5.2](#). Lastly, the number of used crossovers refers to the number of actually used crossover measurements after filtering out crossovers which occur close to the beginning of propagation arcs as shown in [Figure 5.4](#). Since shorter arcs lengths approximate ESA's trajectory much closer, as discussed in [section 6.1](#), it is expected that the difference in trajectories affects the number of selected crossovers. However, the main driver in the difference between used crossovers results from the necessary filtering due to interpolation errors as shown in [Figure 5.4](#) with shorter arcs leading to more crossovers being filtered out. This is an effect specific to this thesis which can be avoided by using different propagation settings. For an arc length of 1 day this leads to a loss of up to 28356 crossovers, which is 4.3% of the selected crossovers, see [Table 8.7](#). Conversely, for an arc length of 10 days only 358 are lost, 0.05% of the selected crossovers. As discussed in [section 7.1](#), it was chosen to interpolate the trajectories to obtain high precision crossover determination while maintaining low computational costs. Unfortunately, the number of used crossovers is also affected by numerical issues as not all selected crossover measurements could be used due to the used storage system used for crossover handling. As maps within C++ only allow each key to exist once, if several crossovers occur during the same epoch t_1 only one of those crossover measurements is used. This effect occurs in areas of high crossover density, such as on Ganymede's poles as shown in [Figure 5.5](#). While having a negative effect on the number of available measurements, it is herein regarded as negligible due to the low number of affected crossovers and the disproportionate amount of work required to include all selected crossovers for estimation.

Another prominent effect of the arc length is the number of estimated parameters since each additional arc leads to 6 additional state elements which must be estimated. Naturally, a higher number of estimated parameters leads to higher computational loads as more partial derivatives must be evaluated. This in turn leads to larger design matrices for shorter arc lengths, whose resulting computational loads can be demonstrated via the file size depending on arc length as shown in [Table 8.8](#). Regarding this issue, it is recommended that future works decrease the computational costs of large design matrices by using sparse matrices.

As clearly visible, orbit estimation with crossovers requires large additional computational efforts. This can become particularly problematic when attempting to converge towards a solution due to the long computation times for the DoXo case. While for an arc length of 1 day the Dopp case requires on average 5 minutes to evaluate [Equation 5.23](#) and [Equation 5.24](#), the DoXo case requires around 25 minutes using the same computational resources. Additionally, the computational efforts for crossover determination must also be considered. As all trajectories are interpolated using a stepsize of 1 s, as discussed in [section 6.3](#), all arc lengths required the same average of about 53 minutes for crossover determination.

| | | | | | |
|------------------------|--------|--------|--------|--------|---------|
| Arc length: | 1 day | 2 days | 3 days | 4 days | 5 days |
| H-file size Dopp [Gb]: | 1.42 | 0.82 | 0.63 | 0.53 | 0.46 |
| H-file size DoXo [Gb]: | 15.16 | 9.00 | 6.94 | 5.82 | 5.18 |
| Arc length: | 6 days | 7 days | 8 days | 9 days | 10 days |
| H-file size Dopp [Gb]: | 0.43 | 0.41 | 0.38 | 0.36 | 0.35 |
| H-file size DoXo [Gb]: | 4.76 | 4.44 | 4.18 | 4.02 | 3.87 |

Table 8.8: Design matrix H file size depending on arc length.

Lastly, choice of arc length is also noticeable in the condition number of the respective POD schemes as shown in [Table 8.9](#) with the condition number reflecting the ratio between the largest and smallest eigenvalue within the normal matrix for each case. The order of magnitude k of the condition number signals how many digits must be regarded with caution

when evaluating the POD scheme's results [van der Wal, 2017]. Unsurprisingly, this number is particularly high in the Dopp cases where there are arcs without measurements as the used a priori information leads to particularly high eigenvalues, while the low uncertainty values of the spherical harmonic coefficients lead to particularly low eigenvalues. Conversely, when crossovers are used there are always sufficient measurements to estimate parameters leading to comparatively low condition numbers.

| | | | | | |
|--|----------------------|----------------------|----------------------|----------------------|----------------------|
| Arc length: | 1 day | 2 days | 3 days | 4 days | 5 days |
| Condition number Dopp: | 9.2×10^{36} | 9.2×10^{36} | 8.8×10^{36} | 9.7×10^{36} | 1.5×10^{37} |
| Condition number DoXo: | 3.5×10^{16} | 1.3×10^{17} | 2.1×10^{17} | 2.3×10^{17} | 8.8×10^{17} |
| Arc length: | 6 days | 7 days | 8 days | 9 days | 10 days |
| Condition number Dopp: | 1.4×10^{37} | 1.8×10^{37} | 2.0×10^{37} | 2.8×10^{37} | 2.7×10^{11} |
| Condition number DoXo: | 1.5×10^{17} | 4.2×10^{17} | 1.4×10^{17} | 5.4×10^{18} | 4.1×10^{11} |
| Condition number using custom arc length (Dopp): | 1.8×10^{12} | | | | |
| Condition number using custom arc length (DoXo): | 1.8×10^{12} | | | | |

Table 8.9: Design matrix H condition number depending on arc length.

It should be mentioned however, that a condition number of 10^{11} is still very high especially when considering that the number of digits usual numerical schemes store is 15 [Villamil, 2019]. However, the study of these particularly high condition numbers is outside the scope of this thesis.

8.3. Influence of Measurement Errors

To analyse the influence measurement errors have on JUICE's POD, the same settings are used as for the nominal case discussed in section 8.1 with the only difference being the used measurement uncertainties as described in subsection 5.6.3. For convenience, the evaluated error cases are shown in Table 8.10 again. Therein, case 1 corresponds to the nominal mission case as discussed in section 8.1.

| | Case 1 | Case 2 | Case 3 | Case 4 |
|----------------------|----------------------|--------------------|----------------------|--------------------|
| Doppler error [m/s]: | 1.5×10^{-5} | 5×10^{-4} | 1.5×10^{-5} | 5×10^{-4} |
| Crossover error [m]: | 4.48 | 4.48 | 9.68 | 9.68 |

Table 8.10: Error cases based on Table 5.1 and Table 5.6.

Of these 4 cases, case 2 is the most favourable one for crossover measurements as the larger Doppler uncertainty decreases the weight of Doppler measurements in the POD.

Table 8.11 shows the stark worsening of estimation uncertainty when comparing the Dopp error case 2, to the Dopp error case 1. As for the nominal case discussed in section 8.1, arcs which with no Doppler measurements, i.e. occultation periods, are not taken into account for the calculation of the change of estimation uncertainty shown in Table 8.11. Therein, the *relative* difference demonstrates the strong worsening in estimation uncertainty due to a worse Doppler uncertainty. Conversely, the *absolute* difference gives insights into the magnitude of the estimation uncertainty for the Dopp error case 2. The respective plot showing the relative differences in radial, cross-track and along-track direction can be found in Appendix A.9. Conversely, Table 8.12 shows the average relative improvement in radial, cross-track and along-track direction when using both crossover and Doppler measurements. The respective

plot showing the relative differences in radial, cross-track and along-track direction can be found in [Appendix A.9](#). As for [Table 8.11](#), occultation periods are not considered in the calculation of the average estimation improvement. For convenience, the estimation improvements for error case 1 already discussed in [section 8.1](#) are shown in [Table 8.12](#) again.

| Average degradation in position uncertainty. Dopp error case 2 w.r.t Dopp error case 1 | | | |
|---|----------|-------------|-------------|
| | Radial | Cross-track | Along-track |
| Absolute [m] | 0.379 | 9.76 | 74.168 |
| Relative [%] | 3224.392 | 3124.673 | 3123.581 |

Table 8.11: Degradation of position uncertainty resulting from worse Doppler measurement uncertainty.

| Average improvement in position uncertainty using crossover measurements [%]. | | | |
|--|--------|-------------|-------------|
| Error | Radial | Cross-track | Along-track |
| Case 1 | 3.925 | 2.907 | 2.939 |
| Case 2 | 49.619 | 56.2 | 56.447 |
| Case 3 | 1.122 | 0.814 | 0.822 |
| Case 4 | 37.347 | 41.628 | 41.88 |

Table 8.12: Improvement in position uncertainty using both crossover and Doppler measurement for the 4 error cases shown in [Table 8.10](#).

As expected and shown in [Table 8.12](#), error case 2 leads to the largest uncertainty improvements as crossover measurements have their best measurement uncertainty while Doppler measurements have their worst measurement uncertainty. Surprisingly, in error case 4 the additional use of crossover measurements also leads to large uncertainty improvements even though both Doppler and crossover measurements have their worst measurement uncertainty. It is surmised that this improvement results mainly from the lower weight factor for Doppler measurements allowing the large number of crossover measurements to contribute more amply. The uncertainty improvements for the error cases 2 and 4 are non-negligible and demonstrate the high potential of crossovers for orbit estimation. As already discussed for the error case 1 in [section 8.1](#), the uncertainty improvement from using crossover measurements is largest at later arcs where estimation degradation is largest due to the insufficient geometrical constraints of Doppler measurements as discussed in [section 5.3](#). This spike in improvement is evident in all error cases with individual relative improvements up to 35% for error case 1, 96% for error case 2, 12% for error case 3 and 92% for error case 4

Naturally, larger uncertainties in Doppler measurements lead to larger uncertainties in the estimation of global parameters as well.

| Average degradation in global par. uncertainty. Dopp error case 2 w.r.t Dopp error case 1 | | | |
|--|------------------------|------------------------|----------|
| | C_{nm} | S_{nm} | k_2 |
| Absolute [m] | 5.987×10^{-9} | 3.529×10^{-9} | 0.002 |
| Relative [%] | 3227.381 | 3228.572 | 3179.793 |

Table 8.13: Degradation of position uncertainty resulting from worse Doppler measurement uncertainty.

As was the case for the uncertainties of position elements, the addition of crossover measurements leads to uncertainty improvements for the estimation of global parameters as shown

in Table 8.14. The respective plots which show the relative improvement for every gravity coefficient are shown in Appendix A.9. Here also, the cases where crossover measurements improve estimation the most are those where Doppler measurements have a larger measurement uncertainty. The lower uncertainty improvements shown in Table 8.14 in comparison to those shown in Table 8.12 originate in the larger number of measurements available for parameter estimation. While for the estimation of local parameters only measurements of the respective arc can be used, the estimation of global parameters makes use of measurements in every arc.

| Average improvement in global par. uncertainty using crossover measurements [%]. | | | |
|--|----------|----------|--------|
| Error | C_{nm} | S_{nm} | k_2 |
| Case 1 | 0.732 | 0.752 | 5.194 |
| Case 2 | 9.232 | 9.179 | 69.163 |
| Case 3 | 0.199 | 0.206 | 1.356 |
| Case 4 | 7.332 | 7.182 | 59.285 |

Table 8.14: Improvement in position uncertainty using both crossover and Doppler measurement for the 4 error cases shown in Table 8.10.

Although neither error case 2 nor 4 is representative for JUICE's tracking error budget, they provide a strong argument for using crossover measurements should JUICE's Doppler measurement uncertainty not meet expectations. Additionally, these 2 cases also show that it is possible to further improve the orbit determination uncertainties of prior missions without precise tracking measurements as available for the JUICE mission.

8.4. Influence of Estimated Parameters

To analyse the influence the number of estimated parameters has on JUICE's POD, the same settings are used as for the nominal case discussed in section 8.1 with the only difference being the parameters being estimated. Therein, two cases are evaluated: Within the first one, fewer parameters are estimated resulting in the estimation of only JUICE's state in time. This case is a merely theoretical one, since it implies a perfect knowledge on JUICE's environment during its trajectory. Within the second case, in addition to the nominal estimation of JUICE's state, Ganymede's SH up to degree and order 12 and Ganymede's Love number k_2 , so called empirical accelerations are estimated as well. As discussed in section 7.2 the estimation of empirical accelerations is done to include the effect of unmodeled forces during orbit estimation. Herein, they are used to imitate the estimation of accelerometer errors as described in section 7.2.

Estimating JUICE's state only, using a nominal arc length of 1 day and Doppler measurements only results in an estimation uncertainty improvement in comparison to the nominal case. Disregarding occultation periods, the average uncertainty improvement is shown in Table 8.15. The respective plots which show the Dopp relative uncertainty *improvement* when estimating fewer parameters in comparison to the nominal Dopp case can be found in Appendix A.10.

| Average improvement in position uncertainty using crossover measurements [%] | | |
|--|-------------|-------------|
| Radial | Cross-track | Along-track |
| 26.366 | 41.982 | 41.322 |

Table 8.15: Position uncertainty improvement resulting from fewer estimation parameter.

Conversely, when only JUICE's state is estimated the additional use of crossover measurements results in lower average relative uncertainty improvements as shown in Table 8.16. The respective plots which show the relative uncertainty improvement for each arc can be found in Appendix A.10. For convenience, the DoXo uncertainty improvement of the nominal case as discussed in section 8.1 is also shown in Table 8.16. As for the nominal case, occultation periods are disregarded for the calculation of the average improvement as they can be seen as exceptions within JUICE's nominal POD.

| Average improvement in position uncertainty using crossover measurements [%] | | | |
|--|--------|-------------|-------------|
| | Radial | Cross-track | Along-track |
| Nominal case | 3.925 | 2.907 | 2.939 |
| Reduced case | 1.0196 | 0.5235 | 0.5771 |

Table 8.16: Degradation of position uncertainty resulting from worse Doppler measurement uncertainty.

Table 8.16 shows that the average uncertainty improvement in the DoXo case decreases with a decrease in estimated parameters. However, equal to the nominal DoXo case, uncertainty improvements noticeably increase towards the later arcs, with individual uncertainty improvements up to 20%. As in section 8.1, it can be surmised that this improvement originates in crossover measurements alleviating estimation degeneration due to the inability of Doppler measurements to geometrically constrain JUICE's orbit.

Regarding the correlation of state parameters, there are slight differences as the addition of crossover observables lowers many of the correlations within the initial 30 arcs but less in the later arcs, see Figure 8.14. As before, this improvement is of very low magnitude, being only of order 10^{-6} to 10^{-9} in addition to not being consistent. Conversely, estimating more parameters has a strong effect on the attainable formal uncertainties.

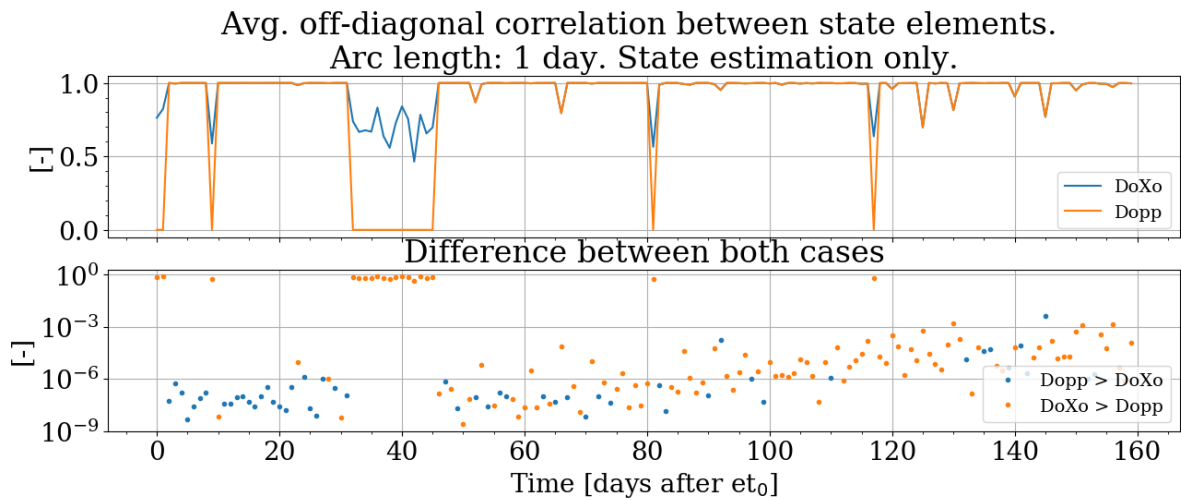


Figure 8.14: Comparison of correlation between state elements. Arc length 1 day, state estimation only.

The additional estimation of 480 local parameters, 3 for each axis in all of the 160 estimated arcs, has a negative impact on the attainable Dopp position uncertainties as shown in Table 8.17. Therein, the extended Dopp case is compared to the nominal Dopp case, disregarding the position estimation uncertainties during occultation periods which equal to the a priori information in both cases. As shown in Appendix A.10, the degradation is strongest in radial and cross-track direction with individual estimation worsening of up to 7563% in radial

and 11948% in cross-track direction. For the SH degradation individual estimation degradation is up to 275% for C_{nm} and up to 297% for S_{nm} .

| Dopp average degradation in uncertainty [%] | | | | | |
|---|-------------|-------------|------------------|----------|---------|
| Position parameter | | | Global parameter | | |
| Radial | Cross-track | Along-track | C_{nm} | S_{nm} | k_2 |
| 792.881 | 774.917 | 501.99 | 22.389 | 23.502 | 275.408 |

Table 8.17: Dopp degradation in estimation uncertainty for an extended parameter estimation.

Additionally, the estimation of additional parameters leads to noticeably larger uncertainty improvements when crossover measurements are included as shown in Table 8.18. In comparison to the nominal case discussed in section 8.1, these larger improvements present a much stronger argument for using crossover measurements for orbit determination. This is more so the case since it can be expected that for JUICE's actual POD even more parameters will be estimated, leading to even larger uncertainty improvements. Additionally, it must be stressed that in all results presented the addition of crossover measurements has consistently resulted in improved estimation uncertainties.

| DoXo average improvement in emp. acc. uncertainty [%] | | | | | | |
|---|--------------------|-------------|-------------|------------------|----------|--------|
| | Position parameter | | | Global parameter | | |
| | Radial | Cross-track | Along-track | C_{nm} | S_{nm} | k_2 |
| Nominal case | 3.925 | 2.907 | 2.939 | 0.732 | 0.752 | 5.194 |
| Extended case | 35.35 | 11.072 | 9.699 | 4.303 | 4.691 | 31.024 |

Table 8.18: Improvement in position uncertainty from using both Doppler and crossover measurements. Extended parameters estimation.

As for the nominal case, the uncertainty improvements noticeably increase during the last 60 estimation arcs/days with improvements up to 95% in radial, 78% in cross-track and 46% in along-track direction as shown in Appendix A.10.

Figure 8.15 shows the estimation uncertainties for the empirical accelerations in radial, cross-track and along-track direction in the Dopp case. Conversely, Figure 8.16 shows the estimation uncertainties for the empirical accelerations in the DoXo case. Furthermore, the improvement in the uncertainty of the estimated empirical accelerations through the inclusion of crossover measurements is shown in Figure 8.17.

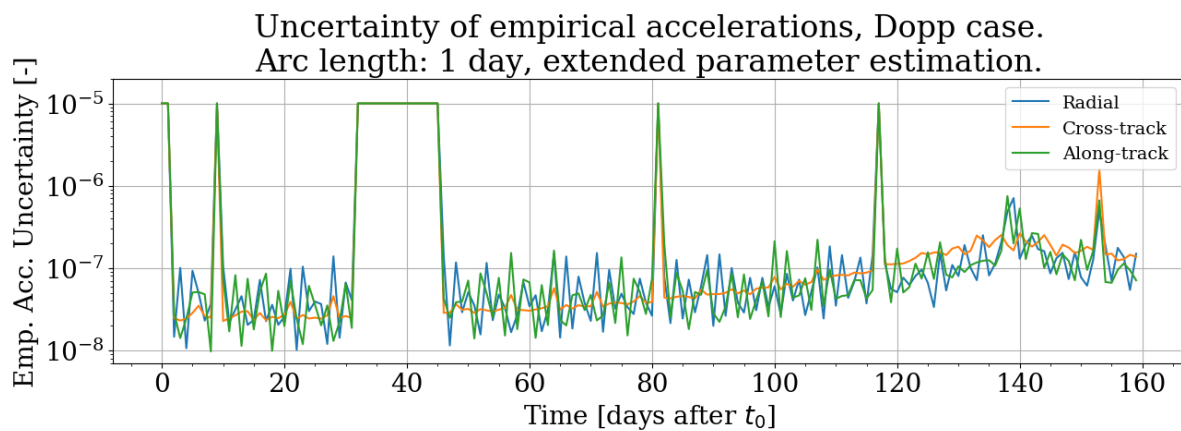


Figure 8.15: Empirical accelerations uncertainty for the Doxo case using an arc length of 1 day. Extended parameter estimation.

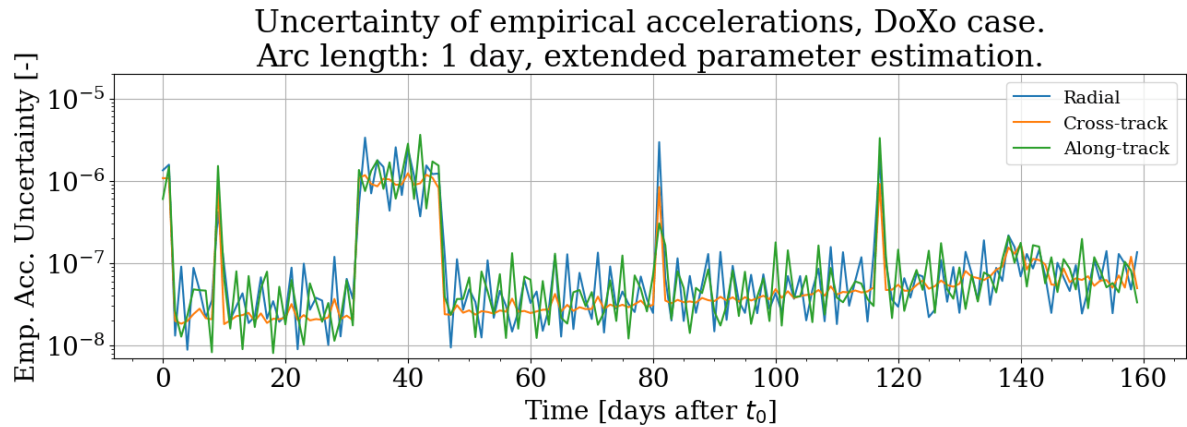


Figure 8.16: Empirical accelerations uncertainty for the Doxo case using an arc length of 1 day. Extended parameter estimation.

Equal to the estimation of other local parameters such as JUICE's position at each arc, for periods without Doppler measurements, i.e. occultation periods, no estimation is possible leading to spikes in uncertainty equal to the used a priori information, as shown in Figure 8.15. As shown in Figure 8.16, in the DoXo case the estimation of empirical accelerations for arcs during occultation periods is possible, albeit to a worse uncertainty than for arcs with Doppler measurements. Equally, the estimation of empirical accelerations also shows a noticeable estimation degradation in later arcs, due to the insufficient geometrical constraints of Doppler measurements. While for the position uncertainties the radial uncertainty degraded while the cross-track uncertainty improved, for the estimation of the empirical accelerations all three directions degrade together. As shown for the nominal case in section 8.1, the addition of crossover measurements leads to an improvement in estimation uncertainties for empirical accelerations, in particular in the later estimation arcs as shown in Figure 8.17.

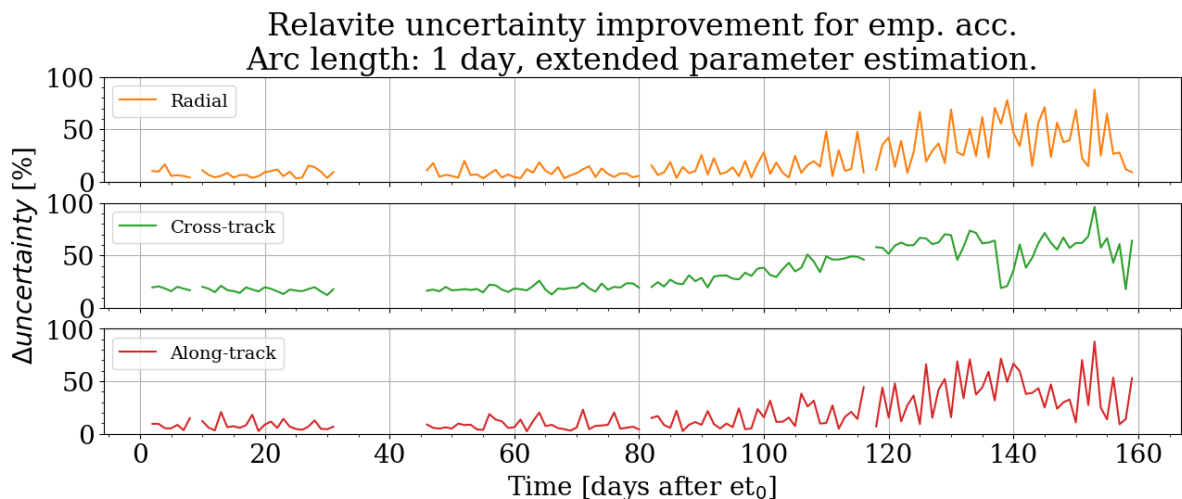


Figure 8.17: Comparison of empirical accelerations uncertainty between nominal Dopp and DoXo cases, arc length: 1 day.

Table 8.19 quantifies the average improvement in uncertainty for the estimation of empirical accelerations. Therein, occultation periods have been neglected. In addition to the average uncertainty improvement for all considered estimation arcs, Table 8.19 also shows the average improvement only regarding the first 100 days and only regarding the last 60

days. This difference in average further emphasises the value of crossover measurements in adding geometrical constraints to the orbit determination.

| | DoXo average improvement in emp. acc. uncertainty [%] | | |
|--------------|---|-------------|-------------|
| | Radial | Cross-track | Along-track |
| pre day 100 | 9.081 | 20.077 | 9.069 |
| post day 100 | 33.153 | 53.298 | 33.296 |
| total | 19.154 | 33.978 | 19.206 |

Table 8.19: DoXo improvement in emp. acc. uncertainty.

Lastly, the correlation averages between the state elements for the Dopp and DoXo cases treated in this section are compared. As shown in Figure 8.18, the differences in average correlation between both cases are larger than for the nominal case. As before, using crossover measurements leads to higher correlations between the individual state elements instead of improving/reducing their correlations.

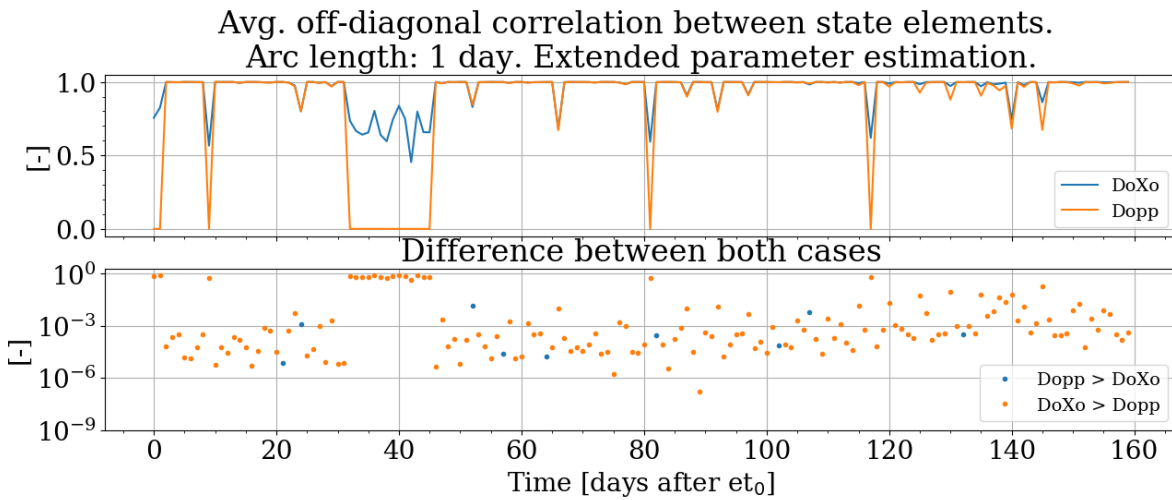


Figure 8.18: Comparison of correlation between state elements. Arc length 1 day, extended parameter estimation.

8.5. Crossover-Only Case

Within this section, the formal errors of JUICE's POD using crossover measurements only are evaluated. Therein, two distinct cases are analysed, with both using the same simulation and estimation settings as the nominal case to allow a consistent comparison to the results of section 8.1. Besides the type of measurements used, the differences to the nominal case are that in the first crossover-only case merely JUICE's state is estimated. Conversely, in the second case JUICE's state, Ganymede's spherical harmonics and Love number k_2 are estimated.

The formal position estimation errors for the first case are shown in Figure 8.19. Surprisingly, the resulting uncertainties are not within the same magnitude range as for the nominal DoXo case during occultation periods, see Figure 8.2 for comparison. Instead, they are noticeably worse. This implies that in the nominal DoXo case, while there are no Doppler measurements for the estimation of JUICE's state during occultations, they do affect their estimation nonetheless presumably through the lower uncertainties for Ganymede's gravity coefficients and Love number k_2 . Equal to the nominal estimation cases, using crossovers measurements only results in the lowest estimation uncertainties being in the radial direction

while being worst in along-track direction. This difference in uncertainty is expected due to the dependency of orbital (potential) energy on semi-major axis/radial position, as discussed in [section 8.1](#). As for the nominal case, an a priori information of 1km for JUICE's position elements was used. Using crossover measurement only, the along-track uncertainty is only improved slightly, having an average uncertainty of 873m.

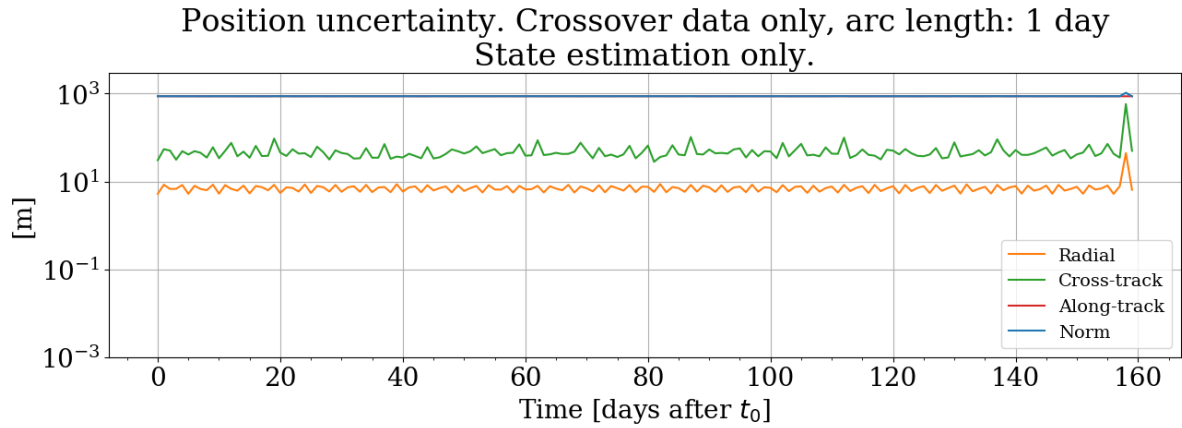


Figure 8.19: Position uncertainty using crossover data only.

As for the nominal cases, the estimation of the along-track velocity is the velocity direction with the lowest estimation uncertainty. Here again, this results from the high dependency of orbital (kinetic) energy on the along-track velocity. The respective velocity estimation uncertainty plot can be found in [Appendix A.11](#).

The position estimation uncertainties for the second crossover-only case are shown in [Figure 8.20](#). As expected and discussed in [section 8.4](#), an increase in the number of estimated parameters leads to an increase in estimation uncertainties. As for the first case shown in [Figure 8.19](#), the position uncertainty in along-track direction is only slightly better than the a priori information having an uncertainty average of 880m.

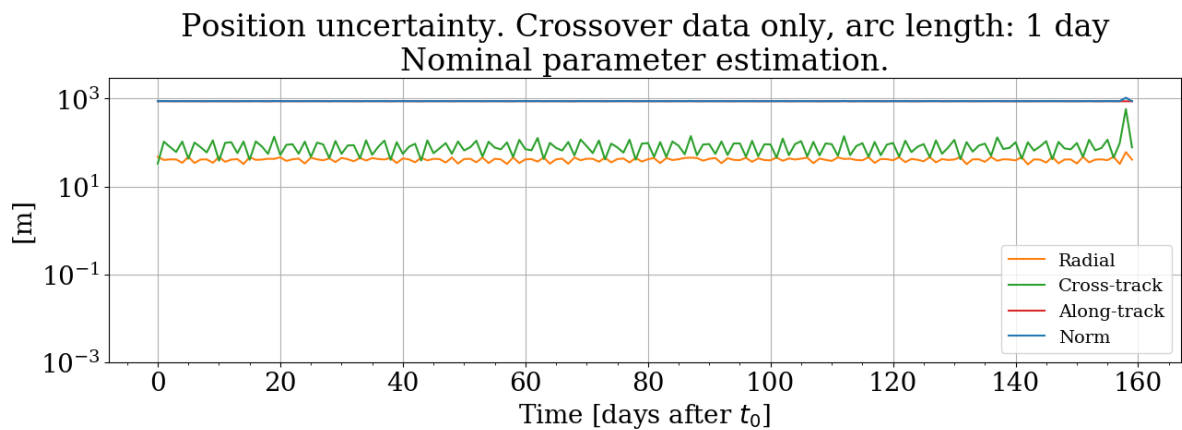


Figure 8.20: Position uncertainty using crossover data only.

While the estimation uncertainty for global parameters is on average 3 orders of magnitude worse than in the nominal cases, [Figure 8.21](#) demonstrates that the estimation of global parameters is nonetheless possible using crossover measurements only.

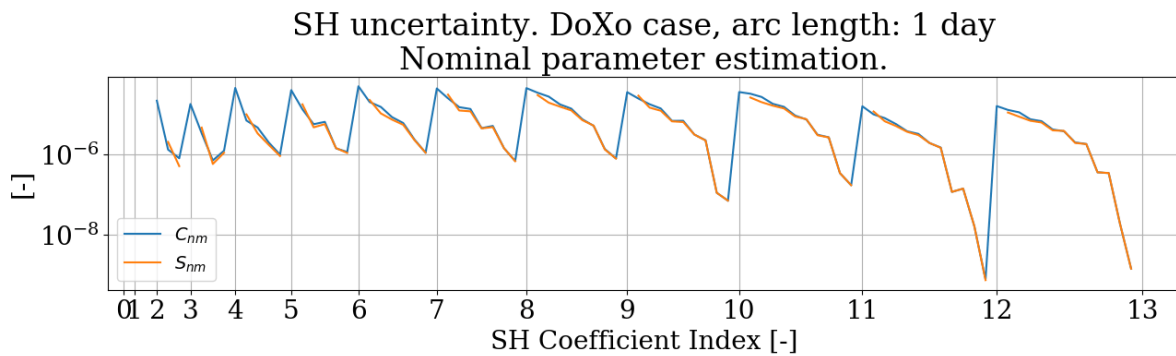


Figure 8.21: Spherical Harmonics (SH) uncertainty using crossover data only, arc length: 1 day.

Regarding the correlations for the case where only JUICE’s state is estimated, [Figure 8.22](#) shows a strong lack in inter-arc correlations. This lack of correlations demonstrates that crossover measurements allow to estimate JUICE’s state at a given arc without affecting the estimation of a different arc. This is particularly noteworthy since crossover measurements are dependent on two arcs by definition. This lack of correlations further emphasises the high quality of the crossover partial derivatives which was discussed in detail in [section 7.4](#).

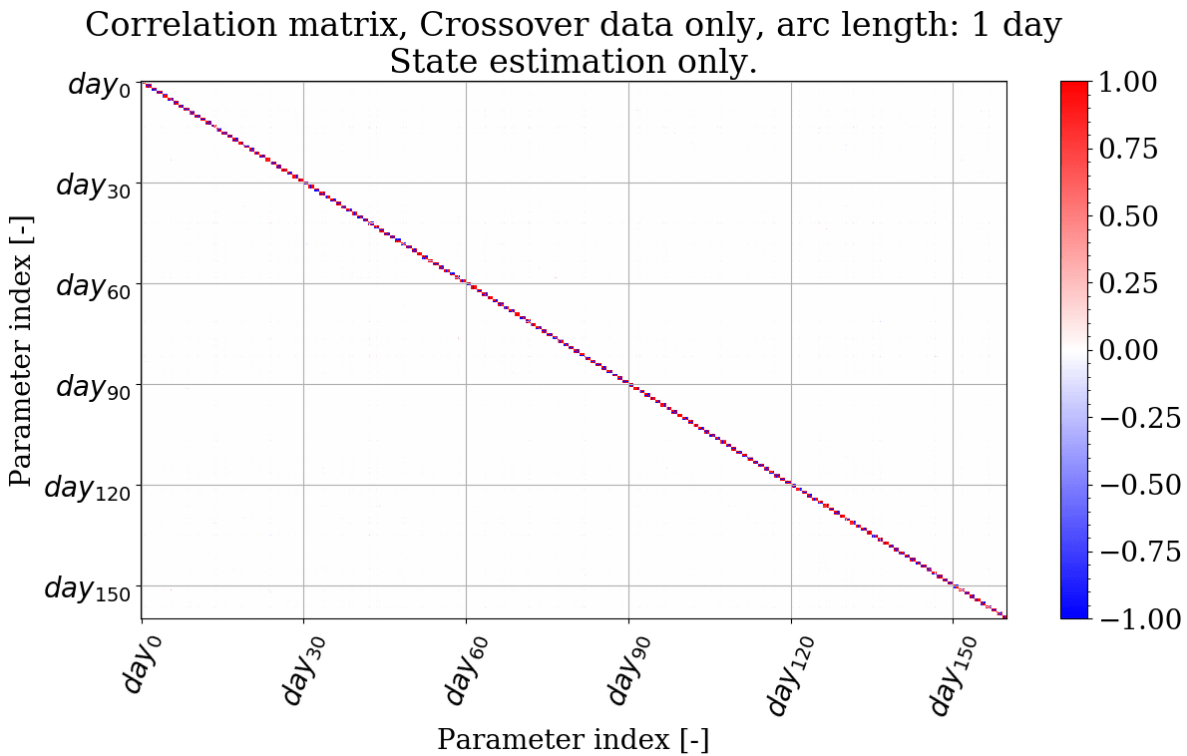


Figure 8.22: Parameter correlation using crossover data only.

The correlation for the nominal Dopp and Doxo cases shown in [Figure 8.7](#) and [Figure 8.8](#), show that the estimation of global parameters introduces correlations between different arcs. This addition of correlations also occurs when using crossover measurements only as shown in [Figure 8.23](#), albeit to a much lower degree than for the Dopp case. Disregarding occultation periods, the average of the absolute correlation values between all JUICE state parameters for the nominal Dopp case is 0.182. Conversely, regarding the same JUICE states the correlation average using crossover measurements only is 0.029. That the JUICE state average correlation

for the Dopp case is on average 6.276 times larger than for the crossover-only case is further emphasised in the much stronger colours in [Figure 8.7](#) in comparison to [Figure 8.22](#).

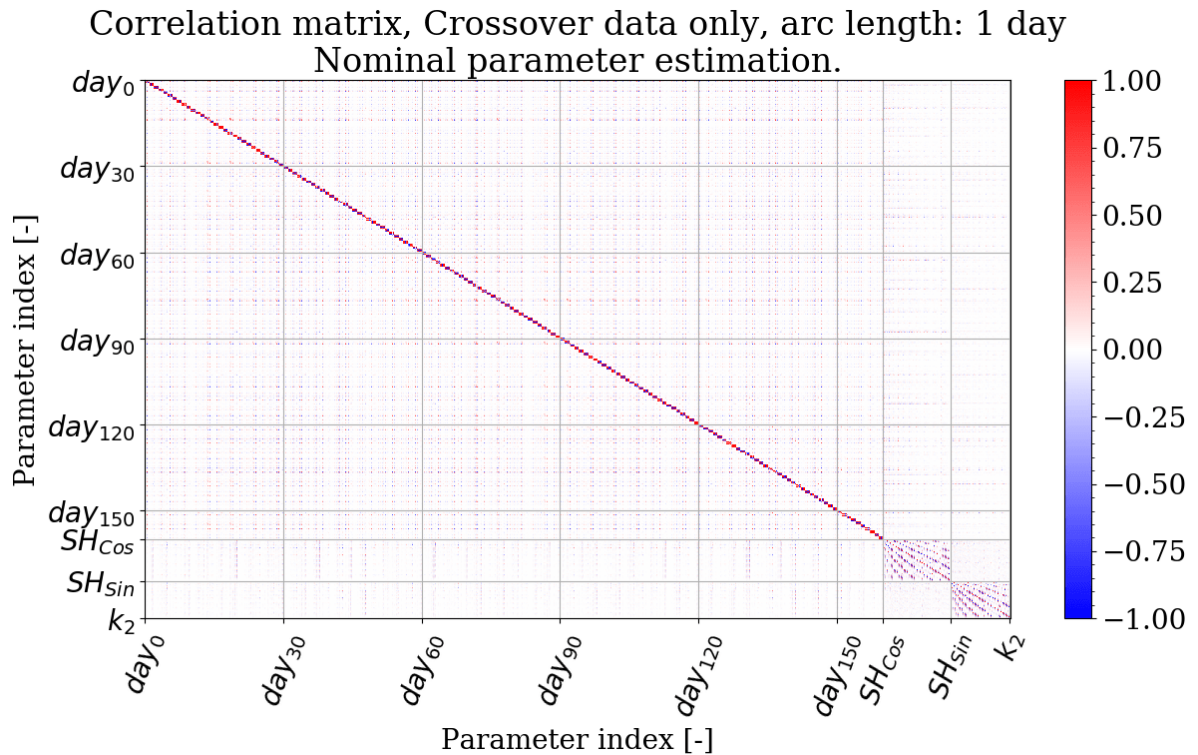


Figure 8.23: Parameter correlation using crossover data only.

Furthermore, the average off-diagonal element correlation between the state elements in each arc is also lower for the crossover-only case than for the Dopp case. Disregarding occultation periods, the Dopp case has an correlation average of 0.991 as shown in [Figure 8.9](#). Conversely, the crossover-only case has an correlation average of 0.933 when estimating the state only and an average of 0.825 for the estimation of JUICE's state and global parameters as shown in [Figure 8.24](#).

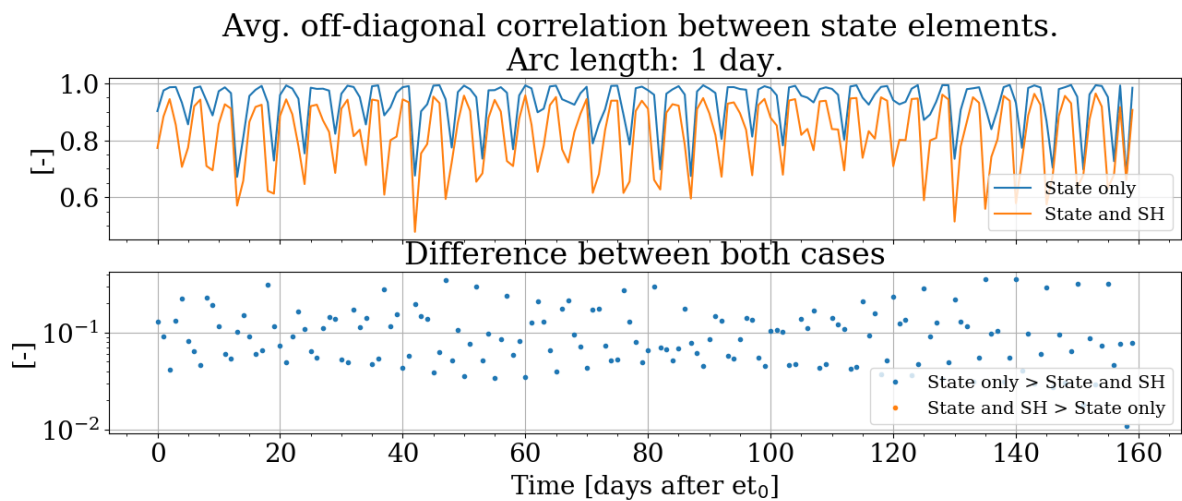


Figure 8.24: Comparison of correlation between state elements using crossover data only. Arc length 1 day.

The analysis of the crossover-only correlations demonstrate that crossovers enable a much more independent estimation of the individual spacecraft state parameters than Doppler measurements. This result was already alluded to in [section 8.1](#), where it was shown that the uncertainty improvement obtained with crossover measurement was largest for the later estimation arcs where the insufficient geometrical constraints of Doppler measurements became more prominent. However, as shown in [Figure 8.19](#) in [Figure 8.20](#) the ability of crossover measurements to constrain JUICE's state is much more limited, in particular in along-track direction. This result is unsurprising due to the much lower measurement uncertainty of Doppler measurements.

8.6. Estimation of Tidal Amplitude

By including the tidal partial derivatives, whose calculation was verified in [section 7.7](#), it is possible to estimate Ganymede's love number h_2 using the modified crossover measurement equation defined in [Equation 5.92](#). While the estimation of h_2 is not yet implemented in Tudat, it is possible to do so nonetheless by adding the tidal partial derivatives as additional column to the design matrix as defined in [Equation 5.94](#). Herein, the design matrix of the nominal DoXo case as defined in [section 8.1](#) is used. As the calculation of h_2 is only dependent on crossover measurements merely two of the presented error cases are treated: Case 1 and Case 3 which reflect the nominal and pessimistic crossover measurement error budgets, respectively. For the estimation of h_2 no a priori covariance is used.

Using the nominal crossover error budget, an h_2 estimation uncertainty of 0.002 was attained. Conversely, using a pessimistic crossover error budget led to a h_2 uncertainty of 0.003. These h_2 uncertainty results represent a more optimistic estimation precision than shown in a previous study where the attained h_2 estimation uncertainty was 0.02 [[Steinbruegge et al., 2015](#)]. This difference in estimation uncertainty is unsurprising as that study's estimation included more measurement uncertainties than treated here. Of those additional uncertainties, the largest difference is their inclusion of uncertainty in the guidance pointing angle which results from JUICE's trajectory uncertainty. That error is not included here, as it is a result of JUICE's orbit determination. As discussed in [section 5.1](#), all the estimation results presented here are too optimistic as many uncertainties are not considered resulting in overly optimistic estimation uncertainties.

Conclusion and Recommendations

9.1. Conclusion

Consistent with previous orbit determination studies which employed crossover measurements, this thesis' work has shown that the inclusion of crossover measurements can improve spacecraft orbit estimation, using the JUICE mission as case study.

Therein, all primary research subquestions as posed in [section 1.1](#) were answered: The mathematical formulation that includes all required dependencies to implement laser altimetry crossovers into an orbit determination procedure was presented in [subsection 5.5.3](#). Therein, it was demonstrated that a simplified, first-order approximation is insufficient for the inclusion of crossovers into orbit determination procedures. Not previously done in literature, a more elaborate formulation was presented, implemented and tested which includes the change in crossover location due to changes in the crossover times t_1 and t_2 [Dirkx, 2019]. Furthermore, conservative error budgets for laser altimetry measurements, pointing and attitude and Doppler measurements were established in [section 5.6](#). The budget for comparable POD estimation errors was established in [section 7.6](#) and it was used to successfully verify this thesis' results. The relevant force model elements to include in the simulation were quantified in [chapter 4](#), wherein a new Ganymede atmosphere model was calculated for the evaluation of atmospheric drag. In [section 6.3](#) apt numerical propagation and integration schemes were chosen to obtain an adequate trade-off between numerical accuracy and computational times. These choices were done in approximation of the nominal mission trajectory as published in JUICE's Consolidated Report on Mission Analysis (CReMA) 3.0. The final choice of the numerical settings, was made to minimise errors in the determination of crossover locations. These errors were quantified and it was demonstrated that high density measurements are required for an accurate and precise determination of crossovers.

Finally, the results of the research subquestions were used to answer this thesis central research question. Therein, it was shown that crossover measurements can significantly improve the estimation uncertainty of local and global parameters. The extent of the attained improvement is dependent on the uncertainty in Doppler measurements and the number of estimated parameters, being more profitable for a larger number of parameters yielding average position improvements of 35.4% in radial, 11.1% in cross-track and 9.7% in along-track direction in the case where the largest number of parameters are estimated. Additionally, crossovers allowed the estimation of JUICE's state for occultation periods wherein spacecraft tracking is unavailable. During these occultations, if no crossovers were used, the lack of conventional tracking measurements led to rank deficiency problems resulting in a highly limited estimation of the spacecraft state.

The orbit estimation results presented here were obtained using synthetic Doppler and crossover measurements, created through numerical simulations. The evaluated orbit estimation scheme uses a multi-arc approach, with the estimated parameters being JUICE's state in addition to several environment model parameters and empirical accelerations. The orbit estimation results presented here do not aim to represent realistic estimation uncertainties as many influencing factors are not included, leading to too optimistic formal errors. Instead, these thesis' results show the potential benefit of including crossover measurements was evaluated by comparison to JUICE's orbit estimation without crossovers. Due to the many model simplifications and assumptions made, a conservative approach was chosen for the calculation of the crossover measurements error budget.

Unfortunately, the inclusion of crossover measurements requires high computational loads which were quantified. These high computational loads originate in the necessary high density measurements for accurate crossover determination. Another factor which heavily impacts computational loads is the exceptionally large number of crossover measurements which leads to large design matrices. This large availability of measurements originates in the number of crossovers growing in an approximately quadratic manner per orbital revolution. Additionally, it was shown that crossover measurements are highly sensitive to trajectory changes at the linearisation point since such changes not only affect the magnitude of the crossover measurements. Instead, they also affect the total number of measurements, an effect not present for any other kind of tracking measurements. Importantly, it was also shown that orbit determination using crossover measurements only is possible. However, The resulting estimation uncertainties are several orders of magnitude worse than using conventional tracking measurements. Nevertheless, the correlation values between estimated parameters were extraordinarily low demonstrating a high ability to estimate parameters independently from one another.

9.2. Recommendations

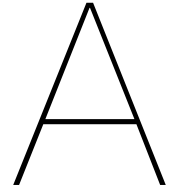
While the necessary framework to include crossover measurements into orbit determination schemes was presented, there are several areas with room for improvement.

Since crossover measurements are highly sensitive to changes in trajectory, it is recommended to implement a scheme that ensures that for iterative approaches the same crossovers are compared to one another. This is necessary since the addition or loss of individual crossover measurements leads to a rearrangement of crossovers for comparison. Potential suggestions therein are crossover tagging/classification systems that do not only rely on the crossover times t_1 and t_2 , as done here, but on the crossover longitude and latitude as well. Alternatively, the crossover's orbit number could also be used to tag the crossover times t_1 and t_2 . Therein, any crossovers that do not have a respective crossover after trajectory changes must be discarded. While setting up such a system, a numerical issue which also merits effort is the loss of crossover times which occur at the same crossover time t_1 . Within this thesis all crossover measurements are ordered, stored and evaluated depending on the key crossover time t_1 . Unfortunately, numerically handling systems such as python's dictionaries or maps within C++ do not allow several copies of the same key to exist. Due to the concentration of crossovers in specific areas, such as polar regions for the trajectory treated here, different crossovers can occur during the same epoch t_1 . Using t_1 as key for crossover handling resulted in the loss of several thousands crossovers. Another numerical issue to tackle is the implementation of multi-core support for the calculation of the design matrix and the use of sparse matrices, resulting in much shorter calculation times. An improvement which would benefit conventional orbit determination schemes as well. Furthermore, it would be insightful to study the dependency of the number of crossovers on changes in orbital elements. Therein,

it is recommended to evaluate the dependency of crossovers on the orbit's inclination if relevant for the mission's scenario. Within the limit case of an orbit with an inclination of zero degrees, every single measurement inevitably becomes a crossover measurement. In regard to the spacecraft inclination, it can also be expected that the number of crossovers has a strong dependency on whether the orbit is prograde or retrograde, in addition to having a strong dependency on the orbital direction and speed of the rotated body.

Another possible area of study is the inclusion of so called consider parameters to obtain a more realistic orbit determination error estimate. The here presented estimation uncertainties are highly optimistic as they do not include uncertainties regarding factors affecting JUICE's motion such as the location of the celestial bodies, Ganymede's pole position, rotational state or gravity field among others. The choice of which parameters to estimate and which to include as consider parameters should coincide with the parameter's influence on the spacecraft orbit and the used tracking measurements. Therein, the uncertainty of orbit driving parameters such as the central body's gravity field should be estimated while perturbing factors, such as the location of celestial bodies, such be included as consider parameters. Additionally, the used measurement type must be considered as it has been shown that Doppler measurements are better suited to estimated the spacecraft orbit, while range measurements are better suited for the estimation of planetary ephemerides.

Lastly, it is recommended to quantify the potential added benefit of crossover measurements for spacecraft attitude estimation. In doing so, the evaluation of off-nadir measurements should also be evaluated. While star tracker based pointing determination already gives insight into the instruments' pointing, off-nadir crossover measurements could aid in independently determining biases and errors in instrument pointing as well as alignment errors between the instrument and the star-trackers. Additionally, it can be expected that off-nadir measurements aid in constraining spacecraft position in its horizontal plane.



Appendix

A.1. Ganymede Gravity Field

| n | m | C | S |
|----|----|------------------------|------------------------|
| 2 | 0 | 5.69×10^{-5} | 0 |
| 2 | 1 | 0 | 0 |
| 2 | 2 | 5.91×10^{-5} | 0 |
| 3 | 0 | 1.74×10^{-5} | 0 |
| 3 | 1 | 1.69×10^{-5} | -4.77×10^{-6} |
| 3 | 2 | -7.82×10^{-6} | -4.97×10^{-6} |
| 3 | 3 | -3.73×10^{-6} | 3.97×10^{-6} |
| 4 | 0 | 3.61×10^{-6} | 0 |
| 4 | 1 | 3.02×10^{-6} | 1.04×10^{-5} |
| 4 | 2 | 4.69×10^{-6} | 3.95×10^{-6} |
| 4 | 3 | 6.70×10^{-6} | -2.49×10^{-6} |
| 4 | 4 | -7.56×10^{-6} | -4.30×10^{-6} |
| 5 | 0 | -4.51×10^{-6} | 0 |
| 5 | 1 | -1.27×10^{-6} | 1.15×10^{-6} |
| 5 | 2 | -2.85×10^{-6} | 5.49×10^{-6} |
| 5 | 3 | -7.46×10^{-6} | 3.33×10^{-6} |
| 5 | 4 | 1.59×10^{-6} | 3.04×10^{-6} |
| 5 | 5 | -1.95×10^{-6} | -2.01×10^{-6} |
| 6 | 0 | 3.13×10^{-6} | 0 |
| 6 | 1 | -4.11×10^{-6} | -1.56×10^{-6} |
| 6 | 2 | 4.01×10^{-6} | 3.64×10^{-6} |
| 6 | 3 | -2.12×10^{-6} | -2.73×10^{-6} |
| 6 | 4 | -2.15×10^{-6} | 1.35×10^{-6} |
| 6 | 5 | -4.43×10^{-7} | -1.90×10^{-6} |
| 6 | 6 | 1.85×10^{-6} | -3.29×10^{-7} |
| 7 | 0 | -1.17×10^{-6} | 0 |
| 7 | 1 | 3.29×10^{-6} | 2.30×10^{-6} |
| 7 | 2 | 7.79×10^{-7} | 9.19×10^{-7} |
| 7 | 3 | -5.73×10^{-7} | -1.23×10^{-6} |
| 7 | 4 | -1.57×10^{-6} | -3.42×10^{-6} |
| 7 | 5 | 2.19×10^{-6} | -4.39×10^{-7} |
| 7 | 6 | -1.99×10^{-6} | -2.40×10^{-6} |
| 7 | 7 | -1.64×10^{-6} | -3.26×10^{-7} |
| 8 | 0 | -1.33×10^{-6} | 0 |
| 8 | 1 | -1.67×10^{-6} | 2.09×10^{-6} |
| 8 | 2 | -5.46×10^{-7} | 1.78×10^{-6} |
| 8 | 3 | 1.79×10^{-6} | 1.07×10^{-6} |
| 8 | 4 | 1.05×10^{-6} | -6.46×10^{-7} |
| 8 | 5 | 3.87×10^{-7} | -7.20×10^{-7} |
| 8 | 6 | -9.49×10^{-7} | 2.67×10^{-6} |
| 8 | 7 | 1.49×10^{-6} | -1.36×10^{-6} |
| 8 | 8 | 1.43×10^{-6} | 1.33×10^{-6} |
| 9 | 0 | -8.40×10^{-7} | 0 |
| 9 | 1 | -4.77×10^{-7} | 1.10×10^{-6} |
| 9 | 2 | -1.06×10^{-6} | -1.70×10^{-6} |
| 9 | 3 | 7.68×10^{-7} | 2.07×10^{-6} |
| 9 | 4 | -1.48×10^{-6} | 4.95×10^{-7} |
| 9 | 5 | -6.81×10^{-7} | 8.14×10^{-7} |
| 9 | 6 | 1.85×10^{-6} | 5.25×10^{-7} |
| 9 | 7 | 7.66×10^{-7} | 7.13×10^{-7} |
| 9 | 8 | -4.61×10^{-7} | -2.13×10^{-7} |
| 9 | 9 | 1.95×10^{-6} | -9.46×10^{-7} |
| 10 | 0 | 5.46×10^{-7} | 0 |
| 10 | 1 | -5.83×10^{-7} | -3.28×10^{-7} |
| 10 | 2 | -1.47×10^{-6} | -7.21×10^{-7} |
| 10 | 3 | -1.35×10^{-6} | 7.54×10^{-7} |
| 10 | 4 | -2.37×10^{-7} | 4.38×10^{-7} |
| 10 | 5 | 7.27×10^{-7} | 1.26×10^{-6} |
| 10 | 6 | 3.60×10^{-7} | 1.61×10^{-6} |
| 10 | 7 | -4.72×10^{-7} | 7.37×10^{-7} |
| 10 | 8 | -4.49×10^{-7} | 4.50×10^{-7} |
| 10 | 9 | 9.27×10^{-7} | -1.57×10^{-6} |
| 10 | 10 | -8.77×10^{-7} | -1.21×10^{-6} |
| 11 | 0 | 3.92×10^{-7} | 0 |
| 11 | 1 | 2.94×10^{-7} | -4.55×10^{-7} |
| 11 | 2 | -9.04×10^{-8} | -7.50×10^{-8} |
| 11 | 3 | -2.75×10^{-7} | 1.26×10^{-7} |
| 11 | 4 | 1.28×10^{-8} | 4.70×10^{-7} |
| 11 | 5 | -1.08×10^{-7} | 5.31×10^{-7} |
| 11 | 6 | 3.23×10^{-7} | -2.62×10^{-8} |
| 11 | 7 | -2.24×10^{-7} | 4.16×10^{-7} |
| 11 | 8 | -2.66×10^{-8} | -2.73×10^{-7} |
| 11 | 9 | 9.49×10^{-8} | 3.47×10^{-7} |
| 11 | 10 | 4.65×10^{-7} | 5.55×10^{-8} |
| 11 | 11 | 5.34×10^{-9} | -5.53×10^{-7} |
| 12 | 0 | -2.09×10^{-7} | 0 |
| 12 | 1 | 2.45×10^{-7} | 2.10×10^{-7} |
| 12 | 2 | 1.13×10^{-7} | -9.68×10^{-8} |
| 12 | 3 | -2.39×10^{-7} | 3.11×10^{-7} |
| 12 | 4 | 3.92×10^{-7} | 1.61×10^{-7} |
| 12 | 5 | 4.62×10^{-7} | -4.77×10^{-7} |
| 12 | 6 | 2.97×10^{-7} | -6.14×10^{-9} |
| 12 | 7 | 3.85×10^{-7} | 3.52×10^{-7} |
| 12 | 8 | -1.82×10^{-7} | -2.45×10^{-7} |
| 12 | 9 | 2.20×10^{-7} | -1.67×10^{-7} |
| 12 | 10 | 3.82×10^{-7} | 3.54×10^{-7} |
| 12 | 11 | 1.76×10^{-7} | -2.96×10^{-7} |
| 12 | 12 | -2.67×10^{-8} | 6.46×10^{-8} |

Figure A.1: Normalized Ganymede gravity field coefficients. n stands for degree, m for order, C for cosine coefficients and S for sine coefficients. Reference radius: 2634.0 km; gm: $9887.83445333 \text{ km}^3 \text{ s}^{-2}$.

A.2. Jupiter Gravity Field

| n | m | C | S |
|---|---|-----------------------|---|
| 2 | 0 | 5.69×10^{-5} | 0 |

Table A.1: Normalized Jupiter gravity field coefficients. n stands for degree, m for order, C for cosine coefficients and S for sine coefficients. Reference radius: 71398 km; gm: $126712767.85779597 \text{ km}^3\text{s}^{-2}$.

A.3. JUICE Instruments

| Instrument | Acronym | Science Contribution |
|--|---------|---|
| Radio Science Experiment | 3GM | Interior state of Ganymede, presence of a deep ocean and other gravity anomalies. Ganymede and Callisto surface properties. Atmospheric science at Jupiter, Ganymede, Europa and Callisto, and Jupiter rings. |
| Laser Altimeter | GALA | Topography and tidal deformation of Ganymede |
| Imaging System | JANUS | Local-scale geologic processes on Ganymede, Europa, and Callisto; Io Torus imaging, Jupiter cloud dynamics & structure Global morphology of the Ganymede surface. Global to regional scale morphology of the Callisto and Europa surface Physical and dynamical properties of minor moons and rings |
| Magnetometer | J-MAG | Ganymede's intrinsic magnetic field and its interaction with the Jovian field. Induced magnetic field as evidence for subsurface ocean on Ganymede, Europa and Callisto. |
| Visible-Infrared Hyperspectral Imaging Spectrometer | MAJIS | Composition of non-water-ice components on Ganymede, Europa and Callisto; State & crystallinity of water ice. On Jupiter: tracking of tropospheric cloud features, characterisation of minor species, aerosol properties, hot spots and aurorae. |
| Particle Package | PEP | Complete plasma composition and distribution in the Jovian magnetosphere. Interaction between Jovian magnetosphere and Ganymede, Europa and Callisto. Energetic Neutral Atom imaging of neutral and plasma tori of Europa and Io, and magnetospheric energetic particle injections. Composition and structure of exospheres and ionospheres of the moons, and response to plasma precipitation. |
| Ice Penetrating Radar | RIME | Structure of the Ganymede, Europa and Callisto subsurface; identify warm ice water "pockets" and structure within the ice shell; search for ice/water interface. |
| Radio and Plasma Wave Instrument | RPWI | Ganymede: Exosphere and magnetosphere; Callisto & Europa: Induced magnetic field and plasma environment; Jovian magnetosphere and satellite interactions |
| Submillimetre Wave Instrument | SWI | Dynamics of Jupiter's stratosphere; Vertical profiles of wind speed and temperature Composition and structure of exospheres of Ganymede, Europa and Callisto. |
| Ultraviolet Imaging Spectrograph | UVS | Composition, structure & dynamics of the atmospheres of Ganymede, Europa, Callisto and Jupiter and their interactions with the Jovian magnetosphere and plasma tori; search for water vapour plumes/geysers. |

Figure A.2: JUICE Instruments [ESA, 2014].

A.4. Downlink Times

| DownLink (DL) Times | | | | | | | | |
|---------------------|--------------|--------|---------------|---------------|--------------|--------------|-------------|--------------|
| DL start [day] | 2.43 | 3.41 | 4.41 | 5.41 | 6.40 | 7.40 | 8.40 | 10.40 |
| DL end [day] | 2.74 | 3.74 | 4.74 | 5.74 | 6.73 | 7.73 | 8.73 | 10.73 |
| DL start [day] | 11.39 | 12.39 | 13.39 | 14.39 | 15.39 | 16.38 | 17.38 | 18.38 |
| DL end [day] | 11.73 | 12.72 | 13.72 | 14.72 | 15.72 | 16.65 | 17.71 | 18.71 |
| DL start [day] | 19.38 | 20.38 | 21.38 | 22.37 | 23.37 | 24.37 | 25.37 | 26.36 |
| DL end [day] | 19.71 | 20.71 | 21.71 | 22.70 | 23.70 | 24.69 | 25.70 | 26.70 |
| DL start [day] | 27.36 | 28.36 | 29.36 | 30.36 | 31.36 | 46.33 | 47.32 | 48.32 |
| DL end [day] | 27.69 | 28.69 | 29.69 | 30.69 | 31.69 | 46.66 | 47.65 | 48.65 |
| DL start [day] | 49.32 | 50.32 | 51.32 | 52.32 | 53.31 | 54.31 | 55.31 | 56.31 |
| DL end [day] | 49.65 | 50.65 | 51.65 | 52.59 | 53.64 | 54.64 | 55.64 | 56.64 |
| DL start [day] | 57.30 | 58.30 | 59.30 | 60.30 | 61.30 | 62.30 | 63.29 | 64.29 |
| DL end [day] | 57.64 | 58.63 | 59.63 | 60.63 | 61.63 | 62.63 | 63.62 | 64.62 |
| DL start [day] | 65.29 | 66.29 | 67.29 | 68.28 | 69.28 | 70.28 | 71.28 | 72.28 |
| DL end [day] | 65.62 | 66.61 | 67.62 | 68.61 | 69.61 | 70.61 | 71.61 | 72.61 |
| DL start [day] | 73.27 | 74.31 | 75.27 | 76.27 | 77.27 | 78.26 | 79.26 | 80.26 |
| DL end [day] | 73.60 | 74.60 | 75.60 | 76.60 | 77.60 | 78.59 | 79.59 | 80.59 |
| DL start [day] | 82.26 | 83.26 | 84.26 | 85.25 | 86.25 | 87.25 | 88.25 | 89.25 |
| DL end [day] | 82.59 | 83.58 | 84.58 | 85.58 | 86.58 | 87.58 | 88.53 | 89.57 |
| DL start [day] | 90.24 | 91.24 | 92.24 | 93.24 | 94.24 | 95.23 | 96.23 | 97.23 |
| DL end [day] | 90.57 | 91.57 | 92.57 | 93.56 | 94.56 | 95.56 | 96.56 | 97.56 |
| DL start [day] | 98.23 | 99.23 | 100.22 | 101.22 | 102.22 | 103.22 | 104.22 | 105.21 |
| DL end [day] | 98.55 | 99.55 | 100.55 | 101.55 | 102.55 | 103.54 | 104.54 | 105.54 |
| DL start [day] | 106.21 | 107.21 | 108.21 | 109.21 | 110.24 | 111.20 | 112.20 | 113.20 |
| DL end [day] | 106.54 | 107.53 | 108.53 | 109.53 | 110.53 | 111.53 | 112.52 | 113.52 |
| DL start [day] | 114.19 | 115.19 | 116.19 | 118.19 | 119.18 | 120.18 | 121.18 | 122.18 |
| DL end [day] | 114.52 | 115.52 | 116.52 | 118.51 | 119.51 | 120.51 | 121.50 | 122.50 |
| DL start [day] | 123.18 | 124.17 | 125.17 | 126.17 | 127.17 | 128.16 | 129.16 | 130.16 |
| DL end [day] | 123.50 | 124.44 | 125.50 | 126.49 | 127.49 | 128.49 | 129.49 | 130.48 |
| DL start [day] | 131.16 | 132.15 | 133.15 | 134.15 | 135.15 | 136.15 | 137.14 | 138.14 |
| DL end [day] | 131.48 | 132.48 | 133.48 | 134.48 | 135.47 | 136.47 | 137.47 | 138.47 |
| DL start [day] | 139.14 | 140.14 | 141.13 | 142.13 | 143.13 | 144.13 | 145.12 | 146.12 |
| DL end [day] | 139.46 | 140.46 | 141.46 | 142.46 | 143.45 | 144.45 | 145.45 | 146.45 |
| DL start [day] | 147.12 | 148.12 | 149.12 | 150.11 | 151.11 | 152.11 | 153.28 | 154.10 |
| DL end [day] | 147.45 | 148.44 | 149.44 | 150.44 | 151.44 | 152.43 | 153.43 | 154.43 |
| DL start [day] | 155.10 | 156.10 | 157.10 | 158.09 | 159.09 | | | |
| DL end [day] | 155.43 | 156.42 | 157.42 | 158.42 | 159.42 | | | |

Table A.2: List of JUICE's DownLink times. Downlink times around an occultation window are marked **bold**.

A.5. Numerical Partial Derivatives

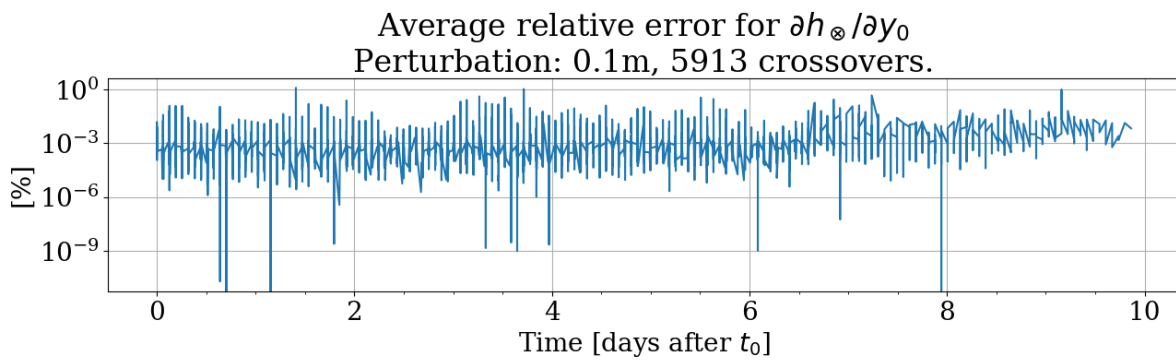


Figure A.3: Numerically obtained partial derivatives for $\partial h_{\otimes} / \partial y_0$.

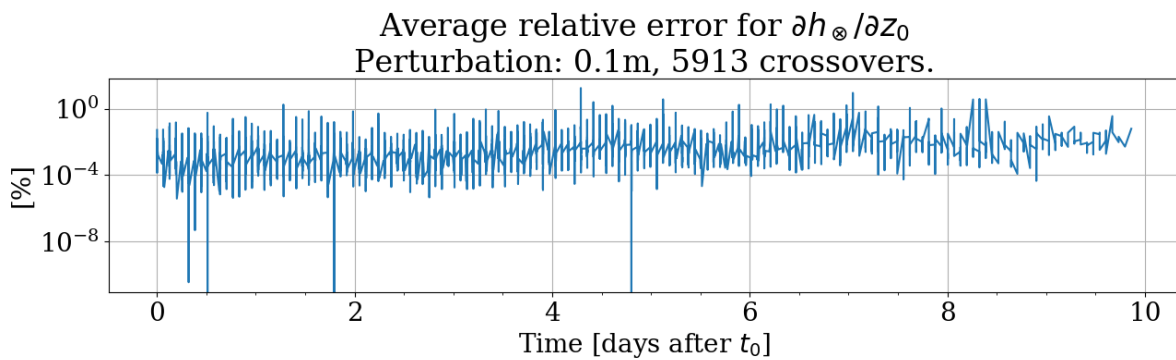


Figure A.4: Numerically obtained partial derivatives for $\partial h_{\otimes} / \partial z_0$.

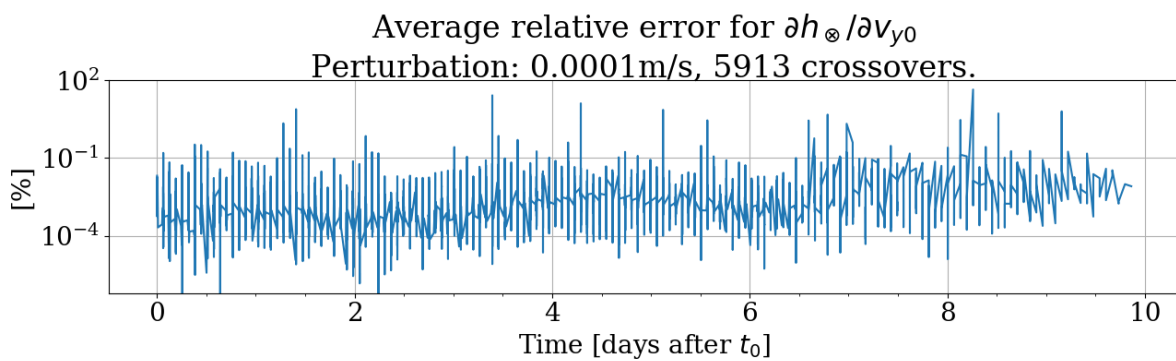


Figure A.5: Numerically obtained partial derivatives for $\partial h_{\otimes} / \partial v_{y0}$.

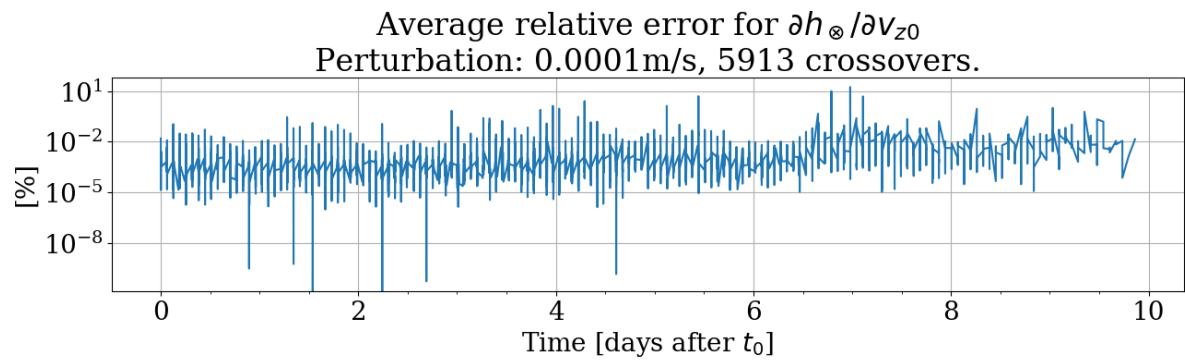


Figure A.6: Numerically obtained partial derivatives for $\partial h_{\otimes} / \partial v_{z0}$.

A.6. Single Arc Verification

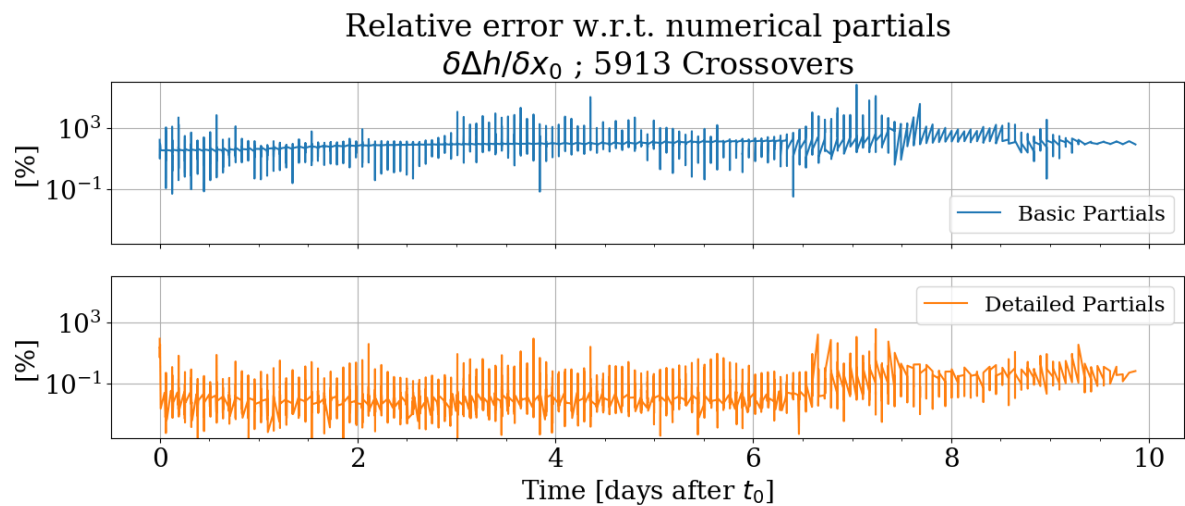


Figure A.7: Comparison of analytical and numerical crossover partials for $\partial h_{\otimes} / \partial x_0$.

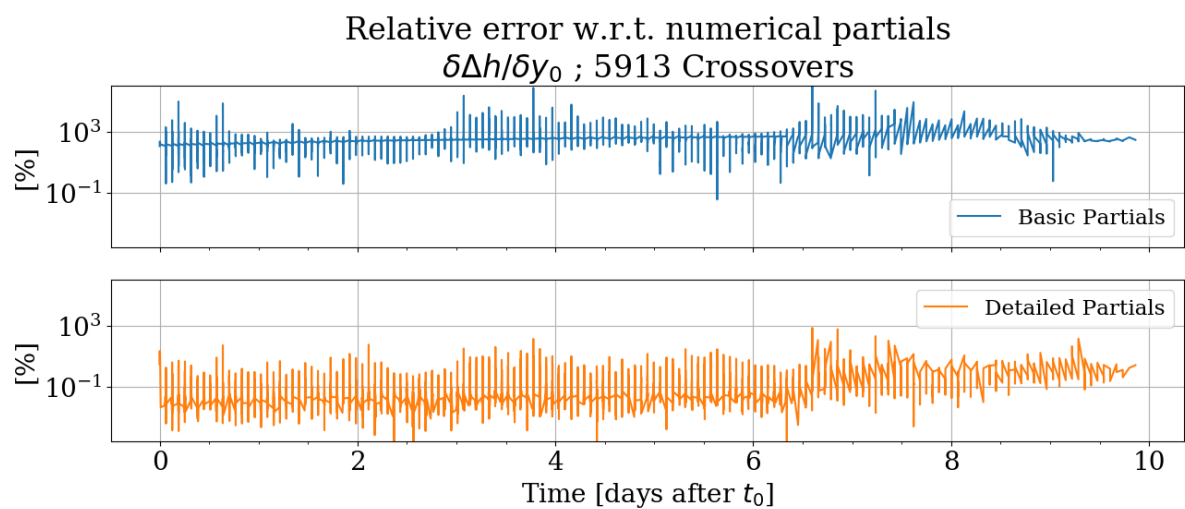


Figure A.8: Comparison of analytical and numerical crossover partials for $\partial h_{\otimes} / \partial y_0$.

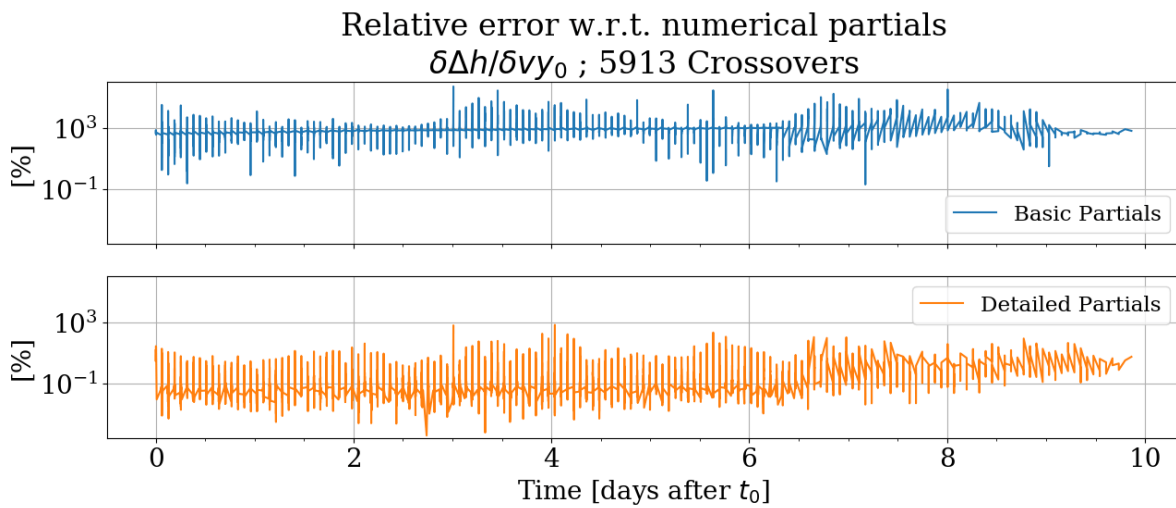


Figure A.9: Comparison of analytical and numerical crossover partials for $\partial h_{\otimes}/\partial v_{y_0}$.

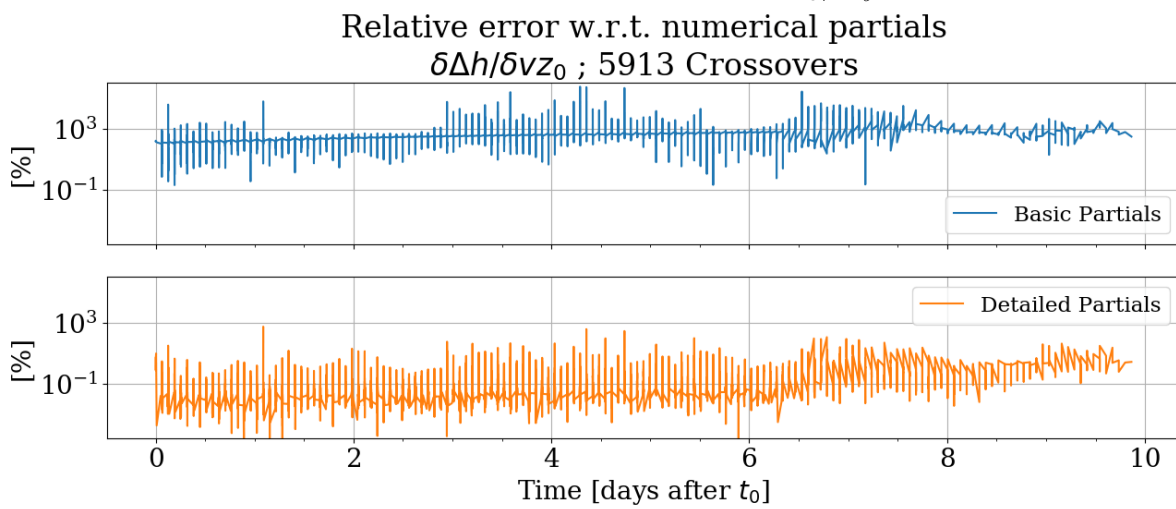


Figure A.10: Comparison of analytical and numerical crossover partials for $\partial h_{\otimes}/\partial v_{z_0}$.

A.7. Multi Arc Verification

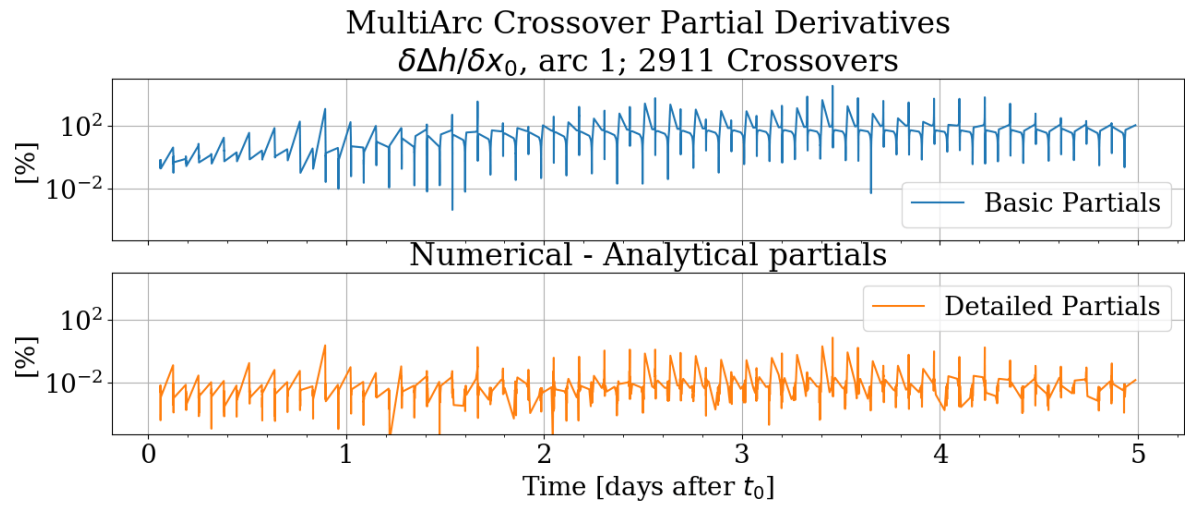


Figure A.11: Comparison of analytical and numerical crossover partials for $\partial h_\infty/\partial x_0$ in arc **1**.

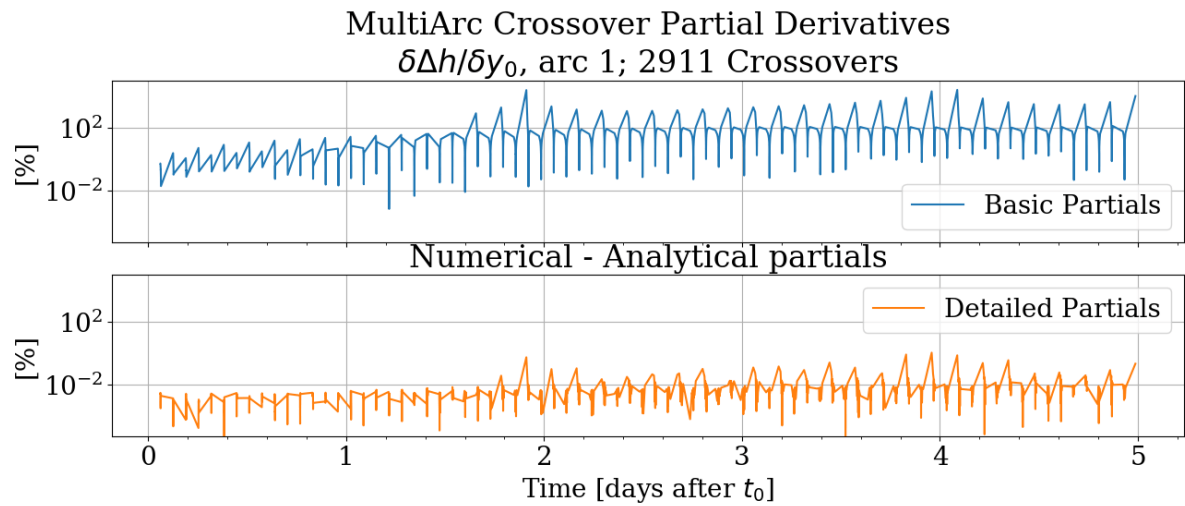


Figure A.12: Comparison of analytical and numerical crossover partials for $\partial h_\infty/\partial y_0$ in arc **1**.

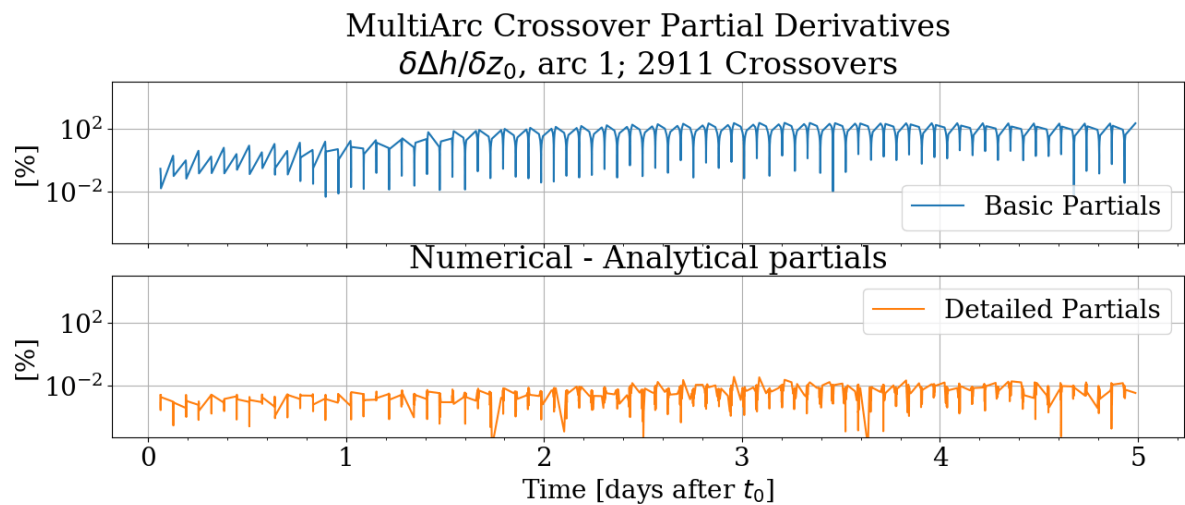


Figure A.13: Comparison of analytical and numerical crossover partials for $\partial h_\infty/\partial z_0$ in arc **1**.

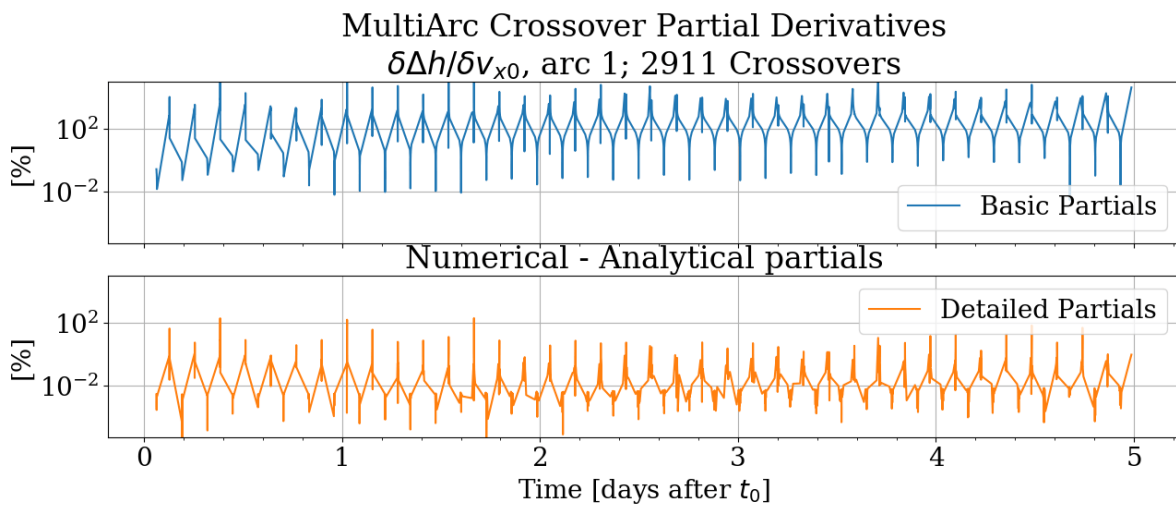


Figure A.14: Comparison of analytical and numerical crossover partials for $\partial h_{\infty}/\partial v_{x_0}$ in arc 1.

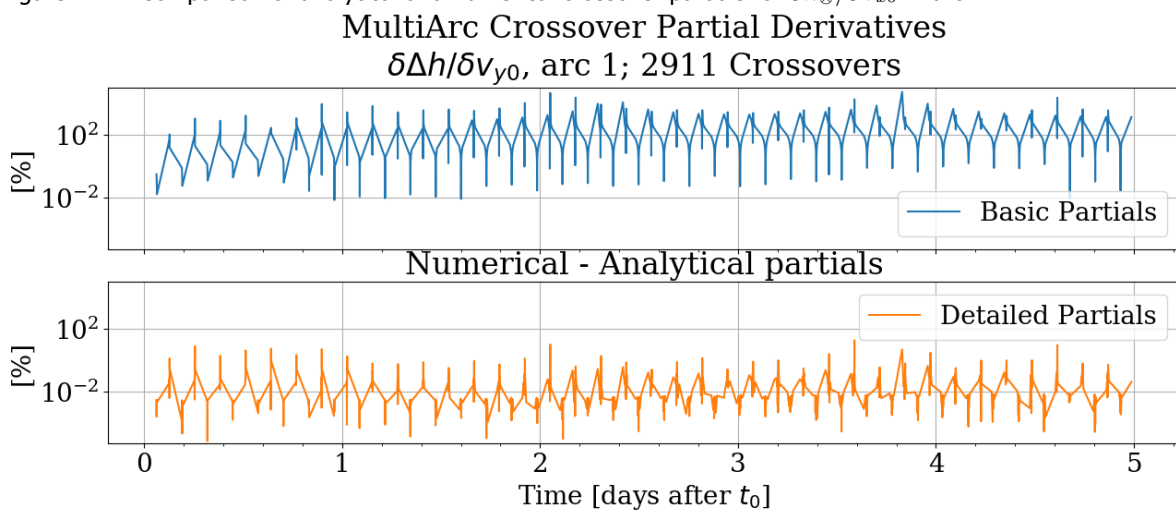


Figure A.15: Comparison of analytical and numerical crossover partials for $\partial h_{\infty}/\partial v_{y_0}$ in arc 1.

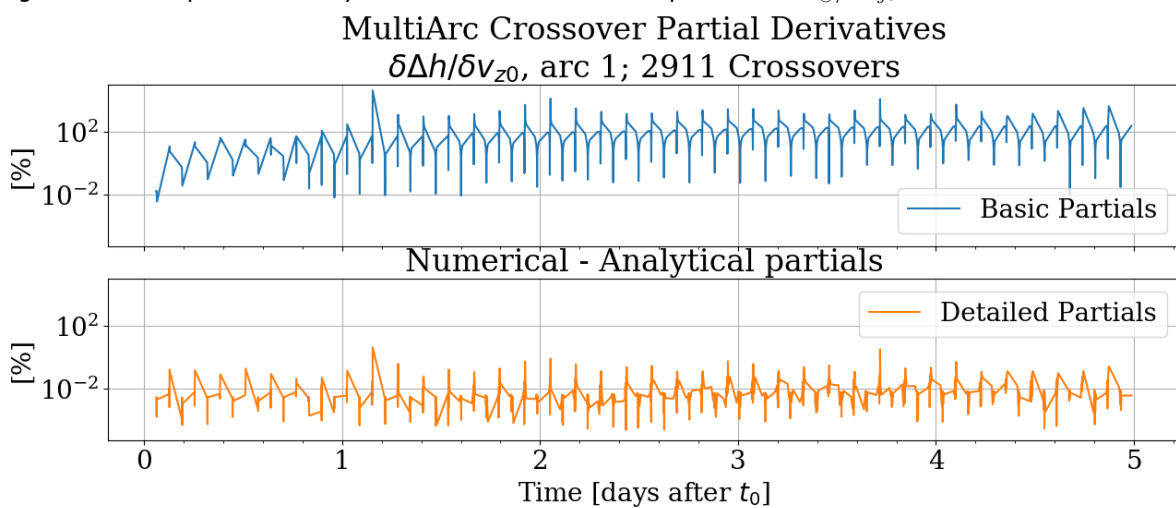
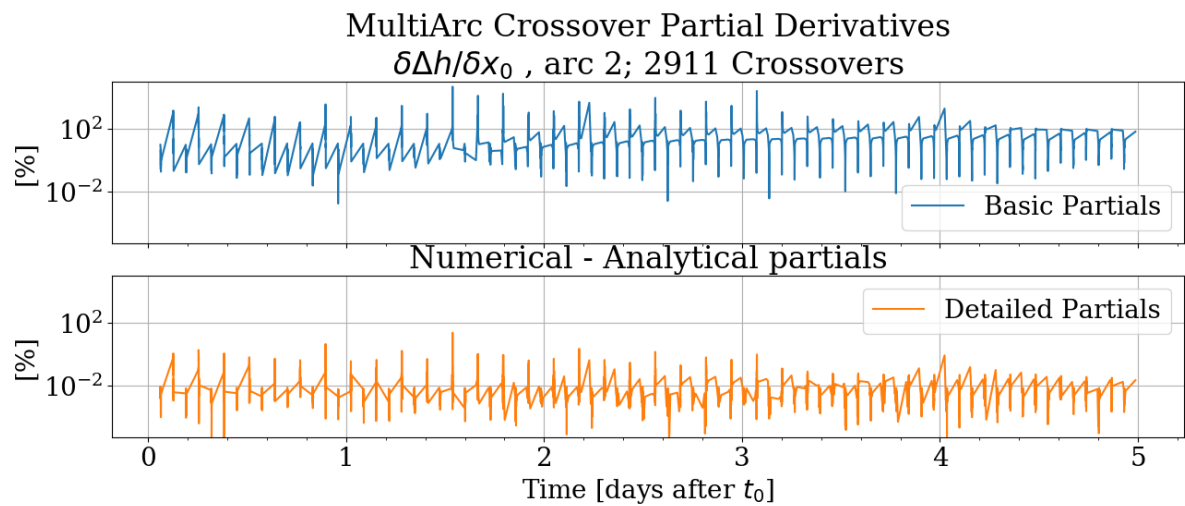
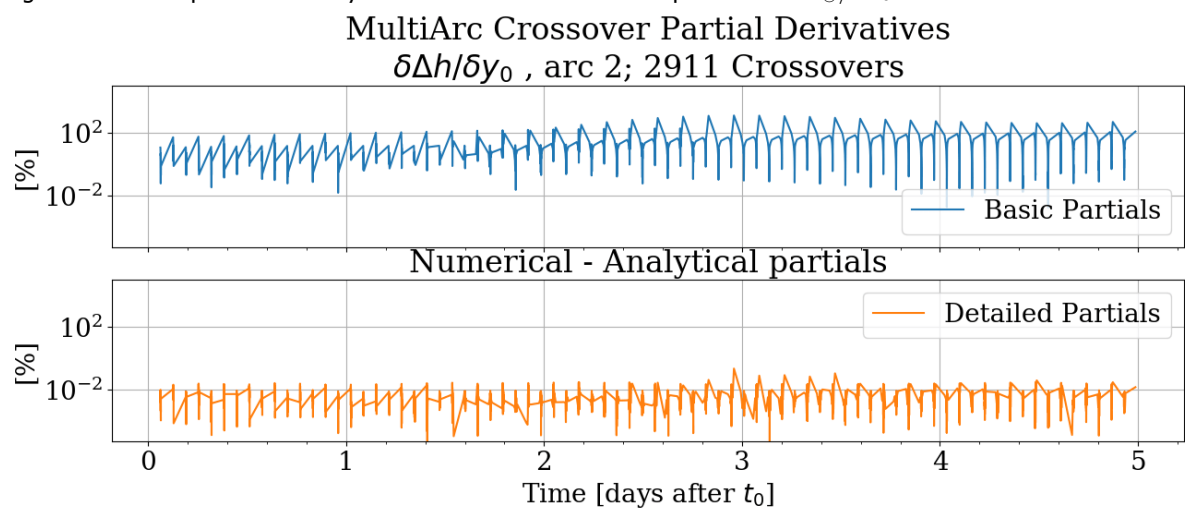
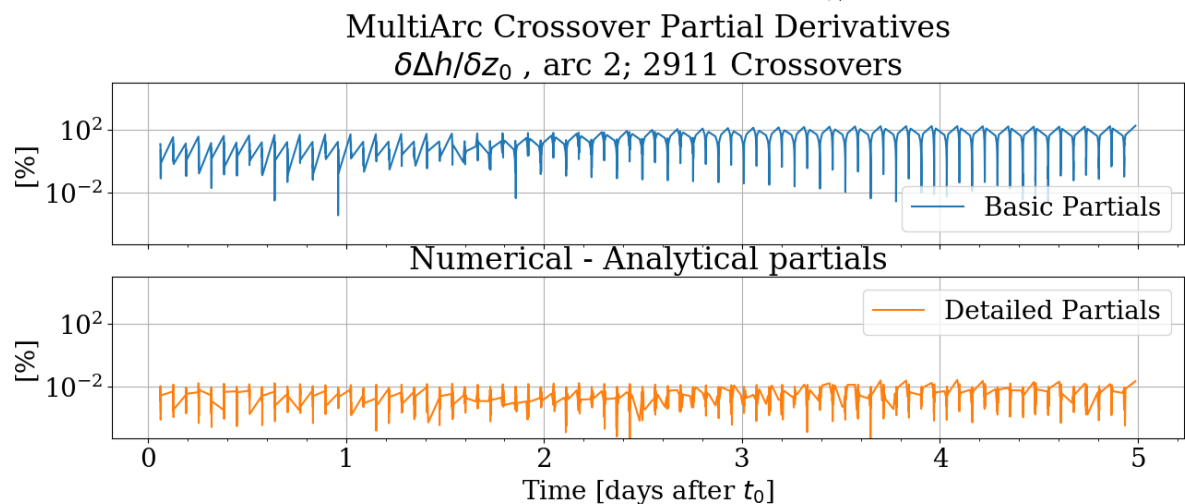


Figure A.16: Comparison of analytical and numerical crossover partials for $\partial h_{\infty}/\partial v_{z_0}$ in arc 1.

Figure A.17: Comparison of analytical and numerical crossover partials for $\partial h_\infty/\partial x_0$ in arc **2**.Figure A.18: Comparison of analytical and numerical crossover partials for $\partial h_\infty/\partial y_0$ in arc **2**.Figure A.19: Comparison of analytical and numerical crossover partials for $\partial h_\infty/\partial z_0$ in arc **2**.

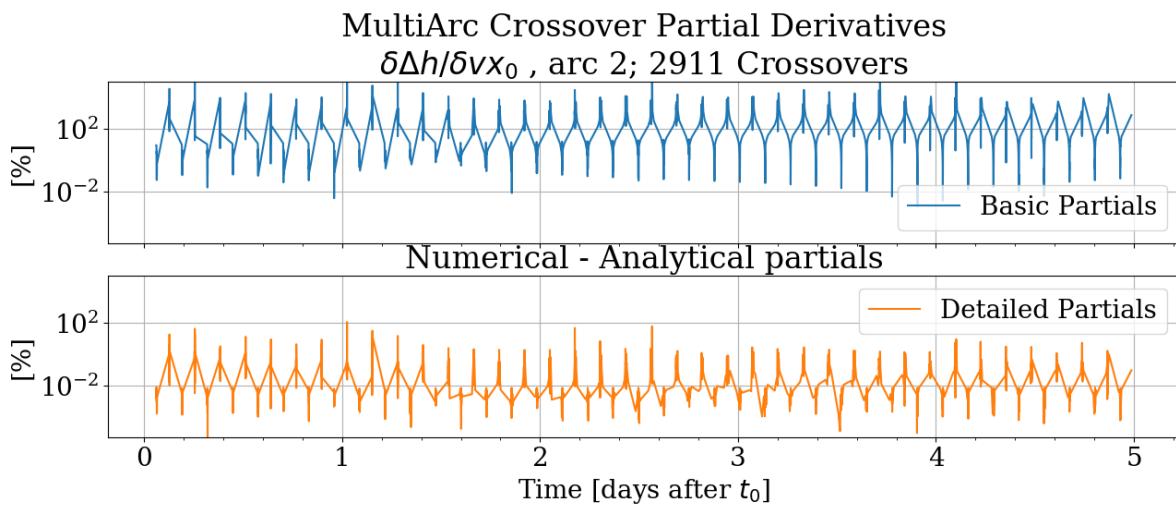


Figure A.20: Comparison of analytical and numerical crossover partials for $\partial h_{\infty}/\partial v_{x_0}$ in arc 2.

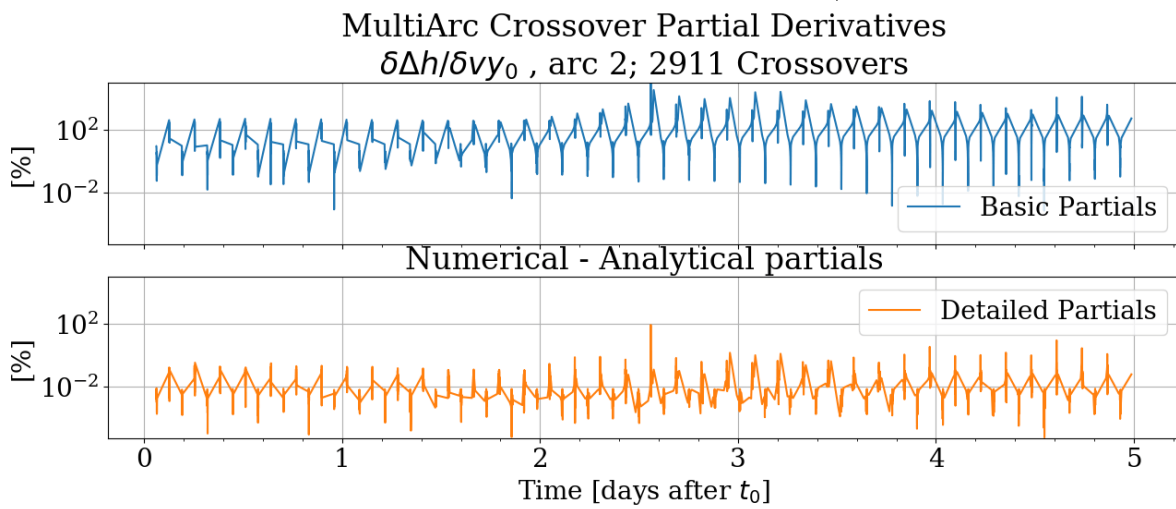


Figure A.21: Comparison of analytical and numerical crossover partials for $\partial h_{\infty}/\partial v_{y_0}$ in arc 2.

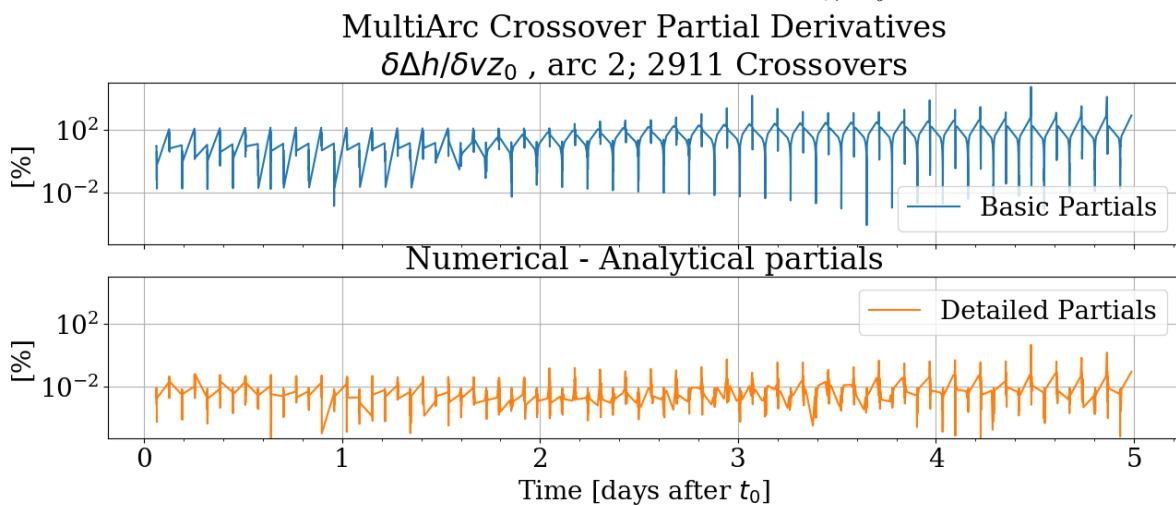


Figure A.22: Comparison of analytical and numerical crossover partials for $\partial h_{\infty}/\partial v_{z_0}$ in arc 2.

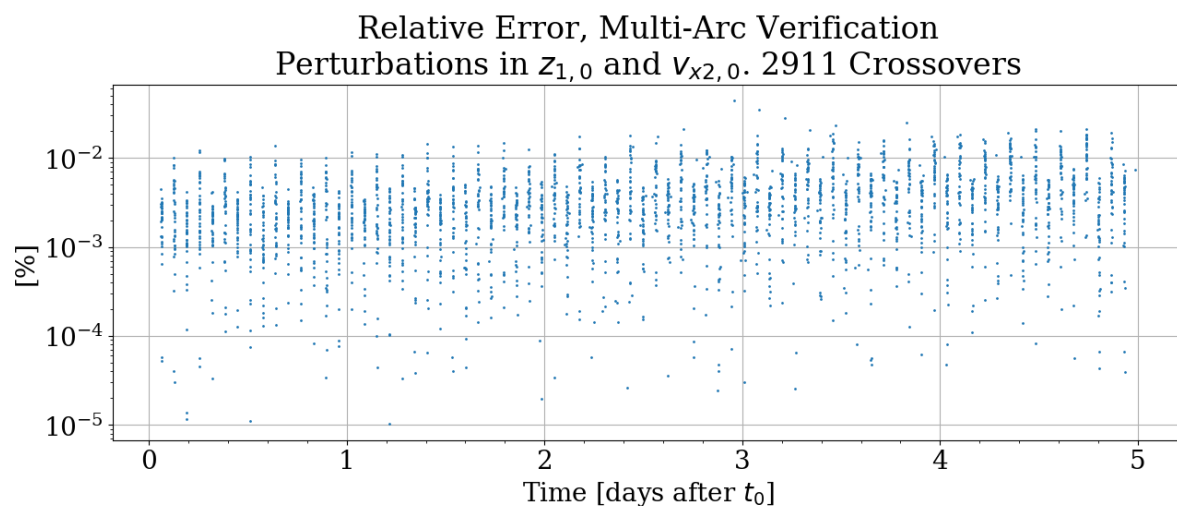


Figure A.23: Relative error for multi arc verification. Within the first arc $z_{1,0}$ is perturbed by +0.1 m. Within the second arc $v_{x2,0}$ is perturbed by +0.0001 m/s.

A.8. Effect of Arc Length

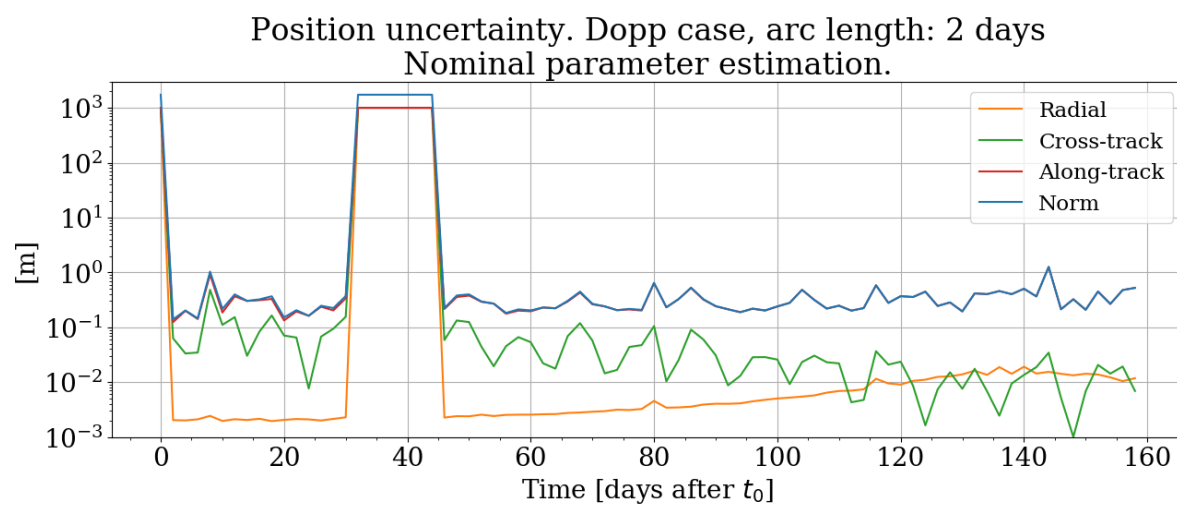


Figure A.24: Position uncertainty using Doppler data only, arc length: 2 days.

Position uncertainty, DoXo case, arc length: 2 days
Nominal parameter estimation.

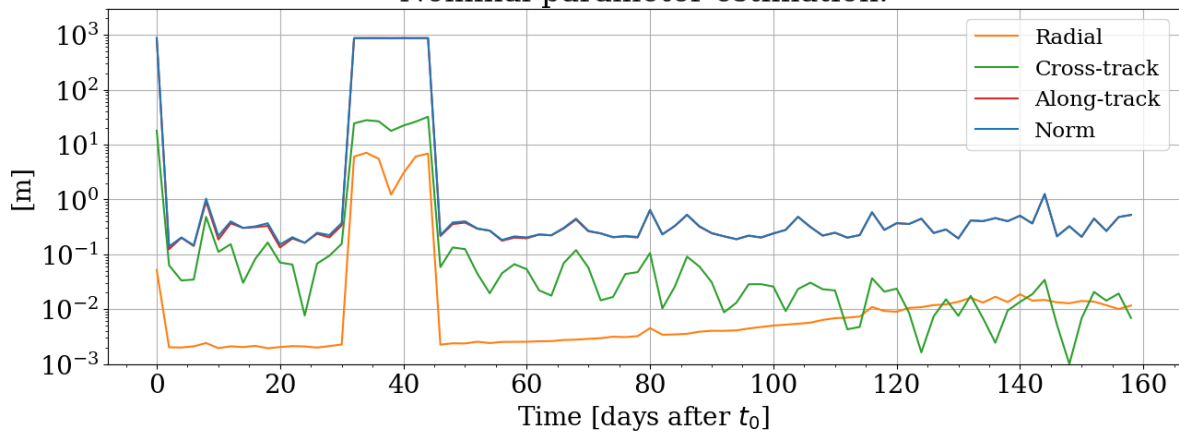


Figure A.25: Position uncertainty using Doppler measurements only, arc length: 2 days.

Position uncertainty. Dopp case, arc length: 3 days
Nominal parameter estimation.

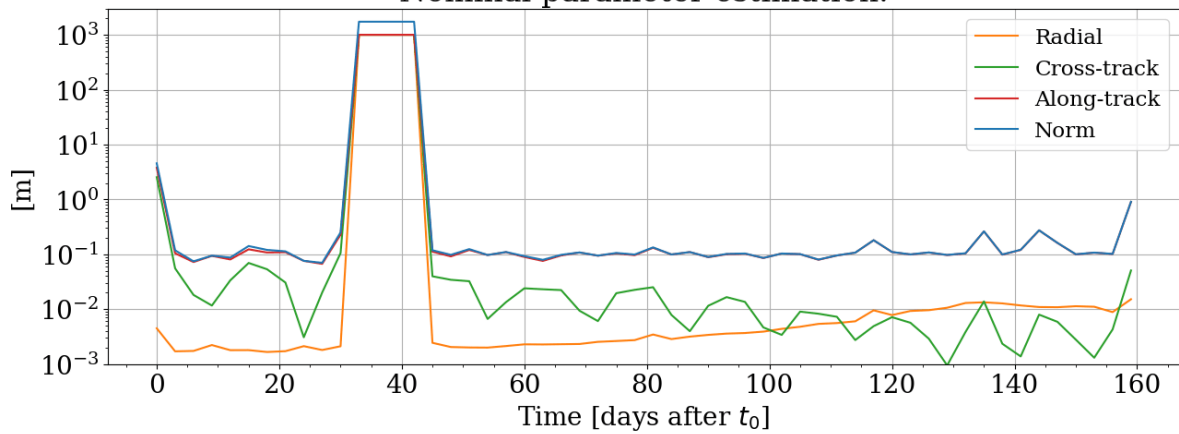


Figure A.26: Position uncertainty using Doppler data only, arc length: 3 days.

Position uncertainty, DoXo case, arc length: 3 days
Nominal parameter estimation.

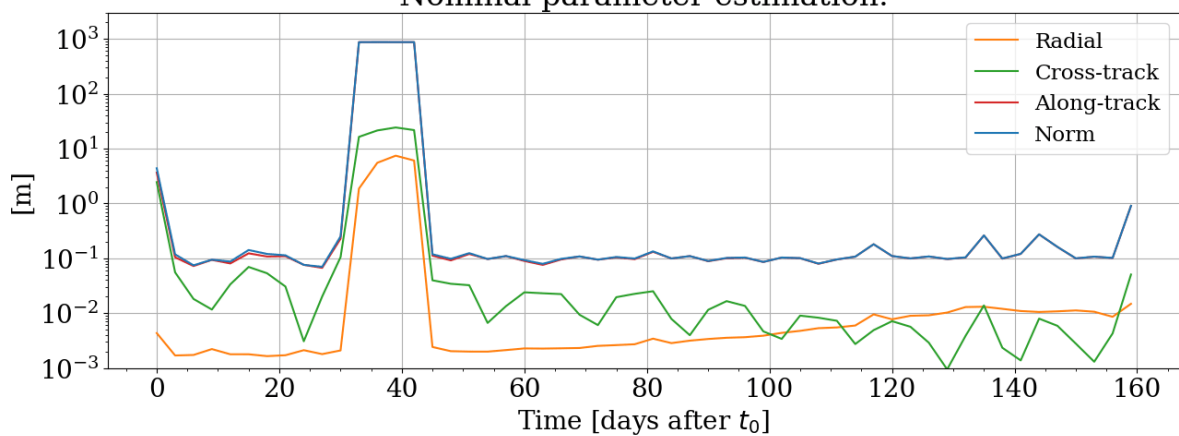


Figure A.27: Position uncertainty using Doppler measurements only, arc length: 3 days.

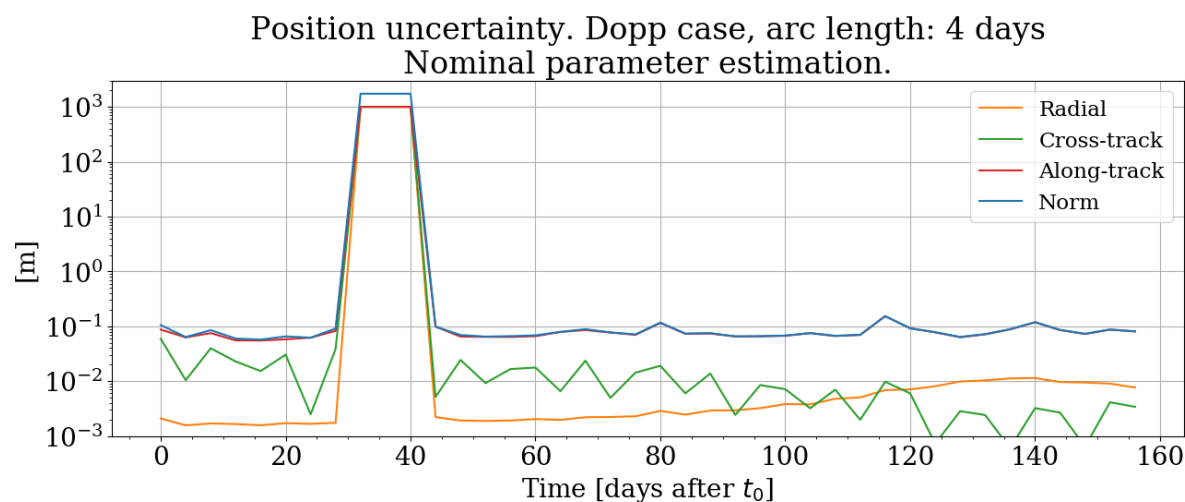


Figure A.28: Position uncertainty using Doppler data only, arc length: 4 days.

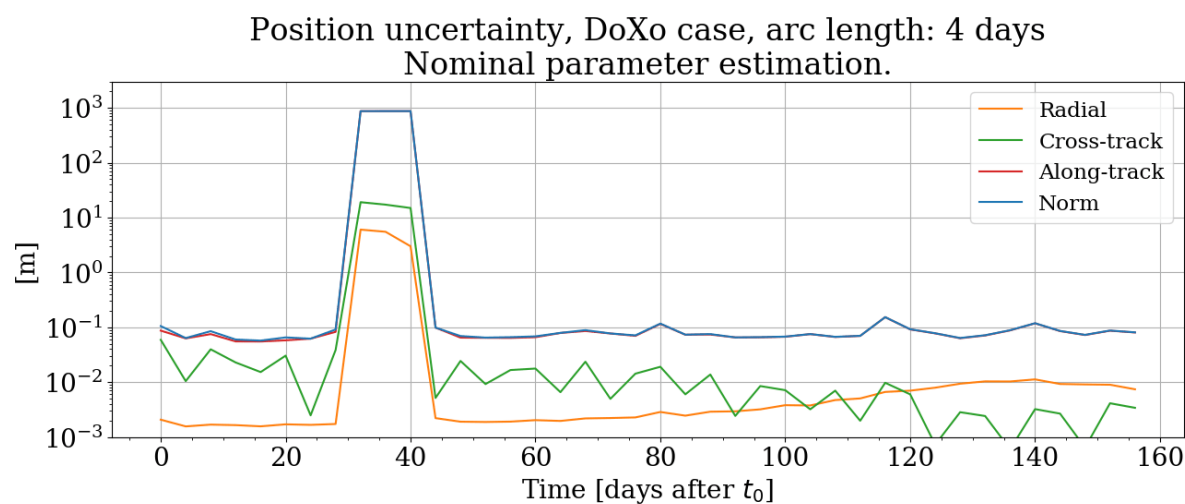


Figure A.29: Position uncertainty using Doppler measurements only, arc length: 4 days.

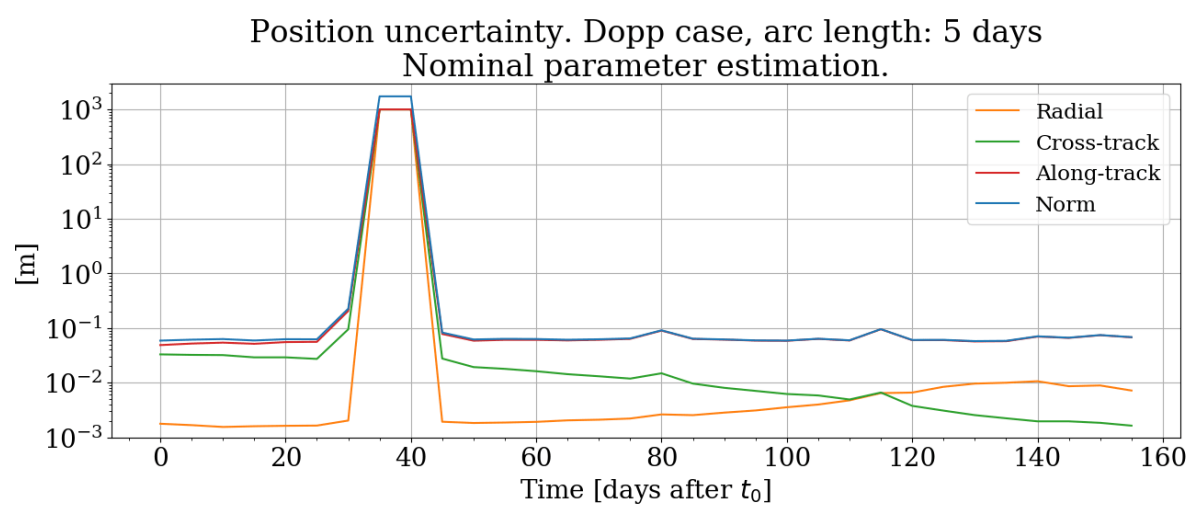


Figure A.30: Position uncertainty using Doppler data only, arc length: 5 days.

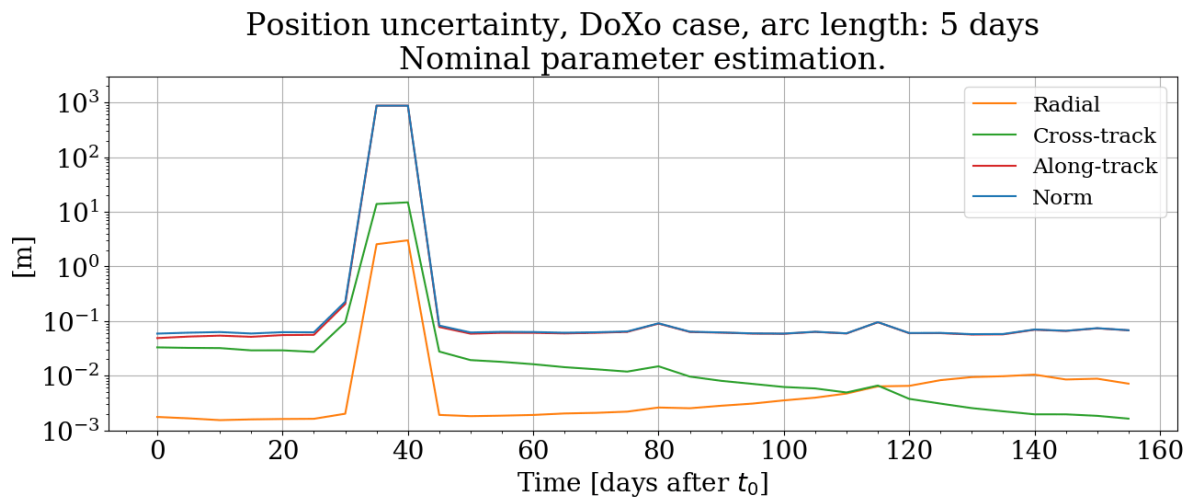


Figure A.31: Position uncertainty using Doppler measurements only, arc length: 5 days.

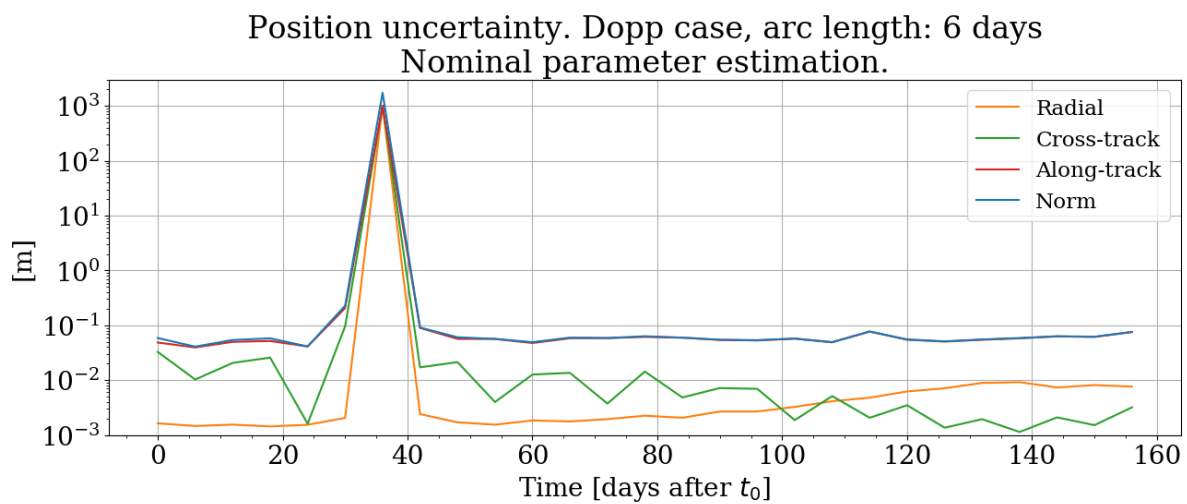


Figure A.32: Position uncertainty using Doppler data only, arc length: 6 days.

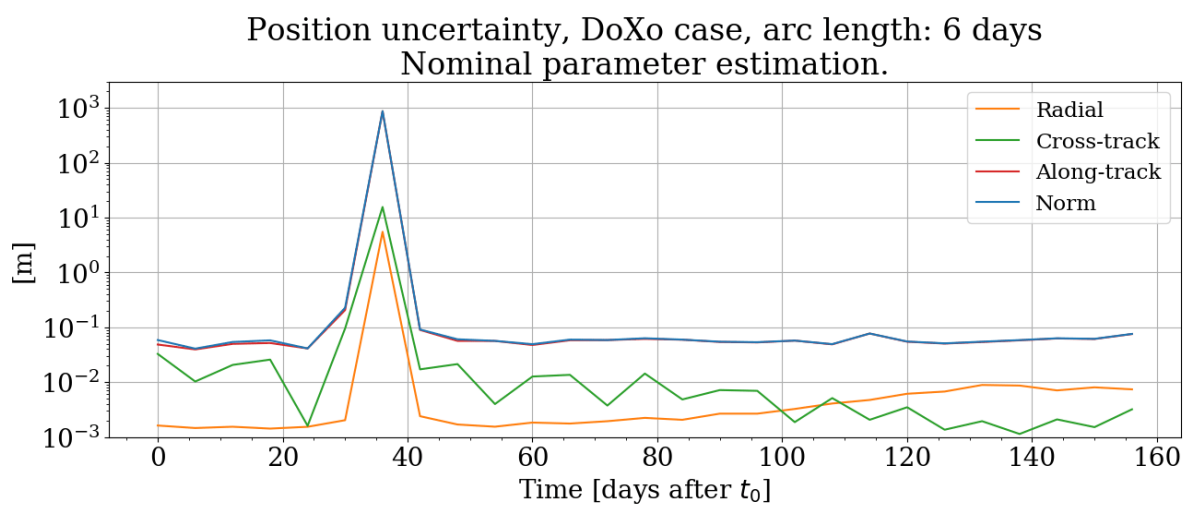


Figure A.33: Position uncertainty using Doppler measurements only, arc length: 6 days.

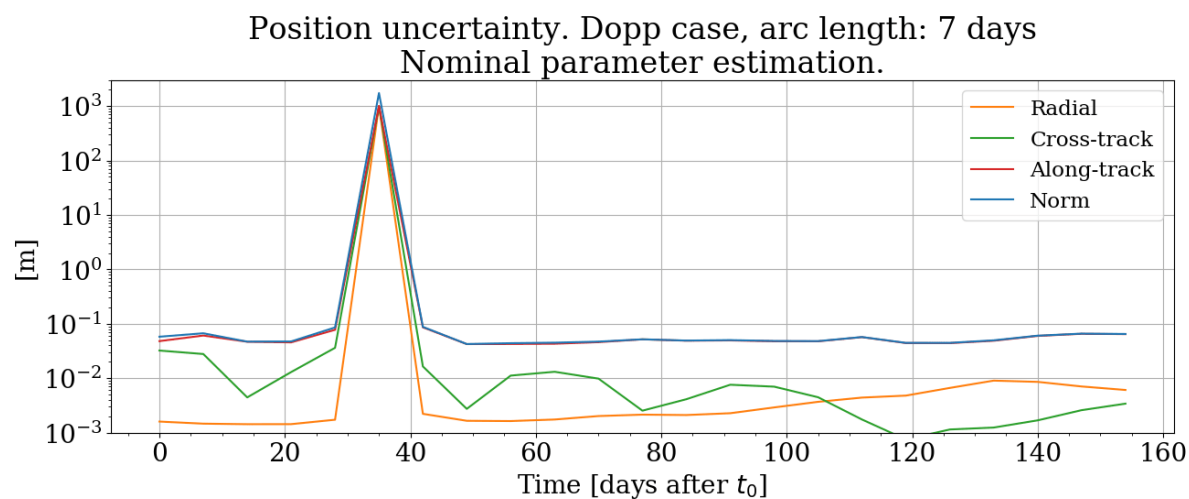


Figure A.34: Position uncertainty using Doppler data only, arc length: 7 days.

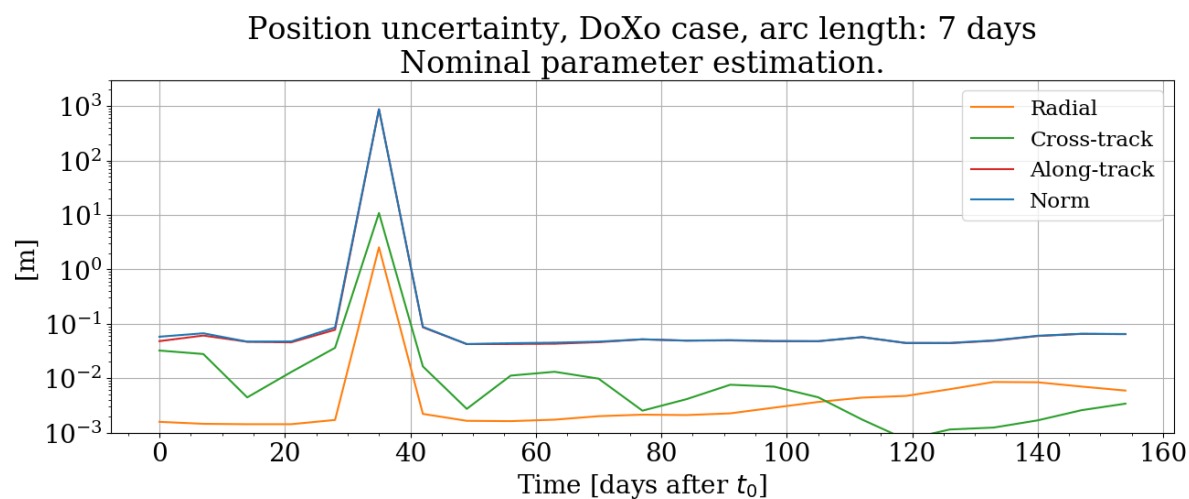


Figure A.35: Position uncertainty using Doppler measurements only, arc length: 7 days.

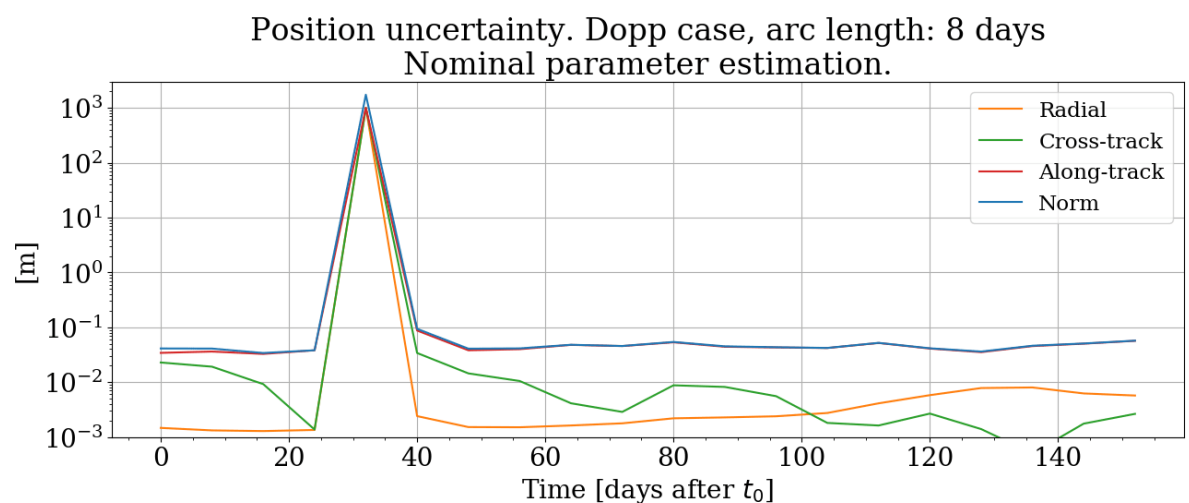


Figure A.36: Position uncertainty using Doppler data only, arc length: 8 days.

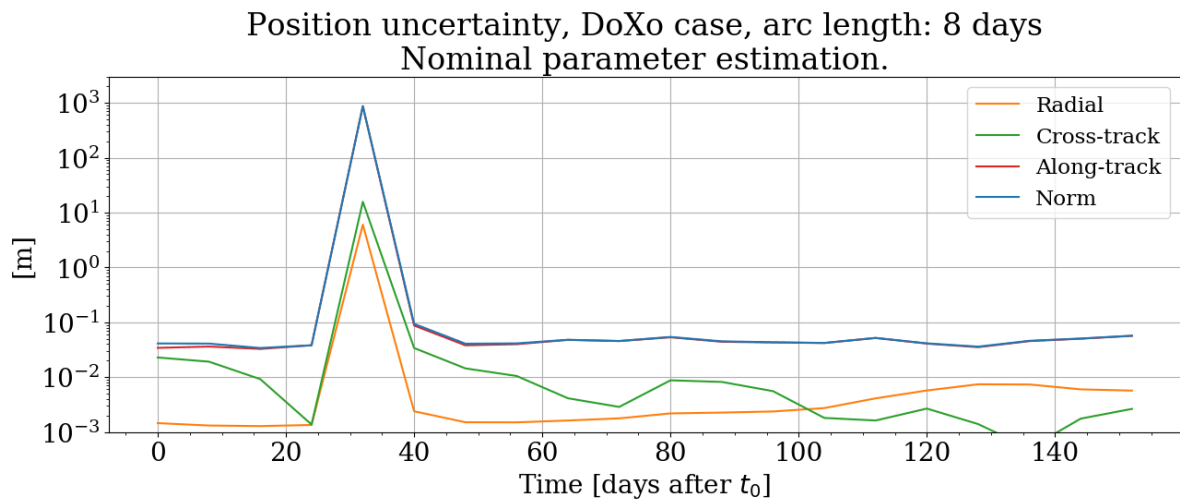


Figure A.37: Position uncertainty using Doppler measurements only, arc length: 8 days.

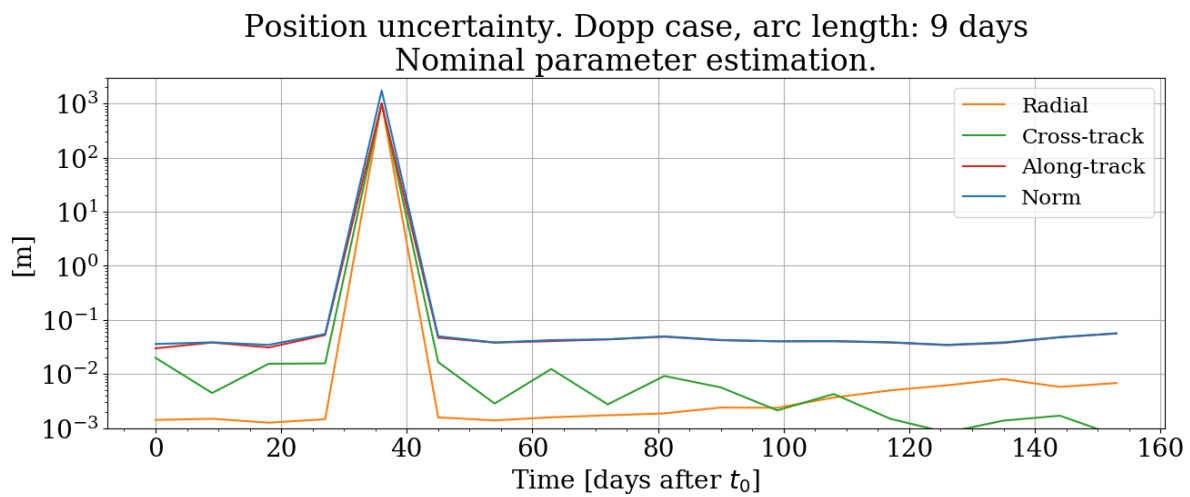


Figure A.38: Position uncertainty using Doppler data only, arc length: 9 days.

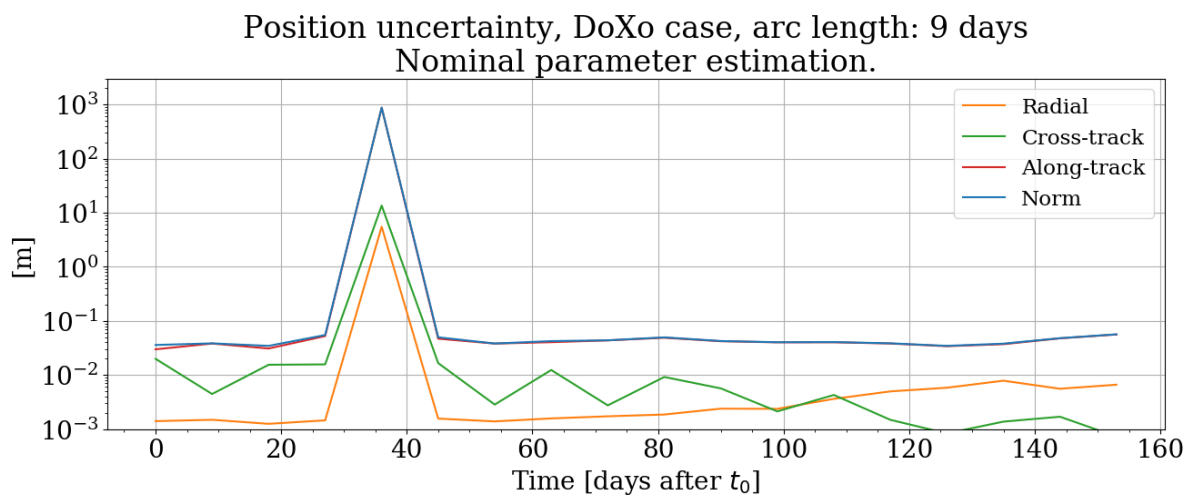


Figure A.39: Position uncertainty using Doppler measurements only, arc length: 9 days.

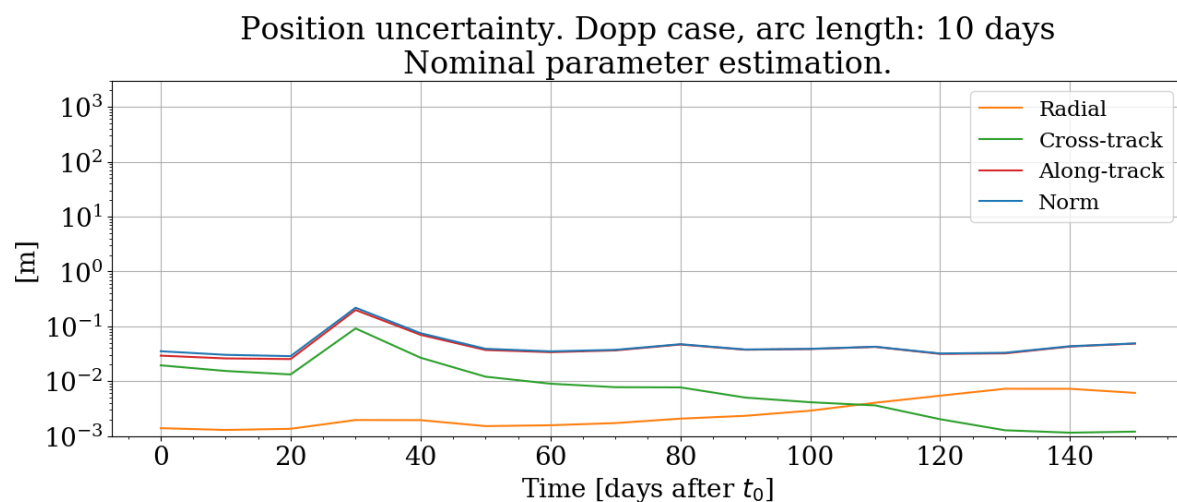


Figure A.40: Position uncertainty using Doppler data only, arc length: 10 days.

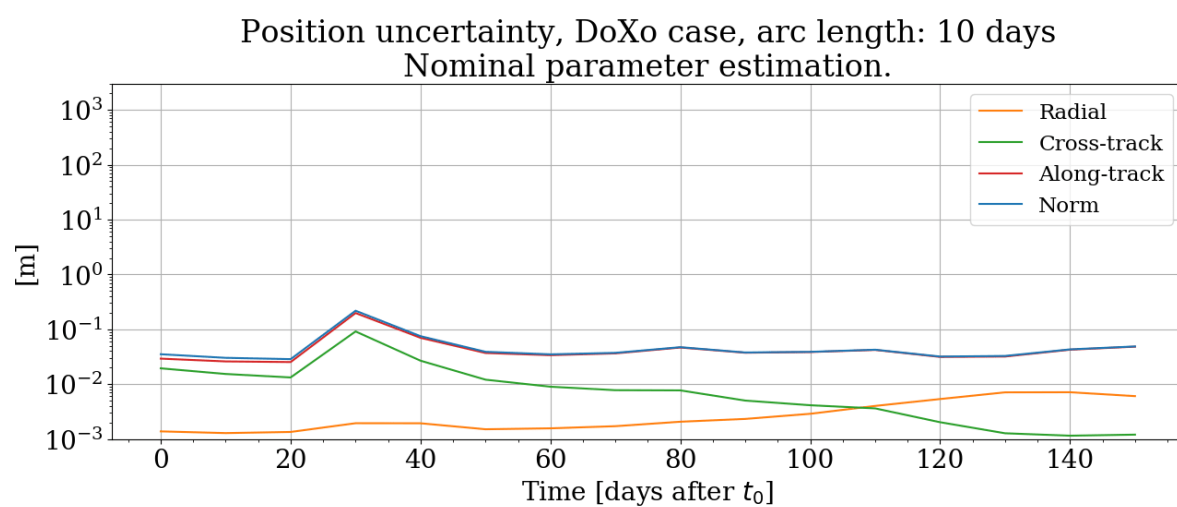


Figure A.41: Position uncertainty using Doppler measurements only, arc length: 10 days.

A.9. Effect of Measurement Errors

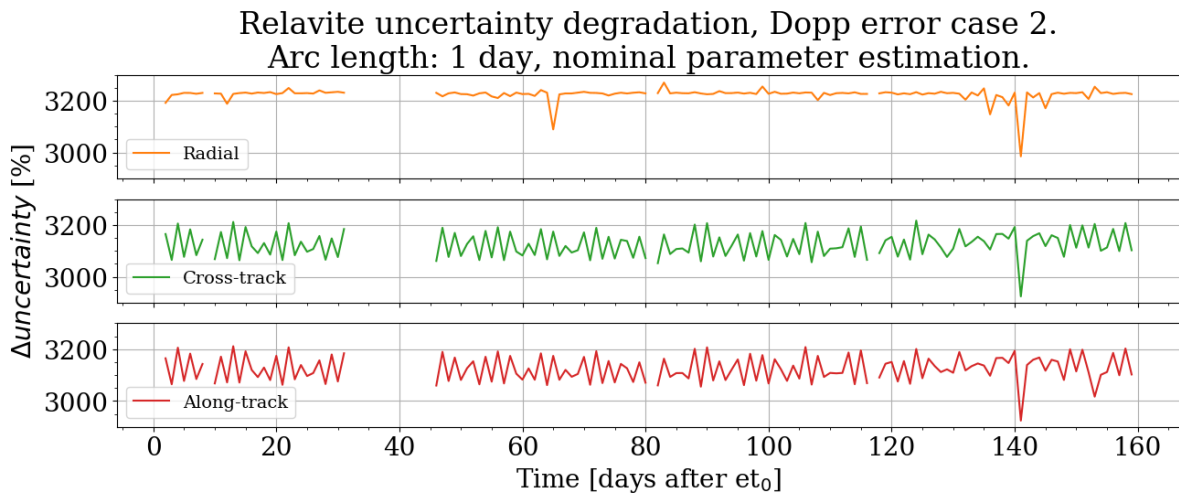


Figure A.42: Position uncertainty degradation, Dopp error case 2.

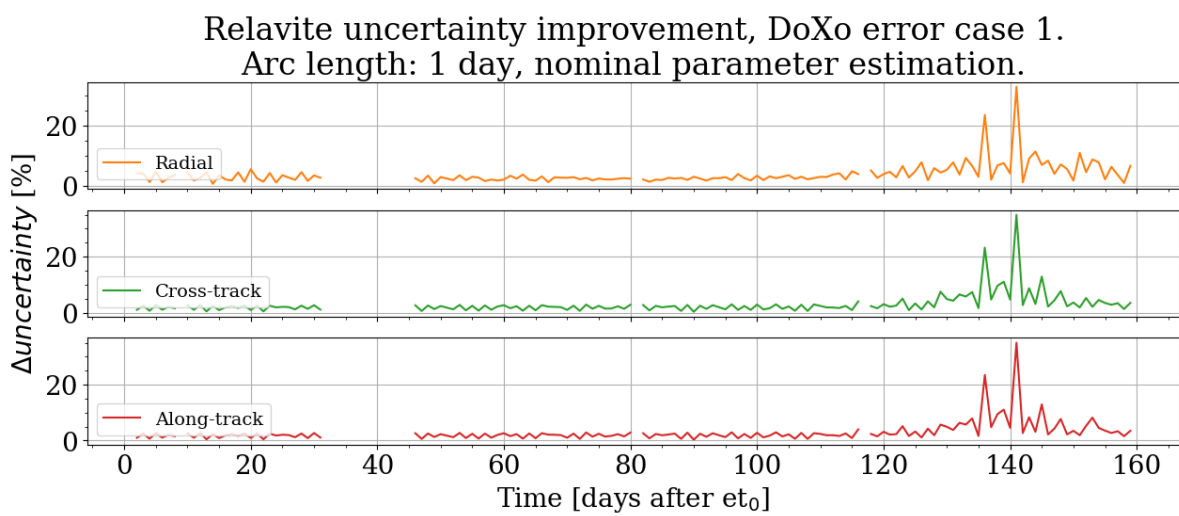


Figure A.43: Position uncertainty improvement using both Doppler and crossover measurements, DoXo error case 1.

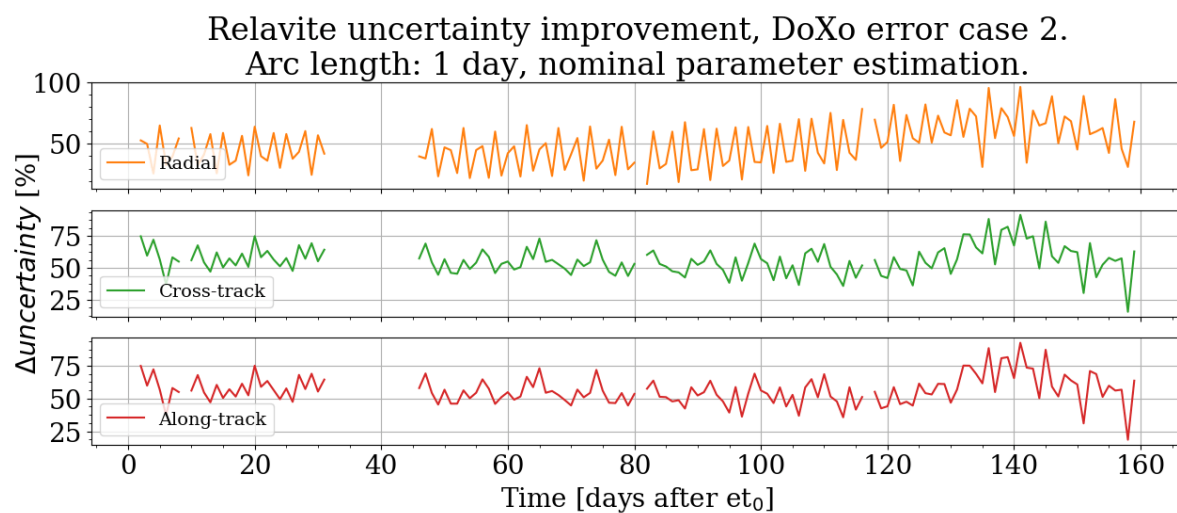


Figure A.44: Position uncertainty improvement using both Doppler and crossover measurements, DoXo error case 2.

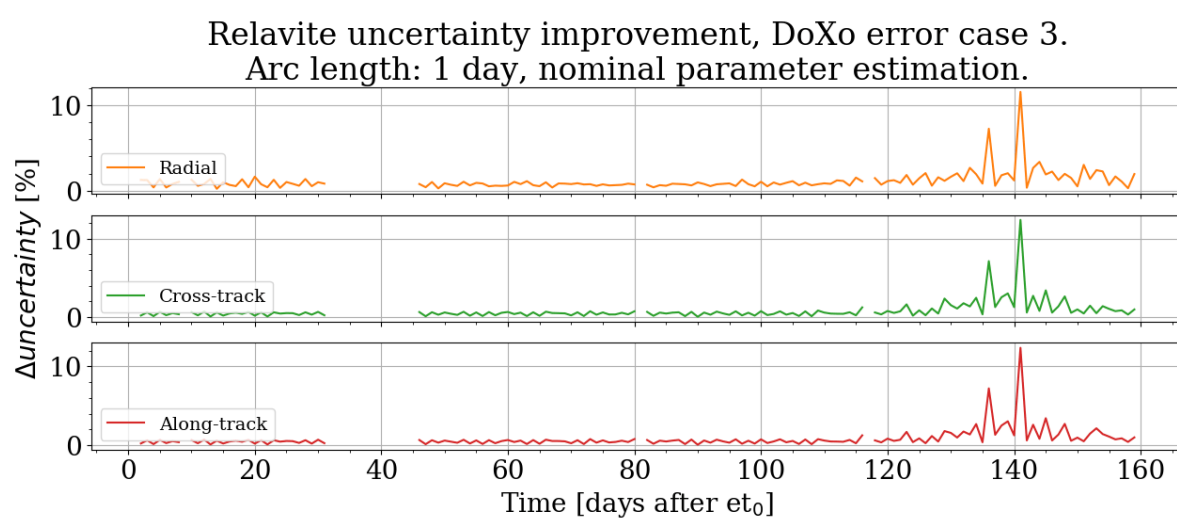


Figure A.45: Position uncertainty improvement using both Doppler and crossover measurements, DoXo error case 3.

Relative uncertainty improvement, DoXo error case 4.
Arc length: 1 day, nominal parameter estimation.

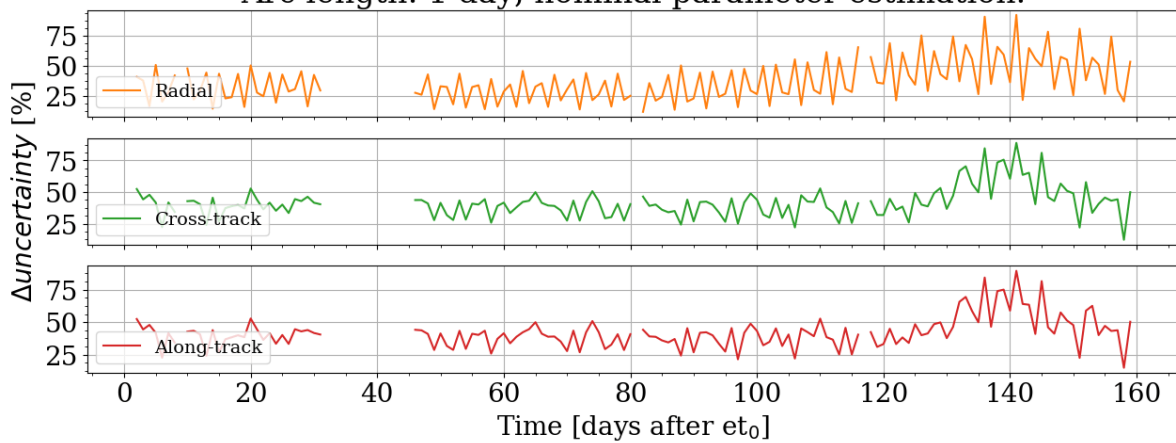


Figure A.46: Position uncertainty improvement using both Doppler and crossover measurements, DoXo error case 4.

Relative SH uncertainty degradation, Dopp error case 2.
Arc length: 1 day, nominal parameter estimation.

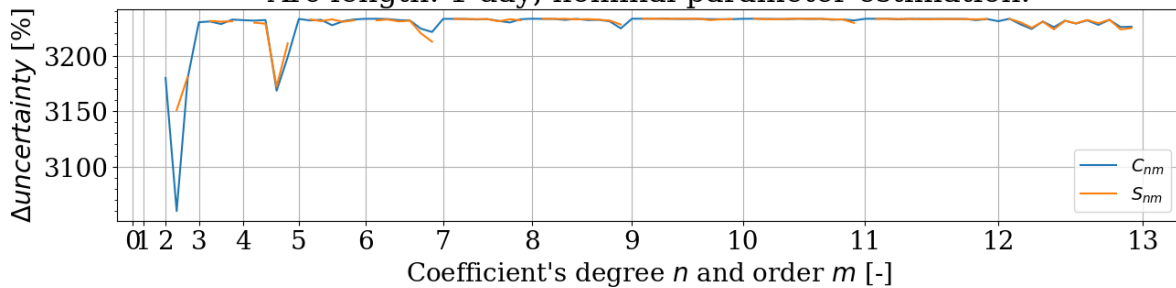


Figure A.47: SH uncertainty degradation, Dopp error case 2.

Relative SH uncertainty improvement, DoXo error case 1.
Arc length: 1 day, nominal parameter estimation.

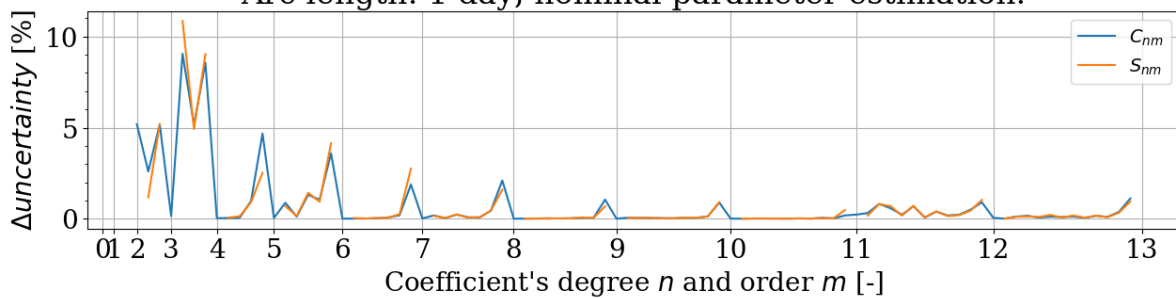


Figure A.48: SH uncertainty improvement using both Doppler and crossover measurements, DoXo error case 1.

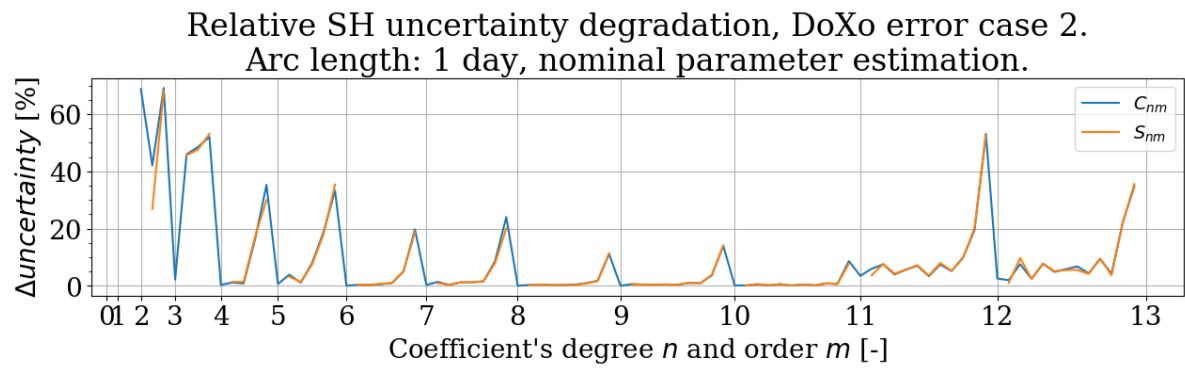


Figure A.49: SH uncertainty improvement using both Doppler and crossover measurements, DoXo error case 2.

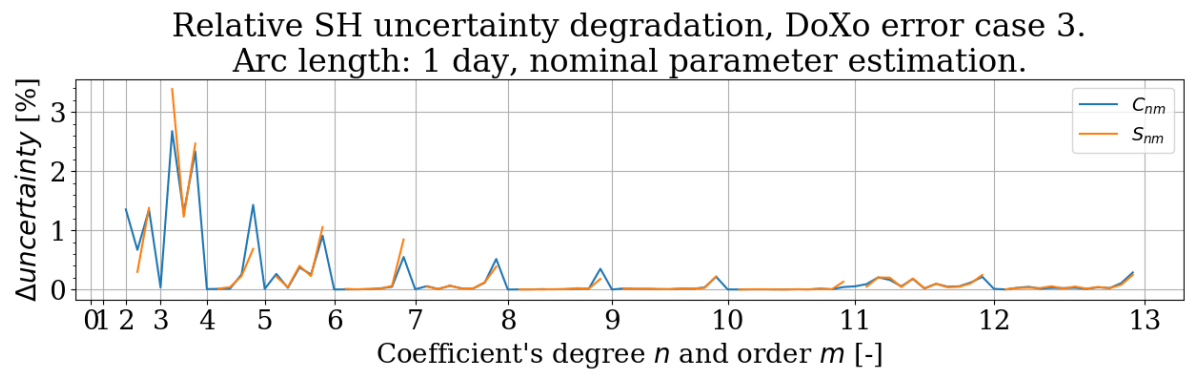


Figure A.50: SH uncertainty improvement using both Doppler and crossover measurements, DoXo error case 3.

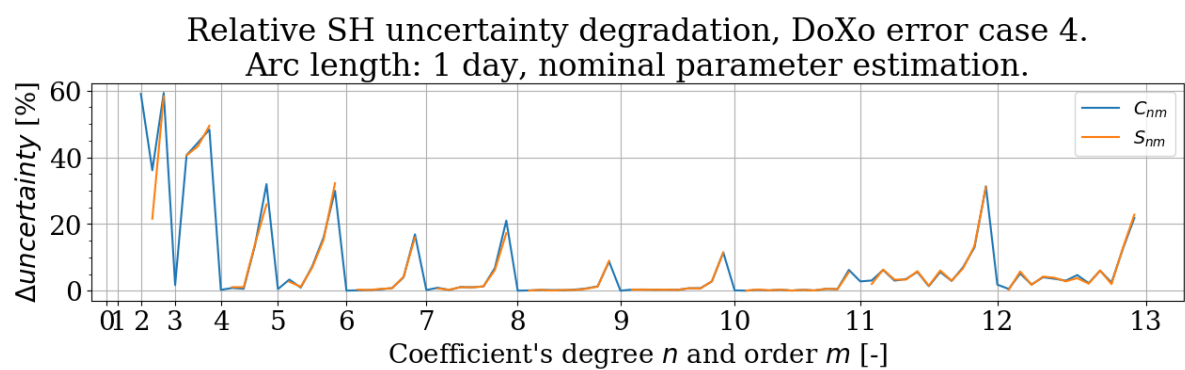


Figure A.51: SH uncertainty improvement using both Doppler and crossover measurements, DoXo error case 4.

A.10. Effect of Estimated Parameters

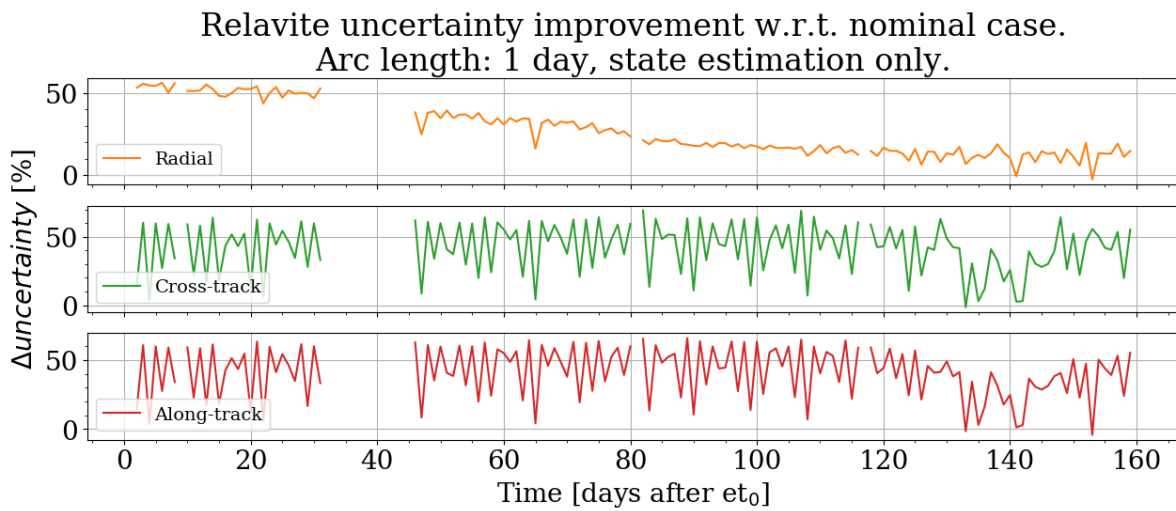


Figure A.52: Dopp position uncertainty improvement w.r.t. nominal case when estimating fewer parameters.

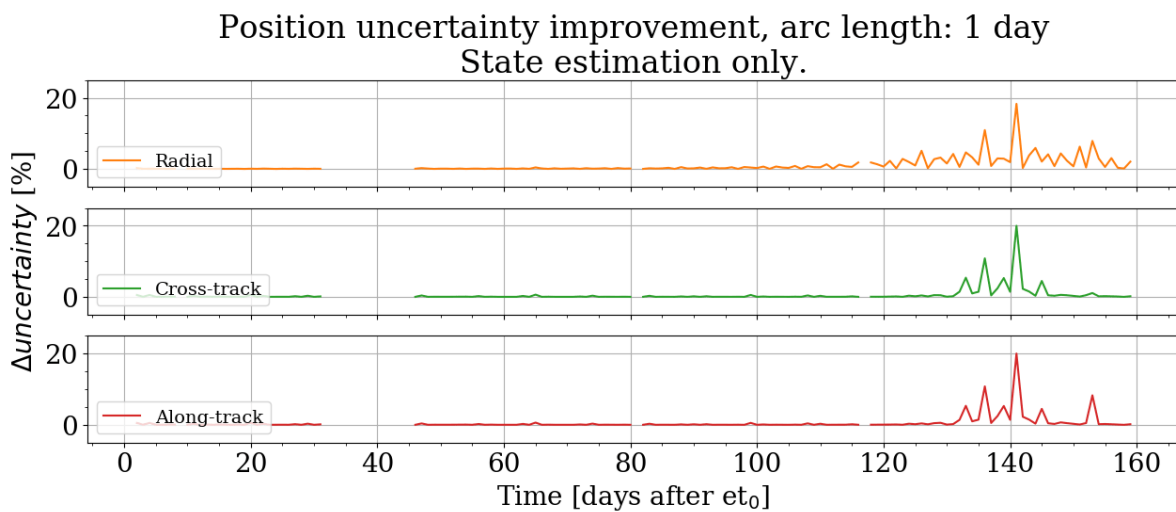


Figure A.53: DoXo position uncertainty improvement when estimating fewer parameters.

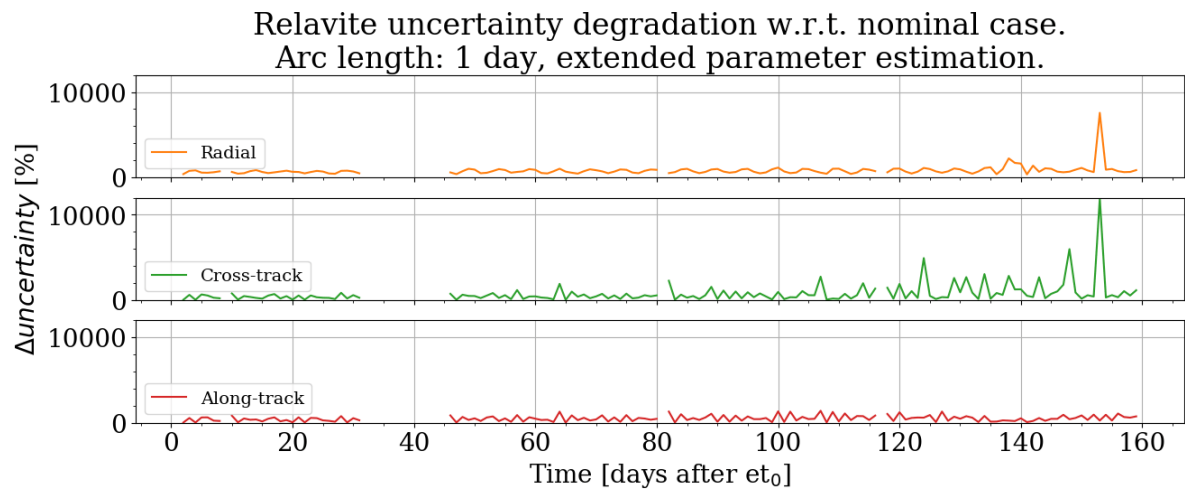


Figure A.54: Dopp position uncertainty degradation w.r.t. nominal case when estimating additional parameters.

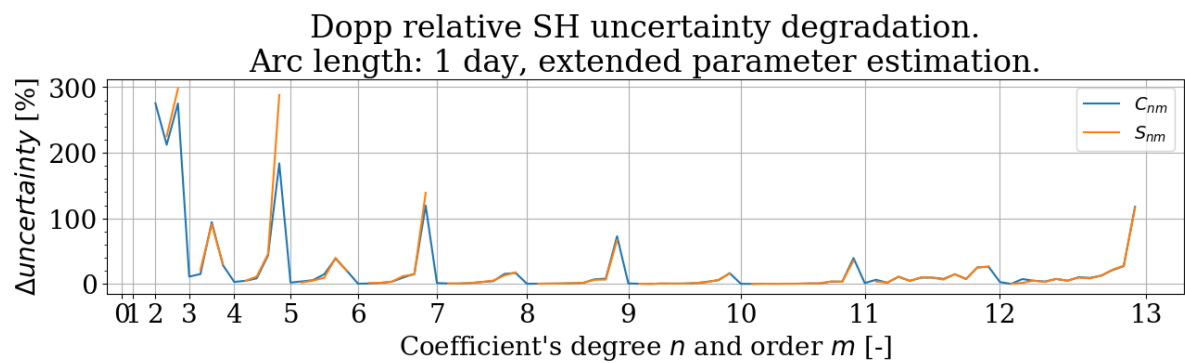


Figure A.55: Dopp SH uncertainty degradation w.r.t. nominal case when estimating additional parameters.

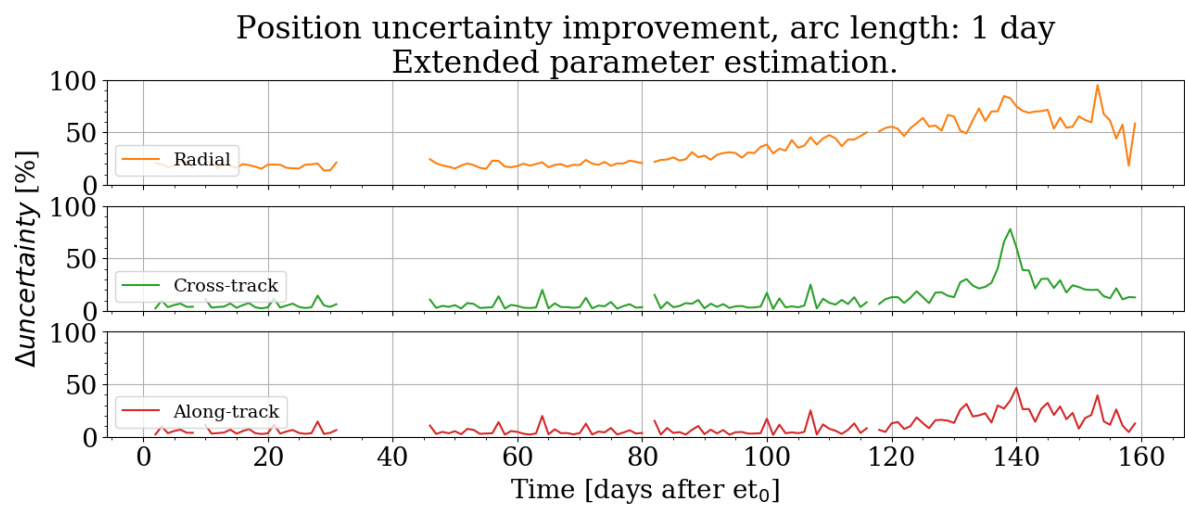


Figure A.56: DoXo position uncertainty improvement when estimating additional parameters.

A.11. Crossover Only

Velocity uncertainty. Crossover data only, arc length: 1 day
State estimation only.

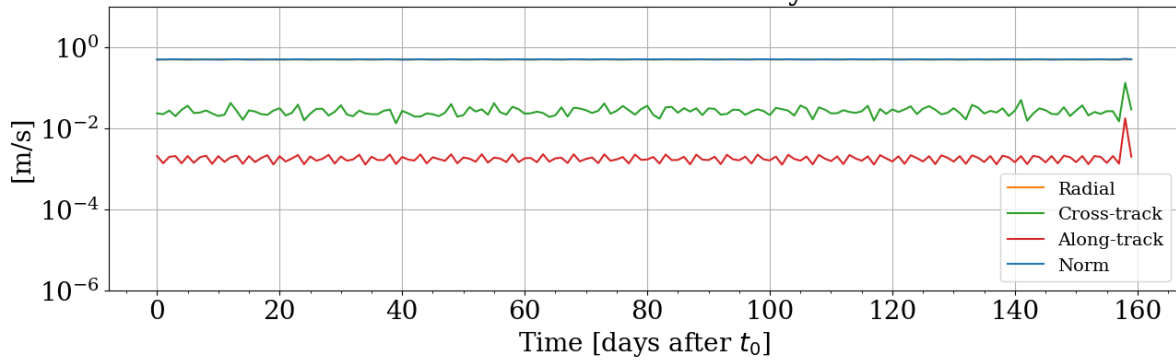


Figure A.57: Velocity uncertainty using crossover measurements only, arc length: 1 day. State estimation only.

Velocity uncertainty. Crossover data only, arc length: 1 day
Nominal parameter estimation.

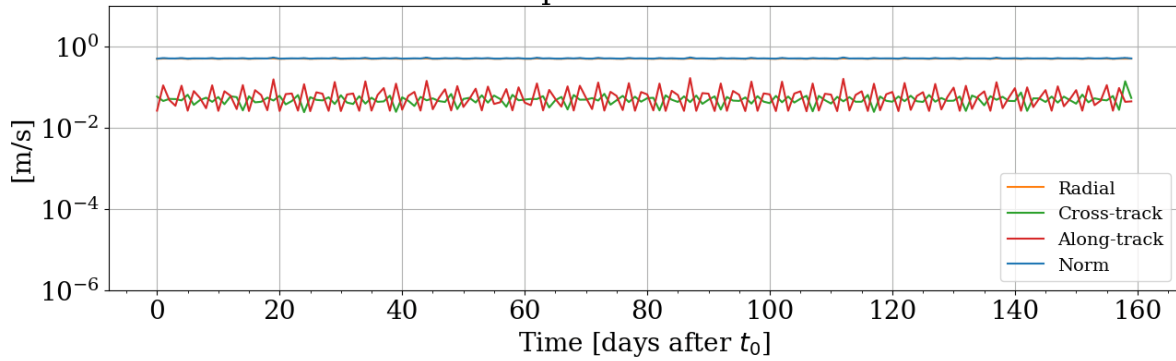


Figure A.58: Velocity uncertainty using crossover measurements only, arc length: 1 day. Nominal parameter estimation.

Bibliography

- Acton, C. H. (1996). Ancillary data services of nasa's navigation and ancillary information facility. *Planetary and Space Science*, 44(1):65 – 70. Planetary data system.
- Alday, J., Roth, L., and Ivchenko, N. (2017). New constraints on ganymede's hydrogen corona: Analysis of lyman- α emissions observed by hst/stis between 1998 and 2014. *Planetary and Space Science*, 148:35 – 44.
- Anderson, J. D., Lau, E. L., Sjogren, W. L., Schubert, G., and Moore, W. B. (1996). Gravitational constraints on the internal structure of ganymede. *Nature*, 384:541–543.
- Anderson, J. D., Schubert, G., Jacobson, R. A., Lau, E. L., Moore, W. B., and Palguta, J. L. (2004). Discovery of mass anomalies on ganymede. *Science*, 305(5686):989–991.
- Bahloul, S. (2013). Effect of planetary thermal radiation and reflected sunlight on spacecraft trajectories: Application to mercury and the bepicolombo mission. Master's thesis, Technische Universität Berlin.
- Bauer, S., Hussmann, H., Oberst, J., Dirkx, D., Mao, D., Neumann, G., Mazarico, E., Torrence, M., McGarry, J., Smith, D., and Zuber, M. (2016). Demonstration of orbit determination for the lunar reconnaissance orbiter using one-way laser ranging data. *Planetary and Space Science*, 129:32 – 46.
- Baù, G., Bombardelli, C., Peláez, J., and Lorenzini, E. (2015). Non-singular orbital elements for special perturbations in the two-body problem. *Monthly Notices of the Royal Astronomical Society*, 454(3):2890–2908.
- Berquin, Y., Kofman, W., Herique, A., Alberti, G., and Beck, P. (2013). A study on ganymede's surface topography: Perspectives for radar sounding. *Planetary and Space Science*, 77:40 – 44.
- Bonanno, C. and Milani, A. (2002). Symmetries and rank deficiency in the orbit determination around another planet. In *Modern Celestial Mechanics: From Theory to Applications*. Springer Netherlands.
- Boutonet, A. (2019). Juice crema 3.0 setting. Email from A. Boutonet (Mission Analyst for the JUICE mission) on 21.05.2019.
- Campbell, J. K. and Synnott, S. P. (1985). Gravity field of the Jovian system from Pioneer and Voyager tracking data. *The Astronomical Journal*, 90:364–372.
- Cappuccio, P. and Cascioli, G. (2018). Esa's juice end-to-end orbit determination simulation to calibrate on-board accelerometer. In *14th Pegasus Student Conference*.
- Cook, G. (1964). The effect of aerodynamic lift on satellite orbits. *Planetary and Space Science*, 12(11):1009 – 1020.
- Dirkx, D. (2015). *Interplanetary laser ranging: Analysis for implementation in planetary science missions*. Phd, Delft University of Technology.

- Dirkx, D. (2019). Crossover partials. Email from 03.05.2019.
- Dirkx, D., Gurvits, L., Lainey, V., Lari, G., Milani, A., Cimò, G., Bocanegra-Bahamon, T., and Visser, P. (2017). On the contribution of pride-juice to jovian system ephemerides. *Planetary and Space Science*, 147:14 – 27.
- Dirkx, D., Prochazka, I., Bauer, S., Visser, P., Noomen, R., Gurvits, L. I., and Vermeersen, B. (2018). Laser and radio tracking for planetary science missions - a comparison. *Journal of Geodesy*.
- Enright, P. and Wong, E. (1994). Propellant slosh models for the cassini spacecraft. In *AIAA Meeting Papers*. Jet Propulsion Laboratory, National Aeronautics and Space Administration.
- Erd, C. (2019). Juice manoeuvre estimates. Telecon with Dr. Christian Erd (JUICE Mission Performance Manager) on 18.06.2019.
- ESA (2011). Juice assessment study report (yellow book). Technical Report 1.0, ESA.
- ESA (2014). Juice definition study report (red book). Technical Report 1.0, ESA.
- ESA (2018a). official juice website. 2018-09-25, <http://sci.esa.int/juice/>.
- ESA (2018b). Sentinel-3 altimetry. 2018-12-21, <https://sentinel.esa.int/web/sentinel/user-guides/sentinel-3-altimetry>.
- ESOC (2015). Consolidated report on mission analysis (crema). Technical Report 3.0, ESA. 2019-02-20, <https://www.cosmos.esa.int/web/spice/spice-for-juice>.
- Estrack (2019). Malargüe station, deep space antenna 3. https://www.esa.int/Our_Activities/Operations/Estrack/Malarguee_-_DSA_3, last visited 25.06.2019.
- Fanale, F. P., Granahan, J. C., McCord, T. B., Hansen, G., Hibbitts, C. A., Carlson, R., Matson, D., Ocampo, A., Kamp, L., Smythe, W., Leader, F., Mehlman, R., Greeley, R., Sullivan, R., Geissler, P., Barth, C., Hendrix, A., Clark, B., Helfenstein, P., Veverka, J., Belton, M. J., Becker, K., Becker, T., and the Galileo NIMS, SSI, U. i. t. (1999). Galileo's multiinstrument spectral view of europa's surface composition. *Icarus*, 139(2):179 – 188.
- Ferraz-Mello, S. (2003). Celestial mechanics and dynamical astronomy. *Springer*, 87.
- Folkner, W. M., Iess, L., Anderson, J. D., and Asmar, S. W. (2017). Jupiter gravity field estimated from the first two juno orbits. *Geophysical Research Letters*, 44(10):4694–4700.
- for Global Earth Models (ICGEM), I. C. (2018). Gravity field models. 2018-10-29, <http://icgem.gfz-potsdam.de/home>.
- Genova, A., Goossens, S., Lemoine, F. G., Mazarico, E., Neumann, G. A., Smith, D. E., and Zuber, M. T. (2016). Seasonal and static gravity field of mars from mgs, mars odyssey and mro radio science. *Icarus*, 272:228 – 245.
- Grasset, O., Dougherty, M., Coustenis, A., Bunce, E., Erd, C., Titov, D., Blanc, M., Coates, A., Drossart, P., Fletcher, L., Hussmann, H., Jaumann, R., Krupp, N., Lebreton, J.-P., Prieto-Ballesteros, O., Tortora, P., Tosi, F., and Hoolst, T. V. (2013). Jupiter icy moons explorer (juice): An esa mission to orbit ganymede and to characterise the jupiter system. *Planetary and Space Science*, 78:1 – 21.

- Greenberg, R. (1989). Time-varying orbits and tidal heating of the galilean satellites. *NASA SPECIAL PUBLICATION SERIES*.
- Gunderson, K., Thomas, N., and Rohner, M. (2006). A laser altimeter performance model and its application to bela. *IEEE TRANSACTIONS ON GEOSCIENCE AND REMOTE SENSING*, 44(11):3308–3319.
- Hussmann, H., Shoji, D., Steinbruegge, G., Stark, A., and Sohl, F. (2016). Constraints on dissipation in the deep interiors of ganymede and europa from tidal phase-lags. *Celestial Mechanics and Dynamical Astronomy*, 126(1):131–144.
- Hussmann, H. and Spohn, T. (2004). Thermal-orbital evolution of io and europa. *Icarus*, 171(2):391 – 410.
- Iess, L. (2019). 3gm data specification. Email from Prof. Luciano Iess (Primary Investigator for 3GM) on 24.04.2019.
- Iess, L., Benedetto, M. D., James, N., Mercolino, M., Simone, L., and Tortora, P. (2014). Astra: Interdisciplinary study on enhancement of the end-to-end accuracy for spacecraft tracking techniques. *Acta Astronautica*, 94(2):699 – 707.
- Iess, L., Folkner, W. M., Durante, D., Parisi, M., and Kaspi, Y. (2018). Measurement of jupiter’s asymmetric gravity field. *Nature*, 555(8):220–222.
- Ip, W.-H., Williams, D. J., McEntire, R. W., and Mauk, B. H. (1998). Ion sputtering and surface erosion at europa. *Geophysical Research Letters*, 25(6):829–832.
- Jacobson, R., R. Haw, T. M., and Antreasian, P. (1999). A comprehensive orbit reconstruction for the galileo prime mission in the j2000 system. *Advances in the Astronautical Sciences*, 103.
- Jacobson, R. A. (2013). The gravitational fields of the galilean satellites – revisited. In *American Astronomical Society, DPS meeting 45, id.418.06*. . Specific Doppler precision confirmed by email on the 06.06.2019.
- Jara-Oru e, H. and Vermeersen, B. (2016). Tides on jupiter’s moon ganymede and their relation to its internal structure. *Netherlands Journal of Geosciences*, 95(02):191–201.
- Jia, X., Kivelson, M. G., Khurana, K. K., and Kurth, W. S. (2018). Evidence of a plume on europa from galileo magnetic and plasma wave signatures. *Nature Astronomy*, 2:459–464.
- Kamata, S., Kimura, J., Matsumoto, K., Nimmo, F., Kuramoto, K., and Namiki, N. (2016). Tidal deformation of ganymede: Sensitivity of love numbers on the interior structure. *Journal of Geophysical Research: Planets*, 121(7):1362–1375.
- Kaula, W. (1966). *Theory of Satellite Geodesy: Applications of Satellites to Geodesy*. Dover Publications, Blaisdell, Waltham.
- Kim, M. C. (1997). Theory of satellite ground-track crossovers. *Journal of Geodesy*, 71(12):749–767.
- Kivelson, M., Khurana, K., and Volwerk, M. (2002). The permanent and inductive magnetic moments of ganymede. *Icarus*, 157(2):507 – 522.

- Kivelson, M. G., Khurana, K. K., Russell, C. T., Walker, R. J., Warnecke, J., Coroniti, F. V., Polansky, C., Southwood, D. J., and Schubert, G. (1996). Discovery of ganymede's magnetic field by the galileo spacecraft. *Nature*, 384:537–541.
- Knocke, P., Ries, J., and Tapley, B. (1988). *Earth radiation pressure effects on satellites*. The University of Texas at Austin.
- Konopliv, A., Park, R., and Ermakov, A. (2020). The mercury gravity field, orientation, love number, and ephemeris from the messenger radiometric tracking data. *Icarus*, 335:113386.
- Konopliv, A. S. and Yoder, C. F. (1996). Venusian k2 tidal love number from magellan and pvo tracking data. *Geophysical Research Letters*, 23(14):1857–1860.
- Lainey, V., Arlot, J.-E., Karatekin, O., and Van Hoolst, T. (2009). Strong tidal dissipation in io and jupiter from astrometric observations. *Nature*, 459:957.
- Lee, A. Y. and Stupik, J. (2015). Inflight characterization of the cassini spacecraft propellant slosh and structural frequencies. *Jet Propulsion Laboratory, National Aeronautics and Space Administration*.
- Lingenauber, K. (2019). Gala instrument requirements document jui-dlrp-gal-rs-11011. Technical Report 4.0, DLR PF.
- Lissauer, J. J. and de Pater, I. (2013). *Fundamental Planetary Science*. Cambridge University Press.
- Marabucci, M. (2012). *The Determination of the Hermean Gravity and Topography from Radio Science and Laser Altimeter data of the Mission Bepi Colombo*. Phd, Sapienza Universita di Roma.
- Marconi, M. (2007). A kinetic model of ganymede's atmosphere. *Icarus*, 190(1):155 – 174.
- Mazarico, E., Barker, M. K., Neumann, G. A., Zuber, M. T., and Smith, D. E. (2014). Detection of the lunar body tide by the lunar orbiter laser altimeter. *Geophysical Research Letters*, 41(7):2282–2288.
- Mazarico, E., Neumann, G. A., Barker, M. K., Goossens, S., Smith, D. E., and Zuber, M. T. (2018). Orbit determination of the lunar reconnaissance orbiter: Status after seven years. *Planetary and Space Science*, 162:2 – 19.
- Mazarico, E., Neumann, G. A., Rowlands, D. D., and Smith, D. E. (2010). Geodetic constraints from multi-beam laser altimeter crossovers. *Journal of Geodesy*, 84(6):343–354.
- Mazarico, E., Rowlands, D. D., and Neumann, G. A. (2011). Orbit determination of the lunar reconnaissance orbiter. *Journal of Geodesy*, 86(3):193–207.
- McCarthy, J. and T., M. (1977). A computer efficient model of earth albedo satellite effects. *NASA Goddard Space Flight Center*.
- McCord, T. B., Hansen, G. B., Fanale, F. P., Carlson, R. W., Matson, D. L., Johnson, T. V., Smythe, W. D., Crowley, J. K., Martin, P. D., Ocampo, A., Hibbitts, C. A., Granahan, J. C., and (1998). Salts on europa's surface detected by galileo's near infrared mapping spectrometer. *Science*, 280(5367):1242–1245.
- McCord, T. B., Hansen, G. B., and Hibbitts, C. A. (2001). Hydrated salt minerals on ganymede's surface: Evidence of an ocean below. *Science*, 292(5521):1523–1525.

- Montenbruck, O. and Gill, E. (2000). *Satellite Orbits: Models, Methods and Applications*. Springer Berlin Heidelberg.
- Moore, W. B. and Schubert, G. (2000). The tidal response of europa. *Icarus*, 147(1):317 – 319.
- Moore, W. B. and Schubert, G. (2003). The tidal response of ganymede and callisto with and without liquid water oceans. *Icarus*, 166(1):223–226.
- Morrison, D. and Matthews, M. S. (1982). *Satellites of Jupiter*. Tucson, Ariz. : University of Arizona Press.
- NAIF (2018). Spice toolkit. 2018-12-21, <https://naif.jpl.nasa.gov/naif/toolkit.html>.
- NASA (2018). Planetary fact sheets. 2018-10-26, <https://nssdc.gsfc.nasa.gov/planetary/planetfact.html>.
- Neumann, G. A., Rowlands, D. D., Lemoine, F. G., Smith, D. E., and Zuber, M. T. (2001). Crossover analysis of mars orbiter laser altimeter data. *Journal of Geophysical Research: Planets*, 106(E10):23753–23768.
- Niemann, H. B., Atreya, S. K., Carignan, G. R., Donahue, T. M., Haberman, J. A., Harpold, D. N., Hartle, R. E., Hunten, D. M., Kasprzak, W. T., Mahaffy, P. R., Owen, T. C., and Way, S. H. (1998). The composition of the jovian atmosphere as determined by the galileo probe mass spectrometer. *Journal of Geophysical Research: Planets*, 103(E10):22831–22845.
- Nimmo, F. (2004). Non-newtonian topographic relaxation on europa. *Icarus*, 168(1):205 – 208.
- Pappalardo, R. T. and Collins, G. C. (2005). Strained craters on ganymede. *Journal of Structural Geology*, 27(5):827 – 838.
- Parisi, M. and Iess, L. (2012). Multi-arc and batch-sequential filters for the orbit determination of esa’s juice mission. In *23rd International Symposium on Space Flight Dynamics*.
- Peale, S. J. (2003). Tidally induced volcanism. *Celestial Mechanics and Dynamical Astronomy*, 87(1):129–155.
- Peale, S. J., Cassen, P., and Reynolds, R. T. (1979). Melting of io by tidal dissipation. *Science*, 203(4383):892–894.
- Petit, G. and (eds.), B. L. (2010). *IERS Conventions*. Verlag des Bundesamts für Kartographie und Geodäsie.
- Plainaki, C., Milillo, A., and Massetti, S. (2015). The h₂o and o₂ exospheres of ganymede: The result of a complex interaction between the jovian magnetospheric ions and the icy moon. *Icarus*, 245:306 – 319.
- Ragent, B., Colburn, D. S., Rages, K. A., Knight, T. C. D., Avrin, P., Orton, G. S., Yanamandra-Fisher, P. A., and Grams, G. W. (1998). The clouds of jupiter: Results of the galileo jupiter mission probe nephelometer experiment. *Journal of Geophysical Research: Planets*, 103(E10):22891–22909.
- Rech, M. (2019). Gala transceiver system mass budget. Technical Report 2.0, Hensoldt Optonics GmbH.

- Rievers, B., Bremer, S., List, M., Lämmerzahl, C., and Dittus, H. (2010). Thermal dissipation force modeling with preliminary results for pioneer 10/11. *Acta Astronautica*, 66(3):467 – 476.
- Rievers, B. and Lämmerzahl, C. (2011). High precision thermal modeling of complex systems with application to the flyby and pioneer anomaly. *Annalen der Physik*, 523(6):439–449.
- Rowlands, D. D., Lemoine, F. G., Chinn, D. S., and Luthcke, S. B. (2008). A simulation study of multi-beam altimetry for lunar reconnaissance orbiter and other planetary missions. *Journal of Geodesy*, 83(8):709.
- Rowlands, D. D., Pavlis, D. E., Lemoine, F. G., Neumann, G. A., and Luthcke, S. B. (1999). The use of laser altimetry in the orbit and attitude determination of mars global surveyor. *Geophysical Research Letters*, 26(9):1191–1194.
- Rückriemen, T., Breuer, D., and Spohn, T. (2015). The Fe snow regime in Ganymede's core: A deep-seated dynamo below a stable snow zone. *Journal of Geophysical Research-Planets*, 120(6):1095–1118.
- Rückriemen, T., Breuer, D., and Spohn, T. (2018). Top-down freezing in a Fe-FeS core and Ganymede's present-day magnetic field. *Icarus*.
- Showman, A. P., Malhotra, and Renu (1999). The galilean satellites. *Science*, 286(5437):77–84.
- Spohn, T. and Schubert, G. (2003). Oceans in the icy galilean satellites of jupiter? *Icarus*, 161(2):456 – 467.
- Stark, A. (2019). Crossover determination algorithm. Email from A. Stark (DLR, alexander.stark@dlr.de) on 06.2019.
- Steinbruegge, G. (2018). *Tidal deformation of planets and satellites, Models and methods for laser- and radar altimetry*. Phd, Technical University Berlin.
- Steinbruegge, G., Stark, A., Hussmann, H., Sohl, F., and Oberst, J. (2015). Measuring tidal deformations by laser altimetry. a performance model for the ganymede laser altimeter. *Planetary and Space Science*, 117:184–191.
- Steinbrügge, G., Stark, A., Hussmann, H., Wickhusen, K., and Oberst, J. (2018). The performance of the bepicolombo laser altimeter (bela) prior launch and prospects for mercury orbit operations. *Planetary and Space Science*, 159:84 – 92.
- Steinke, T. (2015). Ganymede's rotational state and interior structure from laser altimetry - a pre-mission analysis. Msc. thesis, Karlsruhe Institute of Technologie.
- Strom, R. G., Woronow, A., and Gurnis, M. (1981). Crater populations on ganymede and callisto. *Journal of Geophysical Research: Space Physics*, 86(A10):8659–8674.
- Tai, C.-K. (1989). An efficient algorithm for computing the crossovers in satellite altimetry. *Journal of Atmospheric and Oceanic Technology*, 6(1):13–18.
- Thomas, N., Spohn, T., Barriot, J.-P., Benz, W., Beutler, G., Christensen, U., Dehant, V., Fallnich, C., Giardini, D., Groussin, O., Gunderson, K., Hauber, E., Hilchenbach, M., Iess, L., Lamy, P., Lara, L.-M., Lognonné, P., Lopez-Moreno, J., Michaelis, H., Oberst, J., Resendes, D., Reynaud, J.-L., Rodrigo, R., Sasaki, S., Seiferlin, K., Wiczorek, M., and Whitby, J. (2007).

- The bepicolombo laser altimeter (bela): Concept and baseline design. *Planetary and Space Science*, 55(10):1398 – 1413.
- Thomas, P. J. and Schubert, G. (1986). Crater relaxation as a probe of europa's interior. *Journal of Geophysical Research: Solid Earth*, 91(B4):453–459.
- Tobie, G., Mocquet, A., and Sotin, C. (2005). Tidal dissipation within large icy satellites: Applications to europa and titan. *Icarus*, 177(2):534 – 549. Europa Icy Shell.
- TUDelft (2019). Tu delft astrodynamics toolbox. 2019-06-01, <http://tudat.tudelft.nl/index.html>.
- Urkullu, G., de Bustos, I. F., García-Marina, V., and Uriarte, H. (2019). Direct integration of the equations of multibody dynamics using central differences and linearization. *Mechanism and Machine Theory*, 133:432 – 458.
- Vallat, C. (2019). Juice downlink times. Email from Dr. Claire Vallat (Operation Scientist for the JUICE mission) on 22.05.2019.
- van der Wal, W. (2017). Lecture notes for satellite orbit determination.
- Villamil, S. (2019). Literature study: On the effect of laser altimeter crossover observables on orbit determination based on the juice mission. Technical report, Delft University of Technology.
- Wakker, K. F. (2015). *Fundamentals of Astrodynamics*. Delft University of Technology.
- Wang, H. and Luo, B. (2017). Fast numerical algorithm for the calculation of altimetric crossovers from satellite ground tracks. *GEOMATICS AND INFORMATION SCIENCE OF WUHAN UNIVERSITY*, 42(3):293.
- Yoder, C. F. (1979). How tidal heating in io drives the galilean orbital resonance locks. *Nature*, 279(5716):767–770.
- Yoder, C. F. and Peale, S. J. (1981). The tides of io. *Icarus*, 47(1):1 – 35.
- Zimmer, C., Khurana, K. K., and Kivelson, M. G. (2000). Subsurface oceans on europa and callisto: Constraints from galileo magnetometer observations. *Icarus*, 147(2):329 – 347.